The Interaction between Waves and an Overlying Airflow

by

Duncan Black

A dissertation submitted to the University of London for the degree of Doctor of Philosophy and for the Diploma of the Imperial College of Science, Technology and Medicine.

Imperial College of Science,
Technology and Medicine.

March 1998

PREFACE

The work described in this dissertation was conducted at the Department of Civil Engineering, Imperial College of Science, Technology and Medicine, between July 1993 and October 1996.

The author wishes to express his sincere thanks for the supervision, advice and encouragement provided by Dr. C. Swan. The author would also like to thank Professor P. Holmes and Dr. J.D. Hardwick for their advice and helpful comments. Finally the author is also indebted to Mr. W. Bobinski, Mr. D. Morris and Mr J. Mires for their technical assistance in the laboratory.

This dissertation describes work undertaken solely by the author, with no part having been submitted to any other university.

Imperial College of Science,
Technology and Medicine.

Duncan Black

ABSTRACT

This dissertation examines the interaction between a series of progressive gravity waves and an overlying airflow. A critical review of the existing literature is made, from which it is concluded that although a large number of wind-wave interactions have been proposed, few have been verified experimentally. Furthermore, virtually no consideration has been given to the effect of the airflow on the underlying wave motion. A comprehensive experimental investigation of the interaction between wind and waves has therefore been undertaken.

In respect of the airflow, a complete set of kinematics measurements, involving both horizontal and vertical velocity data, is presented. The mean, wave-induced and fluctuating velocities are presented in a wave-following frame of reference. The flow streamlines are deduced from the measured velocity data, and the structure of the airflow examined in detail. Analysis of the velocity profiles using boundary layer theory enables the effects of the flow structure identified above to be quantified and an assessment of the surface stresses made.

A corresponding set of kinematics measurements were undertaken in the underlying water flow. The wind-induced currents and wave kinematics are examined. Numerical models to predict the wave motion in combined wind-wave field are developed. The models incorporate the effects of a wind-induced current and the varying surface stresses, and allow the relative importance of each of these effects to be investigated.

Furthermore, measurements of the water surface elevation are used to investigate the modification to the underlying long waves caused by the airflow, and the nature of the superposed wind-waves. The variation in the properties of the wind-generated waves with the phase of the long waves are also examined. Finally, the fundamental mechanisms of wind-wave interaction are considered, and the relative importance of the various mechanisms assessed. The implications for the offshore engineer, in terms of wind loading, gas ventilation and wave loading are outlined.

CONTENTS

PREFACE 2
ABSTRACT 3
CONTENTS 4
LIST OF FIGURES 8
LIST OF TABLES 11
NOMENCLATURE 12

1. INTRODUCTION 15
   1.1 Background 15
   1.2 Engineering Applications 15
   1.3 The Present Work 17
2. LITERATURE REVIEW AND THEORETICAL BACKGROUND 20
   2.1 Airflow 20
      2.1.1 Theoretical Descriptions 21
      2.1.2 Experimental Measurements 31
   2.2 Water Flow 37
      2.2.1 Theoretical Descriptions 38
      2.2.2 Experimental Measurements 39
   2.3 Summary 41
3. EXPERIMENTAL APPARATUS, DATA ANALYSIS, AND PRELIMINARY RESULTS 42
   3.1 The Wave Flume 42
   3.2 The Wind Tunnel 42
      3.2.1 The Working Section 44
      3.2.2 Fan 44
      3.2.3 Wide angle diffuser 46
      3.2.4 Settling Chamber 46
      3.2.5 Contraction 48
      3.2.6 The Transition Region 48
      3.2.7 Exit Diffuser 50

3.3 Water Surface Elevation Measurements 50
3.4 Kinematics Measurements 51
3.5 Signal Decomposition 52
3.6 Analysis Routines 53
3.7 Preliminary Results 56
3.7.1 Wind tunnel 56
3.7.2 Water Waves 59
3.7.3 Laser Doppler Anemometer. 62
4. AIR KINEMATICS MEASUREMENTS 64
4.1 Experimental Programme 64
4.2 Experimental Methods and Data Analysis 66
4.3 Time Averaged Horizontal Velocity Profiles 68
4.4 Combined Wind and Wave Flow Structure 71
4.4.1 $U_\infty = 5.1$m/s 71
4.4.2 $U_\infty = 3.1$ m/s 78
4.4.3 $U_\infty = 2.4$ m/s 85
4.5 Streamline Amplitude 93
4.6 Wave-Induced Velocity Amplitude 95
4.7 Time Averaged Turbulent Velocity Profiles 97
4.8 Phase Averaged Turbulent Velocity Profiles 101
5. AIRFLOW PROFILE ANALYSIS 104
5.1 Boundary Layer Theory 104
5.2 Time Averaged Horizontal Velocity Profile Analysis 110
5.3 Phase Averaged Horizontal Velocity Profile Analysis. 117
5.3.1 Friction Velocity 120
5.3.2 'Constant' C 123
5.3.3 Matched Height 126
5.3.4 Wake Parameter and Pressure Gradients. 128
5.4 Calculation of Surface Stresses 134
5.4.1 Normal Stress 134
5.4.2 Shear Stress 140

6. WATER KINEMATICS MEASUREMENTS 145
6.1 Experimental Programme 145
6.2 Experimental Methods and Data Analysis 145
6.3 Time Averaged Horizontal Velocity Profiles 146
6.3.1 Wind only Currents 148
6.3.2 Wave only Current 158
6.3.3 Currents in Combined Wind and Waves 159
6.4 Phase Averaged Velocities 162
6.4.1 Phase Average Velocity Profiles 162
6.4.2 Phase Averaged Wind-Induced Velocities 168
7. COMBINED WIND-WAVE-CURRENT MODEL 174
7.1 Introduction 174
7.2 Wave-Current Interaction 175
7.2.1 Overview 175
7.2.2 Wave-Current Model 177
7.3 Wind-Wave Interactions 181
7.3.1 Overview 181
7.3.2 Wind-Wave Model 181
7.4 Comparison between Experimental and Theoretical Results 185
7.4.1 Wave-Current Model 186
7.4.2 Wind-Wave Model 191
7.4.3 Concluding Remarks 194
8. WATER SURFACE ELEVATION MEASUREMENTS 196
8.1 Experimental Programme 196
8.2 Experimental Methods and Data Analysis 197
8.3 Long Wave Analysis 198
8.3.1 Wave Forms 198
8.3.2 Phase Velocity 201
8.3.3 Wave Spectra 203
8.4 Wind-Wave Analysis 205
8.4.1 Wave Spectra 205
8.4.2 Frequency 214

8.4.3 Phase Velocity or Wave Celerity 217
8.4.4 Amplitude 219
8.4.5 Wavenumber 224
8.4.6 Surface Roughness 226
9. SUMMARY AND CONCLUSIONS 232
9.1 Introduction 232
9.2 Experimental 232
9.3 Airflow 233
9.4 Water Kinematics 235
9.5 Surface Elevation 237
9.6 Practical Applications 238
9.7 Further Work 239

CITED LITERATURE 241

APPENDIX A: WAVE-CURRENT MODEL 250
APPENDIX B: WIND-WAVE MODEL 253
APPENDIX C: THIRD ORDER IRROTATIONAL WAVE THEORY 254
APPENDIX D: THE VALIDITY OF VARIOUS WAVE THEORIES 257

LIST OF FIGURES

Figure 2.1: Streamlines in the airflow predicted by Lighthill (1962) 23
Figure 2.2: Surface pressure and shear stress (Gent and Taylor, 1976) 26
Figure 2.3: Streamline patterns (Gent and Taylor, 1977) 27
Figure 2.4: Sketch of streamline pattern (Hsu, Hsu and Street, 1981) 35
Figure 3.1: Wind-wave interaction facility 43
Figure 3.2: Working section 45
Figure 3.3: Wide angle diffuser, settling chamber and contraction 47
Figure 3.4: Transition region 47
Figure 3.5: Exit diffuser 49
Figure 3.6: Air velocity signal decomposition below crest 55
Figure 3.7: Air velocity signal decomposition above crest 55
Figure 3.8: Air velocity sample output 57
Figure 3.9: Flat bed velocity spectrum 57
Figure 3.10: Velocity profiles with fetch 57
Figure 3.11: Velocity profiles across tank 57
Figure 3.12: RMS turbulent velocity fluctuations across tank 57
Figure 3.13: Time averaged horizontal velocity profiles over flat bed 60
Figure 3.14: Static pressure variation with fetch at the tunnel roof 61
Figure 3.15: Sample output of waves only 61
Figure 3.16: Growth in wave amplitude with fetch 61
Figure 3.17: Change in wave frequency with fetch 61
Figure 3.18: Measured velocity traces compared with second order theory 63
Figure 4.1: Airflow wave following co-ordinate definition sketch 67
Figure 4.2: Time averaged horizontal velocity profiles - combined wind and waves ... 70
Figure 4.3: Time averaged horizontal velocity profiles - comparison 70
Figure 4.4: Streamlines from experimental data for U_∞ = 5.1 m/s 72
Figure 4.5: Experimental streamlines in transformed co-ordinates 73
Figure 4.6: Phase of maxima and minima streamline elevations 73
Figure 4.7: Phase averaged horizontal velocities at given elevations 75
Figure 4.8: Phase averaged velocity profiles at given phases 75

Figure 4.9: Phase of maxima and minima horizontal velocity 77
Figure 4.10: Streamlines from experimental data for U_∞ = 3.1 m/s 79
Figure 4.11: Phase averaged horizontal velocities at given elevations 80
Figure 4.12: Phase averaged velocity profiles at given phase 80
Figure 4.13: Phase of maxima and minima horizontal velocity 82
Figure 4.14: Phase of maxima and minima streamline elevations 82
Figure 4.15: Airflow recirculation cell for U_∞ = 3.1 m/s 84
Figure 4.16: Streamlines from experimental data for U_∞ = 2.4 m/s 86
Figure 4.17: Airflow recirculation cell for U_∞ = 2.4 m/s 87
Figure 4.18: Phase averaged horizontal velocities at given elevations 88
Figure 4.19: Phase averaged velocity profiles at given phase 88
Figure 4.20: Phase of maxima and minima streamline elevations 90
Figure 4.21: Phase of maxima and minima horizontal velocity 91
Figure 4.22: Profile of streamline amplitude with depth (U_∞ = 2.4 m/s) 91
Figure 4.23: Profile of streamline amplitude with depth (all cases) 94
Figure 4.24: Profile of amplitude of wave-induced horizontal velocity 96
Figure 4.25: Profile of amplitude of wave-induced vertical velocity 96
Figure 4.26: Time averaged normalised rms horizontal velocity profiles 98
Figure 4.27: Time averaged normalised rms vertical velocity profiles 98
Figure 4.28: Time averaged normalised rms turbulence profiles (U_∞ = 5.1 m/s) 100
Figure 4.29: Time averaged normalised rms turbulence profiles (U_∞ = 2.4 m/s) 100
Figure 4.30: Phase averaged normalised rms horizontal velocity profiles 102
Figure 5.1: Boundary layer theory definition sketch 104
Figure 5.2: Time averaged velocity profiles - combined wind and waves 111
Figure 5.3: Time averaged velocity profiles (U_∞ = 5.1 m/s) 111
Figure 5.4: Time averaged velocity profiles (U_∞ = 3.1 m/s) 112
Figure 5.5: Time averaged velocity profiles (U_∞ = 2.4 m/s) 112
Figure 5.6: Phase averaged velocity profiles (U_∞ = 5.1 m/s) 118
Figure 5.7: Phase averaged velocity profiles (U_∞ = 2.4 m/s) 118
Figure 5.8: Variation of friction velocity with phase of long wave 121
Figure 5.9: Variation of surface parameter C with phase of long wave 124

Figure 5.10: Variation of matched height with phase of long wave 127
Figure 5.11: Variation of wake parameter with phase of long wave 129
Figure 5.12: Variation of pressure gradient with phase of long wave 130
Figure 5.13: Variation of surface pressure gradient with phase of long wave 137
Figure 5.14: Variation of surface pressure with phase of long wave 138
Figure 5.15: Variation of surface shear stress with phase of long wave 142
Figure 6.1: Definition sketch 147
Figure 6.2: Wind-generated currents in the absence of waves 149
Figure 6.3: Turbulence profiles u' rms 157
Figure 6.4: Vorticity profiles 157
Figure 6.5: Wave only current 158
Figure 6.6: Wind-generated currents in the presence of long waves 160
Figure 6.7: Comparison of wind only and combined wind-wave-current profiles 163
Figure 6.8: Phase averaged velocity crest profiles for combined wind and wave 164
Figure 6.9: Phase averaged velocity amplitude profiles for combined wind-waves ... 167
Figure 6.10: Phase averaged horizontal velocities at given y^* 169
Figure 6.11: Phase averaged wind-induced horizontal velocities at given y^* 169
Figure 7.1: Wave-current model definition sketch 178
Figure 7.2: Wind-driven currents - experimental data and least squares fits 187
Figure 7.3: Comparison of wave-current theory with measured crest velocities 189
Figure 7.4: Comparison of wind-wave theory with measured crest velocities 193
Figure 8.1: Comparison between linear and measured long waves 200
Figure 8.2: Spectra for combined wind and waves 204
Figure 8.3: Wind-wave spectra 206
Figure 8.4: Spectra for decomposed wind-wave field 209
Figure 8.5: Variation of apparent frequency of wind-waves with phase 213
Figure 8.6: Effect on spectrum due to modulation in apparent frequency 213
Figure 8.7: Variation of wind-wave frequency and amplitude with long wave phase 216
Figure 8.8: Variation of wind-wave celerity and wavenumber with long wave phase 221
Figure 8.9: Variation of wind-wave steepness and roughness Reynolds number 229

LIST OF TABLES

Table 4.1: Time averaged velocity parameters 69

Table 5.1: Time averaged horizontal velocity profile parameters 114

Table 5.2: Mean and amplitude of phase averaged friction velocity. 120

Table 5.3: Mean and amplitude of phase averaged 'constant' C. 123

Table 5.4: Mean and amplitude of phase averaged matched height 126

Table 5.5: Mean and amplitude of wake parameter and pressure gradients. 131

Table 5.6: Measured surface normal stresses 136

Table 5.7: Measured surface shear stresses 143

Table 6.1: Inertial sub layer parameters from law of the wall curve-fit 150

Table 6.2: Viscous and inertial sub layer parameters 152

Table 6.3: Comparison of measured surface velocity parameters. 154

Table 6.4: Corrected values of the 'constant' C. 155

Table 6.5: Surface stresses 156

Table 6.6: Inertial sub layer best-fit parameters and layer thickness 159

Table 6.7: Surface current and non-dimensional parameters 161

Table 7.1: Coefficients of cubic polynomial curve fits to current profiles. 186

Table 7.2: Phase velocity calculated from wave-current model 188

Table 7.3: Measured surface stress coefficients 191

Table 7.4: Phase velocity calculated from the wind-wave model 192

Table 8.1: Long wave parameters 198

Table 8.2: Comparison of measured and predicted long wave phase velocity 202

Table 8.3: Combined wind and waves spectra values 205

Table 8.4: Wind only waves spectral properties 207

Table 8.5: Wind-wave frequency 214

Table 8.6: Wind-wave phase velocity 218

Table 8.7: Wind-wave amplitude 220

Table 8.8: Wind-wave wavenumber 225

Table 8.9: Wind-wave steepness ak 227

Table 8.10: Wind-wave roughness Reynolds number R_k 228

NOMENCLATURE

a	wave amplitude (half the crest to trough height).
c	wave phase velocity.
C	surface parameter.
C'	surface parameter corrected for surface current.
d	channel water depth.
e	base of natural logarithm (2.71828...).
f	frequency.
f_{app}	apparent wave frequency.
g	acceleration due to gravity.
H	air channel depth.
$\Im[\ ]$	the imaginary part of the included function.
J	the Jacobian.
k	wave number.
k_r	root mean square height of roughness elements.
p	pressure.
P,Q,R,S	coefficients of the cubic polynomial used to describe the current profile.
P_n	normal stress at air water interface.
R_k	roughness Reynolds number.
$\Re[\ ]$	the real part of the included function.
S	spectral density of free-surface displacement.
t	time.
T	wave period.
u_*	friction velocity.
U	mean velocity in the x direction.
U_s	surface velocity in water.
U_∞	mean free stream velocity.
u,v,w	velocity components in the x,y,z directions.
$\tilde{u},\tilde{v},\tilde{w}$	wave-induced velocity components in the x,y,z directions.
u',v',w'	turbulent velocity fluctuations in the x,y,z directions.
W_c	wake parameter.

x,y,z	right-handed Cartesian co-ordinate axis in which x is the fetch defined as positive in the direction of the airflow and wave propagation, and y is defined as being vertically upwards.
$\underline{x}$	position vector in x,y,z co-ordinate frame.
x^*, y^*, z^*	right-handed Cartesian co-ordinate axis transformed from x,y,z co-ordinates using the transformation defined in equation 4.1.
y_m	matched height.
z_o	roughness length.
β	ratio of the pressure gradient to the shear force.
δ	turbulent boundary layer thickness.
δ^*	displacement thickness.
δ_s	unit step function.
ϕ	phase of the long waves, where the trough is defined as zero and 1.0.
$\tilde{\eta}$	displacement of free water surface from mean water level.
κ	Karman constant 0.4.
λ	wavelength.
μ	molecular viscosity.
ν	kinematic viscosity.
π	pi (3.14159....)
ρ	fluid density.
σ	wave frequency.
τ	shear stress.
ω	vorticity.
ξ, η	orthogonal curvi-linear co-ordinates in the water.
ψ	stream function.
ζ	water surface profile.

Subscripts

a	air.
s	at the air water interface.
w	water.

Superscripts

$\overline{X}$	time averaged component.
$\widetilde{X}$	wave-induced component.
X'	turbulent fluctuating component.
$\hat{X}$	amplitude of component.

Further symbols have the meaning as defined in the text.

1. INTRODUCTION

1.1 Background

The combination of water waves with significant wind velocities is a phenomenon frequently encountered in the offshore environment. How wind and waves interact has been the subject of sustained research activity over many years. From the work of Helmholtz (1868) and Kelvin (Thomson, 1871), through to the turbulence modelling techniques used by Harris, Belcher and Street (1996), much of the research has focused on predicting the rate of wave growth.

For the engineer, the motivation for studying wind-wave interactions is not merely the determination of wave growth, nor the consequent modified wave characteristics, as in a given situation, both the wind and wave characteristics can be measured or estimated. Instead, the motivation comes from the need to extend the knowledge of the nature of the interaction between the two, and the resulting fluid kinematics. In particular, an understanding of the interaction between wind and waves has a number of important applications for the offshore engineer.

1.2 Engineering Applications

The principle application of the current work is in the calculation of the loads on offshore structures. The large waves used in design will occur during heavy storms when there will tend to be significant wind speeds. The models used to calculate the kinematics of the wave motion, and hence the wave loading, assume zero shear stress and constant atmospheric pressure at all points on the water surface. These assumptions are clearly not valid for waves in the presence of significant wind velocities, and the wave kinematics predicted when using existing irrotational models may be somewhat different to those observed. The wave loading is proportional to the square of the velocity, so even a small error in predicting the kinematics may significantly affect the wave loading. One well known effect of wind on a water surface is the generation of highly sheared currents which has been found to significantly modify the wave kinematics (Cummins and Swan, 1994a).

Wind blowing over a water wave may be expected to alter the kinematics of the underlying wave but, conversely, the kinematics of the airflow would be expected to be modified by the wave. The wind loading on the 'top sides' of offshore structures is usually calculated using simple models, similar to those used over land, with the waves simply treated as a surface roughness. The air flow over a progressive water wave however, as is shown in this study, is considerably more complex, producing a cyclically varying loading and velocity maxima potentially much larger than the mean wind speed. The kinematics of the airflow need to be determined accurately in order to calculate the wind loading.

A further application is in determining the transport of pollutants in both air and water. At the water surface, the transport and dispersion of oil slicks will be affected by the wind-induced surface shear stresses. In the airflow, the transport and dispersion of gas clouds, of particular importance in the ventilation on offshore platforms, will depend upon the airflow above the wave. In each case, the turbulent velocity fluctuations as well as the mean flow will be required in order to determine the pollutant's behaviour.

There are a number of current developments for which a knowledge of the wind-wave field is essential. The growing popularity of offshore wind farms as a source of energy provides perhaps one of the best applications for the work, with a full description of the wind velocity field being essential for the generator design as well as for the tower, and the wave kinematics essential in designing the support structure. In the UK the area of greatest interest at present for offshore oil and gas exploration is on the Atlantic margins, west of Shetland. This is a much more harsh environment than the North Sea, with greater water depths, larger waves and stronger winds. The effect of any wind-wave interaction would therefore be expected to be of greater significance. The improved description of the wave kinematics could contribute towards areas of research such as the 'ringing' or dynamic response of deep water offshore structures.

1.3 The Present Work

A review of the available literature is first made and is presented in Chapter 2. This provides a historical overview of the subject and focuses on the various mechanisms which have been suggested for wind-wave interaction. Although a large number of mechanisms have been proposed, few have been verified experimentally, due to the lack of a comprehensive set of experimental data. Furthermore, virtually no consideration has been given to the effect of the airflow on the underlying wave motion which, as described in the previous section, is potentially of key importance to the engineer.

The present work therefore has three key objectives:

1. To investigate the characteristics of the airflow over a mechanically generated wave train to enable description of the mean wind velocities, the wave-induced perturbations to the wind velocities, and the turbulent velocity fluctuations. This information will allow the surface stress conditions to be determined.

2. To examine the kinematics of the underlying wave motion and determine whether the dominant effect of the wind on the waves is a result of modified surface stress conditions, or due to the interaction of the waves with a wind-generated shear current. Numerical models capable of incorporating both of these effects have been developed.

3. To consider the fundamental mechanisms of wind-wave interaction and assess their relative importance. In particular, the mechanisms outlined by Belcher and Hunt (1993) will be examined in detail.

A comprehensive laboratory based experimental investigation has therefore been undertaken in order to investigate the interaction between wind and waves. In the laboratory, storm conditions are modelled by blowing air over a mechanically generated wave train which simulates an oceanic swell. The waves so produced are often called 'wind-ruffled waves' since, at the wind speeds used in the study, the result is that the long waves have short wind-generated waves superposed on them. Phillips (1977)

considers the transfer processes to be similar, both physically and dynamically, for wind-ruffled mechanically generated water waves in the laboratory as for oceanic waves, so the results may be considered comparable with field data. The use of an underlying regular wave form also makes the wave-induced perturbations easily extractable.

In order to carry out this experimental investigation, a new wind-wave interaction facility was designed by the author, as part of the current project. This facility is described in Chapter 3. The experimental equipment, procedures and analysis routines are also outlined. Preliminary results are then presented to demonstrate that the new facility performed as intended.

The results of the experimental investigation are divided into three sections: the airflow kinematics and structure, the water particle kinematics, and the surface elevation measurements. In Chapter 4, the kinematics measurements for three flow cases are presented along with the streamlines describing the airflow. The structure of the flow is examined in detail. In Chapter 5, the basic concepts of boundary layer theory are introduced, and an attempt to quantify the effects described in the previous chapter made. The time averaged kinematics are analysed and compared both with measurements over a flat bed and for wind over water in the absence of mechanical waves. The variations of the flow with the phase of the long wave are examined and the stresses at the water surface then deduced.

A corresponding set of measurements is presented in Chapter 6 for the water kinematics. The wind-generated currents in the presence and absence of mechanically generated waves are examined, and the boundary layer theory developed in Chapter 5 applied. The variation in the wind-generated current with the phase of the underlying long waves is investigated by separating the orbital wave motion and the varying wind-induced current. In Chapter 7, an attempt to model the effect of the airflow on the underlying wave motion in made. The effect of the measured highly sheared current on the kinematics is first investigated, corresponding to the effect of a mean shear stress. In a separate model, the effect of the fluctuating surface stresses is then evaluated. The relative importance of each of these effects is then assessed.

Surface profile measurements are presented in Chapter 8, investigating the effect of the airflow on the underlying wave form. The generated wind-waves are analysed and their dependence upon the phase of the long wave examined, in relation to the effect of the long wave on the wind-waves, as well as the effect of the wind-waves on the surface stresses.

In Chapter 9, the effects discussed in each of the preceding chapters are drawn together in an attempt to understand the interaction between wind and waves. The deduced structure of the flow in the air is related to that observed in the water, as well as the surface profile observations. The thesis concludes by outlining the important implications of the study for the engineer and the key conclusions to be drawn from the work. Some suggestions for further work are made.

2. LITERATURE REVIEW AND THEORETICAL BACKGROUND

This review attempts to classify the available literature into that relating to the airflow, and that relating to the water waves. In addition to providing a historical review of the development of the subject, from the early pioneering work through to the most recent developments, it sets out some of the underlying theory and highlights the areas of particular relevance to this study.

The review first considers the effects of water perturbations on the overlying airflow, focusing on the airflow structure and the resulting surface stresses. The interaction mechanisms which have been proposed are examined, reviewing the theoretical work and then the corresponding experimental results. The problem is then considered from the opposite viewpoint, investigating the influence of the perturbed airflow on the characteristics of the water flow. In particular, it examines the kinematics of the underlying fluid motion and the perturbations to the surface itself. The limited amount of theoretical work is reviewed, and the available experimental results considered. A greater emphasis is placed upon the airflow in this review, with various aspects of the water motion being considered in greater detail in later chapters. At the end of this chapter, a summary is made highlighting the perceived gaps in the experimental work and demonstrating the relevance of the proposed study.

2.1 Airflow

Much of the research into the interaction between wind and waves has attempted to account for wave growth. The work has focused on the airflow, and the mechanisms by which energy is transferred from the wind to the wave. Although the present study is not concerned with wave growth, consideration of the mechanisms proposed to explain wave growth assists in the understanding of the nature of the interaction. A review of these mechanisms highlights the factors influencing wind-wave interactions.

2.1.1 Theoretical Descriptions

One of the earliest theories for wind-wave interaction, dating from the last century, is the Kelvin-Helmholtz instability mechanism (Lamb, 1932, Ursell, 1956). This adopted perhaps the most simple model for the airflow, assuming it to be laminar and inviscid, with a discontinuity at the water surface. The perturbed motion arising from a small surface sinusoidal perturbation can be described by a velocity potential. The motion is exactly in-phase with the surface elevation, with the pressure maxima above the trough, and minima above the wave crest. If the induced suction at the crest is sufficient to overcome the restoring forces due to gravity and surface tension, then the motion is unstable and wave growth occurs. The model assumes that the boundary layer thickness is very small, so this mechanism is most likely to be applicable at high wind speeds. Miles (1959b) develops this instability model and confirms that it is only likely to be significant at very high wind speeds.

The next significant development was Jeffreys' (1925) semi-empirical sheltering hypothesis, which modelled the interaction between a wave and a mean shear flow. Turbulence effects are included in determining the mean shear flow. Jeffreys assumed that the flow separates from the leeward side of the crests, forming a low velocity and high turbulence region on the leeward side of the crest before reattaching ahead of the next crest. The pressure on the leeward side of the crest is therefore less than on the windward side, and a pressure component in-phase with the wave slope develops. It is this component of the pressure, in phase with the wave slope, which gives rise to wave growth, the pressure difference producing a drag on the waveform. The magnitude of the pressure difference across the wave was expressed by the sheltering coefficient, which provides an indication of wave growth. If the wind velocity is greater than the wave velocity (or phase velocity) then the wind does work on the waves, and wave growth results if the energy transferred from the wind to waves exceeds the viscous dissipation.

Ursell's (1956) review, which concluded that the state of knowledge at that time was 'profoundly unsatisfactory', led to renewed interest in the problem. Miles (1957) showed theoretically that even in the absence of flow separation, a significant pressure

in-phase with the wave slope is developed. He developed a mechanism for wave growth by a parallel shear flow using a stability analysis based on the inviscid Orr-Sommerfeld equation. The model is quasi-laminar, in that the turbulent stresses are considered only in producing the sheared mean velocity profile, and not in the subsequent analysis. By neglecting the turbulent stresses, the stability analysis can be solved analytically using a linearised perturbation expansion. He shows that the resulting wave growth is exponential and is due to the component of the pressure in phase with the wave slope which is proportional to the curvature of the velocity profile $U''(y)$ at the so-called critical height. This critical height, or matched height as it is increasingly called (and as it will be referred to in this study), is defined as that height at which the wind velocity is equal to the phase velocity.

Miles' original model was further developed by Brooke Benjamin (1959) and Miles (1959a), transforming the problem into curvi-linear co-ordinates and including viscous effects to form narrow friction layers at the surface and around the matched height. Brooke Benjamin (1959) calculated the surface stresses and found that they were distributed as if the leeward slopes of the waves were sheltered. This led him to consider Miles' mechanism as quasi-sheltering, showing effects similar to Jeffreys' sheltering hypothesis but without the flow separating, the effects of which could not be considered in this first order analysis. Brooke Benjamin (1959) found that in the limit as the Reynolds number tends to infinity, Miles' mechanism reduced to a Kelvin-Helmholtz instability.

Lighthill (1962) provides a physical interpretation of Miles' mechanism. The airflow in a frame of reference moving with the phase speed of the wave is shown in Figure 2.1. At a first approximation, the pressure is at a minimum at the wave crests, and a maximum in the troughs. This is the potential flow solution, the streamlines for which are illustrated in Figure 2.1a. However, consider the flow very close to the matched height. Just above the matched height, the air is moving a little faster than the phase velocity. As it moves from the crest towards the trough, it is turned back by the higher pressure in the trough, causing it to move down beneath the matched height and return towards the crest. The re-circulating streamlines shown in Figure 2.1b therefore develop, centred around the

matched height, but bent to follow the shape of the matched height. At the matched height there is a large excess of vorticity which induces a velocity field in phase with the wave slope and hence a component of pressure which lags 90° behind the surface profile. The minimum pressure would therefore be expected to occur on the leeward slope of the crest, so the "cats eye" pattern would be shifted downstream.

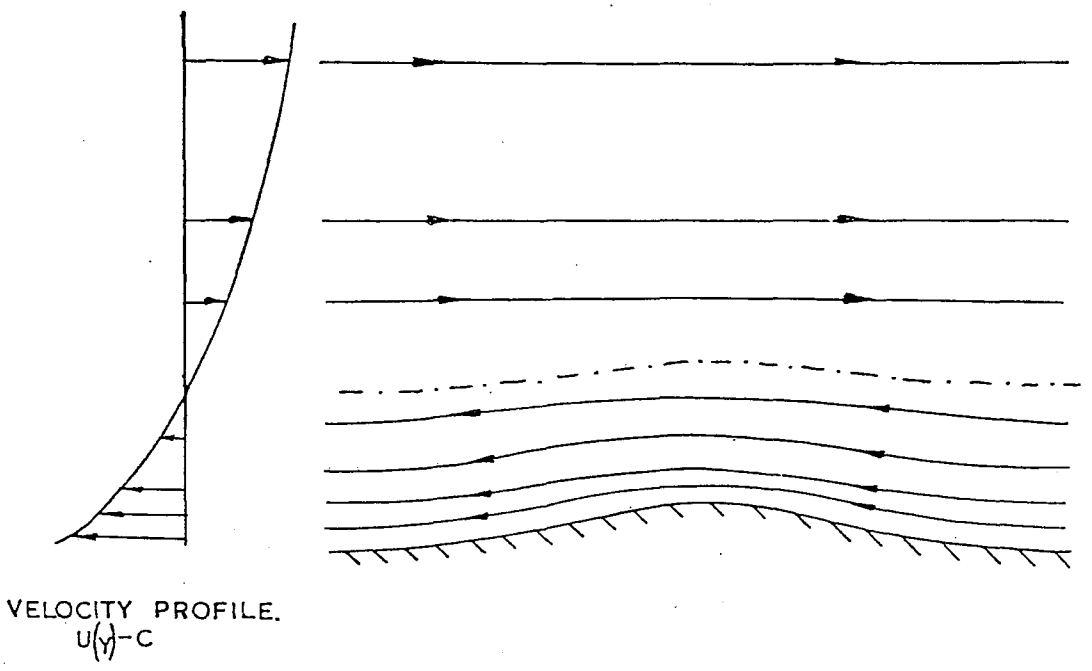


Figure 2.1a: Potential flow pattern.

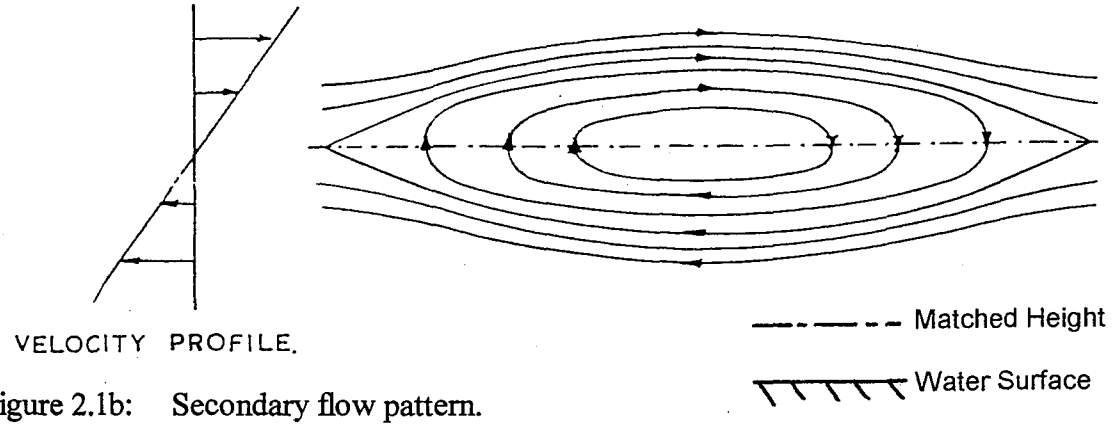


Figure 2.1b: Secondary flow pattern.

Figure 2.1: Streamlines in the airflow predicted by Lighthill (1962). (after Holmes, 1963).

Miles' model requires an initial perturbation and then the instability analysis predicts an exponential wave growth. It cannot account for the initial generation of wind-waves from an unperturbed water surface. Phillips (1957) considers a stationary random turbulent fluctuating pressure distribution acting on an initially flat water surface and being convected downstream as a rigid pattern. The pressure fluctuations generate small forced oscillations at the surface. The response of the surface is greatest to those components of the imposed pressure fluctuations whose frequency equals that of the free-surface waves of the same wave number. Wave growth is therefore by a resonance-type mechanism and the resulting rate of wave growth is linear. Miles (1960) showed that Phillips' mechanism provides the initial wavy disturbance of the water surface, after which his exponential growth mechanism dominates.

Experimental measurements in both the laboratory (Bole and Hsu, 1969, Shemdin and Hsu, 1967, and Stewart, 1970) and in the field (Longuet-Higgins et al., 1963, Snyder and Cox, 1966, and Dobson, 1971) found that the measured growth rates were up to one order of magnitude greater than those predicted by Miles' theory. This suggested that effects not considered in Miles' theory, namely turbulence and non-linear mechanisms, were of considerable importance. Longuet-Higgins (1969b) found that a variable tangential stress in phase with the surface elevation was dynamically equivalent to a pressure fluctuation in phase with the wave slope. The oscillatory shear stress at the surface could therefore be as significant as the wave-induced pressure in producing wave growth. Kendall (1970) measured the wall pressures and velocities at a moving wavy wall in a wind tunnel. The wall pressure was found to be highly asymmetric, resulting in a pressure drag much greater than that predicted by Miles' theory. The drag was not caused by flow separation but by the strongly perturbed turbulent structure. Miles' (1957) assumption that perturbations of the turbulent Reynolds stresses can be neglected is clearly not valid, and the wave-induced turbulent Reynolds stresses must be considered in any wind-wave model.

To include the wave-induced turbulent stresses requires the formulation of a numerical model, with the wave-induced turbulent stresses appearing in the linearised perturbation equations. Some form of closure model is required to solve these equations. A number

of existing closure models have been applied. For example, Davis (1972) uses a variety of closure models and finds the surface pressures to be very sensitive to the closure assumptions and the near-surface velocity profile. He presents his results in terms of the amplitude of the pressure components in phase with the surface profile and in phase with the wave slope. He does not however consider the tangential stresses, nor does he consider the structure of the resulting airflow.

Gent and Taylor (1976) and Gent (1977) present an eddy viscosity model. They investigate non-linear effects with increasing wave steepness and also include the effect of a variable surface roughness. Unlike the preceding models, the surface is assumed to be rough rather than smooth. Their work shows that the linearised models of Miles (1957, 1959) and Townsend (1972) are valid only for small wave slopes ($ak < 0.05$), and at larger slopes non-linear effects become important. Gent and Taylor (1976) model a varying surface roughness by assuming that the small gravity waves and ripples riding on the dominant wave will be steepest just forward of the wave crest (Longuet-Higgins, 1969b). For a number of cases, Gent and Taylor (1976) calculate the surface stresses and determine the flow streamline patterns. The variation in the surface stresses with phase for one flow case are reproduced in Figure 2.2. They find that significant modifications to the surface stresses result from the non-linearity introduced by greater wave steepness. At a steepness of approximately $ak = 0.3$, where a is the amplitude and k is the wavenumber (or $2\pi/\lambda$ where λ is the wave length), the pressure component in-phase with the wave slope is more than 50% of the value in-phase with the surface profile. They find that the variation in surface roughness with phase of the long wave significantly affects wave growth.

Gent and Taylor (1977) present predicted streamline patterns for a given surface roughness and flow velocity but for a number of different wave steepnesses. The streamlines for three cases are presented in Figure 2.3, calculated using their model which was described above (Gent and Taylor, 1976). The streamlines are presented in a frame of reference moving with the phase speed of the wave. They find a re-circulation

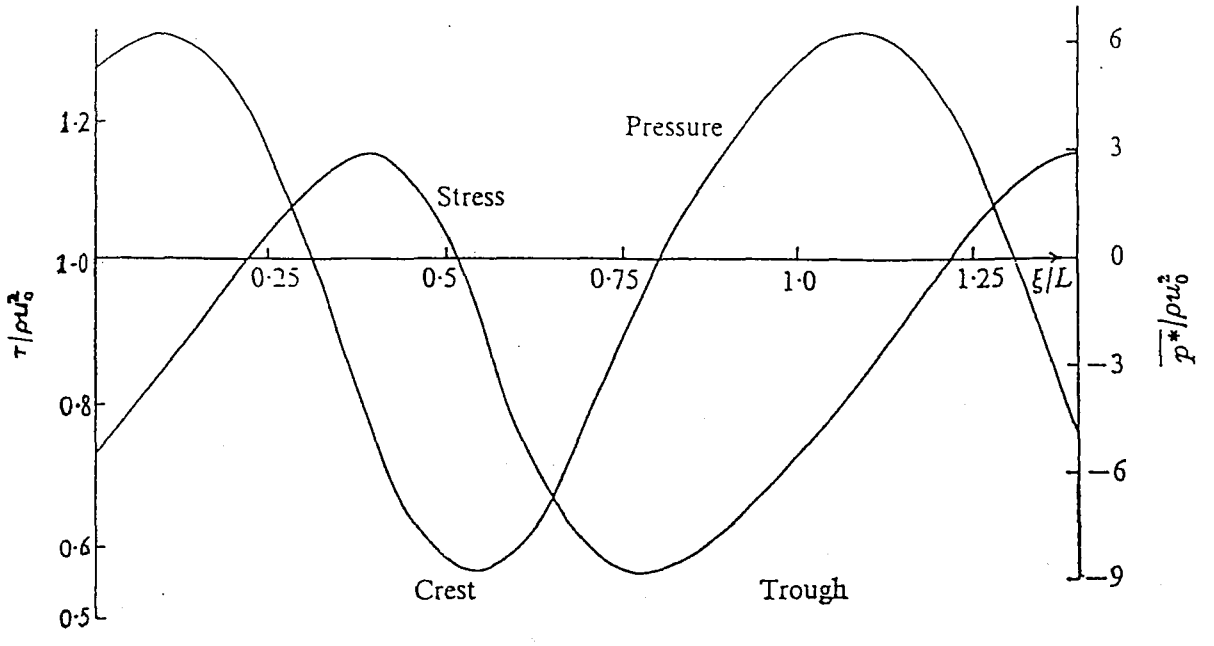


Figure 2.2: Surface pressure and shear stress. $R = 8$, $ak = 0.157$, $c = 8u_*$ (after Gent and Taylor, 1976)

centred on the leeside of the crest, the thickness of which increases significantly with increasing wave steepness. For $ak = 0.157$ the re-circulation is very thin, but for $ak = 0.471$ the re-circulations are higher than the waves. (Note that for illustrative purposes, Gent and Taylor use some very steep waves in their model, which in reality would be unstable and would break). The $\psi = 0$ streamline, the first 'continuous' streamline above the recirculations, breaks away from the near-surface region at greater wave steepness, in a similar fashion to separation over a fixed waveform. They find the resulting surface stresses to show significant variation, with the minimum pressure and maximum shear stress being at the wave crest for $ak = 0.157$, but at larger wave steepnesses the phase is almost reversed, so the maximum pressure and minimum shear stress are close to the crest. The flow structure clearly significantly effects the surface stresses. The effect of the wave orbital velocities is included in this analysis, but the effect of the surface drift is also considered. The inclusion of the surface drift significantly increases the surface pressure and reduces the matched height, which consequently reduces the depth of the region of closed streamlines by up to 50%, showing the drift to have an important effect.

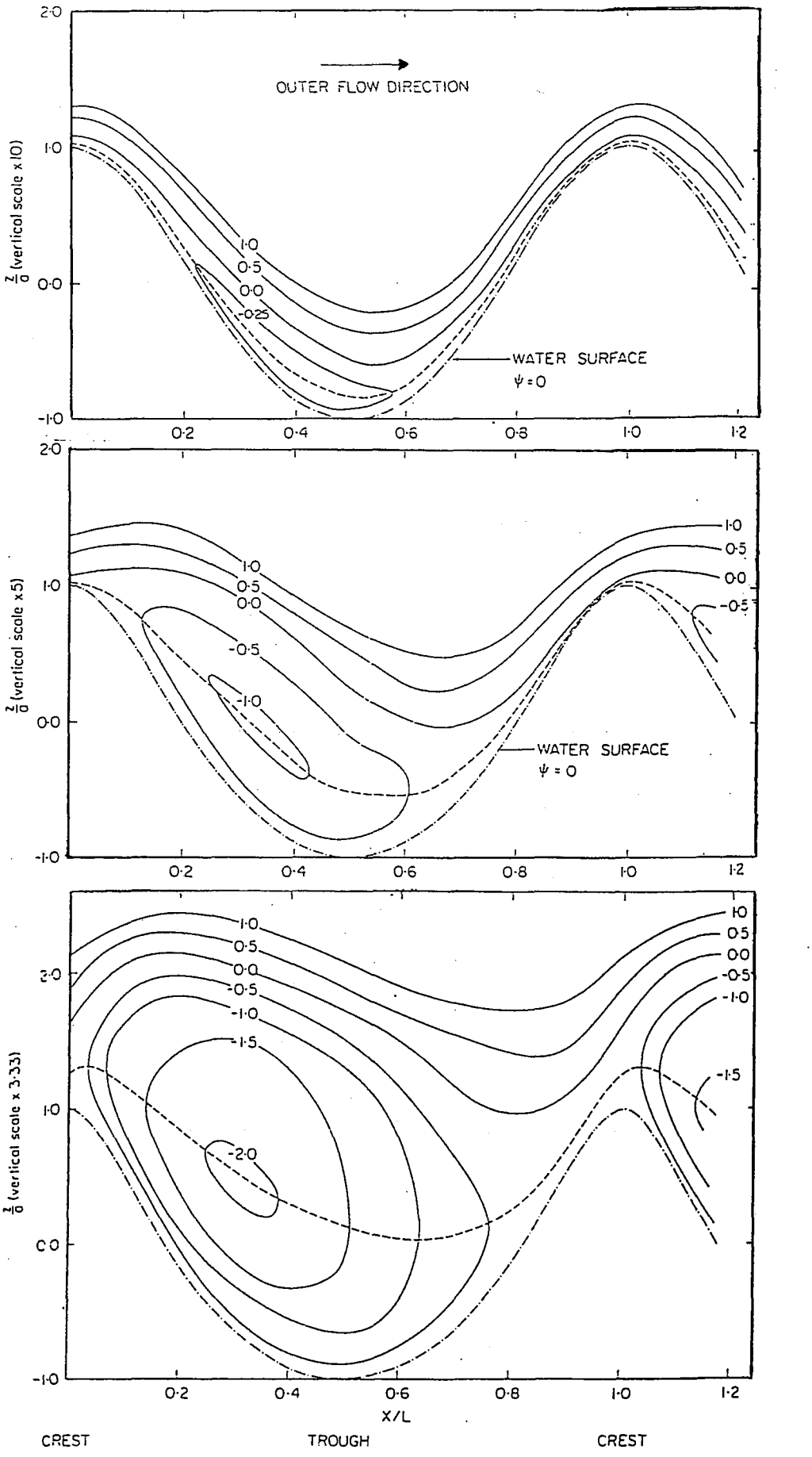


Figure 2.3: Streamline patterns for $R = 8$, $c = 8u_*$. (a) $ak = 0.157$, (b) $ak = 0.314$, (c) $ak = 0.471$. ----- Matched height. (after Gent and Taylor, 1976).

Although the streamlines in Figure 2.3 show behaviour similar to those predicted on the basis of separation, Gent and Taylor (1977) do not consider that the flow has actually separated. The usual flow separation criterion, that the shear stress at the surface tends to zero, is not valid in this situation because the shear stress can be negative, passing through zero without causing a fundamental change to the flow streamlines. Banner and Melville (1976) showed experimentally that separation of the airflow could only occur in conjunction with wave breaking. They found that the breaking of small scale waves near the crests of larger waves caused local flow separation and a substantial increase in drag. Gent and Taylor (1977) develop this argument and conclude that for flow separation, a stagnation point at the surface in a frame of reference moving with the phase speed of the waves is required. This means that the matched height must intersect with the water surface, and there will therefore be a region of closed streamlines which will intersect with the water surface. This discontinuity is only possible if the wave is breaking, suggesting that flow separation over the mechanically generated waves to be used in this study is very unlikely, but is possible over the wind-generated waves which will tend to be much steeper.

Belcher and Hunt (1993) apply the theory developed for flow over a rigid stationary hill by Belcher, Newly and Hunt (1993) to flow over a series of water waves. The key finding from the theory developed for flow over a single stationary rigid hill is that although simple turbulence models based on the local equilibrium between production and dissipation can be used for the unperturbed flow, they are not applicable to the perturbed flow. Instead, it is necessary to divide the perturbed flow into inner and outer regions. In the inner region, the wave-induced turbulence is in local equilibrium, so it is appropriate to use an eddy viscosity model. In the outer region however, an eddy viscosity model significantly over-estimates perturbation stresses, since the flow is advected over the waves too rapidly to transport significant momentum. The wave-induced stresses are therefore calculated using rapid distortion theory in the outer region.

Belcher and Hunt (1993) calculate the linear perturbations to the airflow caused by the water wave and then calculate the resulting growth of the waves. They consider the

wave to produce two forcings on the airflow above, namely the undulating shape of the wave form and the varying tangential surface boundary conditions. The undulation causes a displacement of the flow streamlines about the crest and they become asymmetric, causing a thickening of the boundary layer on the leeward side of the crest. This leads to an asymmetry of the mean flow gradients and hence an asymmetrical perturbation to the normal and Reynolds shear stresses in the inner region. The normal stress minima and the shear stress maxima occur before the wave crest, so producing components of the stresses in phase with the wave slope. This effect they term "non-separated sheltering", since it is similar to Jeffreys' (1925) mechanism, but without flow separation.

In addition to the two forcings produced by the wave, Belcher and Hunt (1993) consider two perturbations to the airflow by the surface boundary conditions: firstly, the non-zero varying tangential surface velocity; and secondly, the effect of a varying surface roughness. The orbital velocities at the water surface accelerate and decelerate the flow in the lower part of the inner region, so the velocities in the airflow close to the water surface will be in-phase with the wave orbital velocities, while those in the outer region will be out of phase. This leads to a perturbation to the streamwise velocity and a pressure perturbation in the outer region which is in anti-phase with the wave slope. This effect is in the opposite sense to non-separated sheltering, and causes a thickening of the boundary layer on the windward side and a thinning on the leeward side of the wave crest. The effect of a mean drift current at the surface is included in the analysis by translating the velocity profile which, in effect, produces a correction to the matched height.

The second surface boundary condition effect, the variable surface roughness, is assumed to be proportional to the local change in the shear stress (Charnock, 1955). At leading order, the surface shear stress is induced by the undulation, so the surface roughness will be increased at the crests and reduced in the troughs. This will have the effect of decelerating the flow at the wave crest and causing a relative acceleration in the troughs. The maximum velocity perturbation due to this effect will be at the zero crossings, hence an out-of-phase velocity and pressure component is generated. This

will cause an effect on the airflow similar to non-separated sheltering, thickening the boundary layer on the leeward side of the crest.

Belcher, Harris and Street (1994) and Harris, Belcher and Street (1996) develop a coupled turbulent air and water model to calculate the turbulent flow in both the air and water. Belcher, Harris and Street (1994) extend the analysis of Belcher and Hunt (1993) to incorporate perturbations to the sheared drift current in the water. They show that the surface stresses exerted by the wind produce a sheared drift current which, even at low wind speeds, experimental evidence has shown to be turbulent. Non-separated sheltering in the airflow causes the pressure minimum to shift downwind of the crest which promotes wave growth. However, in the water, the shift in the pressure minimum is upwind which tends to inhibit wave growth. The varying surface velocity is used to balance the surface stresses across the interface to produce continuity. They find the surface velocity variation has a larger magnitude than if the flow were inviscid and irrotational. This also tends to reduce the effect of non-separated sheltering in the air on the wave and so reduce wave growth by a factor of about two compared with irrotational waves.

Harris, Belcher and Street (1996) develop a numerical model based on the analytical model developed by Belcher, Harris and Street (1994). They use the resulting coupled model in order to calculate the stress and velocity perturbations in the flow, including the effect of the fully turbulent drift flow in the water. The results showed reasonable agreement with the experimental data of Hsu and Hsu (1983). They find the wind-induced flow in the water is irrotational except for a very thin layer beneath the interface, where viscous stresses are significant. They conclude that the characteristics of the near-surface layer are central in determining the nature of the wind-wave interaction.

In addition to wave growth caused directly by the airflow, mechanisms for wave growth via wave-wave interaction have been proposed. Longuet-Higgins (1969a) proposed a non-linear mechanism for short waves transferring energy to the long waves through the short waves breaking on the upwind face of the waves. Hasselman (1962) showed how

energy can be transferred amongst different components in a gravity wave spectrum. Because the mechanism involves resonance amongst particular groups of wave components and is a non-linear process, it is not considered in the models described. From the JONSWAP data, Hasselman et al. (1973) found that following the initial wave growth (Phillips, 1957), 30 - 90% of the observed wave growth is due to non-linear wave-wave interaction. However, for the unsaturated state of mechanically generated waves or ocean swell, the non-linear interaction will be small, and the direct air input provides the dominant energy source.

2.1.2 Experimental Measurements

The earliest laboratory experiments (Motzfeld, 1937) measured the pressures in the airflow close to fixed rigid waves in order to measure Jeffreys' sheltering coefficient. However, stationary profiles fundamentally mis-represent the airflow over a moving wave, because the matched height is at the wave surface. The work of Gent and Taylor (1977) showed that the elevation of the critical height was very important in determining the flow structure and hence the surface stresses. It is therefore not surprising that the values of the sheltering coefficient were smaller than those predicted by Jeffreys. Kendall's (1970) flexible moving wavy surface overcame this objection and his values for the sheltering coefficient and pressure drag were significantly greater than those measured over a stationary wave. Kendall also showed that flow separation over the 'long' waves was exceedingly unlikely and the flow tended to follow the water surface.

The velocities and pressures in the airflow above the waves can be measured and presented in one of two co-ordinate frames. The first is a fixed Cartesian frame which is used in many studies including Bole and Hsu (1969), Shemdin (1970), Stewart (1970) and Mitsuyasu and Honda (1982). The instruments used in these studies were pressure probes or hot wire anemometers which could not be submerged in the water. The probes were positioned at fixed elevations above the still water level and could therefore measure only above the top of the wave crests. Data close to the water surface, which is of the greatest interest, could only be sampled over a small fraction of the wave cycle and only related to conditions in the vicinity of the wave crest. Even if data could be

sampled beneath crest level, mean values are not meaningful in this co-ordinate frame, since neither the air velocity nor the pressure can be defined over the entire phase of the wave cycle. However, perhaps the most important objection to a Cartesian frame of reference is that the measured velocity and pressure will be a function of the instantaneous height of the probe in the boundary layer, as well as the perturbations to the airflow caused by the wave. Clearly the variation due to the relative height of the probe will be greatest close to the water surface where the airflow is most perturbed. These effects will influence the mean as well the wave-induced values.

The alternative to a Cartesian frame is to use a wave-following co-ordinate system which overcomes the problems of defining mean values beneath crest level and the varying relative height in the boundary layer. Much of the theoretical work is carried out in curvi-linear orthogonal co-ordinates (e.g. Brooke Benjamin, 1959), where both the co-ordinate frame and the velocity components are transformed into new co-ordinate directions. Hsu, Hsu and Street (1981), however, use a much simpler but similar co-ordinate transformation which transforms only the vertical co-ordinate, leaving the horizontal co-ordinate as well as the velocity component directions unchanged:

$$t = t^*, \qquad x = x^*, \qquad y = y^* + a\cos(kx^* - \omega t^*)\frac{\sinh(kH - ky^*)}{\sinh(kH)} \tag{2.1}$$

where k, ω, and a are respectively the wave number, wave frequency and wave amplitude of the mechanically generated wave, and H the depth of the airflow. The transformation is clearly not orthogonal, but is similar to Brooke Benjamin's (1959) transformation in that the water surface, or rather a linear approximation to it, is taken as $y^* = 0$. Furthermore, at $y^* = H$ the Cartesian and wave-following co-ordinates are equivalent. In these wave-following co-ordinates, lines of constant y^* may be considered as an approximation to the potential flow streamlines. This therefore enables ready comparison between the measured flow and the potential flow characteristics. In addition, the time-averaged profiles in this frame of reference may be considered comparable to those over a flat bed. The potential flow streamlines in transformed co-

ordinates are simply horizontal lines, as are those over a flat bed, so the profiles may be meaningfully compared. However, the work of Gent and Taylor (1977) suggests that the flow can be very different from the potential flow at larger wave steepness or slow wind speeds, but, at moderate values of the slope and for faster velocities, the flow does essentially follow the water surface. Ideally, the velocities should be measured along the actual flow streamlines, though clearly this is not possible where there are flow recirculations. A wave-following co-ordinate system, such as that defined above, thus appears to be the best alternative.

Hsu, Hsu and Street (1981) and Hsu and Hsu (1983) sample and present their velocity data in the co-ordinate system defined in equation 2.1. They used a wave-following traverse to carry a hot-film probe at a fixed position in (x^*, y^*, z^*) space. The probe is therefore fixed in plan, and its Cartesian elevation modulated to maintain the probe at a fixed value of y^*. The reason for maintaining the velocity components in their fixed Cartesian directions is clear, since it would be experimentally very difficult to modulate the inclination of the probe to measure velocities parallel and perpendicular to the water surface. This system is clearly an improvement on the fixed probes, allowing measurements to be made beneath crest level. However, measurements could only be made to within a minimum of 8 mm of the instantaneous water surface. Furthermore, there appear to be a number of problems associated with this system. By mounting the probe and traverse within the airflow, the flow will be significantly disturbed and the probe will oscillate in the flow. For measurements close to the water surface, particularly at faster wind velocities where there will be large wind-generated waves, there could be significant errors in positioning the probe at a fixed y^* co-ordinate. The velocities in the region close to the water surface are those of greatest interest, and there will be a high degree of uncertainty as regards the elevations at which they are measured. A final problem is the phase lags introduced at all stages of the wave-follower operation, the effects of which may be removed by calibration to some extent, but without great certainty.

Throughout the literature, most of the analysis of velocity data has been limited to calculating the time-averaged velocity profiles, concluding that in the region close to the

water surface, the velocity profile was log-linear, and calculating the friction velocity using the 'law of the wall' (Chapter 5). The time-averaged velocity profiles appeared to demonstrate log-linear behaviour close to the surface irrespective of whether they were measured in Cartesian or wave-following co-ordinates. A comparison of data measured in this study in Cartesian and wave-following co-ordinates shows that the velocity gradients near the water surface and hence the friction velocity are significantly different. Time-averaged data calculated in a Cartesian frame would appear to have no fundamental meaning and is not considered here.

The only data collected in a wave-following frame of reference is that presented by Hsu, Hsu and Street (1981), Hsu and Hsu (1983), and Papadimitrakis, Hsu and Street (1984). For a range of wind speeds, they investigate the turbulent structure above 1 Hz mechanically generated waves with a steepness of $ak = 0.1$. In addition to the turbulent Reynolds stresses, they give some consideration to the mean flow and flow structure. They find that, in all cases studied, from $U_\infty/c = 0.88 \rightarrow 1.87$, the mean flow tends to follow the wave form without separation, confirming earlier experimental and theoretical work. They conclude that the use of the transformed co-ordinate system is clearly therefore appropriate. Hsu, Hsu and Street (1981) 'sketch' the streamline pattern for $U_\infty/c = 1.54$, which is reproduced in Figure 2.4. The flow appears to be similar to that predicted by Gent and Taylor (1977) for $ak = 0.471$, although the region of closed streamlines is centred almost in the trough in Figure 2.4, whereas Gent and Taylor show it to be centred around the zero downcrossing. They also confirm Gent and Taylor's observation that the structure of the flow, and hence the wave-induced velocities, are strongly dependent upon the matched height, which they find to vary non-linearly with phase.

Hsu, Hsu and Street (1981) found the mean velocity profile to be log-linear, and the surface condition as felt by the airflow to be 'super smooth'. The wind-induced current causes a release of the shear stress at the water surface, making the water surface appear to be smoother than a smooth flat plate. This agrees with the measurements of Stewart (1970) over combined wind and waves, and Wu (1968) for wind-generated waves. At

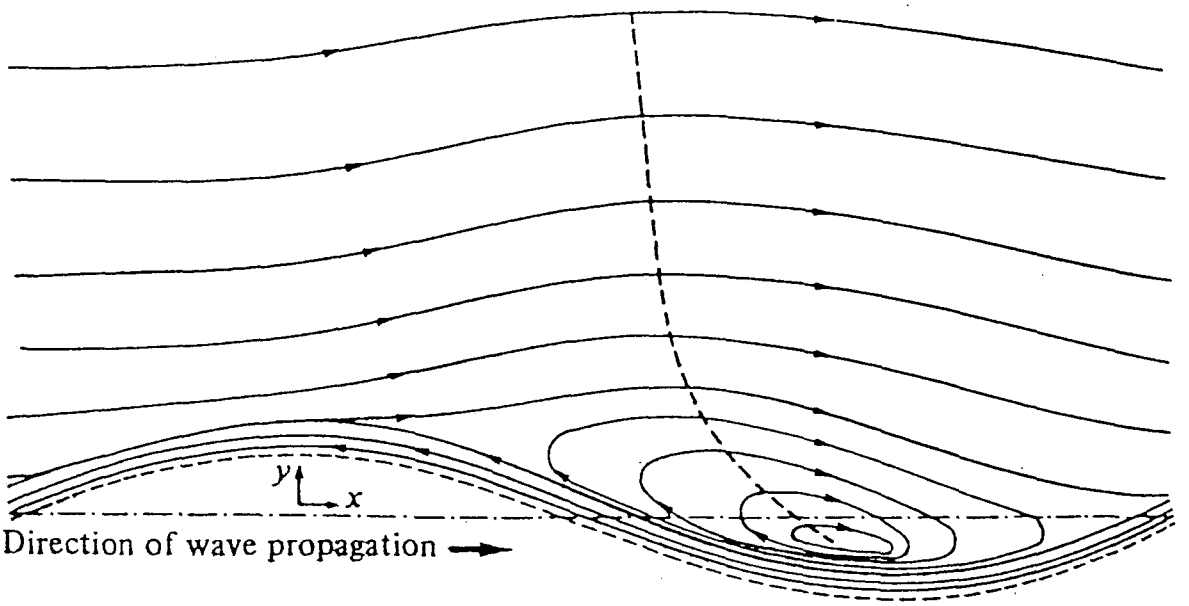


Figure 2.4: Sketch of streamline pattern observed in a frame of reference moving with the speed of the wave ($U_\infty = 2.4$ m/s). (Hsu, Hsu and Street, 1981)

larger wind speeds however, the effect is reduced, suggesting that the surface is becoming significantly rougher. From their measurements of the Reynolds stresses, they find the wave-induced velocity field and turbulence to show significant phase variations and dependence upon the ratio of the phase velocity to the free-stream wind velocity.

Papadimitrakis, Hsu and Street (1986) present a corresponding set of pressure measurements in the same wave-following frame. They measure the wave-induced pressure field in order to evaluate the momentum and energy transfers from the wind to the waves. The wave-induced pressures are found to reduce exponentially with height in all cases. The pressure is found to lag the surface profile by 130° in all the cases studied from $c/U_\infty = 0.39 \rightarrow 1.10$, except for $c/U_\infty = 0.78$ and 0.68. The wave-induced pressure is non-linear, with strong harmonics producing a double-peaked variation with phase. This contrasts with the relatively linear wave-induced velocities, but corresponds to the product of the phase averaged wave-induced velocities. They suggest that this corresponds to Gent and Taylor's (1976) finding that non-linearities are important for wave steepness $ak > 0.05$. The data does, however, show a considerable scatter and

there is some uncertainty as a result of the small magnitude of the pressures, and contamination due to signal noise, acoustic reflections and water wave reflections.

The nature of the turbulent structure of the airflow above the waves is investigated by Papadimitrakis, Hsu and Street (1988) and Kawamura and Toba (1988). Coherent structures or 'bursting' phenomena were observed in the airflow above water waves. The observed phenomena involved a 'burst' originating in the inner boundary layer followed by a 'sweep' in the outer layer. A burst originates close to the water surface and starts with fluid gradually lifting up in the inner layer, then suddenly oscillating before bursting out and being ejected, the fluid moving upwards very quickly through the boundary layer. A sweep is the opposite effect, where fluid is drawn towards the boundary layer. Bursts and sweeps are therefore indicated by corresponding peaks in each velocity component of the opposite sense, producing large positive peaks of the Reynolds shear stress. This mechanism is thought to be responsible for producing a large portion of the turbulent Reynolds stresses in the boundary layer. Papadimitrakis et al. (1988) found that the presence of the wave affects the production of the Reynolds stresses, due to the matched height and the Stokes' layer. These effects are not studied in detail in the present work, but the form of the turbulent structure is discussed.

In addition to laboratory data, a considerable amount of offshore data has been collected. Early field measurements were made using floating buoys and other wave-following devices, to find the air pressure on the surface of the wave. These included work by Longuet-Higgins, Cartwright and Smith (1963), Dobson (1971), Elliot (1972), Snyder (1974), and Snyder, Dobson, Elliot and Long (1981). The principal objective of this work was to determine the phase relation between the wave and the surface pressure. There appear, however, to be significant discrepancies between the results obtained by different investigators.

The velocities above ocean waves have also been investigated by a number of authors, with the primary aim of examining the surface stresses. Much of the work centres around the Charnock (1955) relation, proposed on empirical grounds and linking the roughness length of the sea surface z_o and the friction velocity in the airflow u_*

$$\frac{z_o}{u_*^2 / g} = \text{constant} \tag{2.2}$$

where the constant is referred to as the Charnock constant. The value of the Charnock constant appears to vary with wind and wave conditions (Smith, 1980).

Krügermeyer, Grünewald and Ducknel (1978) investigated the effect of the ocean waves on the time averaged wind profile and showed that the profile is significantly distorted below about three wave heights. Hsu (1974) found that the mean velocity profile follows the 'law of the wall', and further proposed that the wind stress drag coefficient for deep water ocean waves was a constant. Kondo, Fujinawa and Naito (1973) investigated the effect of the high frequency ocean waves on the aerodynamic roughness. They showed that it was the high frequency wave components and not the low frequency dominant waves which determine the aerodynamic roughness and hence the surface shear stress. Smith (1980) found that the drag coefficient increases with increasing wind speed, and that the drag coefficients are more closely correlated to the wind speed than the wave height. This confirmed the work of Kondo et al. (1973), which suggested that the roughness is due to the smaller high frequency waves.

Wills (1990) presents wind speed profiles measured from an offshore platform, which show log-linear mean wind profiles, and the roughness height z_o increasing with wind speed. They suggest that the roughness is due to the short steep superposed waves rather than the swell, but provide no convincing evidence to support this. They also investigated the turbulent intensity profiles and the gust profiles, regarding the latter as being of considerable importance in determining the nature of the interaction, though noting these would be difficult to model in a wind tunnel.

2.2 Water Flow

There has been relatively little work carried out to investigate the effect of the airflow on the underlying wave motion. In a similar manner to the airflow review above, the

theory available for predicting the wave kinematics when the surface stresses are non-zero is first considered, and then the limited number of corresponding experimental papers reviewed.

2.2.1 Theoretical Descriptions

The shear stress exerted by the airflow on the surface of the wave generates a highly-sheared current in the water. The influence of a highly sheared current on the underlying wave motion has been investigated by a number of authors. Regular wave motion in the absence of such a current can be described using established irrotational or Stokes' wave theory. However, Swan (1992) shows that, in the presence of a highly sheared current, there is a significant variation in vorticity with depth, and the interaction of the wave and the current leads to the formation of a rotational wave component. The wave kinematics in the presence of a highly sheared current may therefore be very different to those predicted by Stokes' theory. A review of wave-current theory and a brief outline of methods of modelling the interaction are given in Chapter 7.

Longuet-Higgins (1969b) investigates the action of a variable shear stress at the water surface. A small tangential stress in phase with the surface profile, having a maximum at the crests and minimum in the troughs, will generate a sheared boundary layer close to the water surface. He finds the thickness of the boundary layer will be a minimum on the windward side of the crest, and a maximum on the leeward face. The shear stress maximum at the crest causes an additional acceleration. As a result, the velocity maximum occurs on the leeward side of the wave crest, with a corresponding minimum on the windward side.

Swan (1992) also investigates the action of a variable surface stress on the waveform. He confirms that it is the pressure in phase with the wave slope and the shear in phase with the surface profile which causes wave growth, but finds that it is the other components, namely the pressure in phase with the surface profile and the tangential stress in phase with the wave slope, which modify the wave kinematics. He derives the

velocity potential to a first order of wave steepness, and develops a modified dispersion relation. This model is considered fully in Chapter 7.

Most of the airflow models considered in the previous section did not take account of the motion in the water. Gent and Taylor (1976) and Belcher and Hunt (1993) matched the near-surface air velocities to the first order wave motion, but did not consider any resulting modification to the wave motion. The only model which considers the effect of the airflow on the water motion is that presented by Belcher, Hunt and Street (1994) and Harris, Belcher and Street (1996). In their coupled model, the motions in both the airflow and water are presented. There are however no experimental results with which to compare the phase varying water motion.

2.2.2 Experimental Measurements

The purpose of much of the experimental work relating to the wave kinematics under an overlying airflow has been to measure the current associated with wind-generated waves, in the absence of mechanically generated waves. The most comprehensive study was that presented by Wu (1975), who measured the current velocity profiles using floats and a pressure probe for a wide range of wind speeds. He identified a linear velocity profile very close to the water surface, and a log-linear relationship at greater depths. The current profiles were very highly sheared only when very close to the water surface. He found that the wind-induced surface velocity is directly proportional to the friction velocity, and that the ratio between the total surface drift and wind velocity is approximately 3.5% at long fetches. Although Wu (1975) produced a very comprehensive set of data, the use of surface floats is not an ideal technique for measuring the current, since the floats are unlikely to remain at a constant elevation and can easily be deflected by the airflow itself to give artificially high values. It was therefore considered that Wu's results should be treated with some caution.

Cheng and Mitsuyasu (1992) confirmed Wu's results, again using surface floats, but in addition to measuring the current beneath wind-generated waves, they also measured the wind-generated current in the presence of long waves. For wind and waves

propagating in the same direction, they found the ratio of the current to the friction velocity to be reduced slightly compared with the wind only case. There is again a large amount of scatter in the data, and the measurement technique is not entirely convincing. Only the time averaged velocities are measured, and not the variation of the wind-induced current with the phase of the long wave. If there is a phase variation of the surface shear stress, then a corresponding variation in the wind-induced velocity in the water would be expected, but this effect has not previously been investigated experimentally (see Chapter 6).

Cheung and Street (1988) measured the velocities beneath the water surface using a laser fixed in Cartesian space, for both wind-generated waves and combined mechanically and wind-generated waves. They did not sample above trough level, presumably due to the limitation of their laser processor, so their data is not useful in elucidating the near-surface velocity field. Furthermore, in making comparisons between the velocities measured in the presence and in the absence of long waves, they compare velocities under wind only waves in a Cartesian frame, to data in a Cartesian frame for the combined wind and waves frame; this is equivalent to comparing wave-following to Cartesian velocities, and is not valid. Indeed, they find that their velocities measured in the presence of the long waves do not appear to fit a log-linear profile, which is perhaps to be expected given the comments in section 2.1.2. Floats clearly have the advantage that they will in effect measure in a wave-following frame.

Magnaudet and Thais (1995) measured the wave motion and velocity fluctuations beneath laboratory wind-generated waves. Fast wind speeds and large fetches were used, so well-developed waves were generated, with frequencies of up to 2 Hz and 14 mm root mean square amplitude. Thais and Magnaudet (1995) developed a triple decomposition method to calculate the potential (or irrotational) and rotational parts of the orbital motion, as well as the turbulent fluctuations. The turbulence was found to be essentially unaffected by the orbital motion. They analysed the rotational wave component, which they considered important in energy transfer, and found that a significant part of the orbital motion is a result of wave-current interaction due to the highly sheared profile.

2.3 Summary

From the above review it is apparent that a large amount of theoretical work has been carried out in the airflow, focusing on determining the rate of, and mechanisms for, wave growth. A number of airflow structures have been proposed over a range of wind speeds, and it is clear that a comprehensive set of airflow measurements is required in order to attempt to verify the proposed structures. In the water, a model is required to predict the effects of an overlying airflow on the wave motion, together with a comprehensive set of data against which to compare its results, in order to understand the modifications to the wave motion caused by the overlying airflow. It is essential that a combined set of measurements in the air and water is taken, to enable the flows in the air and water to be considered together as a coupled flow, allowing elucidation of the flow structure. In particular, there is a need for a set of measurements which shows the variation with the phase of the underlying long wave of the characteristics of the flows in both the air and the water. The most recent work of Belcher et al. (1994) attempts to model the whole flow. To verify such a model, measurements throughout the flow field are required, and must include, not just the wind and water kinematics, but also the wave characteristics and measurements of the nature of the water surface. Only with such a complete set of flow data is it possible to attempt to fully understand the nature of the interaction between wind and waves.

3. EXPERIMENTAL APPARATUS, DATA ANALYSIS, AND PRELIMINARY RESULTS

This chapter details the new wind-wave facility, designed by the author, which was used in the experimental investigation. The instrumentation used is described and the methods of data analysis outlined. The results of a preliminary testing programme are reported and used to validate the performance of the new facility.

3.1 The Wave Flume

The wave flume is 20 m long, 0.3 m wide and has a working water depth of 0.7 m. (Figure 3.1). The side walls are constructed of plate glass. Waves are generated by a flat-backed, bottom-hinged, paddle which is numerically controlled. Only regular waves were used in the present study, so the paddle was controlled using a sinusoidal wave signal generator. At the downstream end of the flume, a block of polyether foam, with hole gauge 2 mm, is used as a passive wave absorber. The foam is 2 m in length, and the leading edge is cut to form a vertical wedge with an included angle of 30°.

The tank was designed for the study of two dimensional wave forms, and is therefore relatively narrow compared with the water depth. Swan (1990) has shown that a two dimensional wave-current interaction can only be created within a relatively narrow channel. It is considered that this will also be the case for a two dimensional wind-wave interaction.

3.2 The Wind Tunnel

A wind tunnel, designed by the author as part of the present work, has been constructed above the existing wave flume. The wind tunnel is an open-circuit blower tunnel, being open to the atmosphere at each end, and using a centrifugal blower fan. The fan is positioned above the wave maker at the upstream end of the flume to produce an airflow in the same direction as the wave propagation. The tunnel was designed so that the fan could also be located at the downstream end of the flume, to produce an airflow in the opposite direction to the wave propagation.

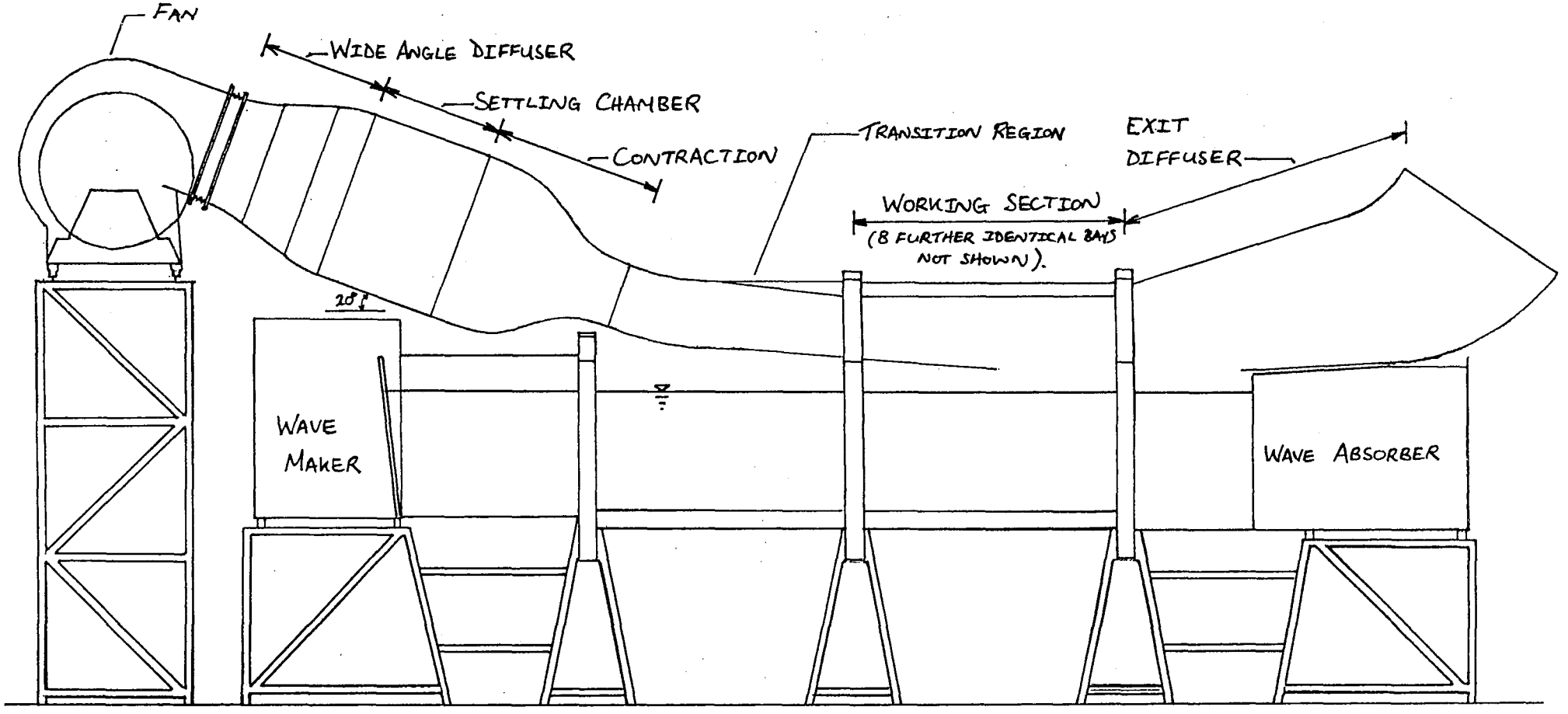


Figure 3.1: Wind wave interaction facility

The principal components of the wind tunnel are identified in Figure 3.1. In the following sections, the function of each of these components is briefly outlined, and their design described and substantiated.

3.2.1 The Working Section

The wind tunnel working section, the area where the wind and waves interact, is 12.7 m long, 0.6 m high and 0.3 m wide, the same width as the wave flume (Figure 3.2). A relatively high and narrow section was adopted for three reasons: to reduce the relative change in area caused by the passage of the wave; to create a region of undisturbed flow towards the tunnel roof; and, to produce a two-dimensional airflow. Like the wave flume, the sides of the wind tunnel are plate glass to facilitate laser measurements. The roof, which is perspex, is lightweight and easily removable, with all joints sealed using rubber 'O' rings to make the working section airtight. The top corners of the tunnel have 45° fillets to reduce the size of secondary flows resulting from stream-wise vorticity, which can cause cross-flows and flow unsteadiness (Rae and Pope, 1984). The design wind speed in the working section was 25 m/s.

3.2.2 Fan

The wind tunnel is powered by a centrifugal blower fan with backward inclined blades, driven by a variable speed DC motor controlled by a tachogenerator feedback system. Mehta (1977) recommends centrifugal blower fans for low speed open-circuit wind tunnels, since they provide a steady airflow over a range of conditions. In addition, they are quiet with low pulsations and negligible traces of the blade passing frequency, thus creating little spurious pressure and velocity fluctuations in the working section. The fan is isolated from the tunnel by means of a flexible coupling and mounted on air springs to avoid the transmission of any vibrations from the fan along the wind tunnel.

The discharge direct from the fan, however, is unsteady and has a three dimensional non-uniform velocity profile. It is thus necessary to pass the airflow through a number of flow-improving devices before it enters the tunnel working section. Three elements

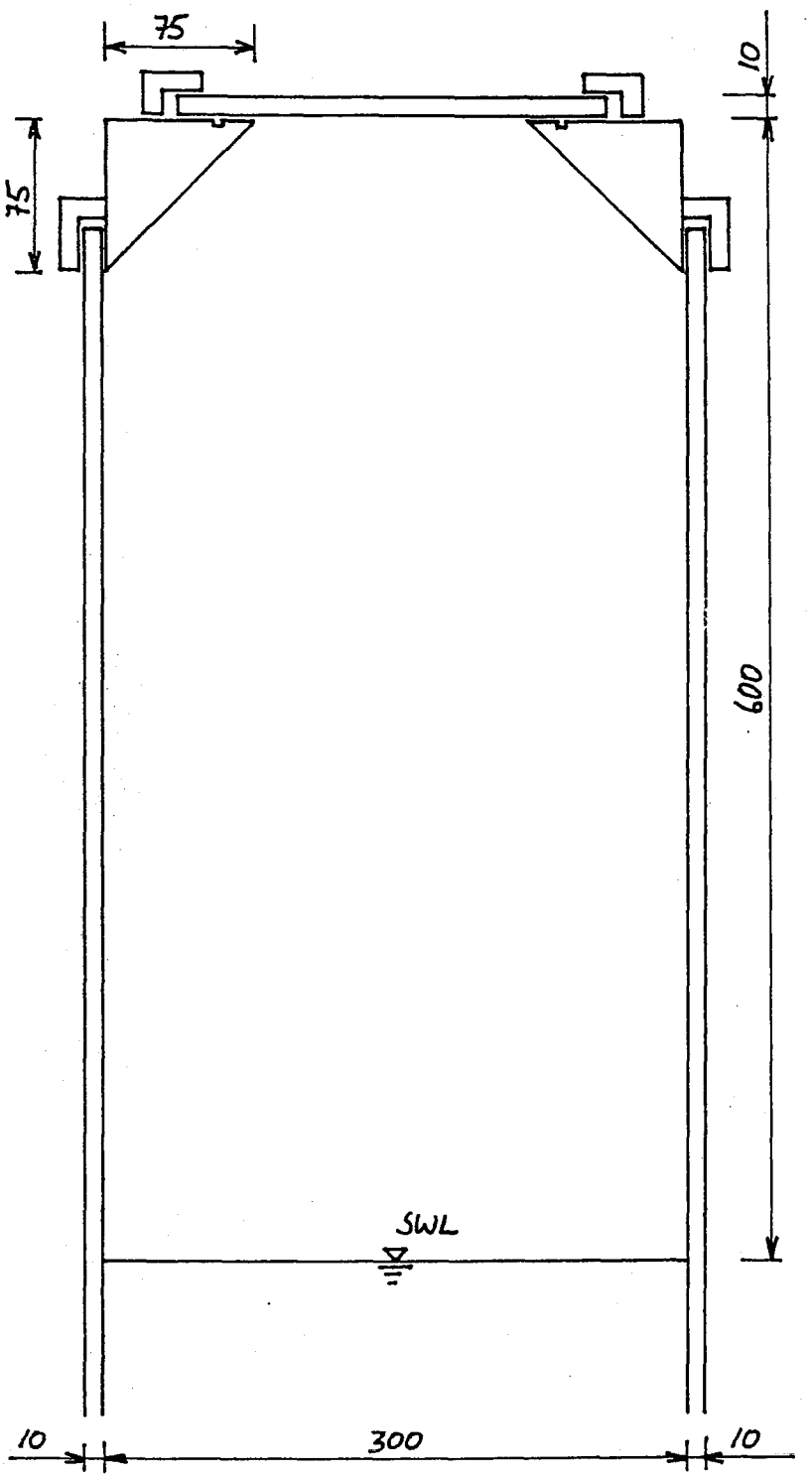


Figure 3.2: Working section (all dimensions in mm)

downstream of the fan are used to improve the flow namely, the wide angle diffuser, settling chamber, and contraction. These components are constructed from timber in a single unit, with the aspect ratio of the rectangular cross section being kept constant throughout to avoid unnecessary distortion the of the airflow.

3.2.3 Wide angle diffuser

The wide angle diffuser rapidly expands the flow from the fan outlet to the start of the settling chamber. The diffuser is formed in both the horizontal and vertical planes by two circular arcs joined by a straight diverging section (Figure 3.3). At each end of the central straight region are curved woven wire mesh screens which are perpendicular to the walls of the tunnel. The curved screens help to diffuse the flow and also reduce the tendency of the boundary layers to separate. The diffuser was designed for a given diffuser expansion ratio. The design charts given by Mehta (1977) were used to select a combination of diffuser angle, number of screens and overall shape, which would just avoid separation at the design wind speed. A moment-type optimisation method was used to determine the location and specification of the gauze screens, and the wall contours were then designed to match the screen positions.

3.2.4 Settling Chamber

The settling chamber, which follows the diffuser, has a large cross-sectional area, the size of which is determined by the required reduction in cross-section in the contraction. The relatively large cross-sectional area slows the flow ahead of the contraction, making the contraction and the flow-improving devices within the settling chamber more effective. The settling chamber is straight and parallel sided, with a cross-section 1000 x 720 mm (Figure 3.3). A sheet of aluminium honeycomb is positioned 150 mm downstream of the start of the settling chamber. The length of the honeycomb cells is eight times the 6.35 mm cell size, which has the effect of reducing the swirl and lateral velocity variations in the flow. The honeycomb also reduces the turbulence of the air flow and, by placing a screen near the wake of the honeycomb, the level of turbulence downstream can be significantly further reduced (Loehrke and Nagib, 1976). One screen

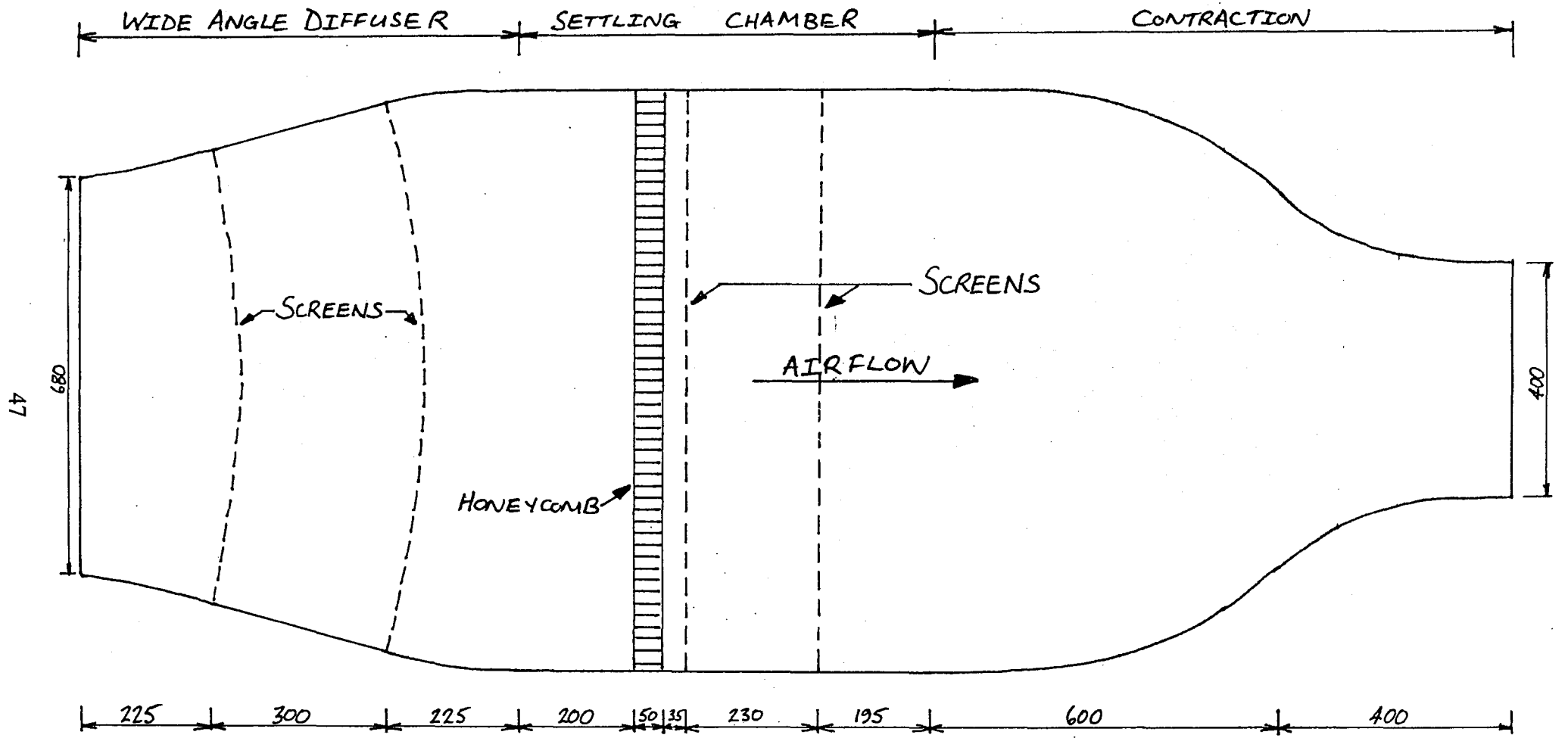


Figure 3.3: Wide angle diffuser, settling chamber and contraction (all dimensions in mm)

was therefore placed 30 mm downstream of the honeycomb, and a second 230 mm further downstream. The screens convert large-scale eddies to a large number of small scale eddies, which decay much more rapidly.

3.2.5 Contraction

The contraction increases the mean velocity and significantly reduces the velocity fluctuations as a proportion of the mean flow. The aim is to deliver as uniform and steady a flow as possible to the working section. Mehta (1978) recommends a minimum contraction ratio of 6, and in order to achieve this in the available space for the settling chamber, the contraction is made in both the horizontal and vertical planes. The wall contours in each plane are formed from two matched cubics (Figure 3.3), which Morel (1975) suggests produce low boundary layer thicknesses and turbulence levels, as well as a relatively mild inlet adverse pressure gradient. The contraction length and match point for the cubics were determined based on Morel's (1975) design method. The match point is located downstream of the contraction mid-point, making the curvature at the inlet less than at the outlet, and thus reducing the tendency of the flow to separate.

3.2.6 The Transition Region

The transition region connects the end of the contraction to the working section, introducing the airflow above the water. As shown in Figure 3.1, the axis of the contraction is inclined at an angle of 20° to the horizontal, enabling it to be accommodated above the wave flume. The first part of the transition region turns the flow through 20° using circular arcs top and bottom, and is followed by a short section with top and bottom plates parallel and horizontal, ensuring the airflow is indeed horizontal (Figure 3.4).

The transition plate introduces the airflow above the water. The plate slopes downwards at 3.5°, gradually expanding the flow and so avoiding separation. It ends at 100 mm above still water level, the gap being kept relatively large to reduce the relative change in cross section as the wave passes beneath. The end of the transition plate is located a

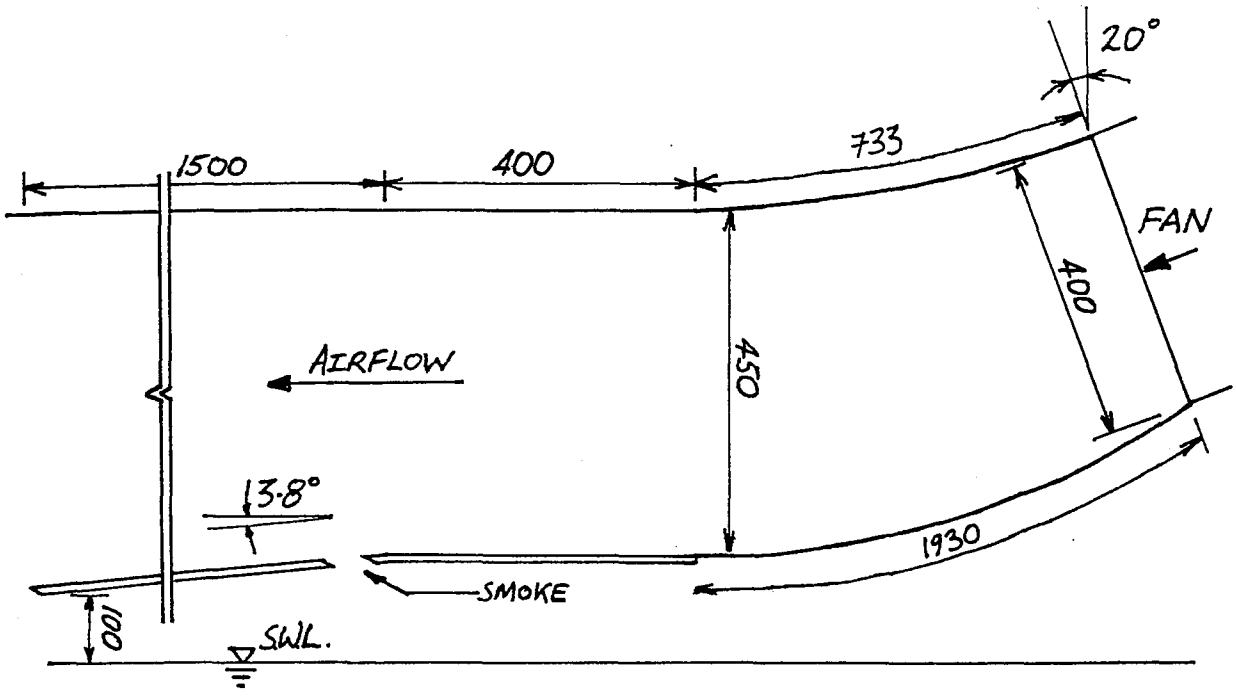


Figure 3.4: Transition region (all dimensions in mm)

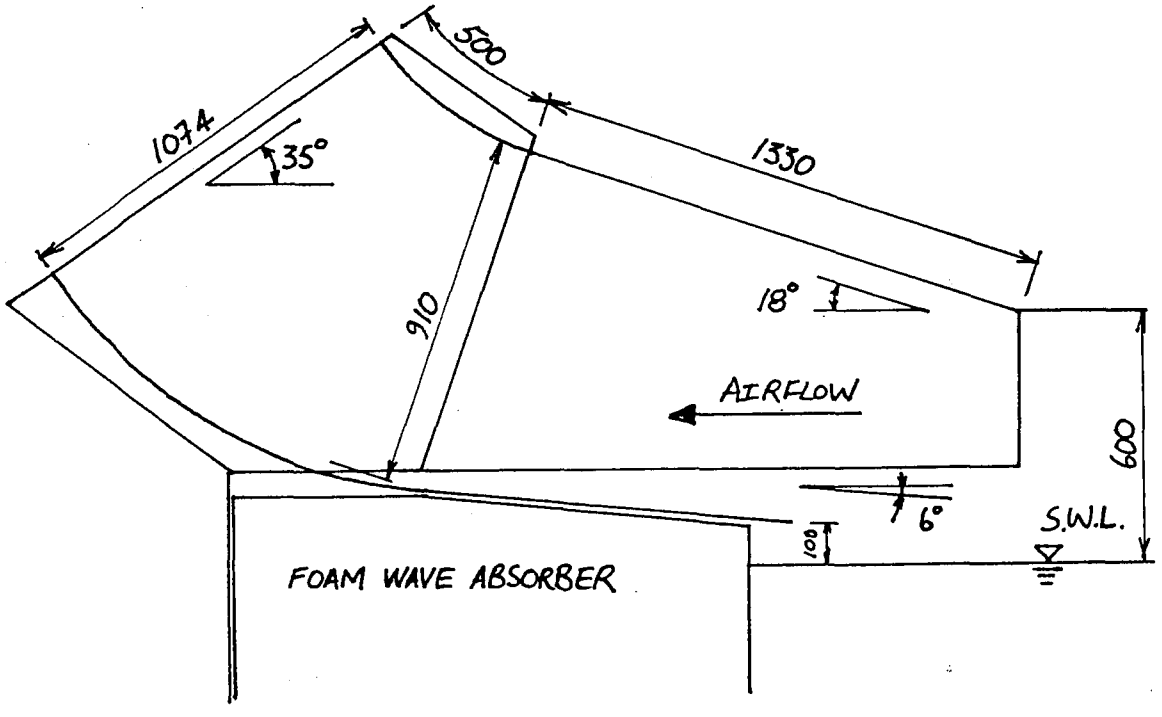


Figure 3.5: Exit diffuser (all dimensions in mm)

distance of three times the water depth from the wave paddle to allow the mechanically generated waves to become fully developed before the airflow was introduced (Shemdin and Hsu, 1967).

3.2.7 Exit Diffuser

The exit diffuser is located at the downstream end of the working section, its purpose being to expand the airflow's cross-section before discharge back into the atmosphere. An inclined straight plate, starting at 100 mm above still water level, directs the airflow away from the water surface and over the end of the wave tank (Figure 3.5). A corresponding straight plate at the roof, diverging from the lower "lifter plate", followed by diverging curved sections top and bottom, expands the area of the flow by a factor of 2.5, with an equivalent divergent cone angle of 7°. The relatively small angle of divergence was designed to avoid flow separation. By gradually expanding the cross-sectional area of the flow, the speed of the airflow is reduced before the sudden expansion as it enters the atmosphere. The aim was to improve the steadiness of the flow at the outlet, so reducing pulsations and reflections disturbing the airflow in the working section.

3.3 Water Surface Elevation Measurements

The time history of the water surface elevation was measured using fixed surface-piercing wave gauges. Each gauge consisted of two 3 mm diameter stainless steel rods spaced 12.5 mm apart. The rods were thicker than the norm, since the standard gauges were found to vibrate in the flow. Each gauge was suspended from a vertical traverse, mounted on a carriage running along rails above the tunnel roof. The gauges were held on airfoil-shaped tubes, which reduced disruption to the airflow, whilst being rigid and so minimising the possibility of vibrations. The gauges were energised with a high frequency square wave voltage, and an output voltage measured which was directly proportional to the depth of immersion. The absolute water surface elevation could be determined to within ± 0.5 mm.

3.4 Kinematics Measurements

Kinematics measurements in both the air and water were carried out using laser Doppler anemometry. A 35 mW helium neon laser was used together with a system of optics and a 'shifter' to produce two beams, whose planes of polarisation were perpendicular to one another. The beams were passed through a 500 mm focal length lens, causing them to intersect within the tank, and create a measuring volume approximately 0.075 mm^3. Two optically flat mirrors were used to position the beams in the vertical plane. The upper mirror and lens were supported on a vertical traverse which allowed the elevation of the beams to be adjusted. The cross-tank and stream-wise position of the measuring volume could be adjusted using a traverse system in the horizontal plane.

The system was used in forward scatter, so that the measuring volume could be observed from the opposite side of the tank using a camera or photo multiplier. The forward scatter arrangement produces a relatively strong signal, and provides no disturbance to the flow since all the instrumentation is located outside the tank. With the system used, only one velocity component could be measured at a time. To measure the second velocity component, the beams were simply rotated through 90°.

The Doppler burst information recorded by the photo multiplier was processed using a burst analyser. Unlike other processors, in particular 'trackers', the burst analyser does not interpolate between bursts. The data was therefore randomly spaced in time, the system recording a velocity measurement whenever a Doppler burst was detected and validated by the processor. The data rate was very sensitive to the amount of seeding, the fluid velocity, and the camera focus. The photo multiplier voltage and a dead time interval, where the processor is switched off for a short period, were adjusted in order to attain the target sampling frequency, and to ensure that it remained as close as possible to constant during each run.

The burst processor (Dantec Flow Velocity Analyser 58N40 Enhanced) was newly acquired for this project, and a large number of problems had to be overcome to produce reliable data. This system was used rather than the existing tracker system for a number of reasons. In airflows, a tracker based system was found to give very poor data

rates because of the nature of the seeding, whereas the burst analyser could sample at up to 30 kHz. In both the air and the water, the region of most interest is very close to the water surface where, due to the passing of the wave, an intermittent signal will be received. The burst analyser has a very rapid response time (or signal establishment time), and produces no signal when the beams are in the fluid in which they have not been focused. In contrast, a tracker samples data continuously, as it searches for the signal, whether the beams are in focus or not, and is much slower to 'lock on' to the signal. The burst analyser was therefore used for all the air and water measurements.

3.5 Signal Decomposition

The method of decomposition of the measured data was similar for both the air and water velocities, and was also applied to the analysis of the surface elevation records. Consider, say, the velocity data. The instantaneous velocity can be decomposed into three quantities at a given spatial position, $\underline{x}$:

$$u(\underline{x},t) = \overline{U}(\underline{x}) + \tilde{u}(\underline{x},t) + u'(\underline{x},t) \tag{3.1}$$

where $\overline{U}(\underline{x})$ is the time averaged mean velocity component, $\tilde{u}(\underline{x},t)$ the wave-induced velocity, and $u'(\underline{x},t)$ the turbulent velocity fluctuation.

The phase averaged velocity, which is the average value at a particular phase of the underlying long wave, is defined as:

$$\langle u(\underline{x},t)\rangle = \lim_{N\to\infty} \frac{1}{N}\sum_{n=0}^{N} u(\underline{x},t-nT) \tag{3.2}$$

where T is the period of the underlying wave motion, and N and n are integers.

The time averaged velocity can then be defined as:

$$\overline{U}(\underline{x}) = \lim_{\tau \to \infty} \frac{1}{\tau} \int_0^{\tau} \langle u(\underline{x},t) \rangle dt \tag{3.3}$$

where τ corresponds to the duration of the given test run. Since these averaging techniques also remove the turbulent fluctuations, the wave-induced velocity may be calculated by subtracting the time averaged velocity from the phase averaged velocity

$$\tilde{u}(\underline{x},t) = \langle u(\underline{x},t) \rangle - \overline{U}(\underline{x}) \tag{3.4}$$

The turbulent fluctuations may then be calculated from

$$u'(\underline{x},t) = u(\underline{x},t) - \langle u(\underline{x},t) \rangle \tag{3.5}$$

3.6 Analysis Routines

The analysis routines used to decompose the horizontal and vertical velocities in both the air and water were similar. For each velocity record, the water surface elevation was recorded simultaneously. From the surface elevation time traces, the zero upcrossing times for the underlying long wave are found, and the average wave period calculated. A linear least squares best-fit of the average period is then made to the recorded upcrossing times, and hence the upcrossings times for the underlying wave are found. The phase averaged water wave can then be calculated.

Using the zero upcrossing times, the velocity can be phase averaged relative to the phase of the water wave. The number of intervals used to phase average the data was taken such that the phase averaging interval was approximately the same size as the data sampling period. The number of intervals per wave period was taken as 2^N (where N is an integer) to facilitate later Fourier analysis. Phase averaging the velocities removes biasing effects due to the variable data rate. This is the reason why the time averaged velocity is calculated from the phase averaged velocities (equation 3.3), rather than by simply time averaging the original data. It was found that more data was collected at

faster velocities, so, for a sinusoidal velocity record, a simple time average would give too large a value for the mean velocity.

In the airflow, although the velocity at each elevation was sampled for 200 seconds, there still appeared to be some fluctuations in the phase averaged velocity traces due to the highly turbulent nature of the flow. The phase averaged records were therefore curve-fitted to filter out these fluctuations. Above crest level, filtering of the data was done in the Fourier domain, removing components above the third harmonic. Below crest level, the phase averaged records were not continuous, so the results of Fourier filtering would not be meaningful. Instead, a linear least-squares curve-fitting routine was used, curve fitting only the non-zero values. The basis function used was:

$$1 + \phi + \cos\phi + \cos 2\phi + \cos 3\phi + \ldots\ldots + \cos 16\phi \qquad (3.6)$$

where ϕ is the phase of the long wave. It was found that at up to one wave amplitude above crest level, the linear least-squares routine produced a better fit than the Fourier filter. Conversely, at greater elevations, the Fourier filtered curve-fit provided a better fit than that from the linear least-squares routine. At around the one amplitude level however, the two curve fits were effectively identical, which provided a useful check.

The filtered velocities were used in the subsequent analysis to find velocity profiles, phase information, and the streamlines (Chapter 4). They were also used in the next stage of the signal decomposition, the calculation of the velocity fluctuations. The filtered phase averaged velocity traces were interpolated to find the phase averaged velocity at the corresponding phase for each velocity record in the original time trace. The phase averaged filtered velocity is subtracted from the original data to obtain the time trace of the turbulent fluctuations. The root mean square fluctuations are then calculated, and phase averaged using a similar phase averaging routine to that used for the velocities. Two examples of this velocity decomposition are provided in Figures 3.6 and 3.7: the first (Figure 3.6) corresponds to a continuous time-history of the air velocity measured above the level of the wave crest; and the second (Figure 3.7) shows

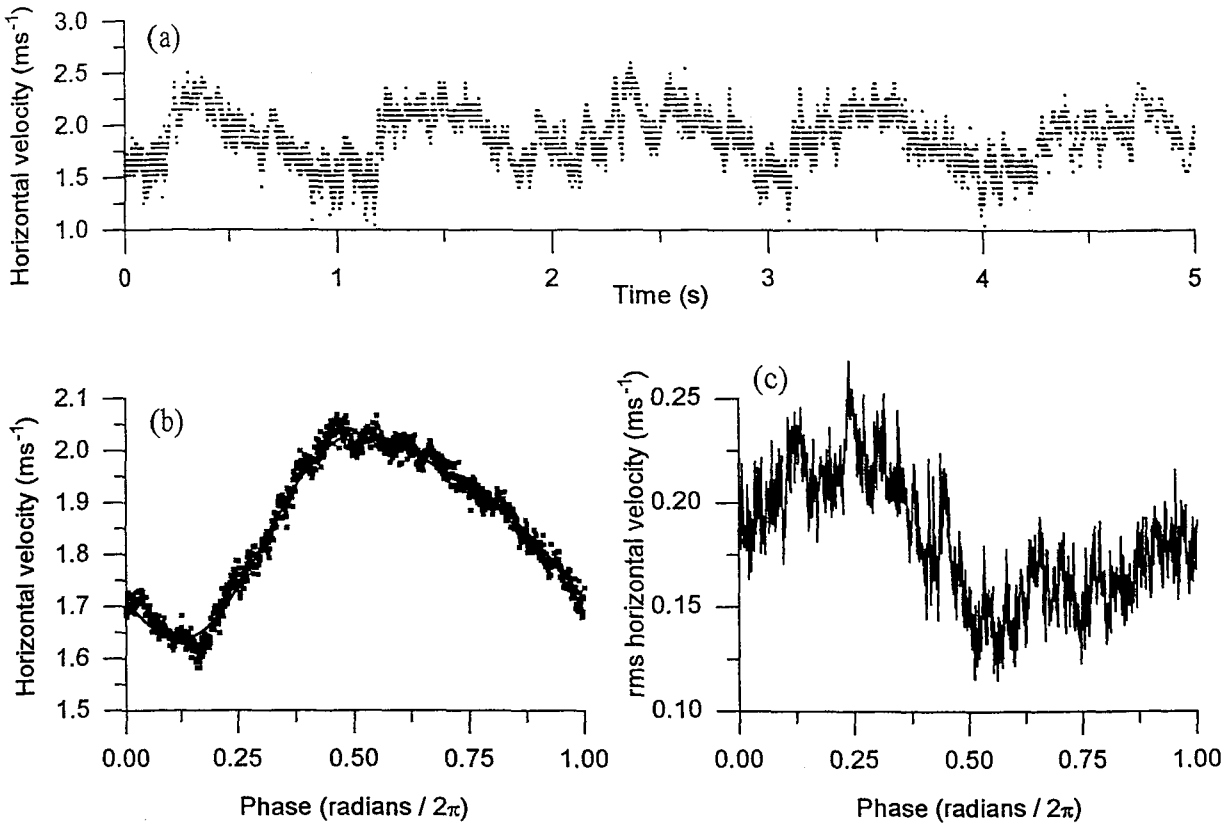


Figure 3.6: Air velocity signal decomposition above crest.
(a) Continuous time history, (b) phase average, (c) root mean square

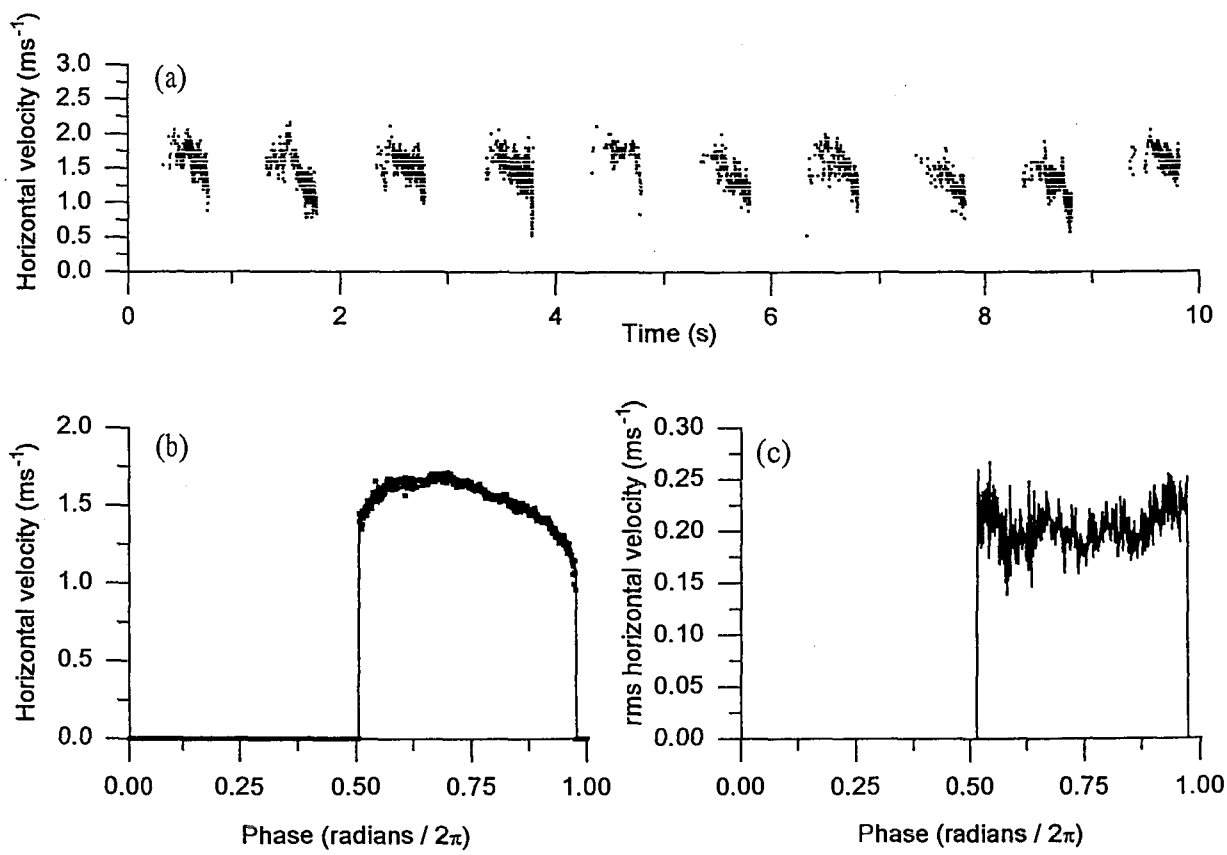


Figure 3.7: Air velocity signal decomposition below crest.
(a) Discontinuous time history, (b) phase average, (c) root mean square

an intermittent time history of the air velocity measured within the crest-trough region. In each case, the figures show the measured velocity time history, the phase averaged velocity, and the root mean square turbulent fluctuations.

The phase averaged velocities obtained as described above are in the time domain, and measured at a fixed point in Cartesian space. However, as discussed in Chapter 2, ideally the data is required in the spatial domain, and in a wave following co-ordinate frame of reference. To transform the data to the spatial domain is relatively simple, provided that it is assumed that the wind-wave system is steady over a time scale longer than the wave period, and that the process has reached a steady state with fetch. In this case, the phase averaged velocities in a temporal domain can be considered equivalent to velocities in a negative spatial domain. It is reasonable to assume that the whole system will become steady in time, but it is unlikely that it will reach equilibrium in space. In a tank of finite length, the waves will continue to develop with fetch, but, at a given fetch, should become steady after having been given sufficient time to reach equilibrium. To transform the data in to a wave following frame, linear interpolation is used. The velocity components are retained in their original directions, and it is only the vertical co-ordinate which is transformed, as indicated in equation 2.1. Continuous velocity records to within 5 mm of the water surface are thus obtained, unlike the intermittent phase averaged records shown in Figure 3.7. Very close to the water surface, linear interpolation and end of record effects lead to some irregularities in the transformed phase averaged velocities. These anomalies are removed by again filtering in the Fourier domain above the third harmonic. The root mean square fluctuations are transformed in an identical way to the velocities.

3.7 Preliminary Results

3.7.1 Wind tunnel

A flat smooth perspex bed at the same elevation as the still water level in the wave flume was fitted in the wind tunnel in order to facilitate measurements to assess the performance of the wind tunnel. A series of horizontal velocity measurements was made in the airflow at mid-depth and mid-fetch in the wind tunnel to examine the flow

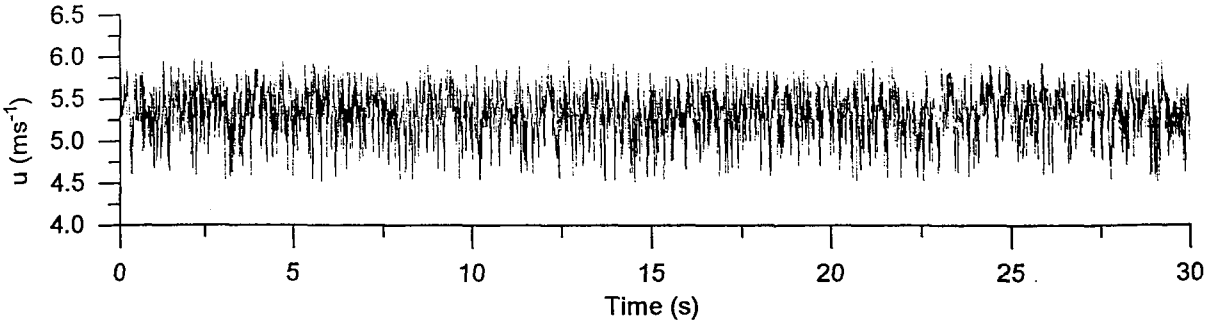


Figure 3.8: Laser Doppler anemometer air velocity sample output

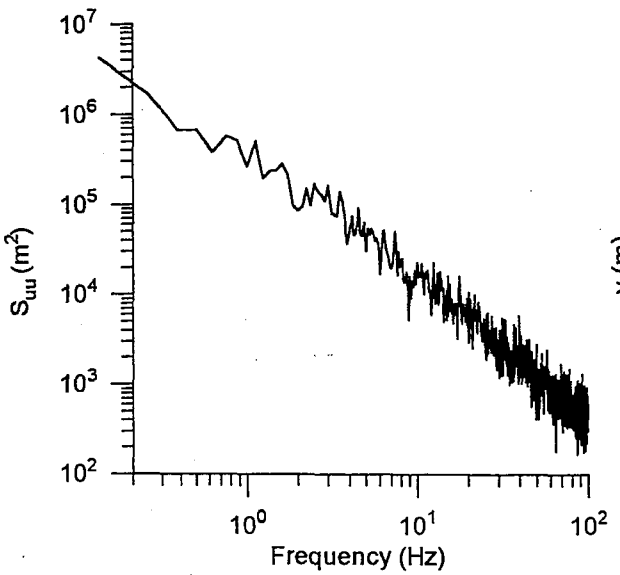


Figure 3.9: Flat bed velocity spectrum

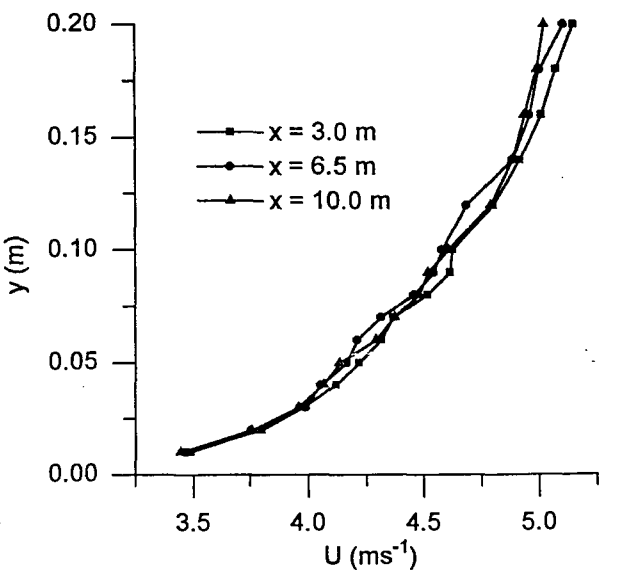


Figure 3.10: Velocity profiles with fetch

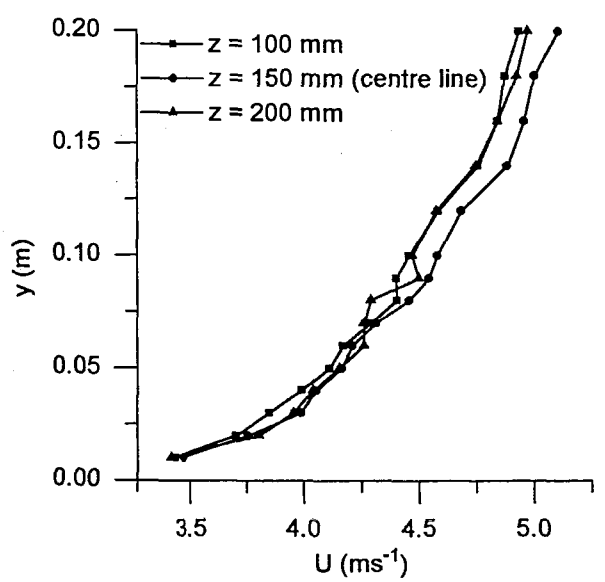


Figure 3.11: Velocity profiles across tank

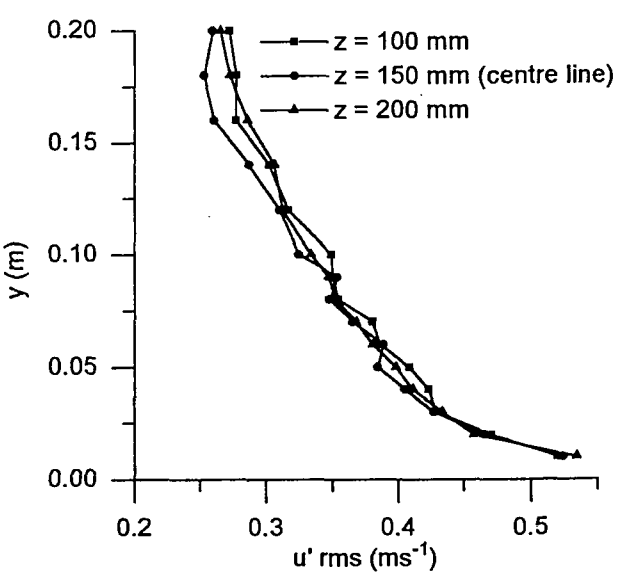


Figure 3.12: rms velocity fluctuations across tank

steadiness. Figure 3.8 shows a 50 second velocity time trace, and it is clear that, although there are large velocity fluctuations, the underlying velocity is not changing. When the velocity was sampled every hour over the course of a day, it was found that the velocity remained remarkably constant, the standard deviation from the mean being only 0.15%. Fourier analysis was done to find the spectra for the velocity records, and the averaged spectrum is given in Figure 3.9. At the low frequency end of the spectrum, there are no significant peaks, suggesting that there are no instabilities developing in the tunnel, and that upstream effects such as the blade passing frequency are not transmitted downstream. Any unsteadiness effects have presumably been absorbed within the settling chamber and contraction, and no further problems have been introduced at the end of the transition plate. The higher frequency end of the spectrum also shows no distinct peaks. The gradient taken between 10 and 100 Hz is $f^{-1.59}$, which is close to the gradient for homogeneous fully developed turbulence of $f^{-1.66}$, suggesting that the flow is close to being fully developed above the flat bed.

The time-averaged root mean square velocity fluctuation was calculated from data at the mid point of the tunnel, and was approximately 4.5%. This is comparable with the values measured in other wind-wave facilities (Kawamura et al., 1981).

For a nominal 5 m/s free stream velocity, the development of the velocity profile along and across the wind tunnel was investigated. Figure 3.10 shows the development of the boundary layer along the length of the tank. The constancy of the velocity profile with fetch suggests that the boundary layer very quickly establishes itself and becomes steady and close to being fully developed. The velocity profiles across the tank at mid-fetch are also very similar (Figure 3.11), showing in the central one third of the wind tunnel that the flow is not influenced significantly by wall effects, and that the flow on the centre-line may thus reasonably be considered to be two-dimensional. Three dimensional effects appear to be confined to regions close to the side walls. The root mean square horizontal velocity fluctuation profiles (Figure 3.12) show the expected reduction in the turbulence with increasing elevation. The turbulence also stays constant in this central region, confirming the two dimensional nature of the flow.

The horizontal velocity profiles with depth for three wind speed cases at the mid-fetch on the tunnel centre-line are presented in Figure 3.13. Over this wide range of free stream velocities, a distinct log-linear boundary layer and constant velocity free stream region are apparent. The wind tunnel appears to perform as expected over a wide range of wind speeds.

The static pressure at the roof of the tunnel was also measured, at eight fetches and for three wind speeds (Figure 3.14). The pressures were measured relative to atmospheric using alcohol manometers, with 0.3 mm tapping points through each perspex roof panel. In all cases, the pressure is negative at the first station, due to the curved roof of the transition region. However, by the second station, the pressure is large and positive. There is clearly a favourable pressure gradient along the tunnel, and the pressure reduces along the tunnel. The pressure reaches a near constant value with only a small favourable gradient between 8 - 10 m, before the pressure gradient increases again towards the exit diffuser. Theses measurements again confirm that the wind tunnel is performing well.

3.7.2 Water Waves

The uniformity of the mechanically generated wave form in the absence of wind was investigated by examining the time traces of a large number of waves. The waves appear steady over time (Figure 3.15), suggesting little evidence of either cross-tank modulation or longitudinal seiching. The paddle was run for at least one hour before sampling to minimise such effects. Baldock et al. (1996) measured the spatial uniformity of a regular wave train in the tank, and determined the reflection coefficient from the variation in wave height. Over a wide range of wave periods, the reflection coefficient was found to be less than 2%. The wave paddle is driven using a signal generator, which allows the frequency and amplitude of the wave to be set very accurately, and which, measurements showed, could reproduce almost identical waves. The wave form appears sinusoidal, and the waves are two dimensional, with no significant side wall effects apparent.

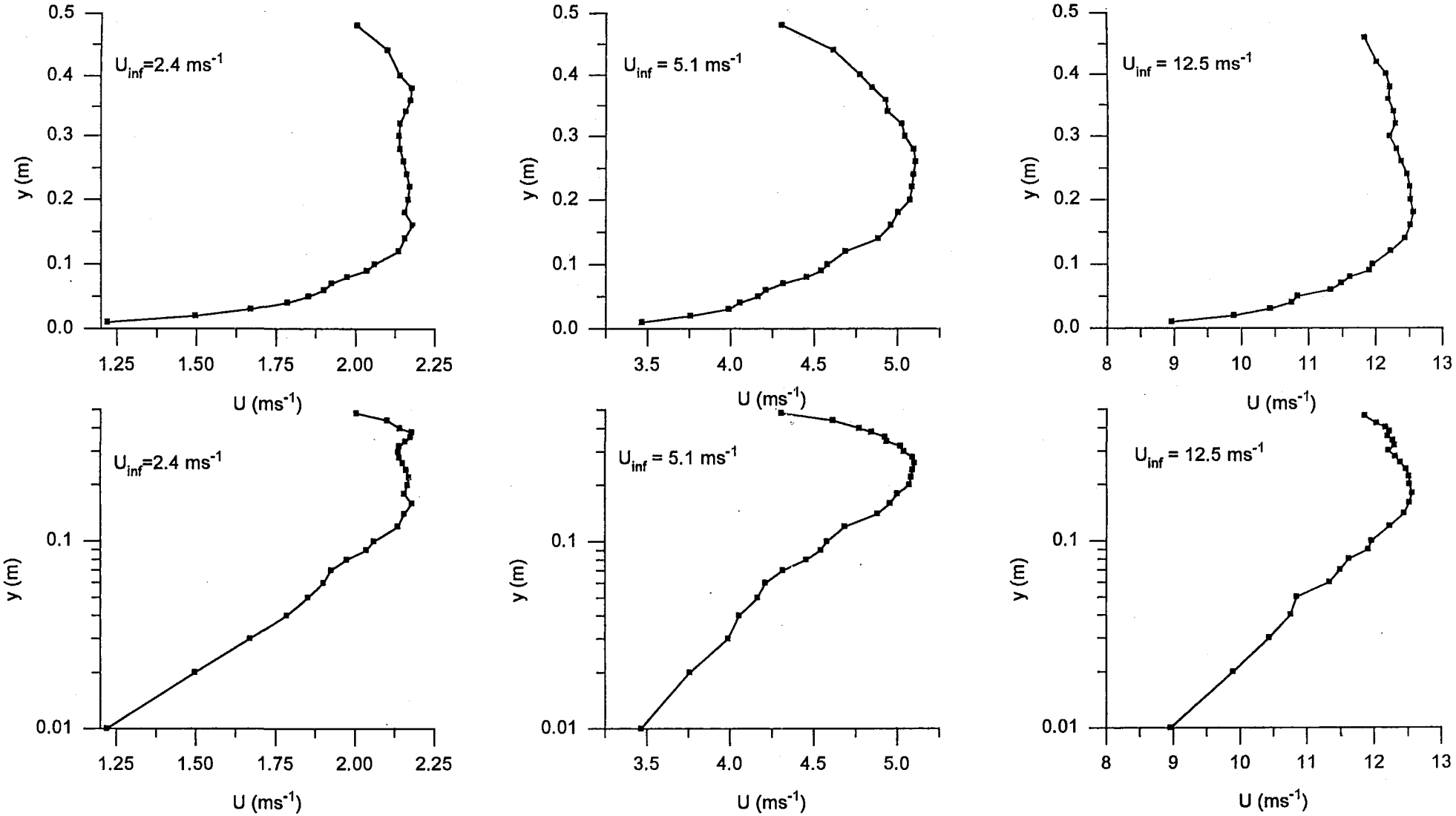


Figure 3.13: Time averaged horizontal velocity profiles over flat bed for U_{inf}= 2.4, 5.1 & 12.5 ms^{-1}

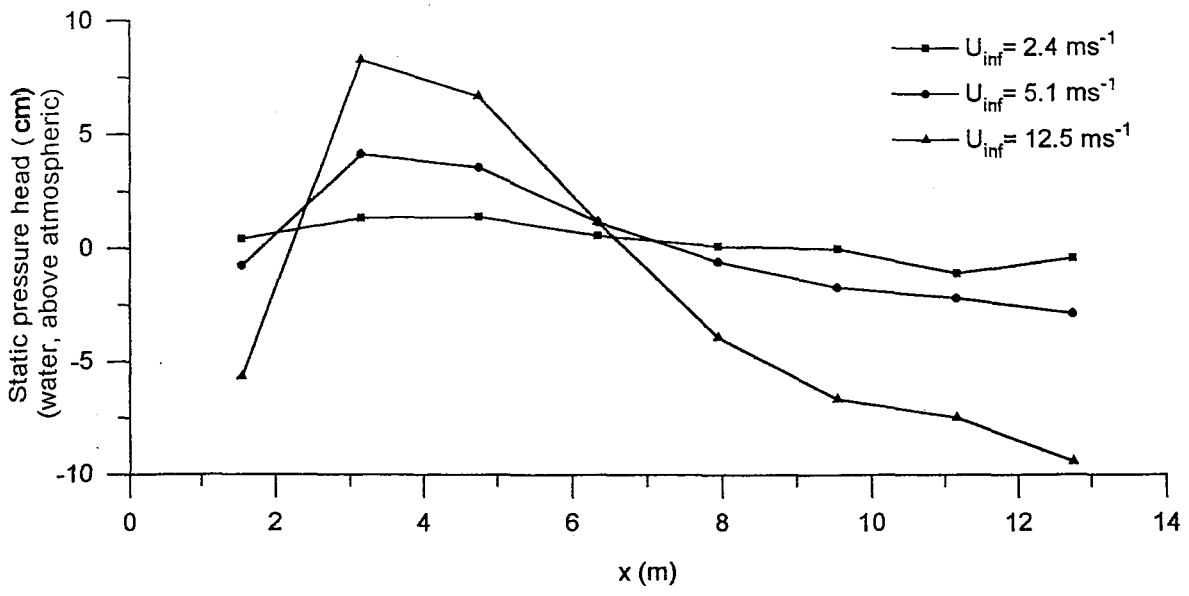


Figure 3.14: Static pressure variation with fetch at the tunnel roof

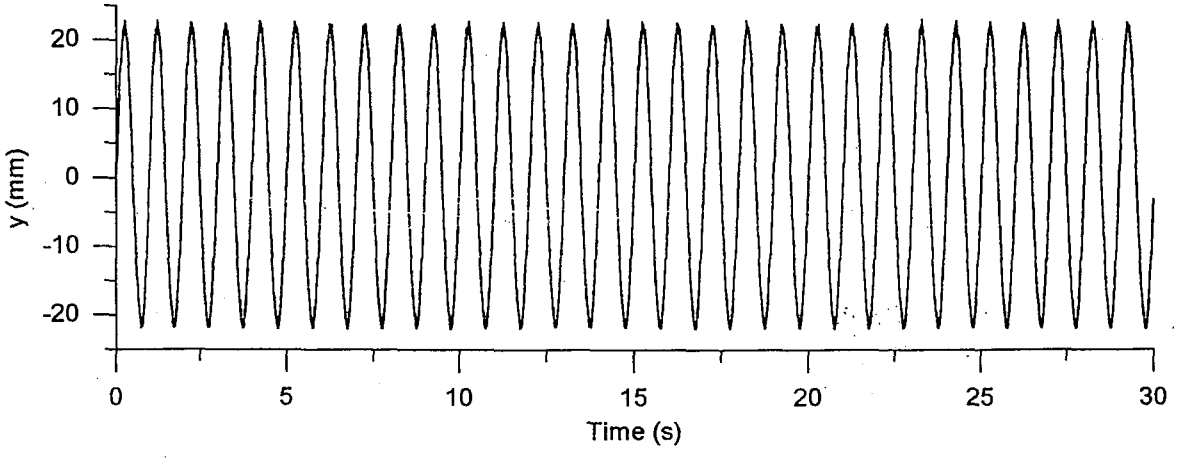


Figure 3.15: Sample output of water surface elevation of mechanically generated waves

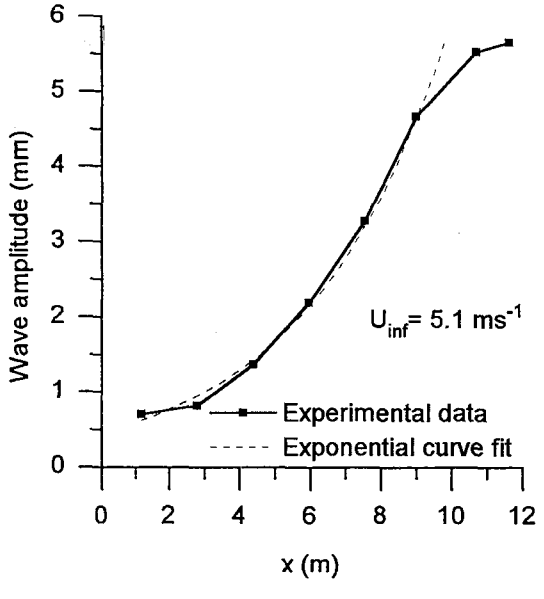


Figure 3.16: Growth in wave amplitude with fetch

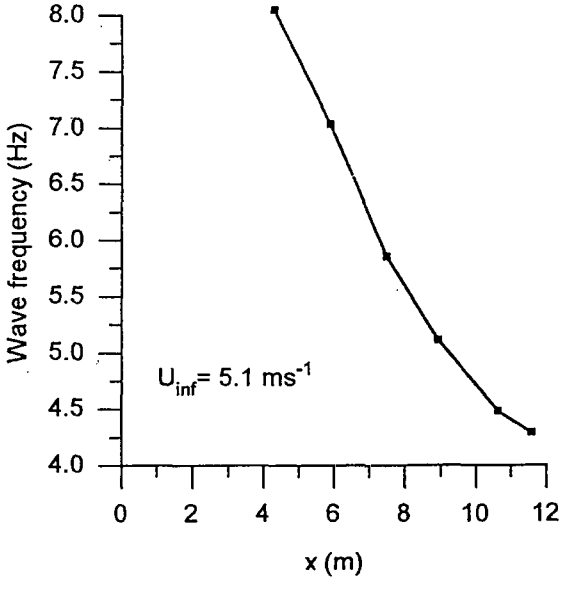


Figure 3.17: Change in wave frequency with fetch

The development of wind-waves in the flume, in the absence of mechanical waves, was investigated for a range of wind speeds. Below 2.5 m/s, no visible wind-waves were generated, although there was clearly a surface current and small disturbances to the water surface. At faster wind speeds, small wind-waves began to form, which at first appeared somewhat three dimensional. As the wind speed was further increased, the wind-waves became much more two dimensional, and continued to grow.

The wave growth along the tank was measured for a free-stream velocity of 5 m/s. For this velocity, waves were not visible until 3 m downstream of the end of the transition plate, after which a rapidly increasing rate of wave growth was observed. The growth in the wave amplitude with fetch appears to be exponential (Figure 3.16), agreeing with the findings of other experimenters and accepted theory. The wave frequency correspondingly decreases as the wave amplitude increases (Figure 3.17). At fetches beyond 10 m, the wave growth quickly reduces as the end of the flume is approached. This decrease is due to the action of the wave absorber, and, in particular, disruption to the airflow at the exit diffuser.

3.7.3 Laser Doppler Anemometer.

The calibration and output of the laser Doppler anemometer was checked by measuring the horizontal and vertical velocities beneath a series of regular waves. The measured velocities were compared with Stokes' second order theory, and the agreement found to be excellent (Figure 3.18). The figure presents velocity traces for three elevations in the water, including one at still water level. The burst analyser appears not to sample data when the measuring volume is in the air, but very quickly re-establishes when the measuring volume re-enters the water, where the beams are focused.

An assessment of the phase lags in the measuring system was made by correlating the water surface elevation and horizontal velocity time traces. The phase lag was calculated to be less than 0.005 seconds, suggesting there was no significant phase lags in the system.

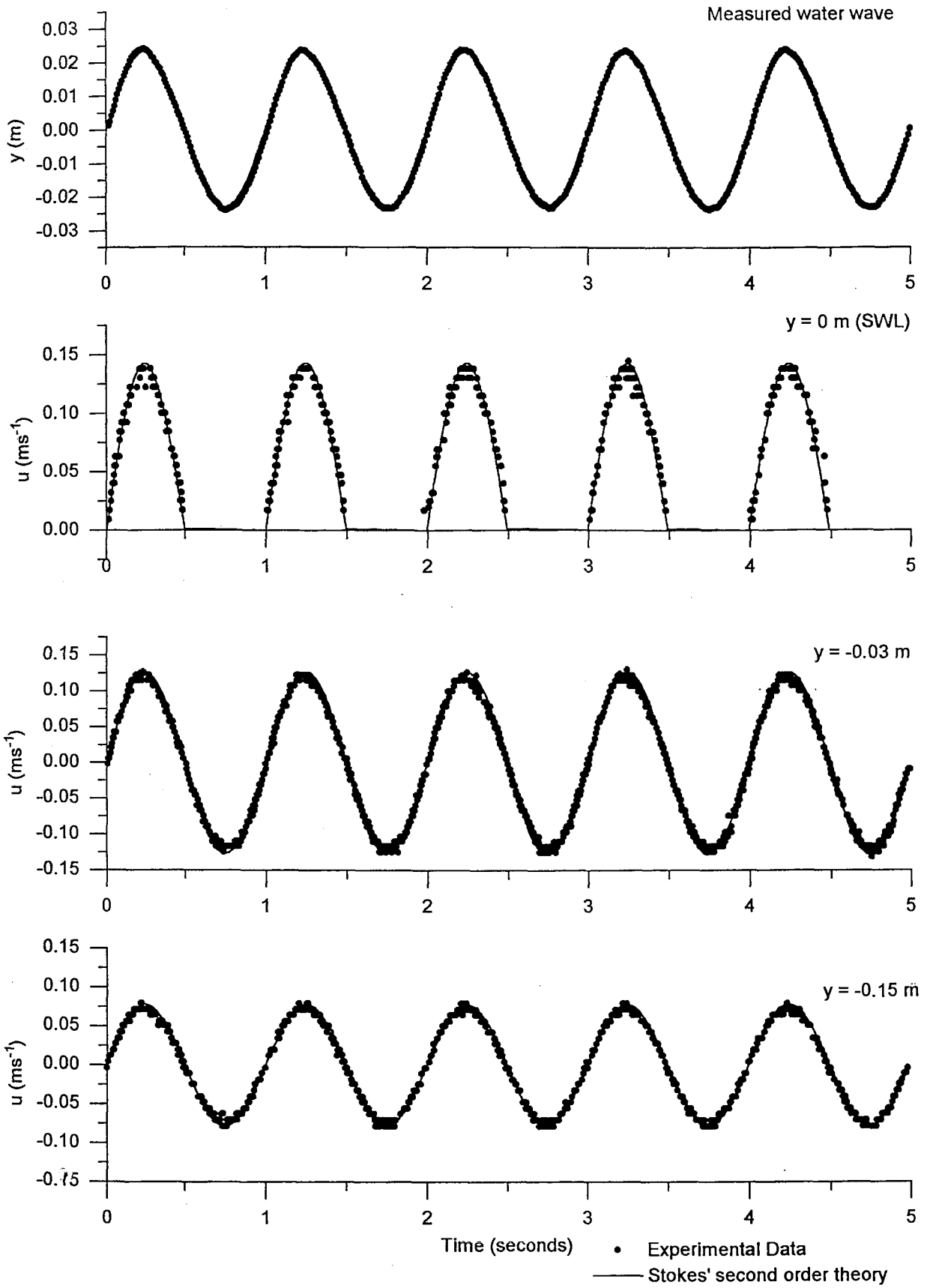


Figure 3.18: Measured velocity traces compared with irrotational theory for waves only

4. AIR KINEMATICS MEASUREMENTS

The following two chapters consider the velocity measurements made in the airflow using the laser Doppler anemometer in the new wind tunnel: the present chapter presents experimental measurements and considers the results in a qualitative sense; the next chapter presents a quantitative analysis of the results, applying key ideas from boundary layer theory.

This chapter seeks to elucidate the structure of the air flow above the waves for three different free stream air velocities. Measurements of the mean, wave-induced and turbulent velocities are presented, and the velocity data used to deduce the streamline patterns. First, the experimental programme conducted is described, and details of the experimental methods and data analysis outlined.

4.1 Experimental Programme

The review in Chapter 2 suggested that the two principle factors determining the structure of the airflow above a water wave are, firstly, the ratio of the phase velocity to the free-stream air velocity and, secondly, the wave steepness, defined as the product of the wave amplitude and wave number *ak*. It was not practicable to take enough measurements to investigate the effects of each of these parameters fully, as the data collection and processing for each case was very time-consuming. Also, as explained in Chapter 1, the purpose of the present work is to determine the effect of an airflow on a prescribed wave, and of that wave on the airflow. It was considered that this could best be achieved by keeping the wave parameters fixed, and varying only the free-stream velocity. While accepting that wave steepness affects the nature of the interaction, it was decided that the variations in the flow with the ratio of c/U_∞ is the more important ratio to investigate in this study.

The mechanically generated sinusoidal waves used throughout this experimental programme had a nominal frequency of 1 Hz and an amplitude of 22.5 mm. These waves will hereafter be referred to as the long waves, since their wave length is

significantly greater than any of the wind-waves generated in the tank. As demonstrated in the previous chapter, such waves can be steadily and repeatedly generated in the wave tank with no significant reflections. For the 0.7 m water depth used in this study, the waves have a depth to wave length ratio of 0.45 (or kd = 2.8), and can therefore be classified as deep water waves. The wave steepness is ak = 0.09, so small amplitude wave theory was considered applicable. (This is verified by the agreement between second order theory and the measured velocities shown in Figure 3.18.) The waves are intended to model the long swell waves traditionally used in the design of offshore structures.

Measurements were made with three wind speeds, specified by their free stream velocities as U_∞= 2.4, 3.1, and 5.1 m/s. For the wave described above, these wind speeds correspond to ratios of phase velocity to wind speed c/U_∞= 0.65, 0.52, and 0.30. Only cases with the wind and wave propagating in the same direction (commonly referred to as favourable cases), and the free stream wind speed greater than the wave phase velocity were considered. These were thought to be the cases of greatest interest to the engineer. Although scaling with real offshore conditions is very difficult, the c/U_∞ values chosen attempt to reflect real conditions. An extreme wave with a period 15 seconds might be expected to occur with a very strong wind, say 45 m/s, which would correspond to a ratio of c/U_∞= 0.51.

For these three wind speeds, the kinematics in the airflow, the kinematics in the water, and the surface elevation were measured in the presence of the mechanical wave. In addition, for each wind speed, the airflow velocities above a flat rigid bed were measured, as well as the velocities in both the airflow and water in the absence of the long waves (so that only wind-generated waves were present). All measurements were made at a single fetch, 9 m from the end of the transition plate. From the preliminary measurements, it was found that, beyond this fetch, the flow starts to be influenced by end effects: the rate of wave growth was seen to reduce, and the pressure gradients increased. At the selected fetch, the pressure gradients are relatively small, and the wave growth rate a maximum. The waves are clearly fetch limited, but this will always be the

case for laboratory tests. However, the preliminary results have shown that a significant amount of wave growth has occurred by the selected fetch, and that, although the system has clearly not reached equilibrium in space, it has reached a steady state in time.

4.2 Experimental Methods and Data Analysis

For all experimental runs, the mechanically generated waves were set up first, and sampled to check the period and amplitude. The fan was then switched on and the speed gradually increased to the required value. The wind and waves were run for at least one hour before sampling, to allow the system to settle down. Velocity measurements were made using the laser Doppler anemometer described in section 3.4. The airflow was seeded for the laser measurements using smoke introduced at the start of the transition plate. As the sampling frequency was very sensitive to the amount of seeding, a steady supply of smoke was introduced. A relatively small amount of seeding was found to give the greatest data rate and the highest signal-to-noise ratio for a given photo multiplier voltage. Fresh water was used for each day's runs, and the tank regularly cleaned.

Velocity measurements were made at the selected fetch from 17.5 mm below still water level, approximately 5 mm above the wave trough, to 400 mm above still water, which was 100 mm above the tunnel mid-depth. Given the importance of the flow very close to the water surface, the vertical spacing of the data points was varied so as to provide greatest detail in the area of most interest. Up to 30 mm above still water, data was sampled at 2.5 mm intervals; at 5 mm up to 100 mm; and then at 10 mm spacing thereafter. The sampling elevations were corrected for the measured wave set up to give heights above the mean water level. A target sampling frequency of 1000 Hz was selected, but the actual sampling frequency varied by up to 200 Hz. For a 5 m/s wind speed, preliminary measurements showed the length of the wind-waves was of order 0.10 m. The resulting frequency of the airflow perturbations would therefore be approximately 50 Hz, so the target sampling frequency should provide 20 samples per perturbation. At each elevation, data was sampled for 200 seconds, corresponding to 200 complete wave cycles. This was found to define the phase averaged and turbulent velocities consistently. The horizontal and vertical velocity components were measured

separately, with the water surface elevation being measured simultaneously to provide reference phase information.

The phase averaging routines described in Chapter 3 were used to decompose the measured velocities. The velocity data was transformed into a new co-ordinate frame defined by:

$$t = t^*, \qquad x = x^*, \qquad y^* = y - \tilde{\eta}\frac{\sinh k(H-y)}{\sinh(kH)} \tag{4.1}$$

where H is the height of wind tunnel, $\tilde{\eta}$ the elevation of the measured phase averaged water wave, and k the corresponding wave number (Figure 4.1). All of the following velocity data is presented in this co-ordinate frame. This is similar to that used by Hsu, Hsu and Street (1981), but uses the actual surface elevation rather than a predicted sinusoid. This was found to be an important distinction close to the water surface.

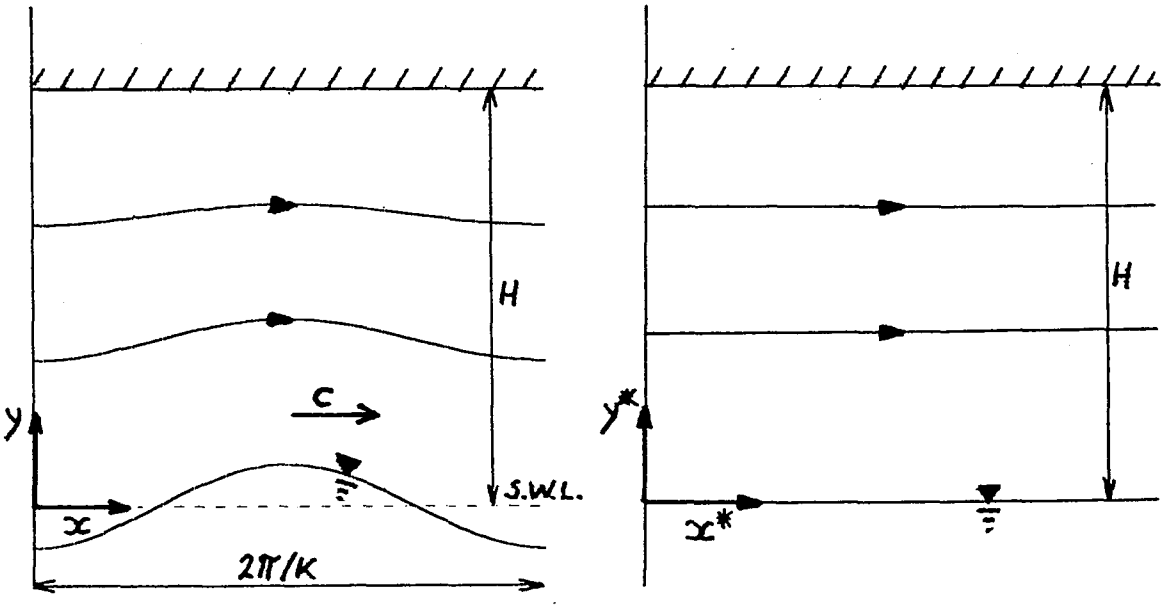


Figure 4.1: Airflow wave following co-ordinate definition sketch

The streamline patterns for the airflow were deduced from the filtered phase averaged velocity data. The streamlines are found in a frame of reference moving with the wave,

so the phase velocity is subtracted from the horizontal velocities, and the velocities are transformed into a spatial domain, as discussed in Chapter 3. Starting above either the wave crest or trough, the horizontal and vertical velocity components at a given elevation were found by interpolation. The time to move a given small horizontal displacement (δx) is calculated from the horizontal velocity. From this time and the vertical velocity component, the vertical displacement (δy) corresponding to the given horizontal displacement is calculated. The new position of the 'particle' of air is therefore calculated from the horizontal and vertical displacements. The velocity components at this new position are found, and the procedure repeated over the whole wave cycle. The locus of these points forms a streamline for the airflow. By taking starting positions over the whole depth of the flow, the streamline pattern is found in a Cartesian co-ordinate frame. The experimental streamlines are compared with the potential flow streamlines, obtained by setting y^* = constant in the above transformation. This process was extremely time consuming, but proved to be successful in allowing the streamline patterns to be accurately predicted. This has never before been achieved in a quantitative manner, and provides a very clear indication of the flow structure associated with the wind-wave interaction.

4.3 Time Averaged Horizontal Velocity Profiles

The time averaged horizontal velocity profiles for combined wind and waves are given in Figure 4.2. The horizontal velocities are time-averaged in wave-following co-ordinates defined by equation 4.1. The profiles demonstrate boundary layer type behaviour, with a region of constant velocity around the tunnel mid-depth, and an exponential type decrease in velocity towards the water surface. The free-stream velocity, U_∞ is taken as the velocity at which the velocity gradient $\partial U/\partial y^*$ first equals zero with increasing y^*. The boundary layer thickness δ is then defined as the height at which the mean velocity is equal to $0.99U_\infty$. The values of the boundary layer thickness together with the flow parameters are given in Table 4.1.

U_∞ (m/s)	c/U_∞	δ (m)
2.4	0.65	0.30
3.1	0.52	0.25
5.1	0.30	0.20

Table 4.1: Time averaged velocity parameters

The boundary layer thickness decreases with increasing free-stream velocity, since the faster velocities tend to reduce boundary layer growth. The velocity profiles appear to be smooth up to the edge of the boundary layer, except for $U_\infty = 2.4$ m/s, where there is a marked discontinuity at $y^* = 0.10$ m. An explanation for this effect is provided in section 4.4.3.

The time averaged horizontal velocity profiles for $U_\infty = 5.1$ m/s for the flat smooth bed (described in Chapter 3), for wind-generated waves, and for wind-waves in the presence of the mechanically generated waves are shown in Figure 4.3. Although all the profiles tend to the same free stream velocity at the edge of the boundary layer, and the boundary layer thickness appears unchanged, there is considerable difference between the profiles at lower elevations. Close to the water surface the largest velocity gradients are for the flat bed case, which suggests that this is the smoothest surface. The velocity gradients for the flow over the wind only waves are the least, suggesting the flow is most disturbed and slowed, and therefore appears to be the roughest. The combined wind and waves case lies between the two, suggesting that the surface is not so rough as for the wind only waves. Anticipating a result from Chapter 8, the amplitude of the wind-waves for the $U_\infty = 5.1$ m/s case is reduced in the presence of the long waves. This suggests that the longer mechanically generated waves do not significantly affect the apparent roughness (see section 8.4.4). Similar patterns are observed for $U_\infty = 2.4$ and 3.1 m/s, but the difference between the profiles is reduced, probably due to the generation of smaller wind-waves.

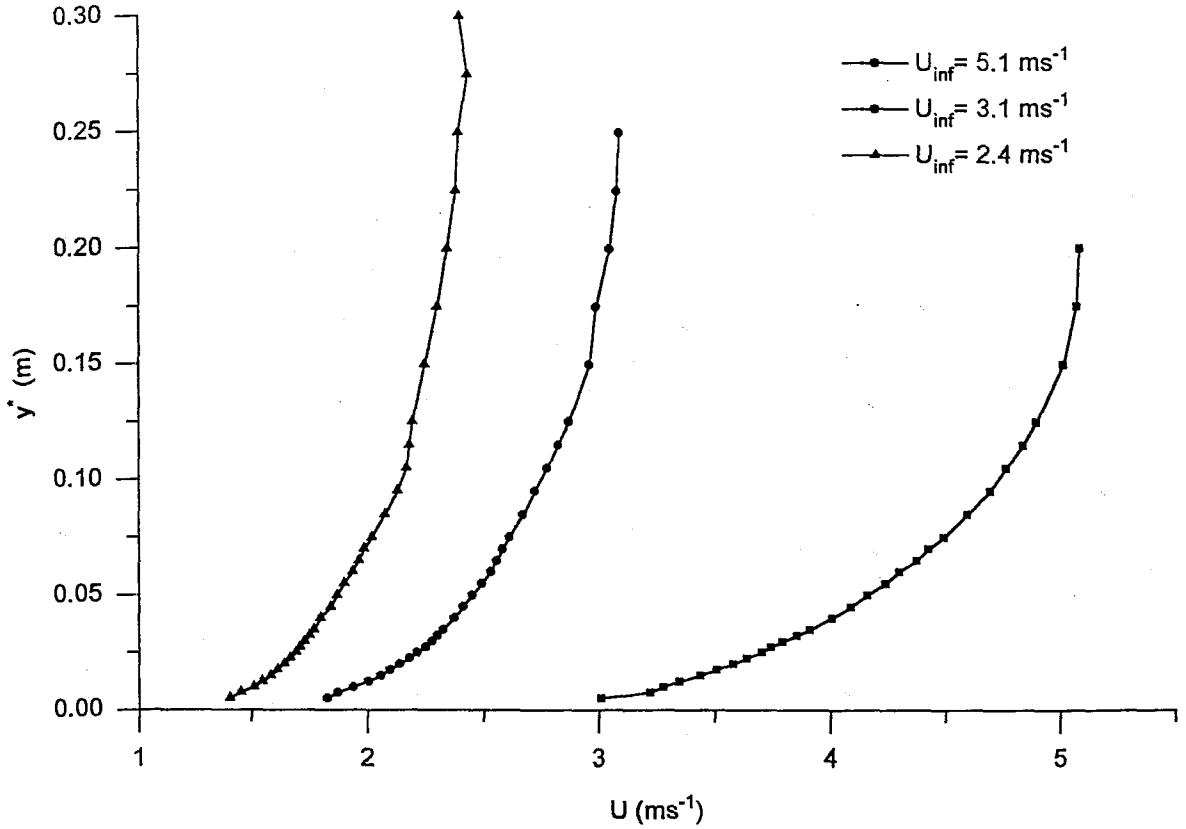


Figure 4.2: Time averaged horizontal velocity profiles for combined wind and waves cases

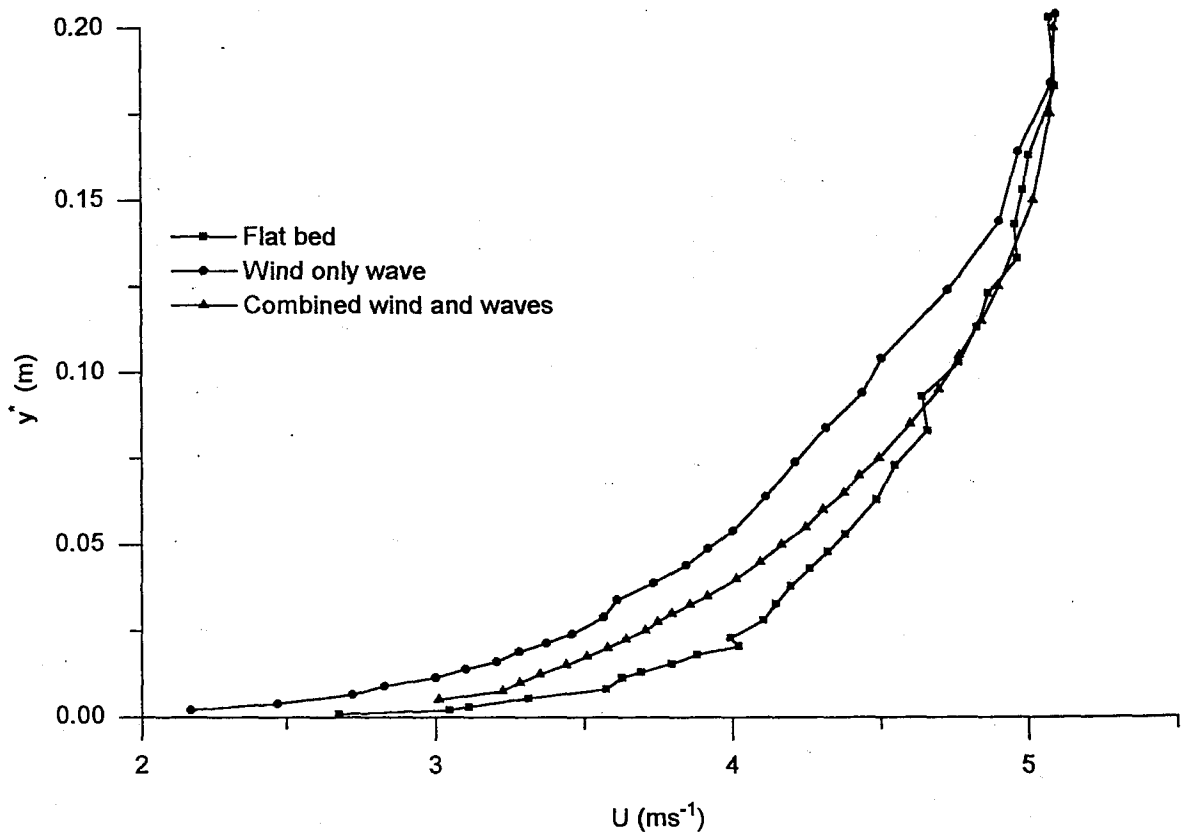


Figure 4.3: Time averaged horizontal velocity profiles for flat bed, wind only, and combined wind and waves (U_{inf}= 5.1 ms^{-1})

In seeking to explain the nature of the airflow in the presence of waves, the time averaged profiles provide very little useful information. Much of the previous work has looked solely at such profiles. In order to deduce the nature of the flow structure, it is clearly essential for the phase variations in the velocity to be examined.

4.4 Combined Wind and Wave Flow Structure

In the following three sections, the structure of the airflow above the wave is considered for each wind speed case. In each case, the streamline pattern deduced from the measured velocity field is presented. A comprehensive description of the flow structure is then developed, incorporating details of the observed phase averaged velocity field.

4.4.1 $U_\infty = 5.1$m/s

The streamlines deduced from the measured velocities are given in Figure 4.4. In this and all subsequent figures the wave trough is located as phase $\phi = 0$ and 1.0, while the wave crest is located at phase $\phi = 0.5$. Furthermore, throughout the present study the terms zero upcrossing and zero down crossing relate to the description of the wave in a spatial domain. These definitions, although different from those normally adopted, which are in the temporal domain, follow logically from the pattern given in Figure 4.4, whereby an upcrossing relates to the conditions at phase $\phi = 0.25$, while a downcrossing relates to the conditions at $\phi = 0.75$. The streamlines, for the $U_\infty = 5.1$ m/s case, appear to be similar to the potential flow streamlines (Figure 4.1), being approximately in phase with the water surface, and of similar amplitude to the water wave close to the surface but decaying steadily with increasing elevation. There are, however, a number of significant differences between the streamlines deduced from the measured velocities, and the theoretical potential flow streamlines.

Figure 4.4 shows that the streamlines are not symmetrical about the wave crest. Close to the water surface, the streamline spacing on the windward side of the crest is less than it is at the corresponding phase on the leeward side. This effect is illustrated in Figure 4.5, in which the experimental streamlines are plotted in the transformed co-ordinates defined by equation 4.1. The experimental streamlines are compared with the potential

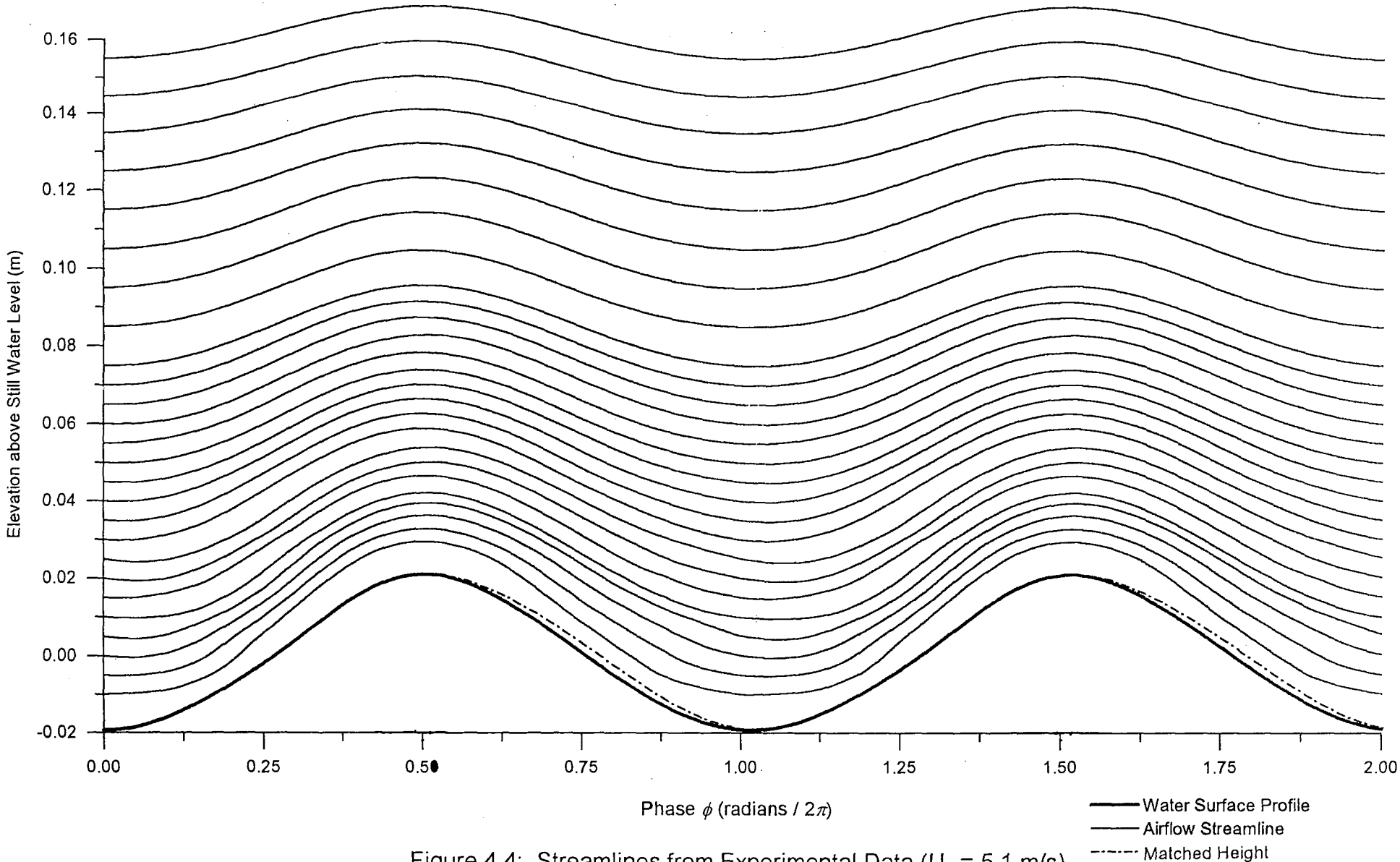


Figure 4.4: Streamlines from Experimental Data (U_{inf}= 5.1 m/s)

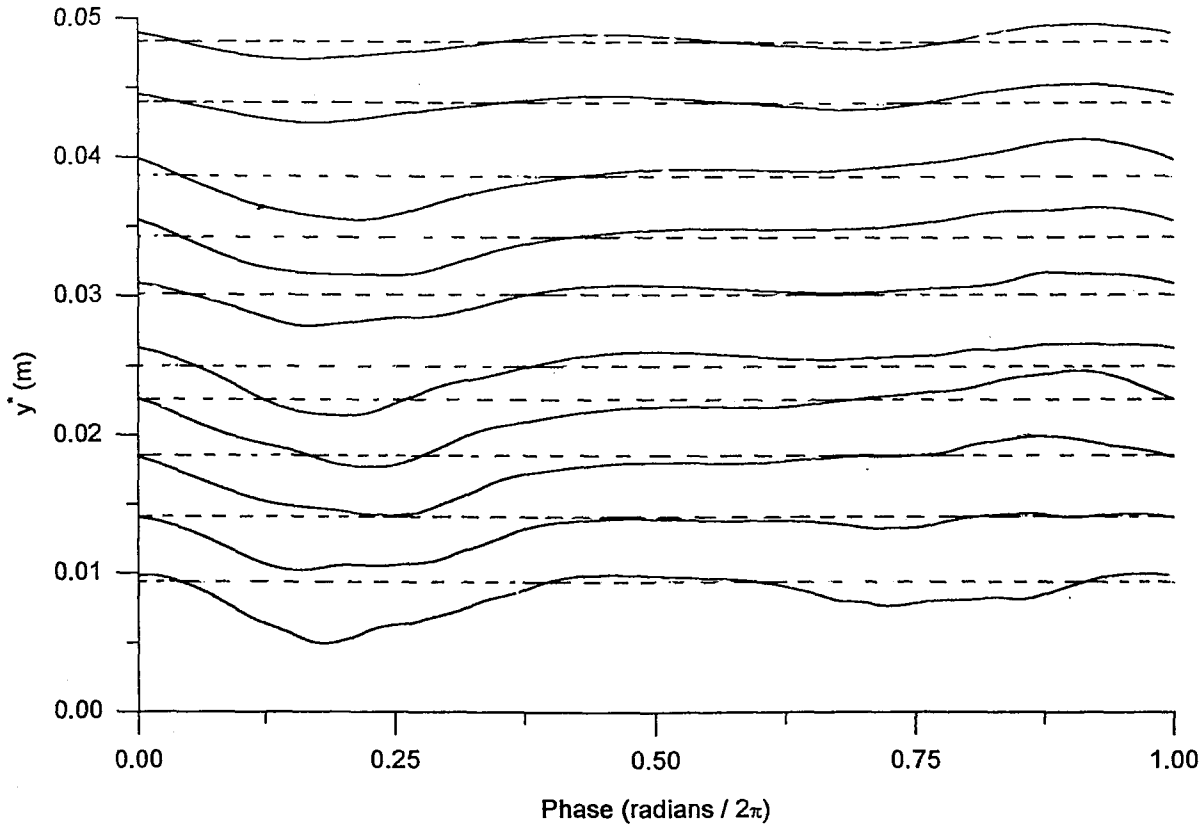


Figure 4.5: Experimental streamlines in transformed coordinates

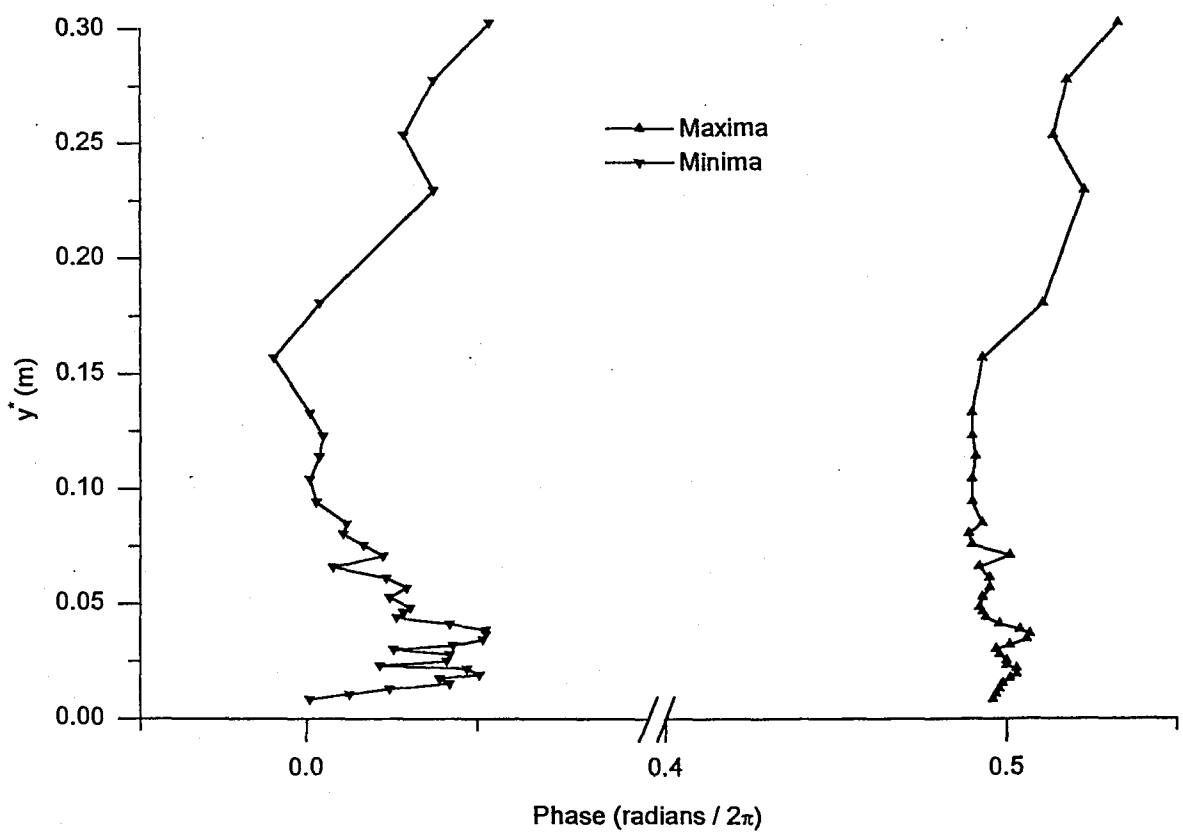


Figure 4.6: Phase of maxima and minima streamline elevations

flow streamlines (shown dotted), which are straight lines in this co-ordinate frame, so illustrating the asymmetries in the experimental streamlines. Figure 4.5 shows clearly the convergence of the streamlines upstream of the crest, and divergence downstream of the crest towards the zero down crossing. In addition to this asymmetry about the crest, the experimental streamlines above both the wave crest and trough are deflected upwards compared with the corresponding potential flow streamlines. Between these points, that is above the zero crossings, the streamlines are drawn towards the water surface. The streamlines above the windward face of the crest are closer to the water surface than those above the leeward face of the crest. This asymmetry appears to be reflected in the asymmetry of the matched height about the wave crest (Figure 4.4). The streamline pattern suggests that there is something above both the wave crest and the wave trough which deflects the flow upwards.

The asymmetry of the streamlines and the phase shifts caused by the above effects are illustrated in Figure 4.6, which shows the variation in the phase of the maxima and minima of the streamlines' elevation. Close to the water surface, the streamlines are in phase with the wave form, but, with increasing elevation, the streamlines' elevation maxima move downstream by a small amount. The effect is much more marked for the streamlines' elevation minima, which are shifted downstream by up to 30°. This is a result of the increased streamline spacing on the leeward side of the crest, which causes an asymmetry of the streamlines so that the trough to crest distance is less than that from crest to trough. The streamline gradient is therefore steeper on the windward side of the crest.

The streamline pattern is reflected in the horizontal velocity traces. The minimum streamline spacing should correspond to the phase of the maximum velocity. For potential flow, this would be above the wave crest, and the streamline spacing would be symmetrical on either side of the crest. Figure 4.7 gives the phase averaged velocities in transformed co-ordinates for a number of values of y^*. Close to the water surface, the maximum velocity is upstream of the crest (corresponding to the observed minimum streamline spacing), and the minimum velocity is between the zero down crossing and trough (where the streamline spacing is a maximum). At corresponding phases either

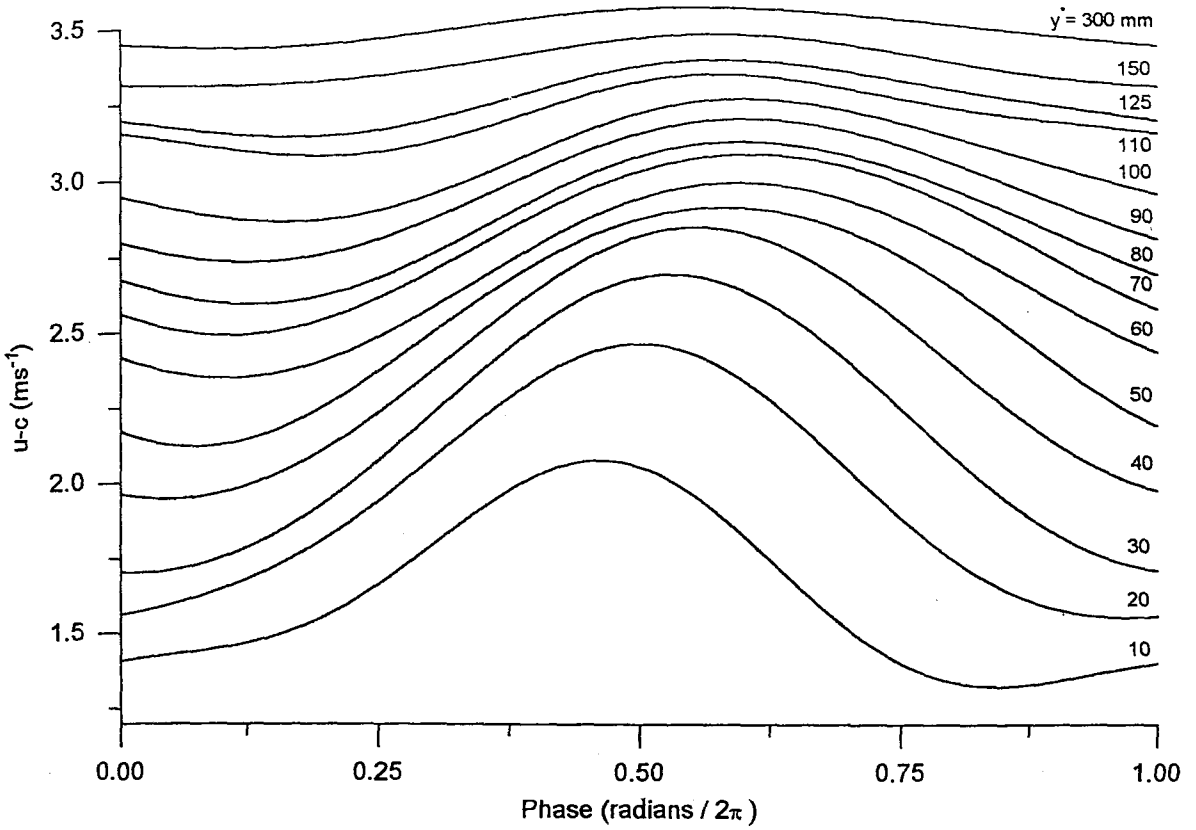


Figure 4.7: Phase averaged horizontal velocities at given elevations (U_{inf}= 5.1 ms^{-1})

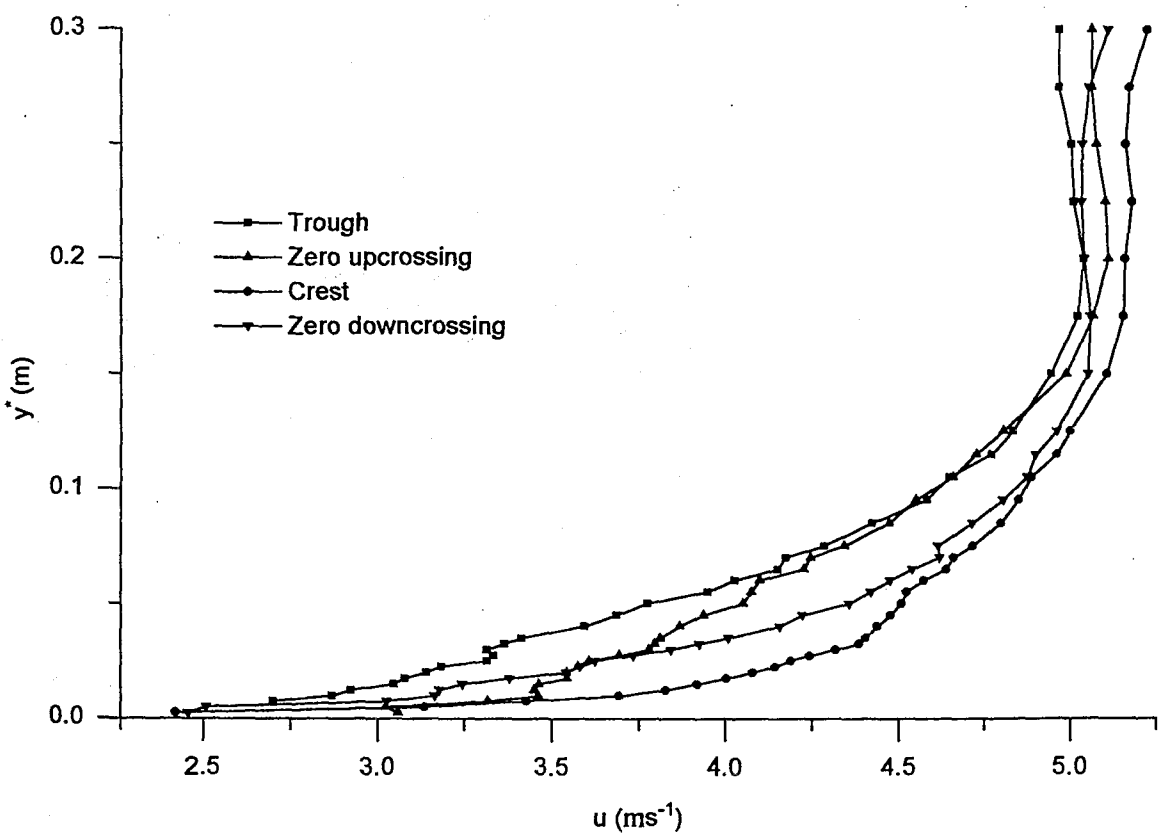


Figure 4.8: Phase averaged velocity profiles at given phase (U_{inf}= 5.1 ms^{-1})

side of the wave crest, the horizontal velocity close to the water surface is clearly greater on the windward side than on the leeward side of the crest.

There is considerable asymmetry in the shape of the phase averaged velocity traces close to the water surface. The velocity gradients are much steeper on the leeward side of the crest than on the windward side, so the peak velocity is just upstream of the crest, and the minimum velocity just downstream of the zero down crossing. The flow accelerates relatively slowly on the windward side of the crest, but is decelerated relatively quickly on the leeward side. This corresponds to the slow convergence of the streamlines on the windward side of the crest, and the rapid divergence once the flow has passed over the crest. The maximum streamwise acceleration $\partial u/\partial x$ on the windward side of the crest is less than the maximum deceleration on the leeward face.

The asymmetry of the velocity gradients with depth, $\partial u/\partial y^*$ near to the water surface are illustrated by the phase averaged velocity traces. In Figure 4.7, the velocity gradients are represented by the spacing between the velocity traces. There is a fixed spacing y^* between each of the velocity traces, so the larger the spacing between the traces, the greater the velocity gradient. The velocity gradient appears to be a maximum around the zero down crossing, and a minimum between the trough and zero upcrossing. The phase averaged velocity profiles (Figure 4.8) clearly illustrate the difference in velocity gradients close to the surface.

The asymmetry of the streamlines and the horizontal velocities about the wave crest are greatest within an elevation one wave amplitude above the water surface. The flow in this region appears to demonstrate the non-separated sheltering behaviour described in Chapter 2. The thickening of the boundary layer on the leeward side of the crest is evident from the streamline asymmetry, illustrated in Figure 4.5, and the asymmetric matched height. However, it is the asymmetry of the velocity traces about the crest, close to the water surface, which provides perhaps the most convincing evidence of a sheltered region on the leeward side of the crest. The occurrence of the maximum velocity and minimum streamline spacing upstream of the crest, very close to the water surface, suggests a separation-type effect starting upstream of the crest. It appears that it

is the flow around the matched height which determines the overall flow structure, but in this case, where no velocity measurements could be made around the matched height, the flow structure is very difficult to interpret.

At one wave amplitude above the water surface, the streamlines and velocities are close to being in phase with the water surface. With increasing elevation however, the phase of the maximum and minimum velocities moves downstream, the maxima moving to 30° downstream of the crest, and the minima to 60° downstream of the trough at $y^* = 0.125$ m (Figure 4.9). This suggests that the minimum streamline spacing is now on the leeward side of the crest, and the maximum streamline spacing is towards the zero upcrossing. The streamlines, however, appear to remain almost exactly in phase with the surface profile. The velocity data again suggests a non-separated sheltering effect, but in the opposite sense to that observed close to the water surface, with the minimum

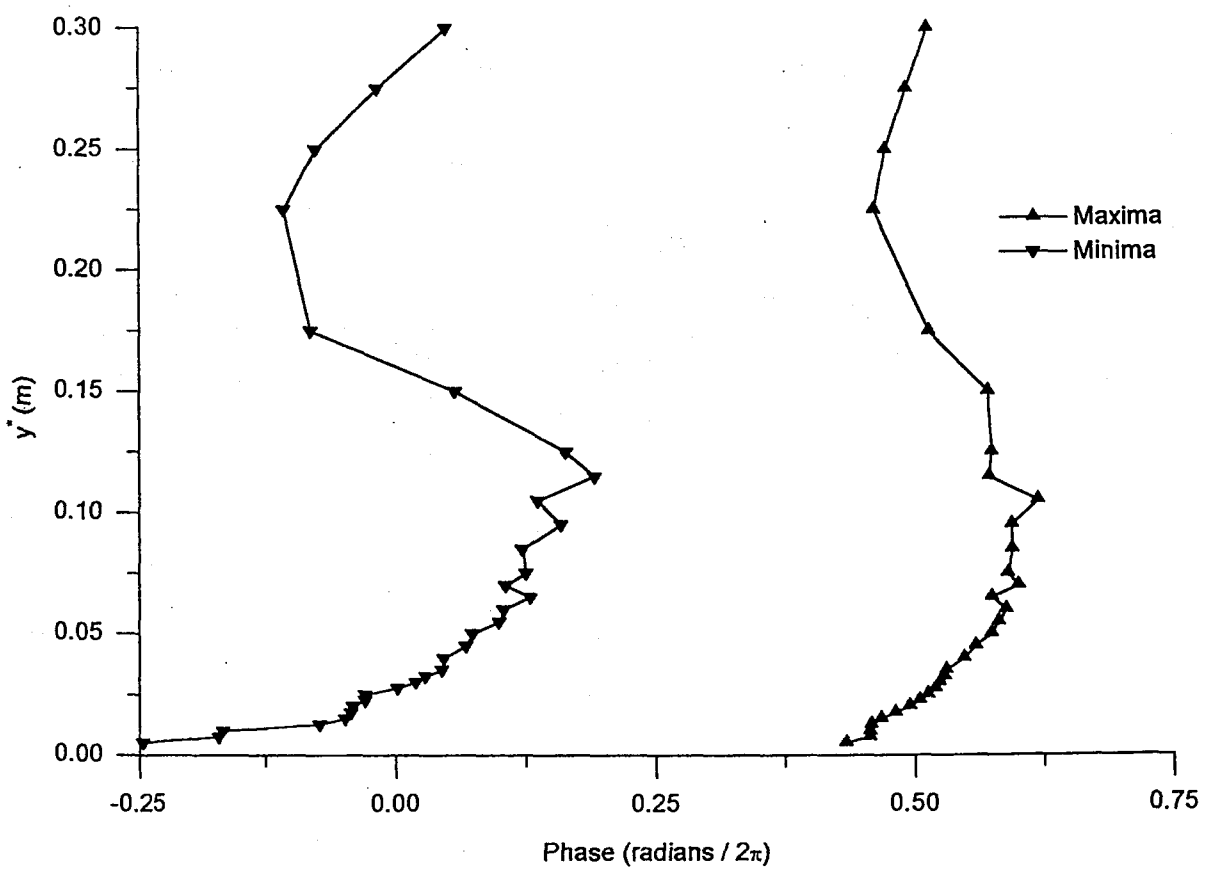


Figure 4.9: Phase of maxima and minima horizontal velocity ($U_\infty = 5.1$ m/s)

streamline spacing now occurring downstream of the crest. The streamline spacing is therefore now greater on the windward side of the crest than on the leeward side, so the velocities on the windward side are less than those on the leeward side. The phase averaged velocities are again asymmetric after being close to symmetrical at $y^* = 0.025$ m, though now reversed in that the velocity gradients and hence accelerations are greater on the windward side of the crest than on the leeward side. The change in the phase of the minimum velocities is close to 180°.

4.4.2 $U_\infty = 3.1$ m/s

The streamline pattern for a free-stream velocity of $U_\infty = 3.1$ m/s is shown in Figure 4.10. Within this figure, the solid lines describe streamlines calculated from the velocity measurements which have undergone no extrapolation, whereas the dashed lines represent streamlines which were not completely defined by the velocity data and therefore involve some degree of extrapolation. The third line, indicated by a dash-dot, describes the position of the matched height. The flow streamlines for this case at greater elevations are very similar to the flow for $U_\infty = 5.1$ m/s. Consider the lowest continuous streamline and the flow above it. The shape of this lowest streamline is very similar to the lowest streamline for the previous case. The streamline is deflected upwards above both the crest and the trough, but between is drawn downwards towards the water surface. The asymmetry of the streamlines above shows evidence of non-separated sheltering, with the streamline spacings on the windward side of the crest being less than those on the leeward side. The phase averaged horizontal velocity traces (Figure 4.11) show similar phase shifts and asymmetries to the first case, but the effects are greatly magnified. At lower elevations, the deceleration on the leeward side of the crest is much greater than the acceleration on the windward side. This asymmetry is related to non-separated sheltering, where the streamlines slowly converge on the windward side of the crest, and then suddenly diverge on the leeward-side of the crest. This is illustrated in Figure 4.11 by the gradual, almost linear, increase in velocity on the windward side of the crest.

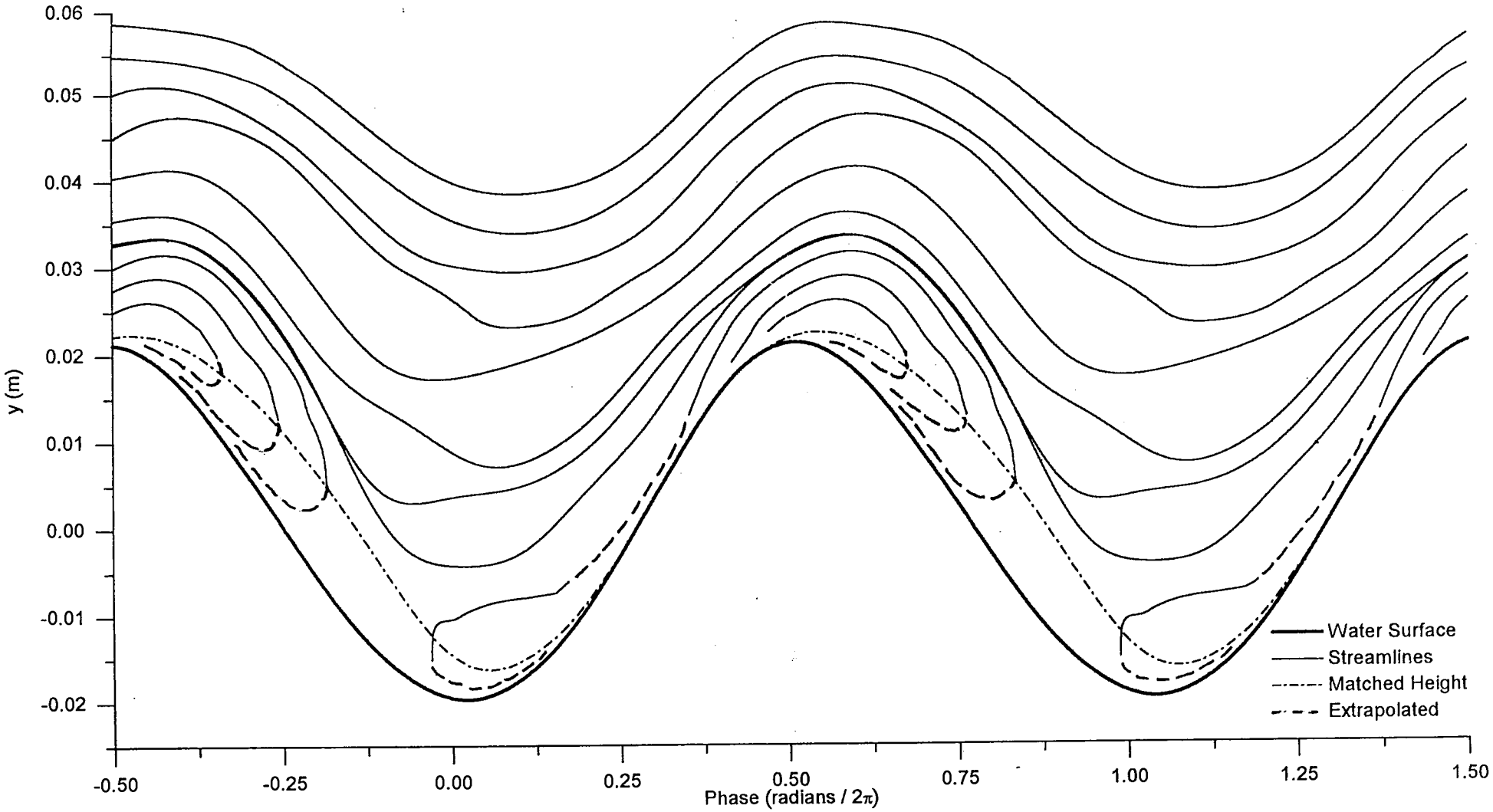


Figure 4.10: Streamlines from Experimental Data (U_{inf}= 3.1 ms^{-1})

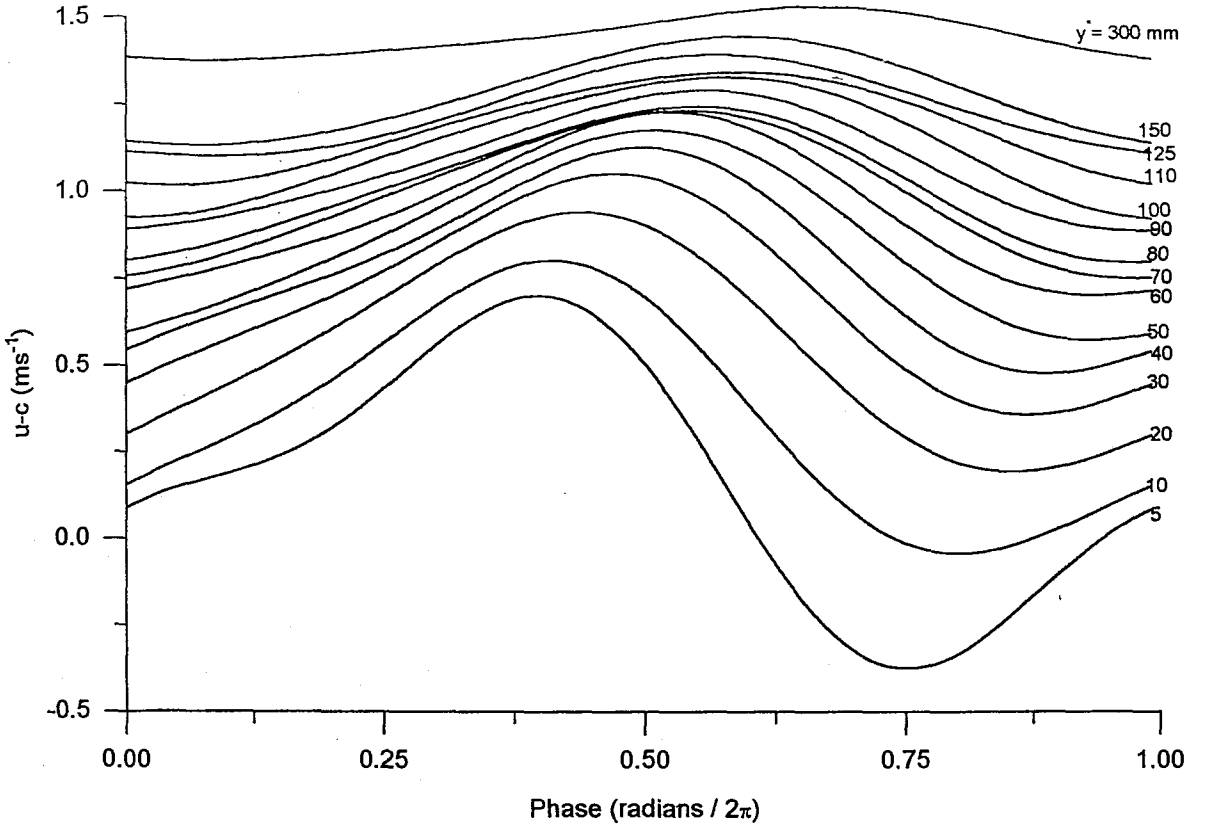


Figure 4.11: Phase averaged horizontal velocities at given elevations (U_{inf}= 3.1 ms^{-1})

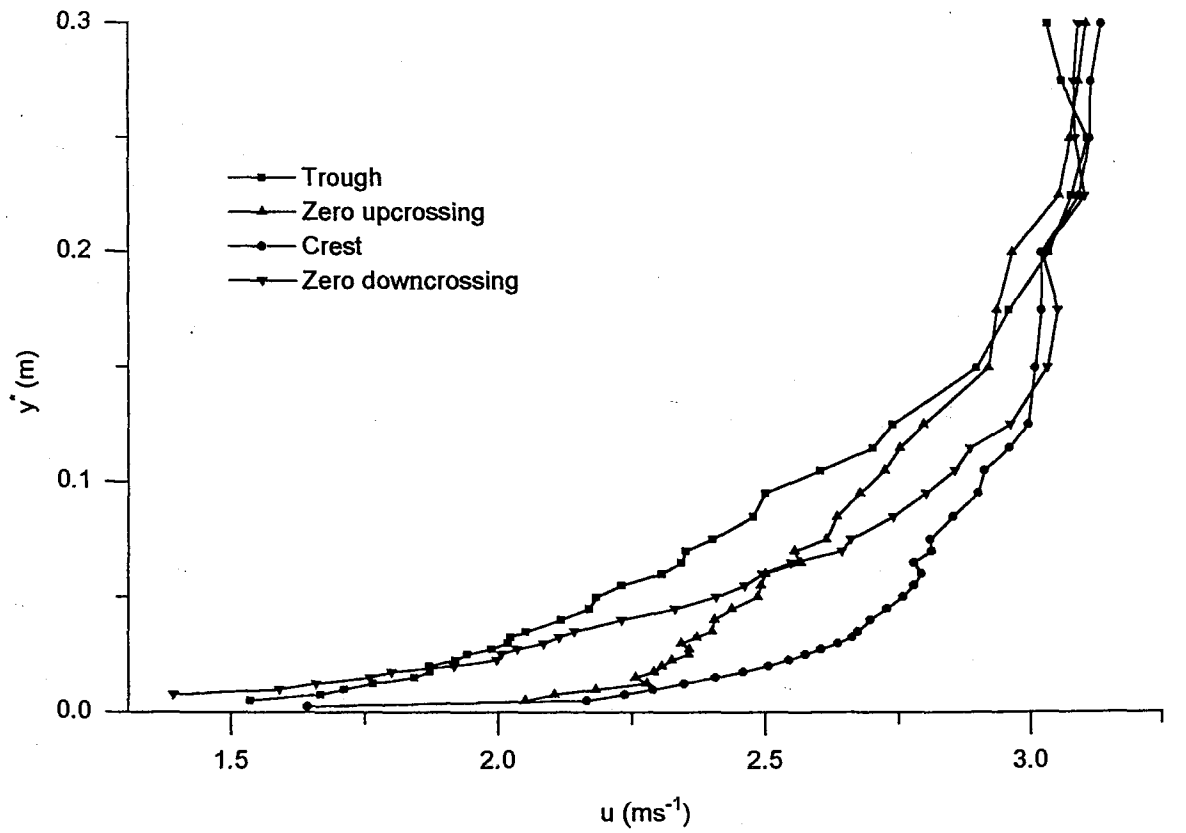


Figure 4.12: Phase averaged velocity profiles at given phase (U_{inf}= 3.1 ms^{-1})

The phase averaged velocity profiles (Figure 4.12) show the same pattern as the previous case, with the horizontal velocities at the zero crossings equal at $y^* = 0.065$ m. This suggests that non-separated sheltering is occurring below about three wave amplitudes, three times the depth observed in the first case. Above this level, the effect appears to be reversed. At higher elevations, around $y^* = 0.25$ m, the effect again appears to reverse in a similar manner to that observed in the first case. The phase of the velocity maxima and minima (Figure 4.13) show considerable phase shifts, almost 180° between the surface $y^* = 0$ and 0.20 m.

The profiles of the phase of the streamlines' elevation maxima and minima (Figure 4.14) show considerably more variation than those for the $U_\infty = 5.1$ m/s case. Up to $y^* = 0.025$ m, the maxima are downstream of the crest, but, above this height, they quickly move back to being upstream of the crest, and continue to move slowly upstream of the crest with increasing elevation. The minima show a similar trend, but the move upstream occurs at a greater elevation, at approximately $y^* = 0.050$ m. These patterns are similar to those demonstrated by the first case, but the phase shifts in this case are considerably larger.

Close to the water surface, below the lowest continuous streamline, there appears to be a recirculation structure (Figure 4.10), with a significant thickening of the matched height on the leeward side of the crest. The flow is accelerated from the trough to the zero upcrossing, reaching a maximum velocity between the zero upcrossing and crest. Beyond this point, the streamlines diverge as the flow approaches the crest, with a rapid accompanying reduction in the velocity. The result of this is as though the flow is separating at the wave crest, the streamlines appearing to overshoot the crest.

Once the airflow has passed over the crest, it is turned back before reaching the wave trough, with the streamlines passing through the matched height. Beneath the matched height, the direction of the flow is reversed, and it returns towards the wave crest. The return flow beneath the matched height itself causes the flow over the wave crest to be deflected upwards. The matched height reduces as the reverse flow moves back towards

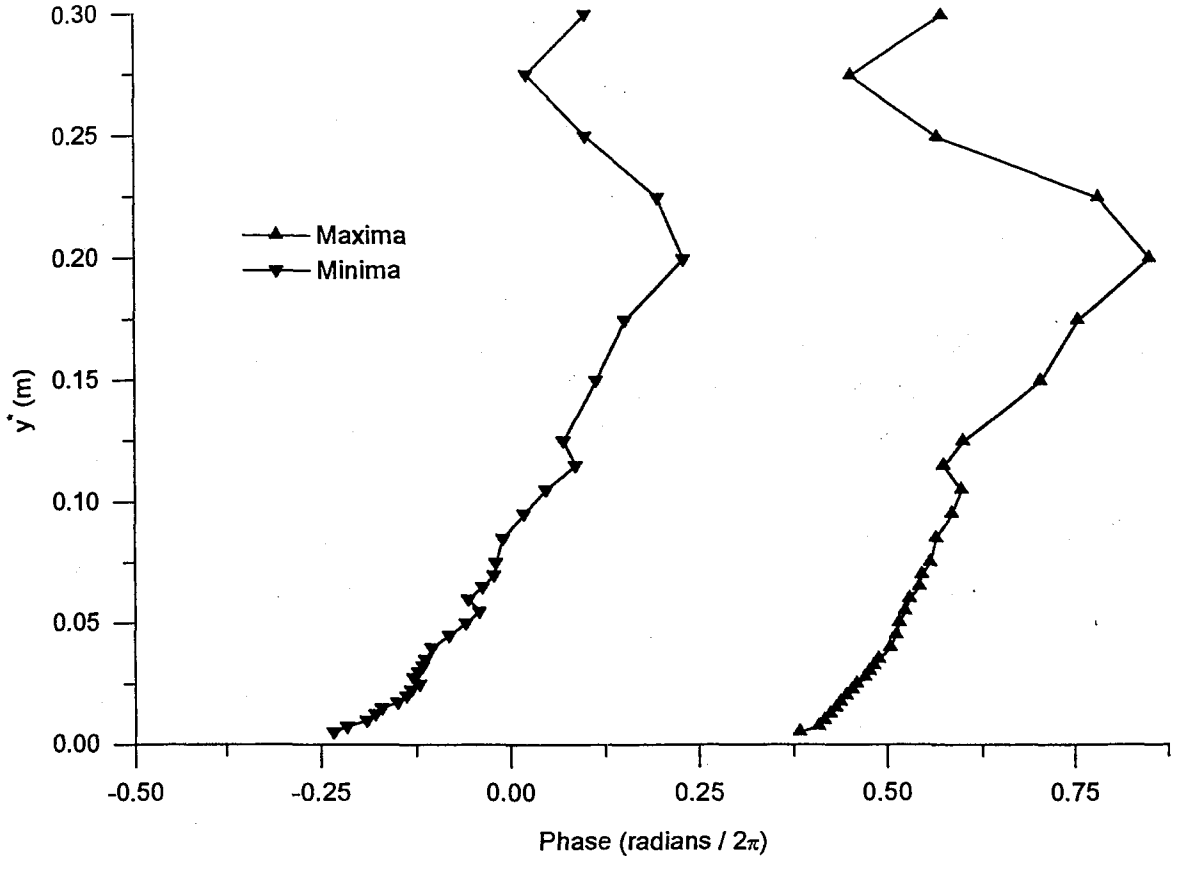


Figure 4.13: Phase of maxima and minima horizontal velocity (U_{inf}= 3.1 ms^{-1})

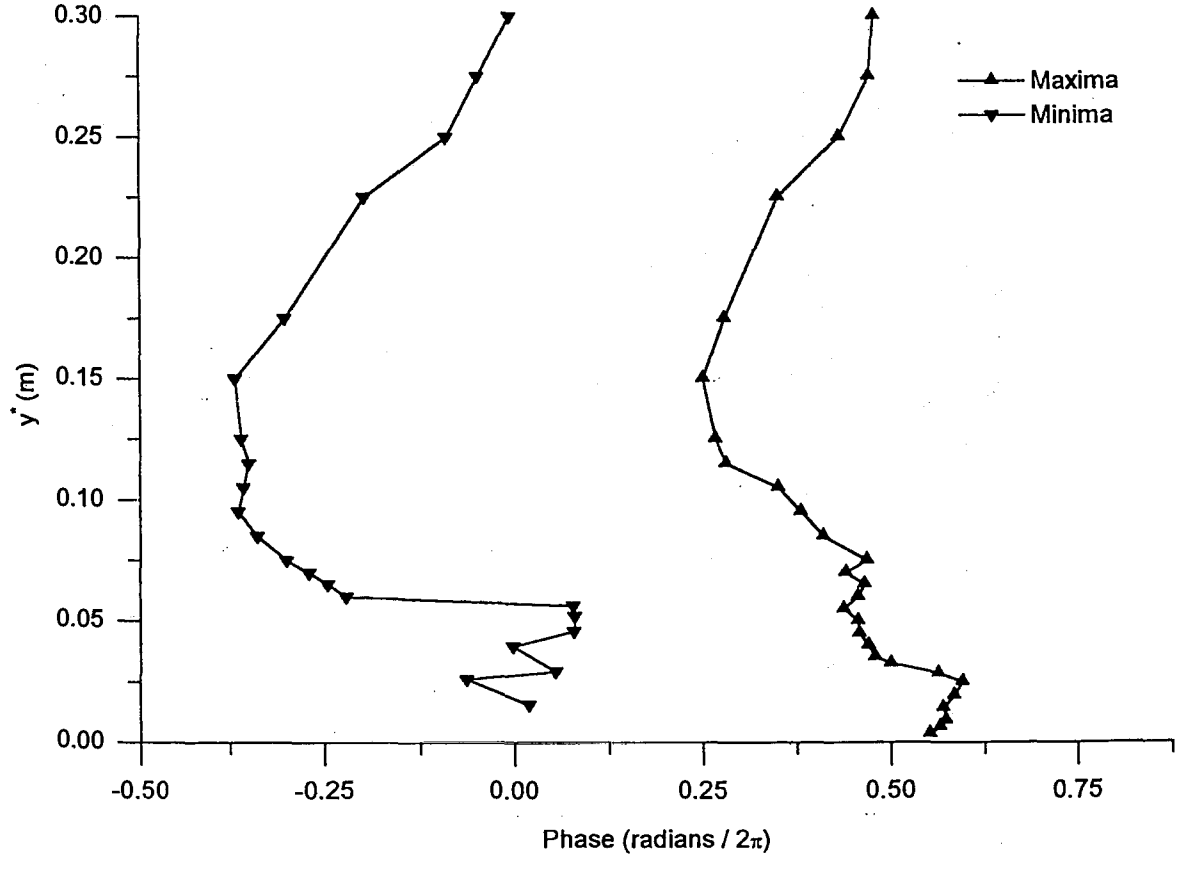


Figure 4.14: Phase of maxima and minima streamline elevations (U_{inf}= 3.1 ms^{-1})

the wave crest, and becomes a minimum between the crest and zero upcrossing. The streamlines below the matched height between the crest and zero upcrossing are very close together, suggesting relatively fast velocities in this region. However, since the velocity at the matched height is fixed, and the velocity at the surface is of one order less, it suggests that the difference is in the velocity profiles beneath the matched height. The velocity profile beneath the matched height on the windward side must be close to being uniform with a value approximately equal to the wave celerity over much of the depth, and reducing towards the surface velocity only when very close to the water surface. On the leeward side, the profile must reduce much more quickly with elevation over the whole depth, leading to smaller velocity gradients very close to the water surface. The lowest measured velocities, which are all above the matched height, show that the velocity gradients are greater on the leeward side of the crest than on the windward face (Figure 4.12). However, by considering the velocity gradients below the matched height, the converse is clearly true very close to the water surface. The velocity gradients in the airflow just above the water surface will be greatest on the windward side and least on the leeward side of the crest.

As the flow continues to move upstream beyond the zero upcrossing towards the trough, the streamlines start to diverge and the velocity reduces. The matched height increases and the flow moves upwards above the matched height. The flow changes direction, and moves forwards, returning towards the crest. The mean flow above pushes the flow back towards the water surface, and the flow is accelerated. A recirculation cell is therefore formed, centred around a point between the zero upcrossing and crest on the windward side of the crest. The recirculation extends to a point between the zero down crossing and trough, on the leeward side of the crest.

The existence of this recirculation indicates that there is a pressure minimum between the zero upcrossing and crest, and a maximum between the zero down crossing and trough. The flow above the matched height in the trough is accelerated towards the zero upcrossing, due to the favourable pressure gradient. However, as the flow moves towards the crest and passes the minimum pressure region, the pressure starts to increase. This adverse pressure gradient decelerates the flow and once it has passed over

the crest, the maximum pressure towards the trough turns the flow away and below the matched height. The flow is now reversed, so the adverse pressure gradient experienced by the forward flow becomes a favourable pressure gradient for the return flow. The flow is accelerated back over the crest to the point of minimum pressure. Upstream of the minimum pressure point, the flow again experiences an adverse pressure gradient, and is turned away before reaching the wave trough. By moving above the matched height, the adverse pressure gradient becomes favourable, and the flow is again accelerated back towards the wave crest.

A sketch of the complete recirculation cell, obtained by extrapolation from the experimental streamlines, is given in Figure 4.15.

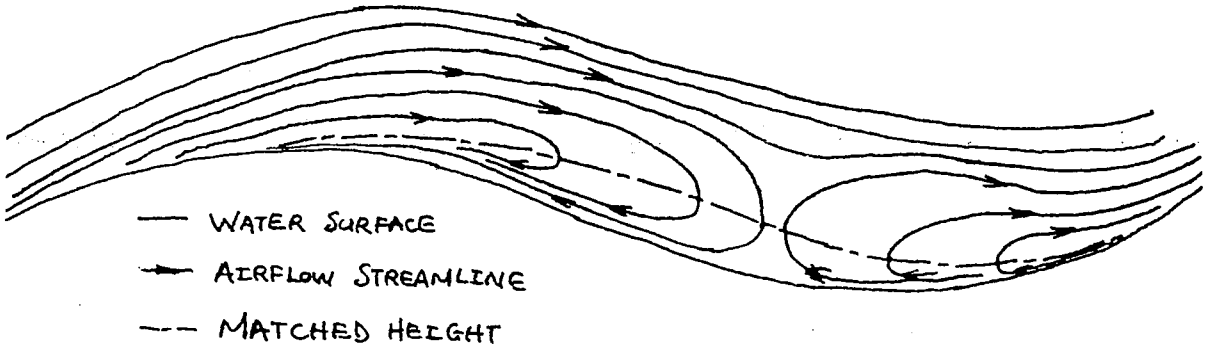


Figure 4.15: Airflow recirculation cell for $U_\infty = 3.1$ m/s

This recirculation is very similar to that proposed by Lighthill (1962) which is shown in Figure 2.1. The streamline pattern deduced from the velocity measurements implies that the maximum pressure appears to be 45° upstream of the trough, and the minimum pressure 45° upstream of the wave crest. Lighthill proposed a recirculation centred about the wave crest, with the minimum pressure at the crest, and the maximum at the wave trough. The observed pattern however appears to be displaced 45° upstream compared with Lighthill's, and therefore shows considerable asymmetries, unlike Lighthill's symmetrical streamlines. Lighthill's solution requires one to combine his secondary flow pattern with the basic flow streamlines. The resulting streamlines would not be dissimilar to the recirculation pattern found here, except for the asymmetry caused by the phase shift.

The observed similarity between the lowest continuous streamline for this case, and that for the previous case suggests that a similar flow structure may exist around the matched height in each case. The faster velocity and resulting thinner boundary layer for the $U_\infty = 5.1$m/s case would cause the recirculation cells to be much thinner, which is reflected in the smaller matched height and reduced asymmetry of the recirculation. The existence of the recirculations explains the shape of the lowest streamlines in each case, the lobes of the recirculation filling regions above the trough and crest, displacing the observed lowest streamlines upwards.

4.4.3 $U_\infty = 2.4$ m/s

The streamline pattern for the slowest case, $U_\infty = 2.4$ m/s is shown in Figure 4.16. Despite the velocity only being 0.6m/s slower than the previous case, the streamline pattern is strikingly different. The most significant characteristic of the flow is the formation of large recirculation cells in the wave troughs. The height of these cells is three times the wave height, extending two wave heights above the level of the wave crests. The asymmetry of the cells increases with height, the streamlines' elevation maxima moving upstream from being in-phase with the wave trough close to the water surface, to mid-way between the zero down crossing and trough at the outside of the cell, a phase shift of approximately 45°. The region of return flow, beneath the matched height, is significantly thicker than in the previous case, with the matched height clearly detached from the water surface at all phases. As a result of the greater matched height, a significant amount of data beneath the level of the matched height could be collected.

Consider the recirculating flow within these cells. A sketch of the recirculation cell is given in Figure 4.17 below:

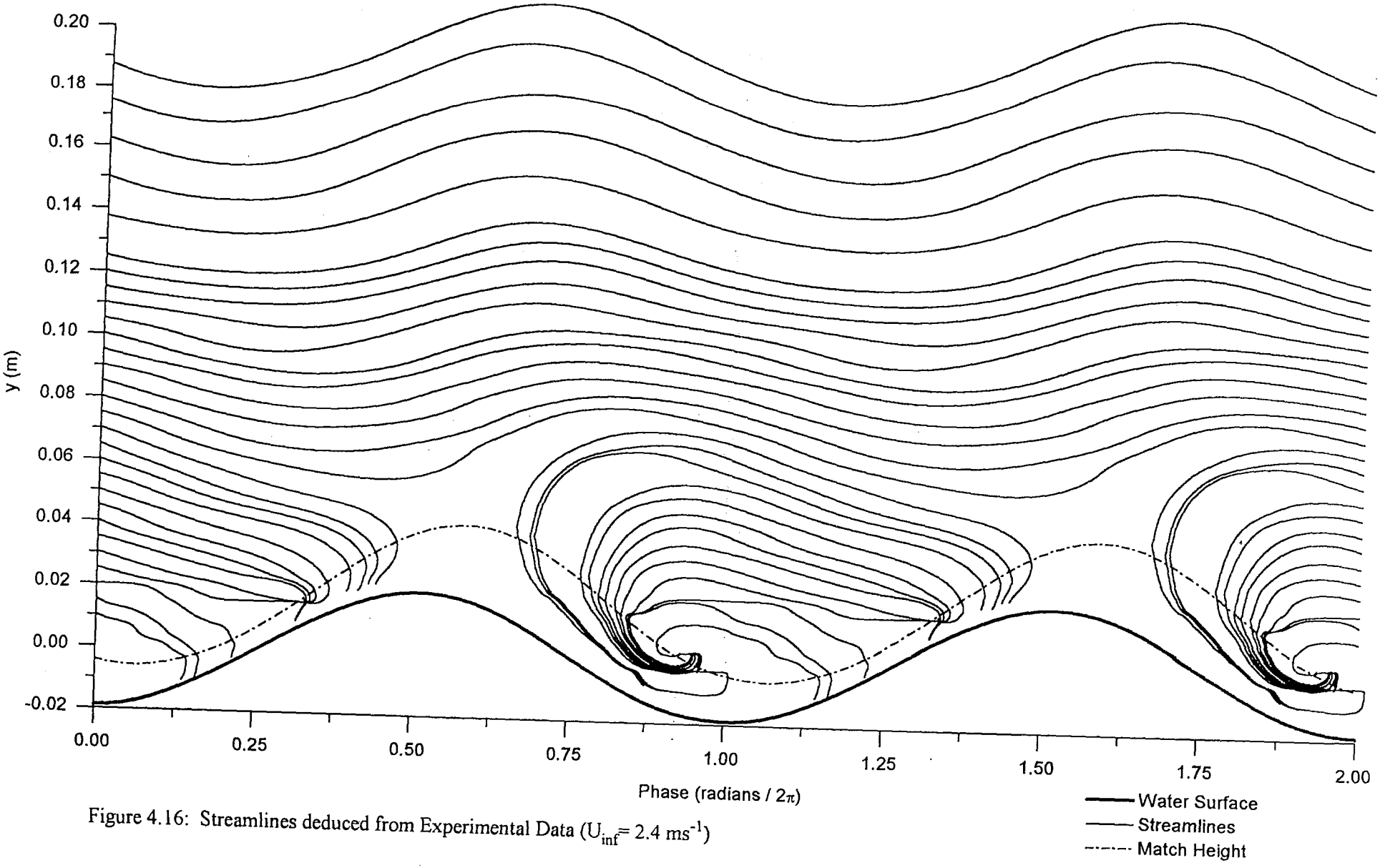


Figure 4.16: Streamlines deduced from Experimental Data (U_{inf}= 2.4 ms^{-1})

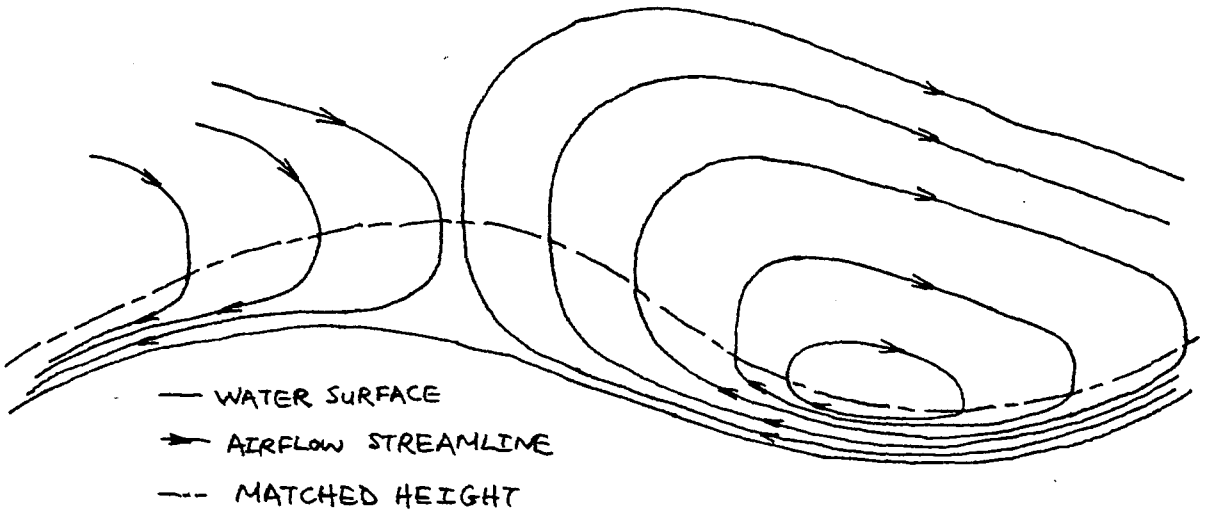


Figure 4.17: Airflow recirculation cell for $U_\infty = 2.4$m/s.

From the phase averaged velocity traces (Figure 4.18), the maximum velocity close to the water surface is around the zero upcrossing, where the matched height is a minimum. As the fluid at this point, below the level of the matched height, moves further upstream, its velocity reduces and the matched height increases. This suggests the pressure is a minimum at the zero upcrossing with the flow experiencing an adverse pressure gradient as it moves upstream. There appears to be an area of high pressure close to the water surface between the crest and zero down crossing, which turns the flow back away from the crest. The streamlines are deflected upwards above the matched height so the flow is now travelling forwards, and the adverse pressure gradient becomes a favourable gradient. This high pressure region above the crest corresponds to the phase of the minimum horizontal velocity, with the flow dominated by the vertical velocity component, and the matched height correspondingly a maximum. The vertical pressure gradient would appear to be favourable at this point, causing the flow to move a large distance upwards.

The flow above the zero downcrossing now experiences a favourable streamwise pressure gradient, and is accelerated forwards to reach a maximum velocity above the zero upcrossing. Beyond the wave trough, the flow is deflected downwards, apparently by the mean flow above the recirculations. This suggests that the vertical pressure

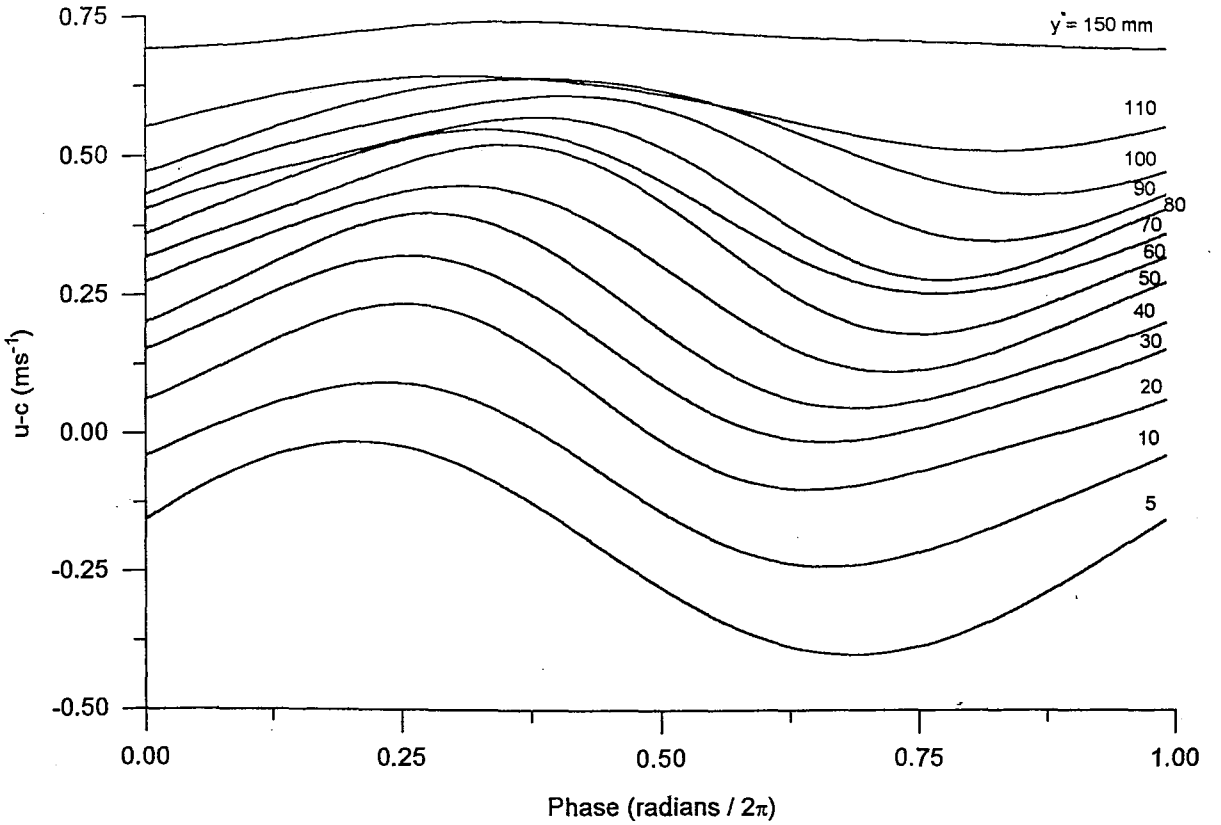


Figure 4.18: Phase averaged velocities at given elevations (U_{inf}= 2.4 ms^{-1})

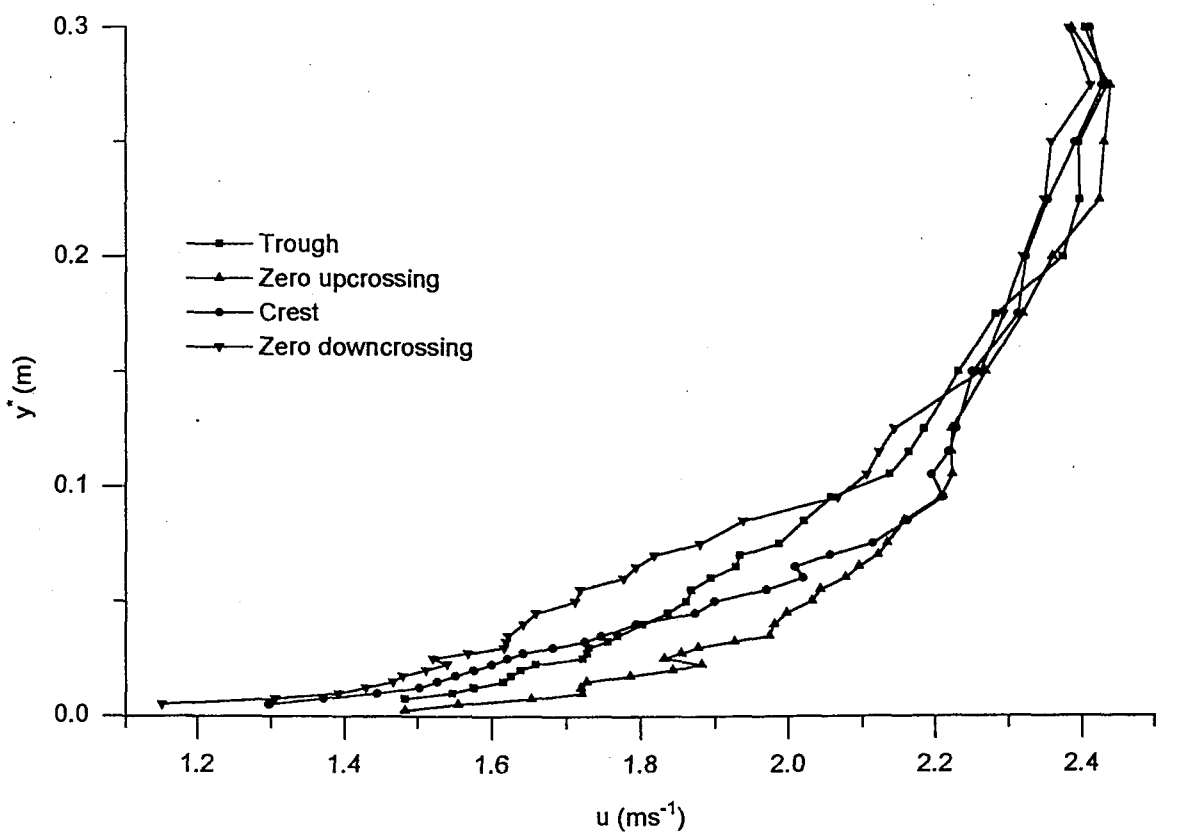


Figure 4.19: Phase averaged velocity profiles at given phase (U_{inf}= 2.4 ms^{-1})

gradient has now reversed. Beyond the zero upcrossing, the flow starts to sense the high pressure region downstream of the crest. The adverse pressure gradient causes the velocities to reduce, and the streamlines to be turned back. By moving below the matched height, the flow is reversed and now experiences a favourable pressure gradient, thus being accelerated towards the maximum velocity point at the zero upcrossing. The matched height correspondingly reduces.

The streamline pattern above the recirculation cells is determined by the form of the cells rather than by the wave form directly. In the outer region of the flow, above approximately half the boundary layer thickness, the streamlines appear relatively symmetrical, but they are shifted almost 90° downstream relative to the surface elevation, and compared with the phase of the streamlines for the first two cases. It is the peaks of the recirculation cells and not the wave crests which determine the flow structure in the outer region. The potential flow streamlines do not resemble the actual flow streamlines at all, but the data is still transformed into the co-ordinate frame defined by equation 4.1. The subsequent analysis was also done transforming the measured velocities on to the non-recirculating experimental streamlines, with very similar results being obtained, except for the obvious phase shift.

The phase averaged velocity traces (Figure 4.18) are much more sinusoidal than for the $U_\infty = 3.1$ m/s case, possibly due to the slower free-stream velocity. The greatest deviation from a sinusoid is around $y^* = 0.05$ m, and not closest to the water surface as in the first two cases. The phase of the velocities is shifted 90° upstream compared with the previous two cases, so that the velocity maxima occur at the zero upcrossing. The phase of the maxima move downstream towards the wave crest with increasing elevation. The phase averaged velocity profiles (Figure 4.19) appear very similar to the faster cases, except that the maximum and minimum velocities occur at the zero upcrossing and downcrossing respectively, rather than at the crest and trough. At lower elevations, the velocity at the trough is greater than that at the crest, but above $y^* = 0.04$ m, the crest velocity is greater than that above the trough. The maximum velocity gradients close to the water surface appear to be at the zero upcrossing,

corresponding to the minimum matched height, and a minimum at the zero downcrossing, corresponding to the greatest matched height. The discontinuity observed in the time averaged profile (Figure 4.2) at $y^* = 0.10$ m is also apparent in the phase averaged velocity profiles, and occurs at the top of the recirculation cells. It appears therefore to result from the discontinuity between the recirculating and non-recirculating flows.

There is a fundamental difference in the relationship between the streamlines and the horizontal velocities up to $y^* = 0.25$ m, compared with potential flow and the first two cases. In the present case, the velocity minima (Figure 4.21) are above the wave zero upcrossing, where the streamlines' elevation is a maxima (Figure 4.20), and conversely the velocity minima above the zero downcrossing where the streamline elevation is a maxima. (This effect is also observed with the velocities transformed into actual streamline co-ordinates.) The horizontal velocities are therefore 180° out of phase with the streamlines, whereas in the previous cases they were approximately in phase.

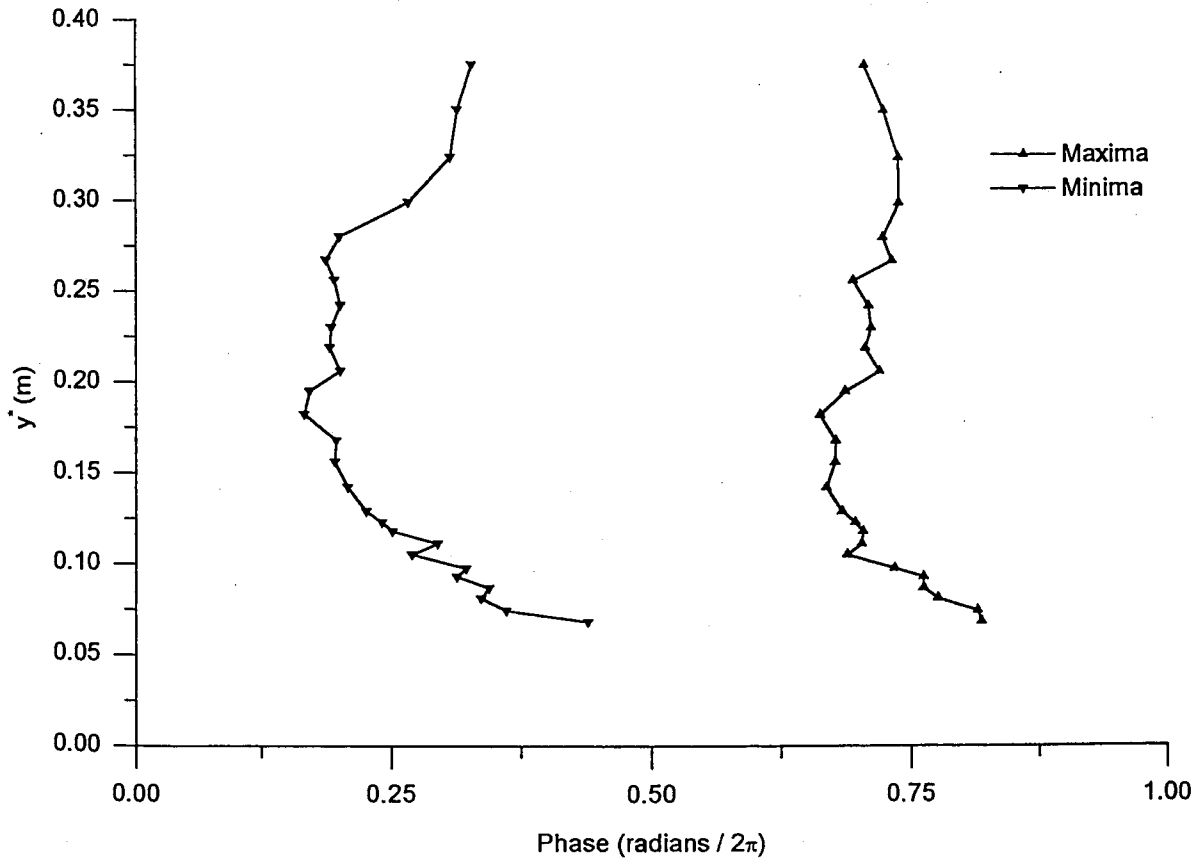


Figure 4.20: Phase of maxima and minima streamline elevations (U_{inf}= 2.4ms^{-1})

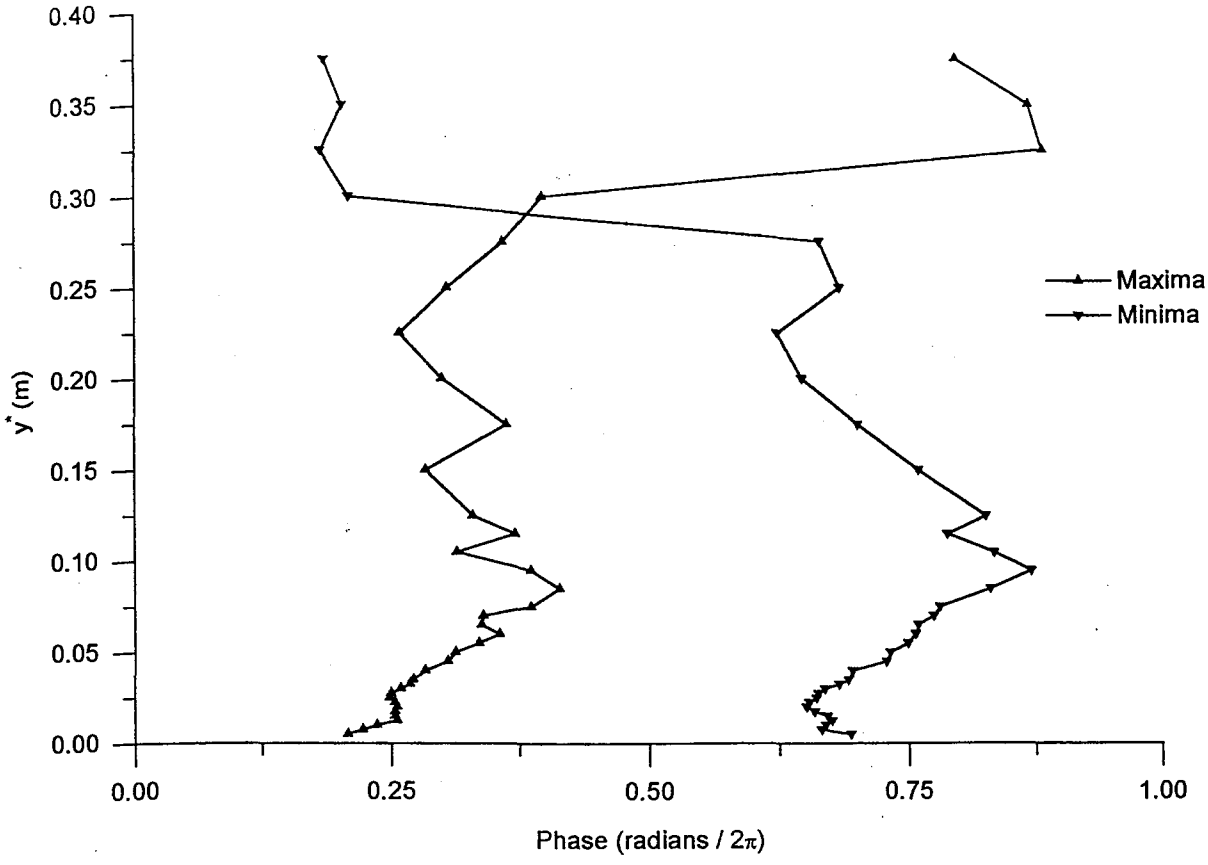


Figure 4.21: Phase of maxima and minima horizontal velocity (U_{inf}= 2.4 ms^{-1})

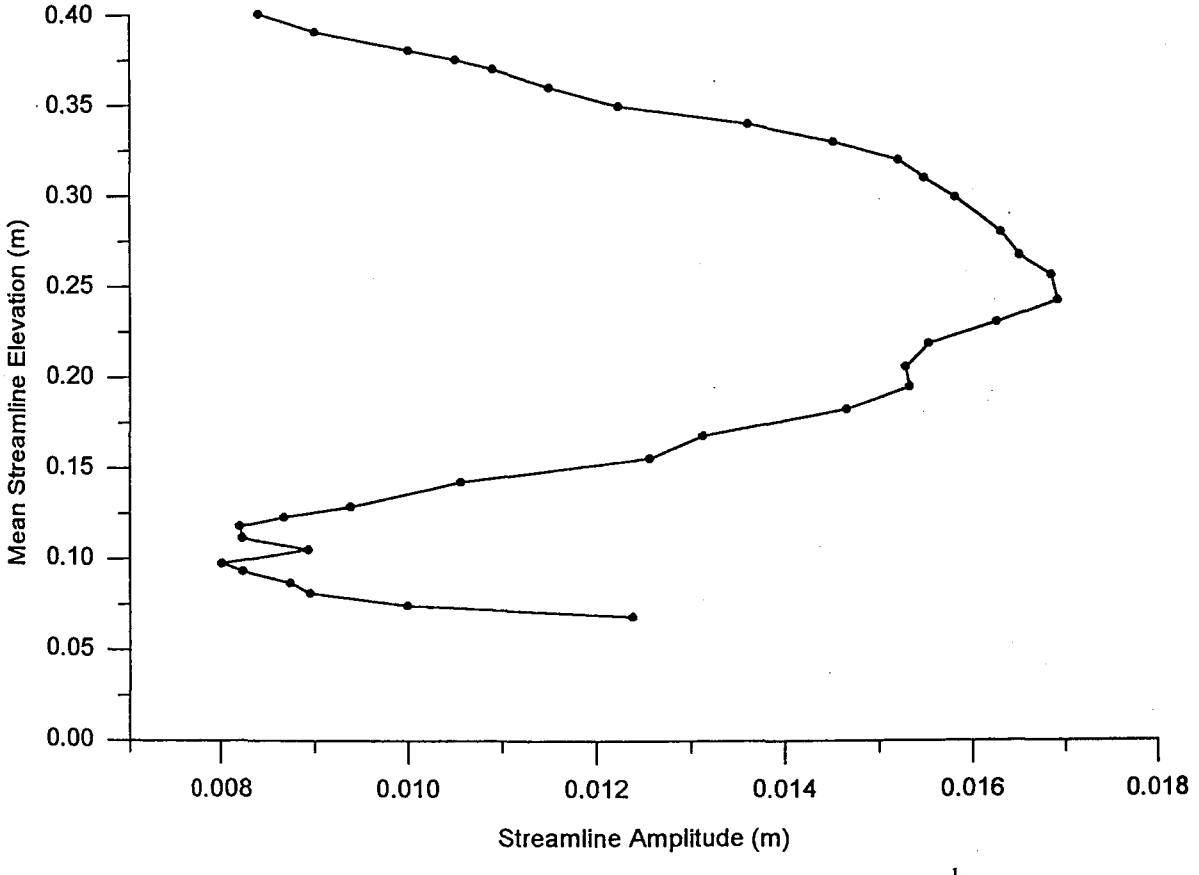


Figure 4.22: Profile with depth of streamline amplitude (U_{inf}= 2.4 ms^{-1})

Figure 4.22 shows that the streamline amplitude in the region between $y^* = 0.10$ and $y^* = 0.25$ m is increasing with elevation, rather than decaying. However, above $y^* = 0.25$ m, the phase of the horizontal velocities shifts by 180°, so that the velocities become approximately in-phase with the streamlines. This behaviour corresponds to that identified in the previous two cases. Correspondingly, the streamline amplitude above $y^* = 0.25$ m starts to reduce with increasing elevation.

These effects appear to be related to the shape of the streamlines. The streamlines around $y^* = 0.10$ m are highly non-sinusoidal, with broad and relatively shallow troughs, and sharp high crests. This asymmetry, which reflects the shape of the recirculation cell, decreases with increasing elevation as the stream-wise pressure gradients reduce. The relative height of the peaks reduces more than that of the troughs, so that the streamline spacing reduces at the crests more than at the troughs. In the region of near-constant streamline amplitude between $y^* = 0.25$ and $y^* = 0.30$ m, the streamlines are approximately sinusoidal, and decay in a similar way to the potential flow streamlines.

In addition to this vertical asymmetry, the streamlines just above the recirculation cells show a considerable amount of lateral asymmetry about the wave crest. The lowest streamline above the recirculation cells has its elevation minimum above the wave crest, and its elevation maximum just downstream of the zero downcrossing. Between the crest and the zero downcrossing, the streamline has a large curvature, caused by the region of high pressure on the leeward side of the wave crest which separates the recirculation cells. The lateral asymmetry of the lowest streamlines appears to be determined by asymmetry of the pressure gradients close to the water surface, and again reflects the shape of the recirculation cells. As the magnitude of the pressure gradients experienced by the flow reduce with elevation, so this lateral streamline asymmetry also reduces. At greater elevations, however, the streamlines appear to be in phase with the near-surface pressure distribution, with the streamline maxima above the pressure minima. The pressure distribution above the wave, rather than the wave itself, also determines the flow structure in the outer region.

Although the structure of the flow described above is very different to the first two cases, the flow characteristics are fundamentally similar. In the present case, the high pressure region is located approximately mid-way between the crest and zero down crossing, and the low pressure region between the trough and zero upcrossing. In the first case, U_∞= 5.1 m/s, the pressure distribution was close to being in-phase with the wave. For the U_∞= 3.1 m/s case, the pressure distribution moved upstream by approximately 45°, but did not significantly alter the flow structure because the region of return flow was relatively thin. In the U_∞= 2.4 m/s case, the pressure distribution appears to have moved upstream a further 90°. The phase of the pressure variation appears to determine the variation of the matched height with phase, the greatest matched height corresponding to the pressure maximum. The large differences in the recirculation cells between cases are simply the geometrical result of the position of the pressure distribution relative to the waveform, coupled with the position of the matched height above the water surface, which is dependent upon c/U_∞. The form of the recirculation then determines the structure of the whole flow.

4.5 Streamline Amplitude

The profiles with elevation y^* of the streamline amplitude, defined as half the difference in elevation between the streamlines' elevation maxima and minima, are shown for the three cases in Figure 4.23(a), and compared with the amplitude of the potential flow streamlines in Figure 4.23(b). The potential flow streamlines are based on the total airflow height, assuming that the streamline amplitude is zero at the tunnel roof. The profiles for U_∞= 3.1 and 5.1 m/s show exponential-type decay with elevation, similar to the potential flow case. The experimental streamline amplitudes decay much more quickly than the potential flow streamline amplitudes, particularly close to the water surface. This is because the potential flow solution assumes laminar flow, whereas the flow is actually highly turbulent with a large amount of mixing, especially close to the water surface where the reduction in amplitude is greatest.

The streamline amplitude for U_∞= 3.1 m/s reduces more quickly at lower elevations than for U_∞= 5.1 m/s. In each case the lowest continuous streamline is displaced

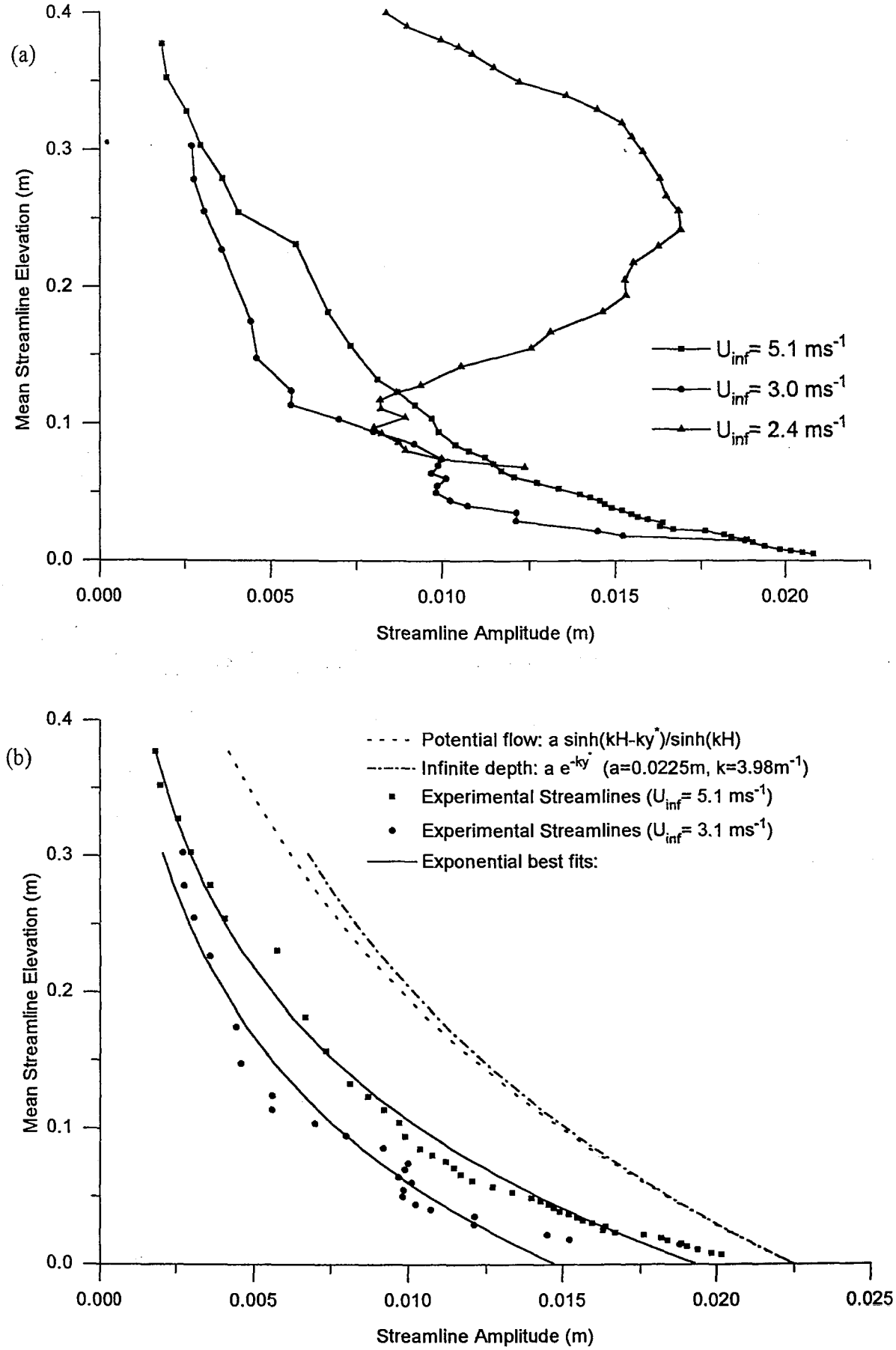


Figure 4.23: Streamline Amplitude Profiles

upwards by the recirculation structures close to the water surface, this effect being more pronounced for the slower case. The reason for the rapid initial decrease in amplitude is that the recirculation cells tend to be deeper in the troughs than above the crest, since the non-recirculating flow will tend to restrict the growth of the recirculation more above the crest more than in the trough. At greater elevations, the rate of decay reduces very rapidly. The amplitudes at the edge of the boundary layer do not appear to go to zero, but instead appear to become asymptotic, to a relatively small value (0.002 m).

For $U_\infty = 2.4$ m/s, the amplitude of the streamlines around $y^* = 0.10$m are approximately the same as in the other cases, but then, above this level, the amplitude increases, as discussed in the previous section. Above $y^* = 0.30$ m however, the amplitude appears to reduce exponentially in a similar way to the other cases. The streamline amplitude for this case is significant over a much greater depth than for the faster flow cases.

4.6 Wave-Induced Velocity Amplitude

Figures 4.24 and 4.25 show the depth variation in the amplitude of the horizontal and vertical wave-induced velocity components. In each case, the measured velocity is non-dimensionalised with respect to the free stream velocity U_∞, and the vertical elevation is non-dimensionalised with respect to the measured boundary layer thickness. For the horizontal velocities, in general the amplitudes reduce almost linearly with increasing elevation, to be approximately 2% of the free-stream velocity at the edge of the boundary layer. The largest relative velocity amplitude is for the $U_\infty = 3.1$ m/s case, with the velocity amplitude increasing down to the water surface, reaching a maximum value of 15%. The velocities decrease slightly towards the surface below $y^*/\delta = 0.15$ for $U_\infty = 2.4$ and 5.1 m/s, each having a value of approximately 7%.

The vertical velocity amplitudes are, as to be expected, considerably smaller than the horizontal amplitudes: of order 2% of the free-stream velocity compared with 10% for the horizontal velocities. The amplitudes again reduce in general linearly with elevation. The relative amplitude of the vertical velocities below $y^*/\delta = 0.25$ is greatest for the

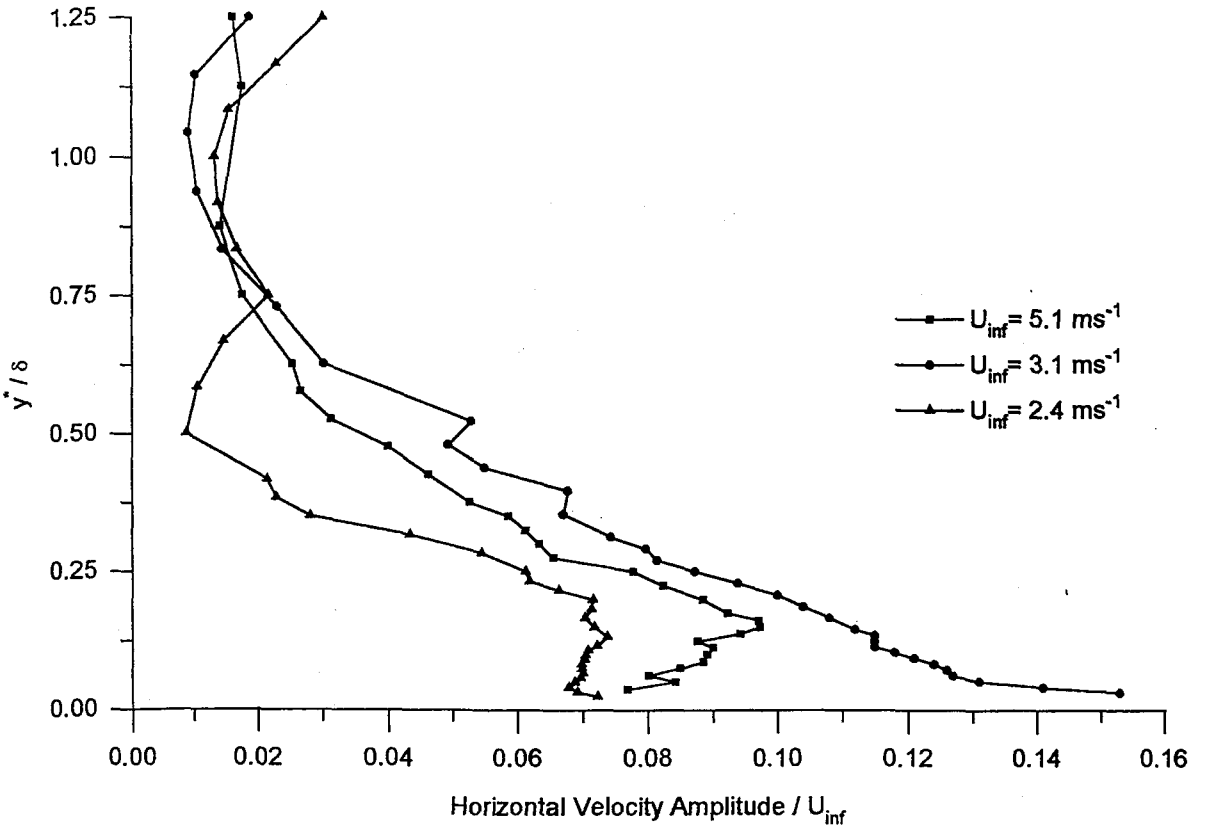


Figure 4.24: Profile of the amplitude of wave-induced horizontal velocity

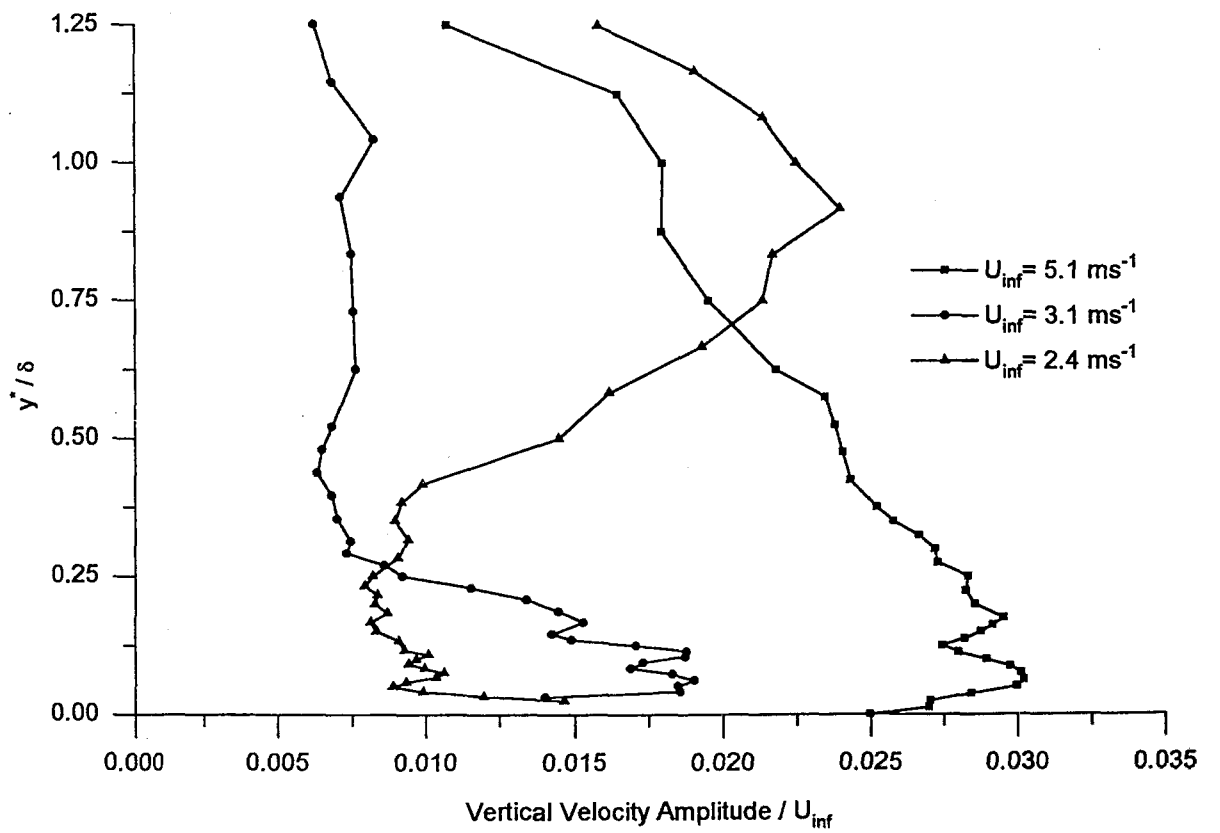


Figure 4.25: Profile of the amplitude of wave-induced vertical velocity

$U_\infty = 5.1$ m/s case, and smallest for the $U_\infty = 2.4$ m/s case, which is a result of the velocities being smaller for the larger recirculation cells. The vertical velocity amplitude for the $U_\infty = 2.4$ m/s case is almost constant up to mid-depth in the boundary layer, but thereafter increases to the edge of the boundary layer before reducing at greater elevations. This corresponds to the growth in the streamline amplitude described in the previous section.

4.7 Time Averaged Turbulent Velocity Profiles

Profiles of the time-averaged root mean square horizontal and vertical turbulent velocity fluctuations are given in Figures 4.26 and 4.27. As for the previous figures, the velocity fluctuations are normalised with respect to the free stream velocity, and the vertical elevation with respect to the boundary layer thickness δ. In all cases, the turbulence is a maximum close to the water surface, and reduces to a minimum at the edge of the boundary layer. However, the form of the horizontal and vertical profiles close to the water surface is fundamentally different. For the vertical fluctuations, the turbulence increases with reducing elevation down to $y^*/\delta = 0.10$. Below this level, the turbulence reduces very rapidly towards the surface. In comparison, for the horizontal fluctuations, the turbulence continues increasing with decreasing elevation, down to the lowest data points at $y^*/\delta = 0.025$. This difference is due to the constraints imposed by the water surface. The zero vertical velocity constraint is felt by the flow at a greater height than the horizontal non-slip condition. The eddies become longer and flatter as the surface is approached, with the horizontal velocity reducing only very close to the water surface.

The highest turbulence levels close to the water surface are for the $U_\infty = 5.1$ m/s case, for both the horizontal and vertical velocity fluctuations. This reflects the large velocity gradient near the water surface, due to the large wind-generated waves and the faster flow. The turbulence appears to reduce almost linearly with increasing height before tending to a constant value towards the edge of the boundary layer. The turbulence levels for $U_\infty = 5.1$ m/s at the edge of the boundary layer are less than for the other two cases, in particular for the vertical velocities.

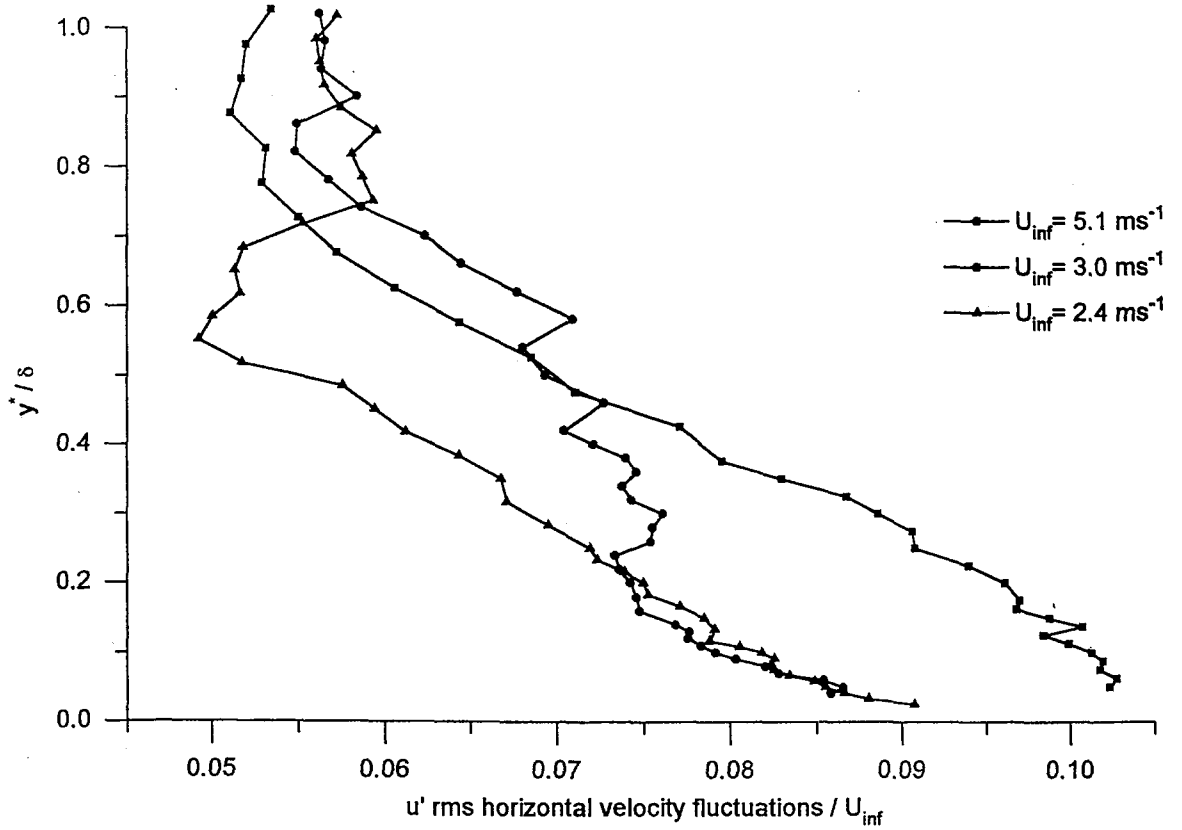


Figure 4.26: Time averaged normalised root mean square horizontal velocity profiles

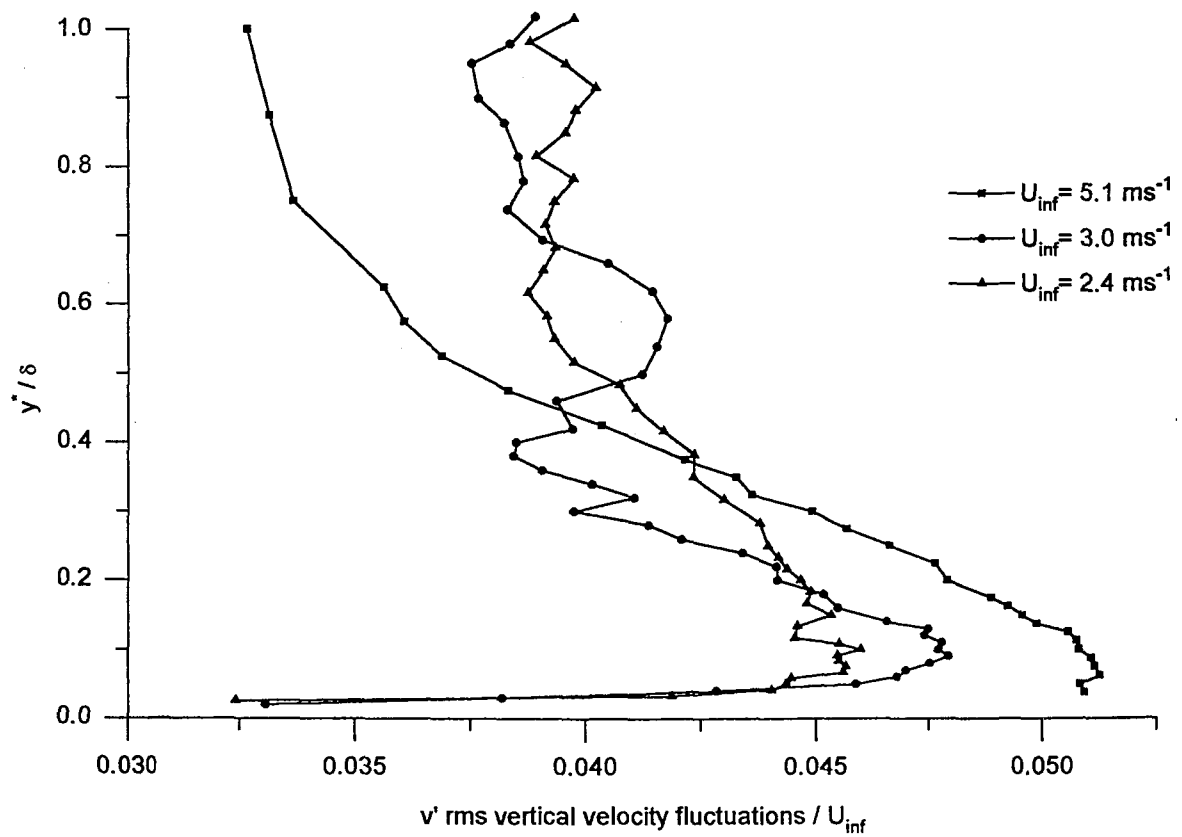


Figure 4.27: Time averaged normalised root mean square vertical velocity profiles

The horizontal turbulence profiles for $U_\infty = 2.4$ and 3.1 m/s have similar values close to the water surface, but between $y^*/\delta = 0.25$ and 0.70, the turbulence for $U_\infty = 2.4$ m/s case becomes significantly less than that for $U_\infty = 3.1$ m/s. This is the region where the streamline amplitude for $U_\infty = 2.4$ m/s is increasing with elevation. Above $y^*/\delta = 0.70$, the horizontal turbulence values suddenly increase to become approximately equal to the values for $U_\infty = 3.1$ m/s. The region of streamline growth therefore appears to be accompanied by low horizontal turbulence values. This pattern is not apparent in the vertical turbulence levels, with the profiles for $U_\infty = 2.4$ and 3.1 m/s being very similar.

The non-dimensional time averaged horizontal turbulence profiles for flow over a flat smooth bed, with wind-generated waves only, and with mechanically generated waves for the $U_\infty = 5.1$ m/s case are shown in Figure 4.28. The profiles reflect the observations regarding the velocity gradients of the time averaged profiles in Figure 4.2. The turbulence for the wind only waves is greatest, reflecting the roughest surface and most perturbed profile. The profile for the flat bed shows the smallest turbulent fluctuations, reflecting the smoothest surface condition. The combined case lies between the two, a result of the apparent attenuation of the wind-waves in the presence of mechanical waves. The turbulence levels all tend to 5% at the edge of the boundary layer, but increase to approximately 10% close to the water surface.

Similar patterns were observed for the $U_\infty = 3.1$ m/s case, but the profiles for $U_\infty = 2.4$ m/s (Figure 4.29) demonstrate very different behaviour. The turbulence levels for the flat bed case are greater than for either of the wave cases, suggesting that the water surface is smoother than the flat solid bed. This is consistent with the observation that virtually no wind-waves were generated for the $U_\infty = 2.4$ m/s case. It also suggests that the long waves do not act as roughness elements. The reduction in the turbulence in the airflows above water is due to a release of the surface shear stress by the wind-induced current. This effect is discussed in detail in Chapter 5.

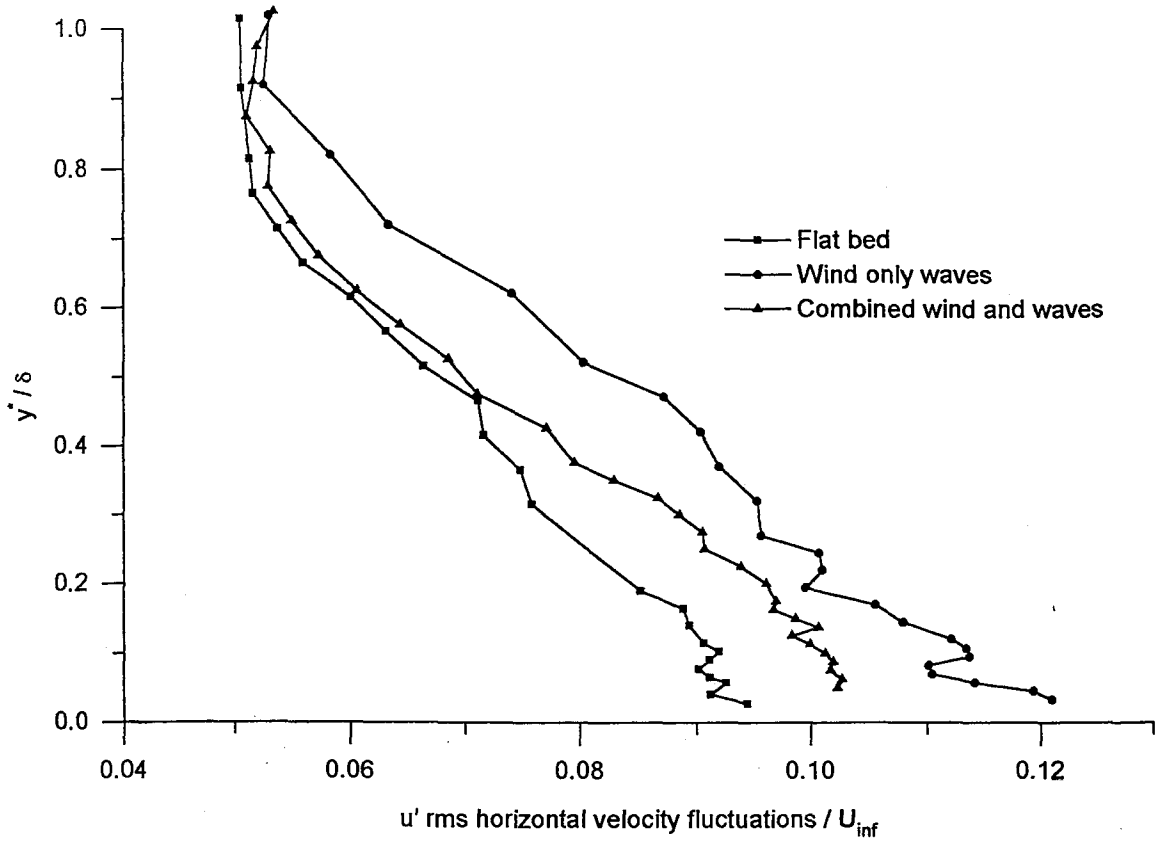


Figure 4.28: Time averaged root mean square turbulence profiles (U_{inf}= 5.1 ms^{-1})

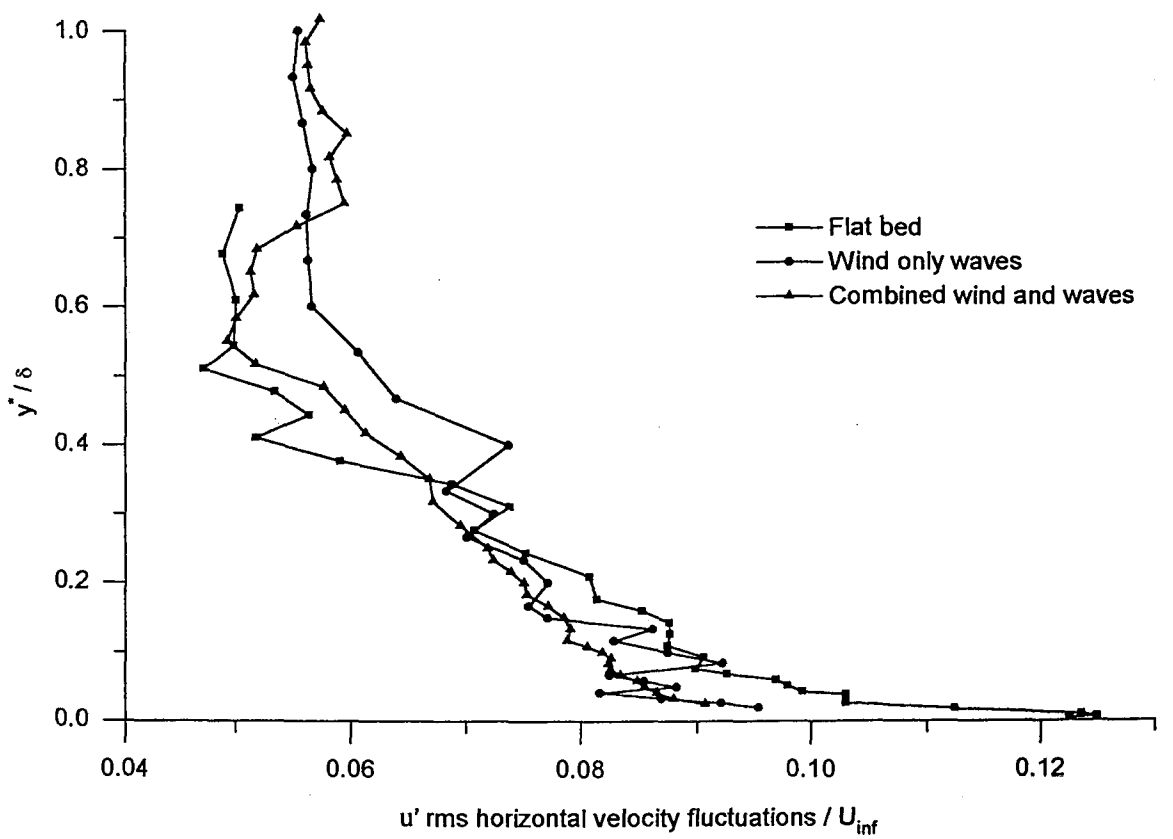


Figure 4.29: Time averaged root mean square turbulence profiles (U_{inf}= 2.4 ms^{-1})

4.8 Phase Averaged Turbulent Velocity Profiles

Profiles of the phase averaged root mean square horizontal velocity fluctuations are given in Figure 4.30 for the $U_\infty = 3.1$ and 2.4 m/s cases. The turbulent fluctuations are normalised with the corresponding phase averaged velocity. For $U_\infty = 3.1$ m/s, the highest turbulence levels in the lower part of the flow are above the zero downcrossing and trough. The turbulence levels above the zero upcrossing and crest are significantly less, particularly beneath $y^* = 0.05$ m. The difference is due to the non-separated effects described earlier. The turbulence on the windward side of the crest, where the flow is accelerated and the streamline spacing small, is less than on the leeward side where the flow is decelerating and the streamline spacing relatively large. A diverging flow will have higher turbulence levels than a converging flow, and at the crest itself turbulence may be introduced due to the streamline curvature.

Similar behaviour was observed for the $U_\infty = 5.1$ m/s case, where non-separated sheltering was also thought to be occurring. However, the pattern is very different for the $U_\infty = 2.4$ m/s case. Beneath $y^* = 0.05$ m, the turbulence is greatest above the wave crest, and also large above the zero down crossing. This corresponds to the interface between adjacent recirculation cells, where, at the front edge of the recirculation, the flow is moving downwards, and at the back edge, upwards. There is therefore a significant amount of turbulent mixing, which is reflected in the observed high turbulence level. Above the wave crest, the turbulence reduces quickly with increasing elevation above the recirculation cells. The phase of the maximum turbulence level remains above the zero downcrossing up to an elevation of $y^* = 0.125$ m, this being the level above which the streamline amplitude starts to increase. This high turbulence region corresponds to the streamline crests. The minimum turbulence region is above the zero upcrossing, which is in the troughs of the streamlines. As for the first case, the minimum turbulence corresponds to the flow from the streamlines' elevation minima to the maxima, and the larger values from the maxima to minima. Above $y^* = 0.15$ m, the turbulence at all phases is relatively small, and tends to an approximately constant value of 5% of the free stream velocity at the edge of the boundary layer.

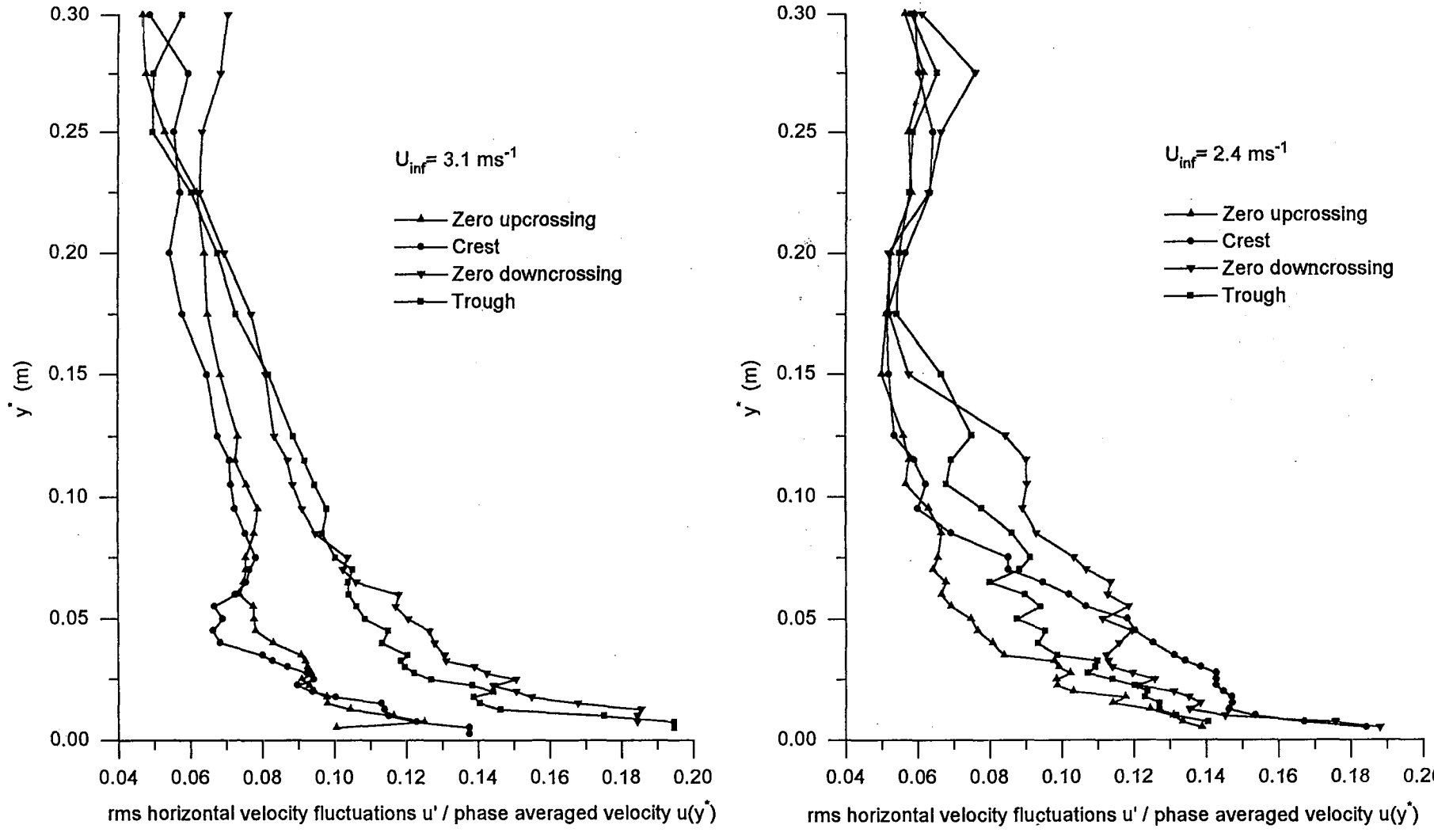


Figure 4.30: Phase averaged normalized rms horizontal velocity fluctuations profiles

The existence of coherent structures or bursting phenomena, described in Chapter 2, has not been examined in this study. Bursts and sweeps are characterised by large positive peaks in the Reynolds shear stress. A short-coming of this investigation was the inability to measure the horizontal and vertical velocities simultaneously, and hence calculate the Reynolds' shear stress in the airflow directly. However, an inspection of the separate horizontal and vertical velocity records revealed a large number of very distinct velocity bursts. These peaks were mostly in regions of high turbulence, and were particularly frequent and distinct just down wind of the wave crest for the $U_\infty = 5.1$ m/s case. The phase dependence of the bursting phenomena is clearly of interest, and should be investigated fully when a two-component burst analyser system is available.

5. AIRFLOW PROFILE ANALYSIS

In this chapter, the fundamentals of boundary layer theory appropriate to the present problem are outlined. These concepts are then used to analyse both the time averaged and phase averaged horizontal velocity profiles presented in the previous chapter. The variations in the deduced flow parameters are discussed in terms of the flow structure, and the approximate normal and shear stresses are calculated at the air-water interface.

5.1 Boundary Layer Theory

Consider a two-dimensional steady turbulent shear flow in an incompressible fluid flowing over a flat smooth wall. Assuming that the streamwise velocity gradients are small compared with the vertical gradients of the mean horizontal velocity, the flow can be divided into four regions (Figure 5.1).

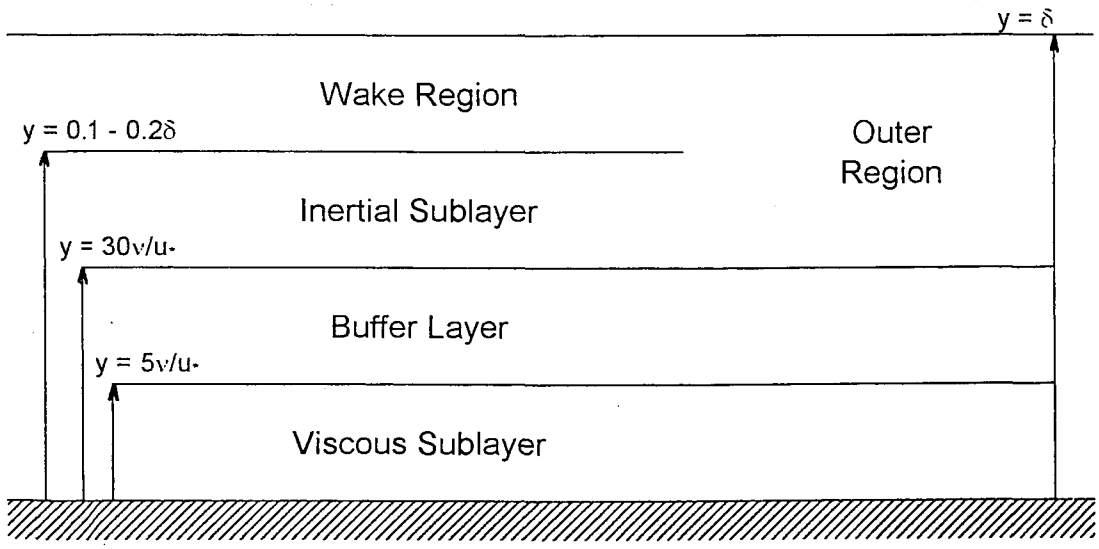


Figure 5.1: Boundary layer theory definition sketch (not to scale)

The region adjacent to the wall is the viscous sub layer. The shear stress τ_w at the wall is

$$\tau_w = \rho u_*^2 \tag{5.1}$$

where ρ is the density of the fluid, and u_* is the friction velocity. In this region, the effects of viscosity dominate the turbulent shear stresses. The viscous sub-layer extends from the wall to $y = 5\nu/u_*$, where ν is the kinematic viscosity of the fluid. The shear stress within this region is taken as being purely viscous, constant, and equal to the surface shear stress. Since the viscosity is defined by:

$$\tau = \rho\nu\frac{\partial u}{\partial y}$$

the velocity varies linearly with height and is given by:

$$U = \frac{u_*^2}{\nu}y \tag{5.2}$$

Above the viscous sub layer there is a region where both viscous and turbulent stresses are significant. This is the so-called buffer layer, which extends up to $y = 30\nu/u_*$. Above this level, the turbulent stresses dominate and viscous stresses can be neglected.

The region above $y = 30\nu/u_*$ and extending up to $y = 0.1\text{-}0.2\delta$, where δ is the boundary layer thickness, is the inertial sub-layer. Within this layer, inertial rather than viscous stresses are dominant. The shear stress is near constant and equal to the Reynolds shear stress $-\overline{u'v'}$. The shear stress throughout the viscous sub-layer, the buffer layer and inertial sub-layer (collectively referred to as the inner layer), is almost constant. It changes however from being a purely viscous stress close to the surface, to purely inertial at greater elevations. Therefore from equation 5.1, in the inertial sub layer, $-\overline{u'v'} \approx u_*^2$. On the basis of empirical arguments Tennekes and Lumley (1992) suggest that the root mean square turbulent intensities may be approximated by $u' \approx 2u_*$, $v' \approx 0.8u_*$, and the product of u' and v' by $u'v' \approx 2.5u_*^2$.

The mean velocity profile in the inertial sub layer is given by the 'law of the wall':

$$\frac{U}{u_*} = \frac{1}{\kappa} In\left(\frac{yu_*}{\nu}\right) + C \tag{5.3}$$

where κ is the Karman constant, taken as 0.40, and C is a constant dependent primarily on the nature of the surface. For smooth walls, the generally accepted value is $C = 5.1$. The law of the wall provides a good description of the flow over a wide range of conditions such as wall curvature, surface roughness, and variations in the outer flow, all of which will affect the value of the friction velocity u_* .

The fourth region is the outer region, which extends up to the edge of the boundary layer $y = \delta$. This outer region also includes the inertial sub layer, which is why the latter is sometimes called the overlap region. The velocity profile in the outer layer is given by:

$$\frac{U_\infty - u}{u_*} = f\left(\frac{y}{\delta}\right) \tag{5.4}$$

where it is the velocity defect (or $U_\infty - u$) rather than the velocity u which varies as a function of the elevation above the boundary. As a result, equation 5.4 is commonly referred to as 'the velocity defect law'. Within the inertial sub-layer, both the 'law of the wall' and the velocity defect law apply, and may be combined to give:

$$\frac{U_\infty - u}{u_*} = -\frac{1}{\kappa} In\left(\frac{y}{\delta}\right) + C \tag{5.5}$$

Above the inertial sub layer, the measured velocity profiles deviate from the law of the wall. Coles (1956) found that this deviation was similar to the velocity profile for a half wake, and that it could be approximated by a sinusoidal function, which he called the wake function. Coles presents the law of the wake as:

$$\frac{U_\infty - u}{u_*} = -\frac{1}{\kappa} In\left(\frac{y}{\delta}\right) + \frac{W_c}{\kappa}\left[2 - w\left(\frac{y}{\delta}\right)\right] \tag{5.6}$$

where $w(y/\delta)$ is the wake function which can be approximated by

$$w\left(\frac{y}{\delta}\right) = 1 - \cos\left(\frac{\pi y}{\delta}\right) \tag{5.7}$$

and W_c is the wake parameter. This latter parameter is usually taken to be a constant, which is dependent upon the flow conditions, primarily the streamwise pressure gradient. The wake function is a universal shape function, and it is the wake parameter which defines the wake component, or the deviation of the flow from the law of the wall. For a boundary layer with a zero streamwise pressure gradient, Coles (1956) found that for a smooth wall $W_c = 0.55$.

The law of the wake is valid only for equilibrium and quasi-equilibrium boundary layers, in which the velocity defect function $f(y/\delta)$ (equation 5.4) is independent of the streamwise co-ordinate x. In an equilibrium boundary layer, the ratio of the pressure gradient to the shear force must be a constant, and can be expressed by:

$$\beta = \left(\frac{\delta^*}{\tau_w}\right)\frac{dp}{dx} \tag{5.8}$$

where p is the pressure and δ^* is the displacement thickness, calculated from:

$$\delta^* = \int_0^\infty \left(1 - \frac{U}{U_\infty}\right) dy \tag{5.9}$$

A quasi-equilibrium boundary layer is thus one in which β varies slowly in the streamwise direction, and no other factors change the shape of the velocity profile. The function $f(y/\delta)$ will then change only slowly with x, and will be determined by the value of β. For quasi-equilibrium boundary layers, White (1985) found that:

$$W_c \approx 0.8(\beta + 0.5)^{3/4} \tag{5.10}$$

By substituting for β in equation 5.8, the pressure gradient can be expressed in terms of the friction velocity and wake parameter:

$$\frac{dp}{dx} = \frac{\rho u_*^2}{\delta^*}\left[\left(\frac{W_c}{0.8}\right)^{4/3} - 0.5\right] \tag{5.11}$$

Favourable pressure gradients, $dp/dx < 0$ correspond to small values of the wake parameter. The velocity profile (equation 5.6), will be dominated by the log term with a small wake component. In Equation 5.10, the limiting large favourable pressure gradient will correspond to $\beta = -0.5$, which will produce $W_c = 0$, and consequently there will be no wake. In contrast, adverse pressure gradients, $dp/dx > 0$, correspond to large values of the wake parameter. The logarithmic part of the profile will be very small with the profile dominated by the wake component. The limiting values of the pressure gradient will be as the flow is on the verge of separating, and the profile will be a wake type profile. For mild and slowly varying pressure gradients, only the value of the wake parameter will vary, so W_c and β will be functions of x.

The law of the wake can be written in the form of the law of the wall (Equation 5.3):

$$\frac{U}{u_*} = \frac{1}{\kappa} In\left(\frac{yu_*}{\nu}\right) + C + \frac{W_c}{\kappa} w\left(\frac{y}{\delta}\right) \tag{5.12}$$

The constant C is equivalent to the constant in the law of the wall profile, and is related to the nature of the surface. It also has some dependence on the Reynolds number and the pressure gradient.

So far, only the flow over smooth walls has been discussed, but consider the case of flow over a rough surface. The roughness of the surface is represented by the root mean square height of the roughness elements, k_r. The effect of the roughness elements on the

flow depends upon the value of k_r relative to the viscous length scale ν/u_*. The ratio of these length scales is the roughness Reynolds number $R_k = k_r u_* / \nu$.

If $R_k < 5$, then the roughness elements are submerged in the viscous sub layer, so that no Reynolds stresses can be generated. This is the fully smooth condition, and neither the value of u_* nor C will be affected by such roughness elements. For $5 < R_k < 30$, the value of the constant is dependent upon the value of R_k. The roughness elements protrude into the buffer layer where turbulent stresses can be generated. The values of u_* and C are therefore affected, but the smooth form of the law of the wall remains valid. The limiting value for the constant in the smooth profile is $C = -2.14$. If $R_k > 30$, the viscosity has virtually no effect on the flow since the roughness elements protrude into the inertial sub layer, and the roughness height becomes the relevant length scale. The law of the wall therefore becomes

$$\frac{U}{u_*} = \frac{1}{\kappa} In\left(\frac{y}{k_r}\right) + C' \tag{5.13}$$

where $C' = 8.48$ for completely rough flow.

In the following profile analysis, it is assumed, and justified *a posteriori*, that the smooth form of the law of the wall is valid. The velocity profiles were fitted to the law of the wake in the form:

$$\frac{U_\infty - u}{u_*} = -\frac{1}{\kappa} In\left(\frac{y}{\delta}\right) + \frac{W_c}{\kappa}\left[1 + \cos\left(\frac{\pi y}{\delta}\right)\right] \tag{5.13}$$

A least-squares curve-fitting routine was used to find the friction velocity u_* and the wake parameter W_c. The value of the constant C was then calculated from:

$$C = \frac{U_\infty}{u_*} - \frac{1}{\kappa} In\left(\frac{\delta u_*}{\nu}\right) - \frac{2W_c}{\kappa} \tag{5.14}$$

The wake function (equation 5.7) is not valid up to the edge of the boundary layer, since $\partial U/\partial y \neq 0$ at $y = \delta$. Therefore only data in the range $30\nu/u_* < y < 0.9\delta$ was used in the curve fits. The data was also fitted to the law of the wall (Equation 5.3) in the range $30\nu/u_* < y < 0.15\delta$.

5.2 Time Averaged Horizontal Velocity Profile Analysis

The time averaged horizontal velocity profiles for the three flow cases above the mechanically generated waves, plotted in semi-logarithmic co-ordinates, are given in Figure 5.2. The law of the wall and Coles' law of the wake best-fits are shown. The lower limit of the inertial sub-layer was calculated to be at approximately $y^* = 0.005$ m for $U_\infty = 2.4$ m/s, $y^* = 0.0035$ for $U_\infty = 3.1$ m/s, and $y^* = 0.002$ m for $U_\infty = 5.1$ m/s, so any data below these levels was excluded from the curve-fitting. For the law of the wall, data up to $y^* = 0.15\delta$ was included, which corresponded to $y^* = 0.045$ m for $U_\infty = 2.4$ m/s, $y^* = 0.038$ m for $U_\infty = 3.1$ m/s, and $y^* = 0.030$ m for $U_\infty = 5.1$ m/s.

The plots clearly demonstrate the existence of a log-linear region in the lower part of the time averaged profiles, with the law of the wall providing a good fit to the data. The elevation at which the measured data starts to deviate from the law of the wall tends to reduce with increasing wind speed, reflecting the smaller inertial sub layer. The Coles' profile shows good agreement with the law of the wall fit in the inertial sub layer, and provides a good fit to the data at greater elevations. The Coles' profile provides a very good fit for $U_\infty = 3.1$ and 5.1 m/s, but is not very good for $U_\infty = 2.4$ m/s. Curve-fitting was also done for the time averaged horizontal velocity profiles measured over the flat bed, and over wind-only waves. Both the law of the wall and Coles' law of the wake profiles provided an excellent fit to these measured profiles. The combined wind and waves profiles are compared with the profiles measured over the flat bed and wind only waves for each wind speed in Figures 5.3, 5.4 and 5.5. The values of the parameters obtained by each curve-fitting method are given in Table 5.1. The approximate pressure gradient is calculated from equation 5.11.

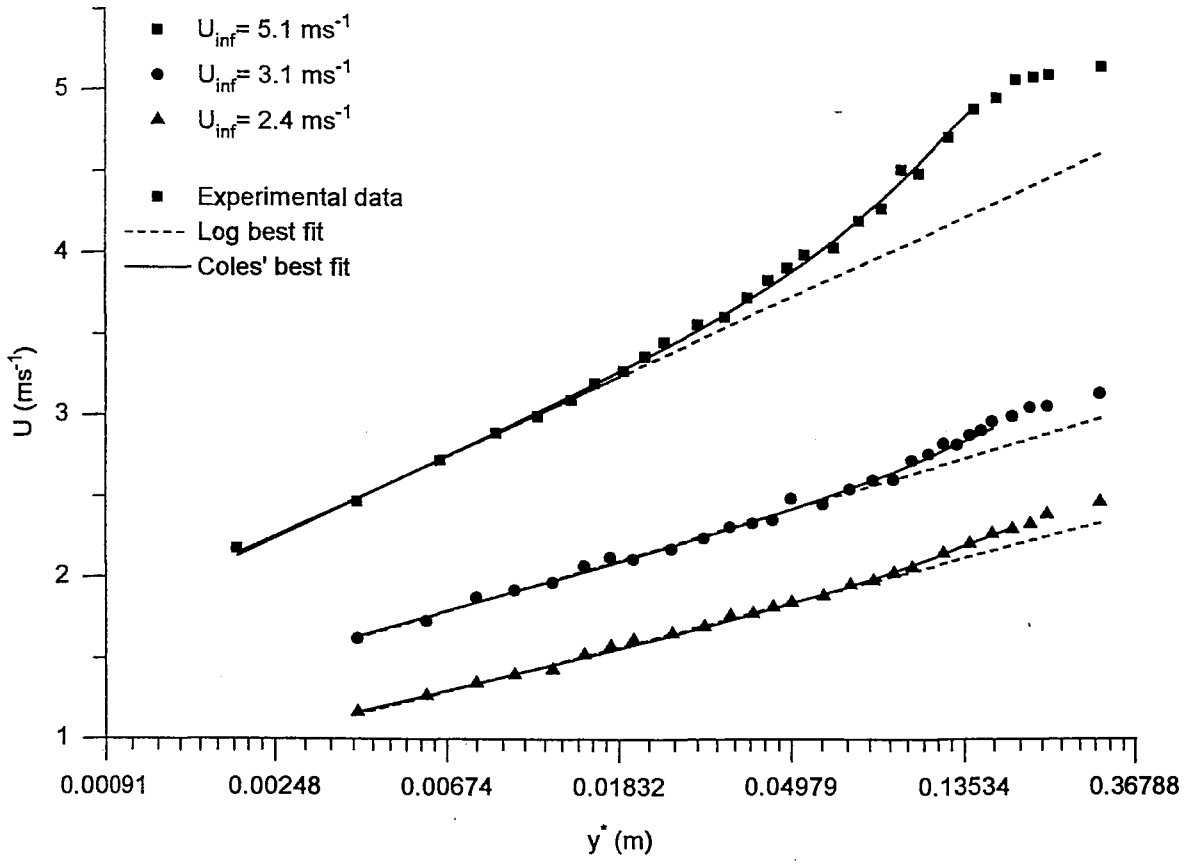


Figure 5.2: Time averaged velocity profiles - wind only - no mechanical waves

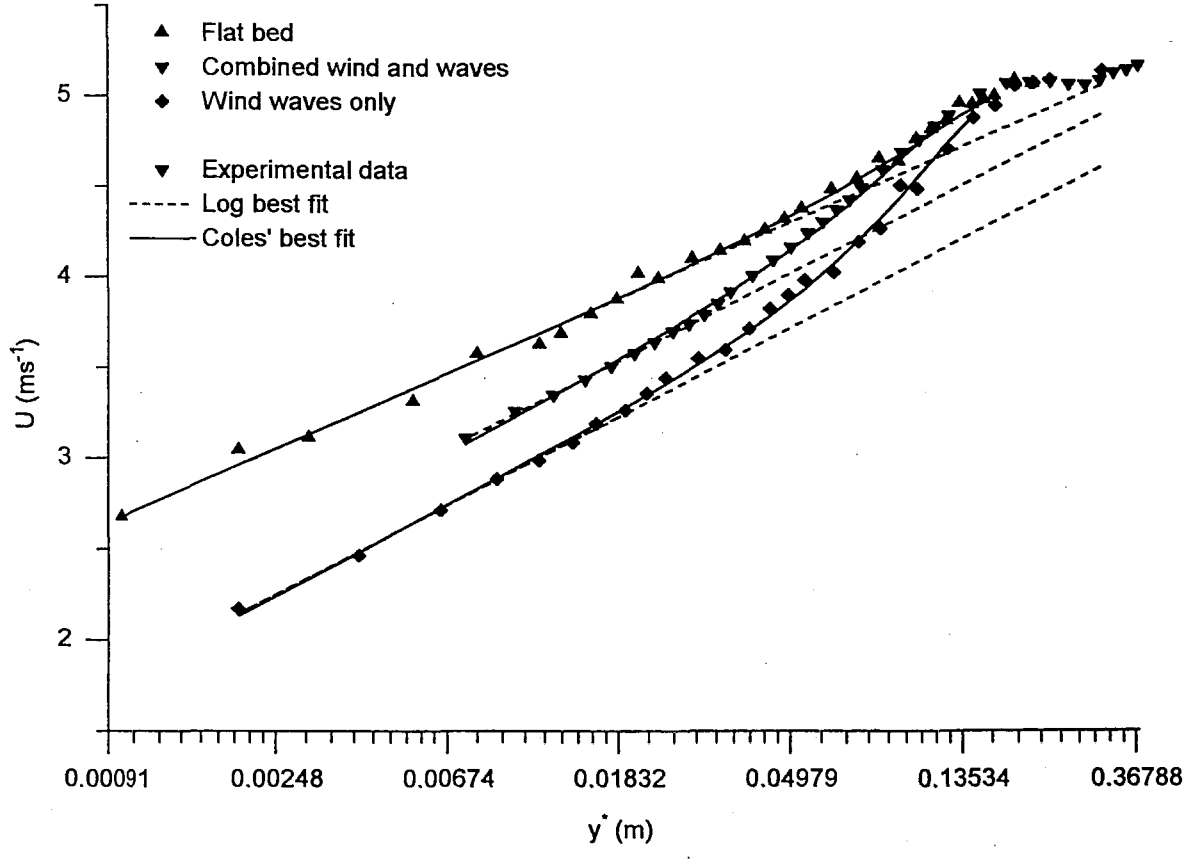


Figure 5.3: Time averaged velocity profiles - U_{inf}= 5.1 ms^{-1}

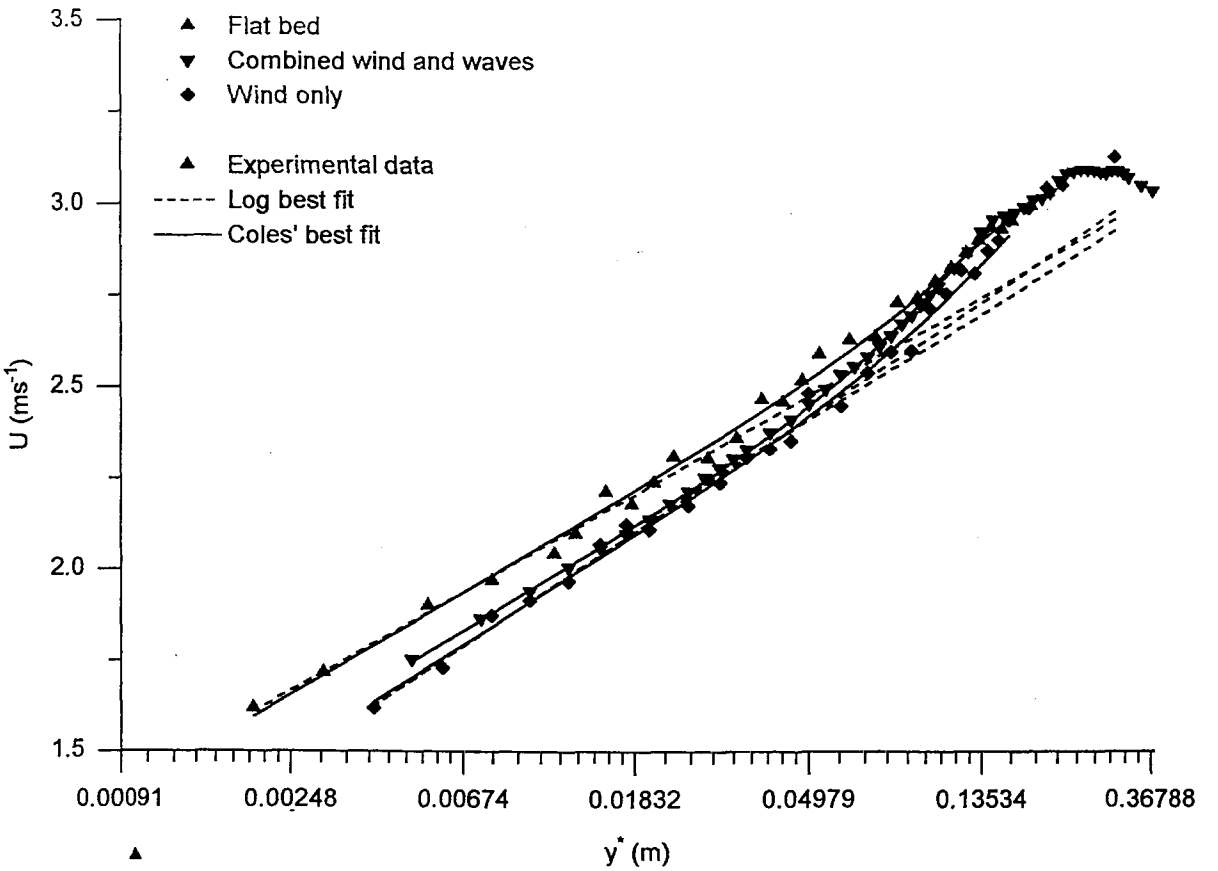


Figure 5.4: Time averaged velocity profiles - U_{inf}= 3.1 ms^{-1}

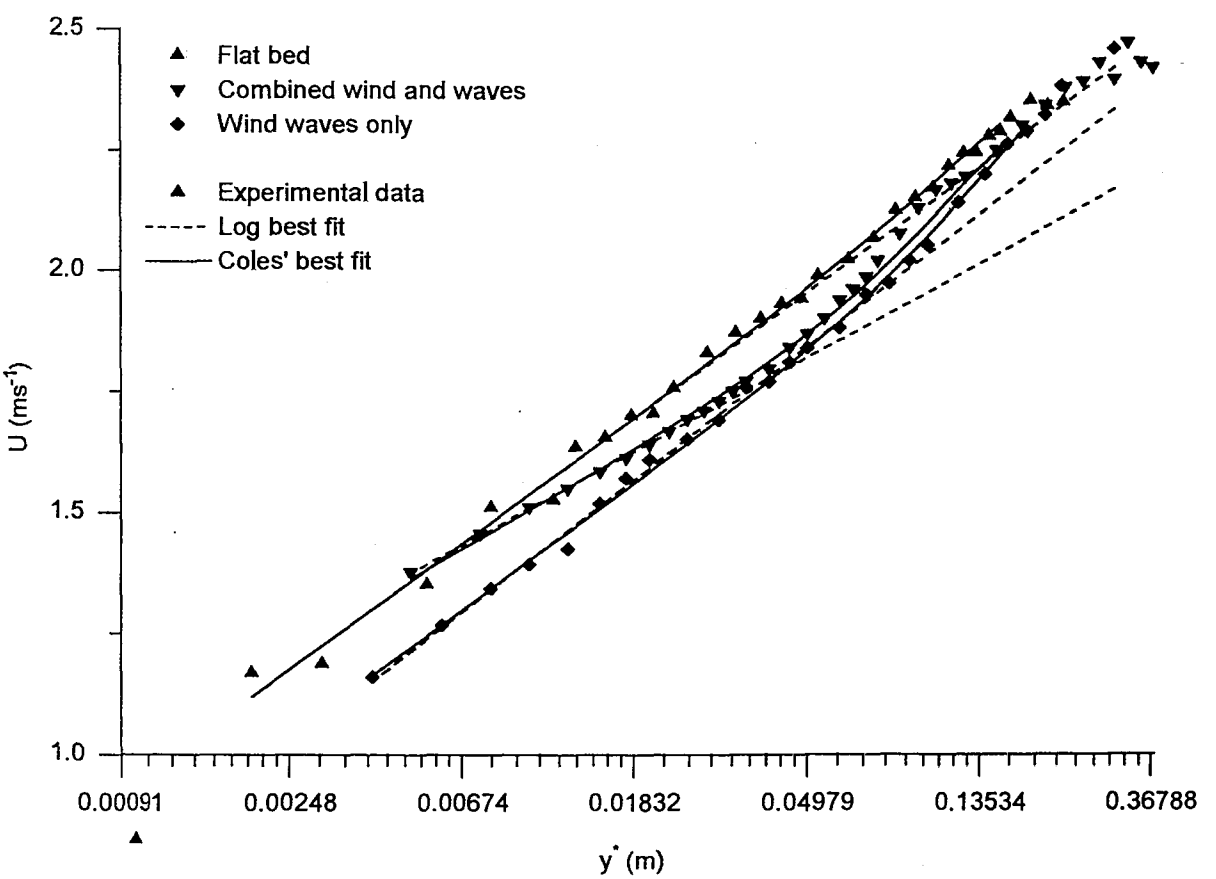


Figure 5.5: Time averaged velocity profiles - U_{inf}= 2.4 ms^{-1}

From Table 5.1, it can be seen that the friction velocity increases with the free-stream velocity, reflecting the increased near-surface velocity gradients. The agreement between the values of the friction velocity calculated using the law of the wall and those found from the law of the wake is very good, the discrepancy being less than 8% in all cases. For the $U_\infty = 3.1$ and 5.1 m/s cases, the friction velocity was smallest for the flat bed cases. This is as expected since the flat bed is smoother than the water surface, and so would generate the smallest surface stresses. For the two faster cases, the friction velocity is greater for the wind only cases than the combined wind and wave cases. This corresponds to the observation that the wind-waves appear to be larger in the wind only case than in the combined wind and waves cases. It also suggests that it is not the long waves which are acting as the surface roughness elements: if they were, then a large increase in the friction velocity from the wind only to the combined wind and wave cases would be observed.

The values of the friction velocity for the $U_\infty = 2.4$ m/s case show different behaviour to the two faster cases. The values for the flat bed and wind only cases are almost equal. This contrasts with a 15% increase in the friction velocity from the flat bed to the wind only waves cases for the faster airflows. The friction velocity for the combined wind and waves case is 25% less than the wind only waves case, compared with 10% for the other two cases. This difference is clearly illustrated in Figure 5.5 by the difference in gradient between the velocity profiles. The wind-waves generated by the $U_\infty = 2.4$ m/s airflow were barely visible, which perhaps explains the apparent smoothness of the wind only waves case. The large reduction in the friction velocity in the combined wind and waves case is a result of the observed flow structure. The recirculation cells tend to cause a reduction in the velocity gradients close to the surface, which is apparent by the increased matched height.

The agreement in the values of the constants calculated from the law of the wall and law of the wake is not as good as for the friction velocity, with discrepancies of up to 30%. The values do however show similar trends. Over the flat bed, the values of the constant

Flat Bed

	Law of the Wall		Law of the Wake			
U_∞ (m/s)	u_* (m/s)	C	u_* (m/s)	C	W_c	dp/dx (N/m^2/m)
2.4	0.1040	3.827	0.1039	3.850	0.1197	-0.0197
3.1	0.1077	7.914	0.1167	7.178	0.2657	-0.0199
5.1	0.1675	9.568	0.1668	9.655	0.2408	-0.0544

Wind only Waves

	Law of the Wall		Law of the Wake			
U_∞ (m/s)	u_* (m/s)	C	u_* (m/s)	C	W_c	dp/dx (N/m^2/m)
2.4	0.1097	1.702	0.1036	2.580	0.3116	-0.0112
3.1	0.1256	3.803	0.1198	4.633	0.3227	-0.0173
5.1	0.1965	2.405	0.2017	1.974	0.6399	+0.0609

Combined Wind and Waves

	Law of the Wall		Law of the Wake			
U_∞ (m/s)	u_* (m/s)	C	u_* (m/s)	C	W_c	dp/dx (N/m^2/m)
2.4	0.0776	9.226	0.0815	8.096	0.4893	-0.0005
3.1	0.1157	5.587	0.1134	5.955	0.4503	-0.0026
5.1	0.1940	4.236	0.2065	2.957	0.3786	+0.0321

Table 5.1: Time averaged horizontal velocity profile parameters

increase significantly with increasing free-stream velocity. The constant is primarily dependent upon the surface roughness, but is also dependent upon the Reynolds number and pressure gradient. The roughness of the flat bed is not changing between cases, so the increase in C appears to be due to the increased free-stream velocity and pressure gradient. Nevertheless, it had been expected that a constant value of $C = 5.1$ would be obtained.

For airflow over water, there are two opposing effects at the water surface which determine the value of the constant C. The generation of larger wind-waves at higher wind speeds makes the surface rougher, and so reduces C. The opposing effect is the release of shear stress at the water surface by the wind-generated current. The greater the wind speed, the greater the surface current, and so the more stress is released at the surface. The water surface will therefore appear smoother to the airflow, and the constant C will be increased. The larger values of the friction velocity for the wind only waves compared with the flat bed case suggests that the increased roughness effect is dominant. This is reflected in the values of C being less than for the flat bed, suggesting that the surface is indeed rougher. The value of C is greater for the $U_\infty = 3.1$ m/s case than for $U_\infty = 2.4$ m/s, suggesting that the surface is smoother, despite the fact that larger wind-waves were observed. Clearly the increase in C caused by the increased current is greater than the reduction due to the increased roughness. For the wind speed increasing from $U_\infty = 3.1$ m/s to 5.1 m/s, the value of C reduces, suggesting the increased roughness effect dominates over the increased current.

The value of C reduces with increasing wind speed for the combined wind and long waves cases. The value for $U_\infty = 2.4$ m/s is significantly larger than the flat bed case. This is a consequence of the small value of the friction velocity resulting from the recirculations already discussed. In addition, there were no wind-waves observed on the water surface, so the surface current would dominate over the roughness effects, thus causing an increase in C. For the $U_\infty = 3.1$ and 5.1 m/s cases, the constant C reduces with increasing wind speed, due to the growth of the wind-waves. The values are

smaller than the wind only case, reflecting the smaller values of the friction velocity and wind-wave amplitude.

The values of the wake parameter, calculated from the Coles' profile, suggest that in all cases, except one, the pressure gradient is favourable at the selected fetch (Table 5.1). As discussed in section 5.1, a favourable pressure gradient is denoted by a value of the wake parameter $W_c < 0.55$. The values of the pressure gradient calculated using equation 5.10 are also given in Table 5.1. The fan produces a large increase in pressure above atmospheric, and the pressure at the exit diffuser is atmospheric, so a favourable pressure gradient between the two is to be expected. The pressure gradient is greatest at the fastest wind speed, as was found from the roof pressure measurements presented in Chapter 3. Reasonable agreement with this data was obtained.

The magnitude of the favourable pressure gradients was greatest for the flat bed profiles. This is presumably a result of the pressure losses in the tunnel being least for the flat bed case, making the pressure gradient at the given fetch greater. For the flow over the water for the $U_\infty = 2.4$ and 3.1 m/s airflows, the pressure gradients are greater for the wind only cases, suggesting greater losses occur in the presence of the long waves. However, for $U_\infty = 5.1$ m/s for wind only waves, an adverse pressure gradient is measured, suggesting that the larger wind-waves have caused significant pressure losses in the tunnel due to the significant wave growth. Rather than the airflow accelerating, the flow has started to slow. This may be due to the faster airflow experiencing a deceleration ahead of the exit diffuser earlier than the slower velocity cases. The purpose of selecting a fetch towards the end of the wind tunnel was firstly to achieve a measure of stability in the wind-wave interactions (although any wave flume is too short to achieve true equilibrium), and secondly to have fairly small mean pressure gradients. This latter point minimises discrepancies with boundary layer theory (section 5.1). As the measured pressure gradients are all relatively small, the flow is experiencing only small accelerations, and boundary layer theory appears to agree with the measured profiles.

5.3 Phase Averaged Horizontal Velocity Profile Analysis.

The profile analysis described in the previous sections was used to analyse the phase averaged velocity profiles for the three combined wind and wave cases. Before discussing the results of the analysis it is important to re-consider the fundamental assumptions upon which boundary layer theory is based. The key requirement is that the streamwise velocity gradients $\partial u/\partial x$ and $\partial v/\partial x$ are very small compared with the vertical velocity gradient $\partial u/\partial y$. For the time-averaged profiles, the preliminary measurements showed that this was a good approximation, with the streamwise velocity gradients being very small. However, the phase averaged velocities presented in Chapter 4 showed that there were significant streamwise velocity gradients at certain phases of the wave cycle, for example, around the zero up crossing for the $U_\infty = 5.1$ m/s case at $y^* = 0.03$ m, $\partial u/\partial x \approx 3$ m/s/m, and $\partial u/\partial y \approx 12$ m/s/m. Although the vertical gradient is still greater than the streamwise gradient, the difference is less than an order of magnitude and the applicability of boundary layer theory starts to become doubtful. Together with the effects of the continually changing surface roughness and curvature, the flow is clearly very complex, and it is difficult to classify as a quasi-equilibrium boundary layer. It would seem, however, that the only practicable method of analysing the flow is to use existing boundary layer theory, though with the caveat that, at certain phases, it may not be valid, and could produce misleading results.

The phase averaged velocity profiles at the crest, trough and zero crossings for the $U_\infty = 5.1$ m/s case are given in Figure 5.6. The law of the wall and Coles' law of the wake best-fit profiles are shown. The data and the curve-fits for the $U_\infty = 3.1$ m/s case show very similar behaviour. The law of the wall shows a reasonable fit to the data in each case below $y^* = 0.15\delta$ ($y^* = 0.03$ m in Figure 5.6), but there does appear to be some systematic deviations from the log-linear plot. The velocity profiles above the wave trough and zero upcrossing are well fitted by the Coles' profile with distinct wake behaviour, and show good agreement with the law of the wall plots in the inertial sub-layer.

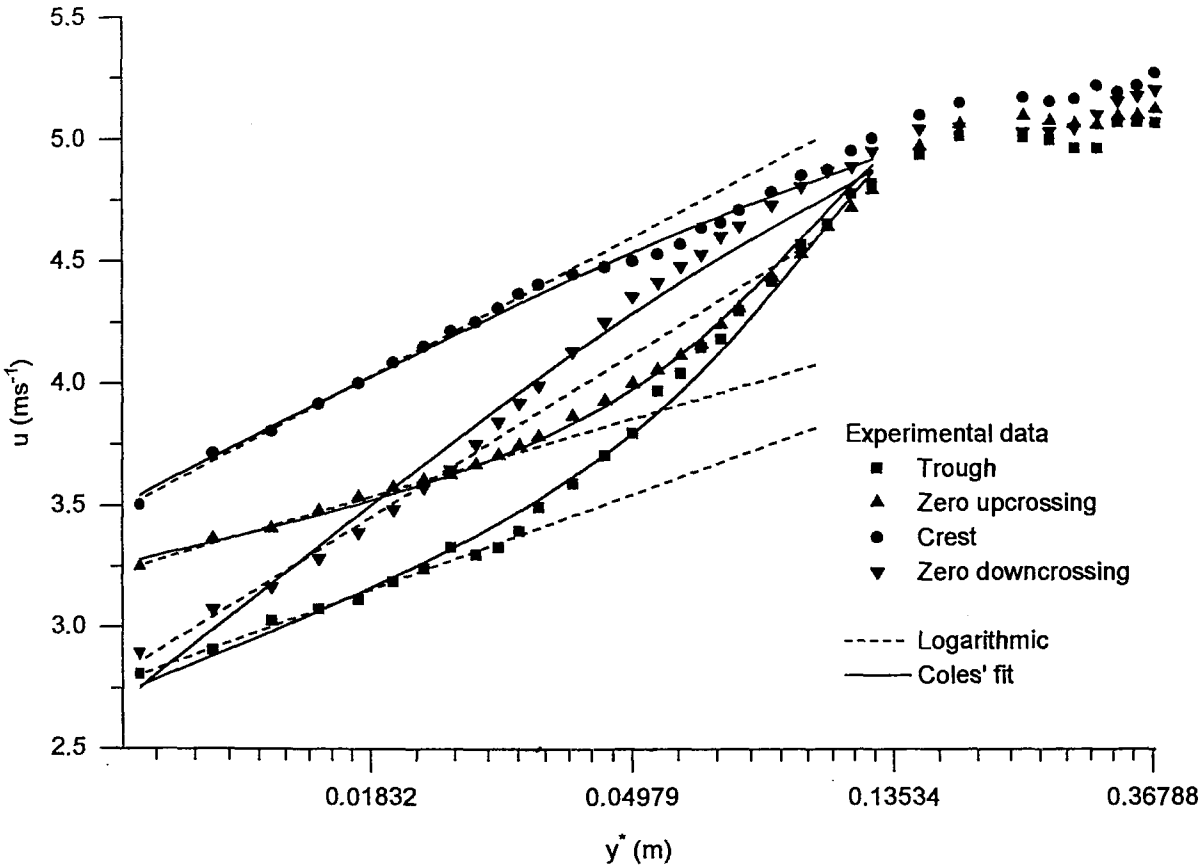


Figure 5.6: Phase averaged horizontal velocity profiles (U_{inf}= 5.1 ms^{-1})

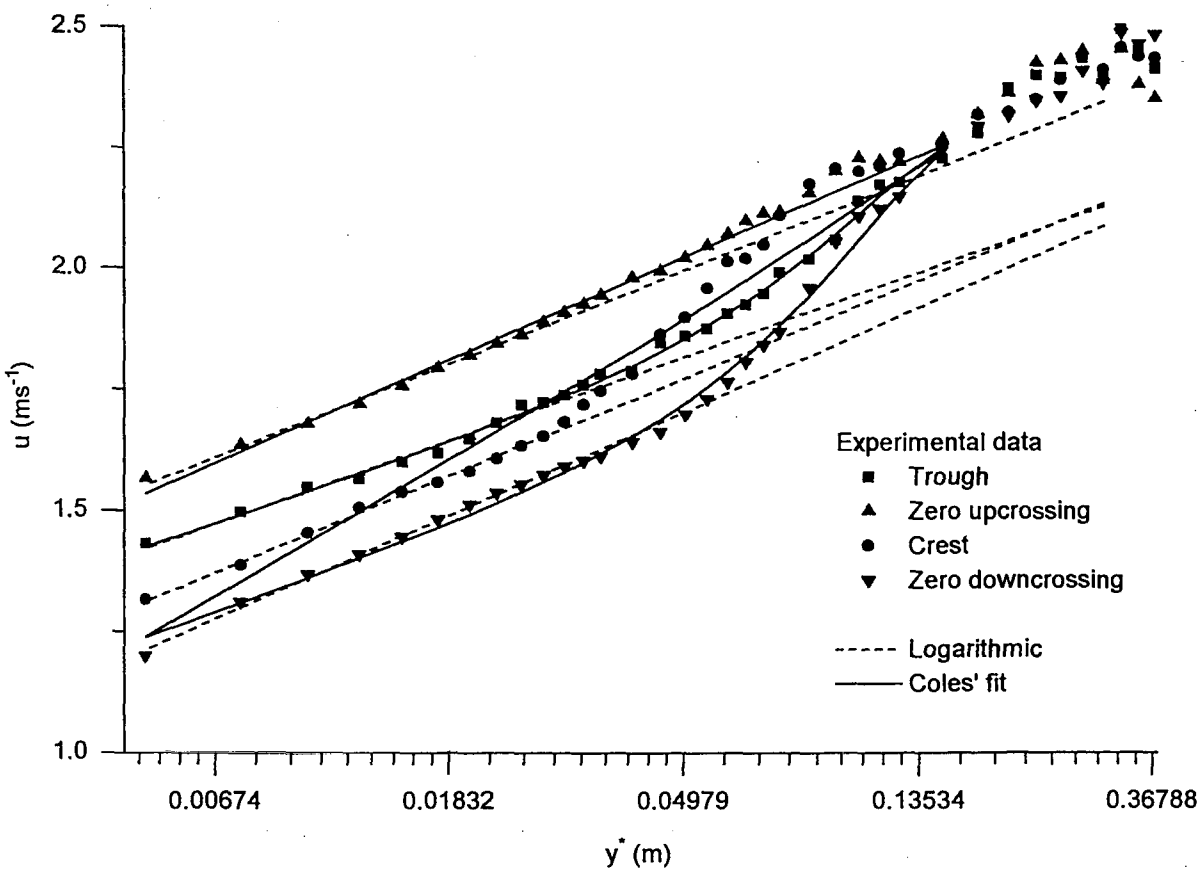


Figure 5.7: Phase averaged horizontal velocity profiles (U_{inf}= 2.4 ms^{-1})

The measured velocity profiles above the wave crest and particularly the zero down crossing, however, show poor agreement with the best-fit Coles' profile. The zero down crossing profile appears to show double curvature, at first deviating above the law of the wall fit, before curving back towards it at greater elevations. The point of inflexion is at approximately $y^* = 0.10$ m. The wake function cannot fit such a profile, so Coles' profile provides a poor fit to the data.

The measured velocity profile above the crest appears to be well fitted by the logarithmic profile up to $y^* = 0.04$ m, considerably higher than for the profiles at other phases. At greater elevations however, although the profile does show wake-type behaviour, the velocities are less than those predicted by the law of the wall, suggesting negative values for the wake parameter. As already discussed, a zero pressure gradient corresponds to $W_c \approx 0.55$, and for a very large pressure gradient $W_c \rightarrow 0$. For equilibrium and quasi-equilibrium boundary layers, a negative wake parameter is physically not possible. The effect is probably a result of the streamwise curvatures and accelerations experienced by the flow close to the surface, causing standard boundary layer theory to break down. The values of the wake parameter between the crest and zero down crossing should therefore be treated with caution.

The profiles for $U_\infty = 2.4$ m/s (Figure 5.7) show similar behaviour to the two faster cases, but with the flow shifted $\pi/2$ radians downstream by the recirculation cells, as discussed in Chapter 4. The profiles above the zero down crossing and trough show good agreement with the Coles' profile, equivalent to the trough and zero upcrossing profiles in the $U_\infty = 3.1$ and 5.1 m/s cases. The zero upcrossing profile provides a reasonable fit to the data, and in this case it is the crest profile which is poorly fitted by the Coles' profile. The double curvature effect is much more pronounced than in the first two cases.

There appears to be a link between the applicability of Coles' profile and the near-surface pressure gradients in the airflow. For all three airflow cases, there was a favourable near-surface pressure gradient at the phases where Coles' profile provided a

good fit to the data. Those profiles which the Coles profile could not fit corresponded to phases where there was an adverse pressure gradient. The profiles which showed significant double curvature corresponded to the phases of significant adverse pressure gradient. This is perhaps to be expected as the greatest losses in the flow are where the flow is decelerating and the adverse pressure gradient is a maximum. This effect is discussed fully in the section 5.3.4.

5.3.1 Friction Velocity

The variation in the friction velocity calculated from both the law of the wall and the law of the wake curve-fits for each of the three wind speeds is given in Figure 5.8. Once again the phase indicated on the abscissa is arranged so that phase $\phi = 0$ and phase $\phi = 1.0$ correspond to a wave trough and phase $\phi = 0.5$ to a wave crest. The mean values and amplitude of these variations are given in Table 5.2.

U_∞	Law of Wall		Law of Wake	
(m/s)	$\overline{u_*}$ (m/s)	$u_{*_{amp}}$ (m/s)	$\overline{u_*}$ (m/s)	$u_{*_{amp}}$ (m/s)
2.4	0.078	0.010	0.084	0.025
3.1	0.116	0.072	0.127	0.090
5.1	0.195	0.082	0.206	0.125

Table 5.2: Mean and amplitude of phase averaged friction velocity.

Both the mean and the amplitude of the phase variation of the friction velocity increase with increasing wind speed. For the $U_\infty = 3.1$ and 5.1 m/s cases, the variation of the friction velocity with phase is very similar: in each case, the maximum friction velocity is just upstream of the zero down crossing, at $\phi = 0.65$ for $U_\infty = 5.1$ m/s, and 0.67 for $U_\infty = 3.1$ m/s. The values from the law of the wall and Coles' profile show good agreement. The variations in the friction velocity with phase are consistent with the near-surface velocity gradients $\partial u/\partial y^*$ observed in Chapter 4, which were attributed to

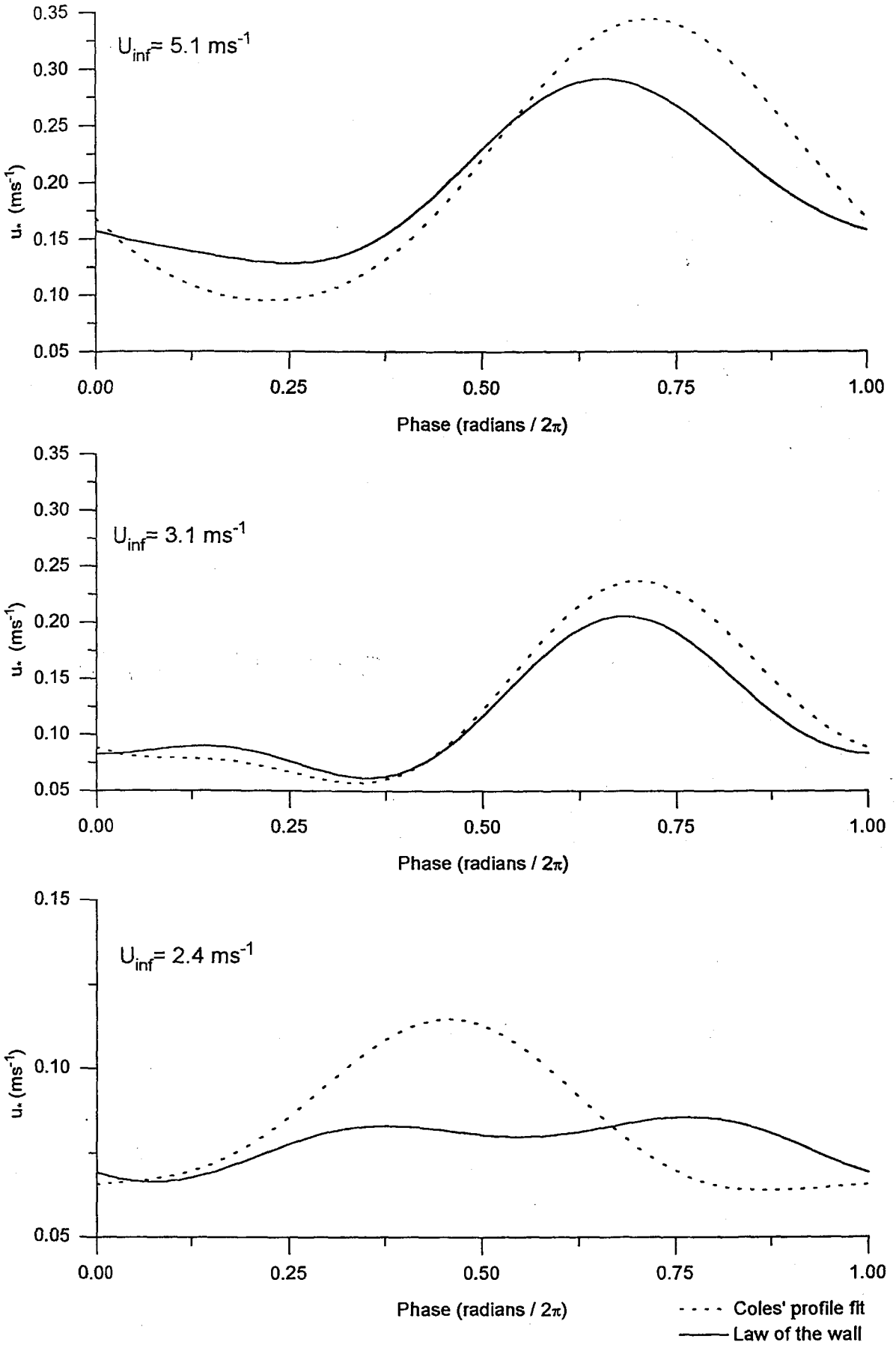


Figure 5.8: Variation of fricition velocity with phase of long wave

non-separated sheltering. The diverging streamlines on the leeward side of the crest produce large velocity gradients $\partial u/\partial y^*$ in the airflow, whilst the accelerating flow on the windward side of the crest has relatively small velocity gradients $\partial u/\partial y^*$. Between the trough and midway between the zero upcrossing and crest ($\phi = 0$ to 0.36), the friction velocity is approximately constant and relatively small. The phase at which the friction velocity starts to increase, which is between the zero up crossing and crest, corresponds to the maximum horizontal streamwise velocity gradient $\partial u/\partial x$; beyond this point the acceleration $\partial u/\partial x$ reduces and the vertical gradients $\partial u/\partial y$ increase. The maximum friction velocity corresponds to the point of maximum deceleration $\partial u/\partial x$ on the leeward side of the crest. Although the patterns of the phase variations for each flow case are almost identical, the magnitude of the mean friction velocity for $U_\infty = 5.1$ m/s is 70% greater than for the $U_\infty = 3.1$ m/s case, and the amplitude 40% greater.

The variation of the friction velocity for the $U_\infty = 2.4$ m/s case shows very different behaviour to that for the first two faster flows. The Coles' profile and the law of the wall best-fits yield very different values. This is particularly so around the wave crest, where, as shown in Figure 5.7, the double curvature in the velocity profile led to a very poor fit, particularly for the Coles' profile. Consequently, only the values of the friction velocity obtained using the law of the wall are considered here. The phase averaged variation shows two peaks, the greater at the zero down crossing, with a second slightly smaller peak mid-way between the zero up crossing and crest, and only a small reduction around the crest. The smallest values are between the trough and zero upcrossing. The largest values of the friction velocity, which are around the crest region, are at the interface between the front and back of the recirculation cells. The streamlines are converging or diverging either side of the crest, with the resulting large velocity gradients $\partial u/\partial y^*$ and turbulent fluctuations. The minimum friction velocity region corresponds to the flow above the centre of the recirculation cells, where the flow is accelerating, and is similar to the potential type flow on the windward face of the crest in the faster cases. The amplitude of the variation is very small, and, although the mean value is only 30% less than that for the $U_\infty = 3.1$ m/s case, the amplitude is almost 90% less.

5.3.2 'Constant' C

The variation in the value of C with phase is given in Figure 5.9, and the mean and amplitude of the variations shown below in Table 5.3. Both the values found by the law of the wall and the law of the wake are given. However, there are some significant discrepancies, largely due to the fact that C is very sensitive to the curve-fitting technique used. Only those values found using the law of the wall are considered in the present discussions.

U_∞	Law of Wall		Law of Wake	
(m/s)	$\overline{C}$	C_{amp}	$\overline{C}$	C_{amp}
2.4	9.293	4.550	8.450	6.185
3.1	8.799	16.48	8.860	18.66
5.1	5.562	8.695	6.763	14.49

Table 5.3: Mean and amplitude of phase averaged 'constant' *C*.

The mean values of C suggest that the flow is smooth, and show reasonable agreement with the values calculated from the time averaged values (Table 5.1). The value of C reduces with increasing wind speed, reflecting the roughening of the surface due to the increased height of the wind-generated waves. Even at the fastest wind speed, $U_\infty = 5.1$ m/s, the mean value of C is greater than the smooth wall value of $C = 5.1$. The values of C show large variations from the mean values with the phase of the long waves.

As with the friction velocity, the variations of C with phase for the $U_\infty = 3.1$ and 5.1 m/s cases are very similar (Figure 5.9), and both show a reasonable agreement between the values calculated using the law of the wall and law of the wake profiles. The maximum value of C is just downstream of the zero upcrossing at $\phi = 0.28$ for the $U_\infty = 5.1$ m/s

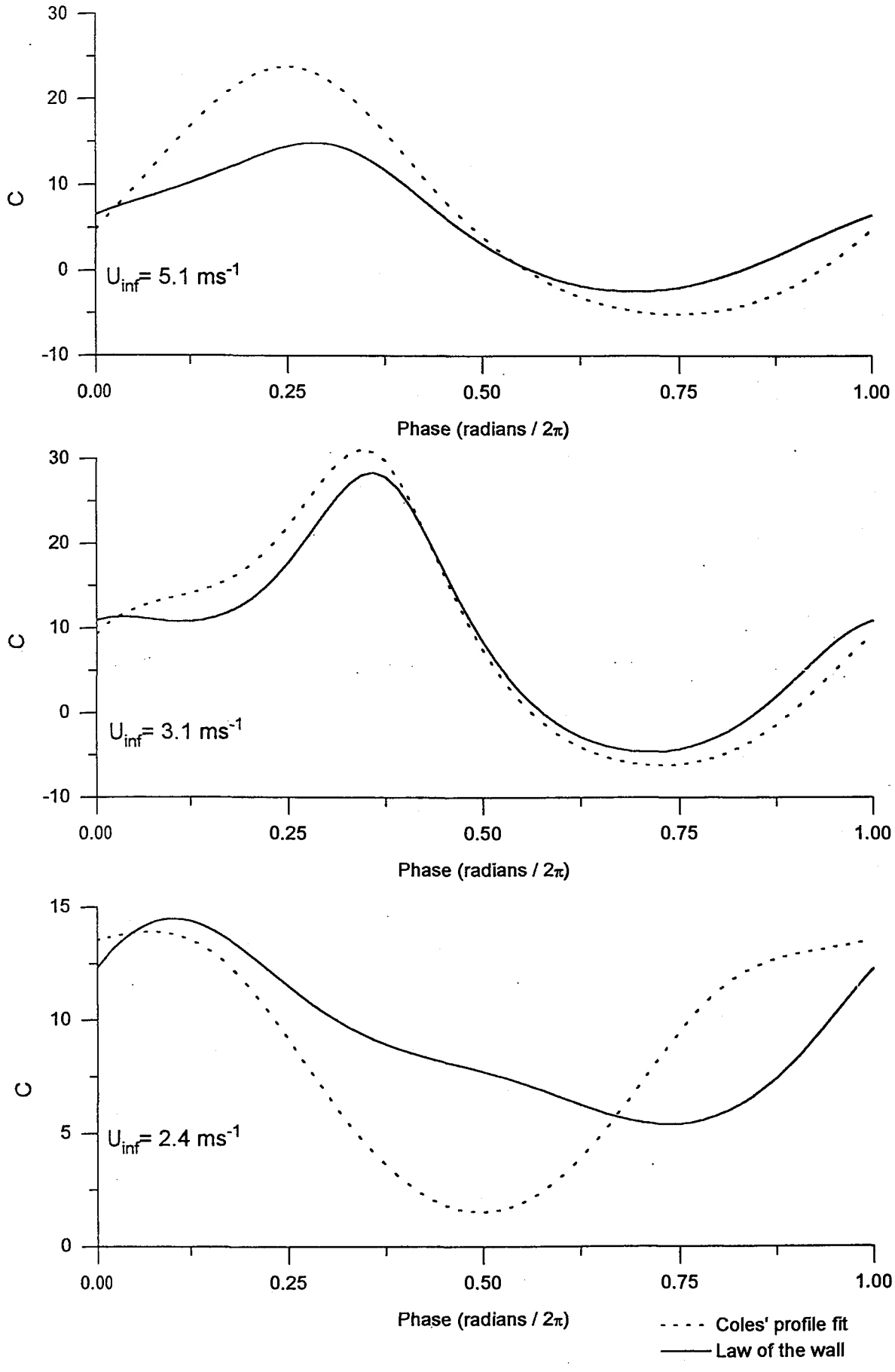


Figure 5.9: Variation of surface parameter C

case, and slightly further downstream at $\phi = 0.35$ for $U_\infty = 3.1$ m/s. The minimum C values are around the zero down crossing, with a sharp decrease in the value over the crest. The values of C around the zero down crossing are negative, and suggest the surface is aerodynamically rough. The very large values of C, up to 30 for $U_\infty = 3.1$ m/s, suggest that the surface is 'super smooth' around the zero upcrossings. These values suggest that there is a transition in the surface roughness condition from the windward side to the leeward side of the crest from aerodynamically smooth to fully rough.

As already discussed, C is primarily dependent upon the surface conditions. For flow over a water surface, this includes not just the roughness of the surface, but also the surface current, which releases a portion of the shear stress and makes the surface appear smoother. However, C is also dependent upon other effects, including the curvature of the boundary and the streamwise pressure gradient, which are significant here and may be responsible in part for the observed variations. For the $U_\infty = 3.1$ and 5.1 m/s cases, the peak C values appear to be where the friction velocity is a minimum, which is where the surface would be expected to be smoothest. This is the region at the centre of the flow recirculation, where the airflow velocity very close to the surface is a maximum. The wind-generated current may be expected to be a maximum at this point, releasing a large portion of the surface stress, and therefore making it appear 'super smooth'. The minimum value of C is where the friction velocity is maximum, which is at the ends of the recirculation, and is where the smallest surface current would be expected. The average value of C is greater for the $U_\infty = 3.1$ m/s case, corresponding to the smaller wind-generated waves. The amplitude of the variation is also considerably greater in the $U_\infty = 3.1$ m/s case, primarily due to the large 'super smooth' peak value.

The mean value of C for the $U_\infty = 2.4$ m/s case is greater than for the $U_\infty = 3.1$ and 5.1 m/s cases, reflecting the smoother water surface, but the peak and amplitude is considerably less. The minimum value of C is greater than $C = 5.1$, suggesting that the flow is smooth over the whole wave cycle. The reduced value of the amplitude probably results from the slower wind velocity producing little surface roughness and smaller surface velocities. The maximum C value is again at the phase of the minimum friction

velocity, which is at the centre of the recirculation where the velocity is a maximum. The minimum value of C, at the zero down crossing, corresponds to the minimum velocity at the interface between adjacent recirculation cells.

5.3.3 Matched Height

The matched height, the elevation above the water surface at which the horizontal velocity is equal to the phase velocity of the long waves, is calculated by extrapolation and interpolation from both the law of the wall and law of the wake profiles. The variations in the matched height with the phase of the wave are shown in Figure 5.10, and the mean value and amplitude of the variations given in Table 5.4.

U_∞	Law of Wall		Law of Wake	
(m/s)	$\bar{y}_m$ (mm)	$y_{m_{amp}}$ (mm)	$\bar{y}_m$ (mm)	$y_{m_{amp}}$ (mm)
2.4	17.1	13.4	16.9	12.5
3.1	4.18	5.57	4.33	5.71
5.1	0.470	0.580	0.694	1.02

Table 5.4: Mean and amplitude of phase averaged matched height

The mean value of the matched height reduces very quickly with increasing free-stream velocity, reducing by more than an order of magnitude for $U_\infty = 5.1$ m/s compared with $U_\infty = 2.4$ m/s. The agreement between the values calculated from the law of the wall profile and the law of the wake profile is good, except for $U_\infty = 5.1$ m/s. In this case, the matched height is very small, of order 10^{-4} m, and is calculated by extrapolating the velocity profiles. However, the matched height appears to lie beneath the inertial sub layer, in either the buffer layer or within the viscous sub layer, so neither the law of the wall nor wake profile is valid, and the matched height will be under-predicted. This problem also occurs at certain phases for $U_\infty = 3.1$ m/s. In each case, the values may not

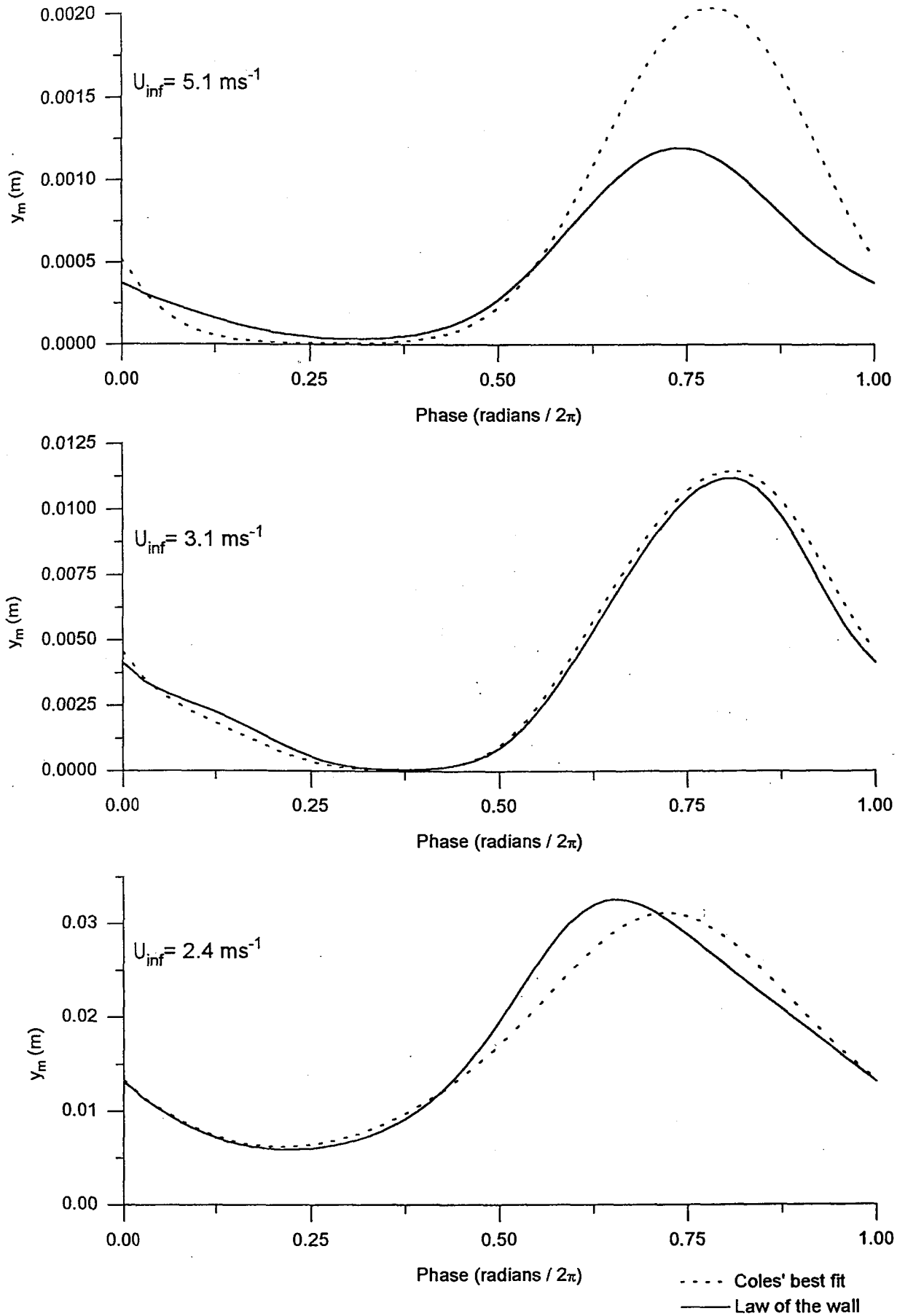


Figure 5.10: Variation of matched height with phase

be numerically exact, but the trends in the value will not be altered, and it is the latter which is of greater importance to the present discussion.

The variation of the matched height with phase (Figure 5.10) shows a similar pattern in all cases although, as discussed above, there is an order of magnitude difference between the values for the fastest and slowest cases. In each case, the maximum matched height is around the zero downcrossing, and the minimum around the zero upcrossing. The matched height variation appears to be approximately in phase with the near-surface pressure distribution, which corresponds to the observed flow structure.

There appears to be a contradiction between the observed matched height and the velocity gradients, which are expressed by the friction velocity. For the two faster flow cases, the matched height (Figure 5.10) and friction velocity (Figure 5.8) appear to be approximately in-phase. Therefore, on the windward side of the crest, there are small matched heights and small velocity gradients; on the leeward side of the crest, large matched heights correspond to large velocity gradients. The velocity at the matched height is by definition fixed, and the velocity at the surface is an order of magnitude less. In order for the velocities to reduce to the surface values, the smaller the matched height, then the larger the expected velocity gradient below the matched height. However, the converse effect is observed in the measured velocity profiles, and in the values of the friction velocity. This would therefore suggest that, very close to the water surface on the windward side of the crest, there exists a very highly sheared layer, and on the leeward side of the crest, a relatively low shear layer close to the water surface.

5.3.4 Wake Parameter and Pressure Gradients.

The wake parameters, found from Coles' law of the wake best-fit profiles, and the corresponding pressure gradients calculated from equation 5.10 are presented in Figures 5.11 and 5.12 respectively. The average values and amplitude of the variations are given in Table 5.5.

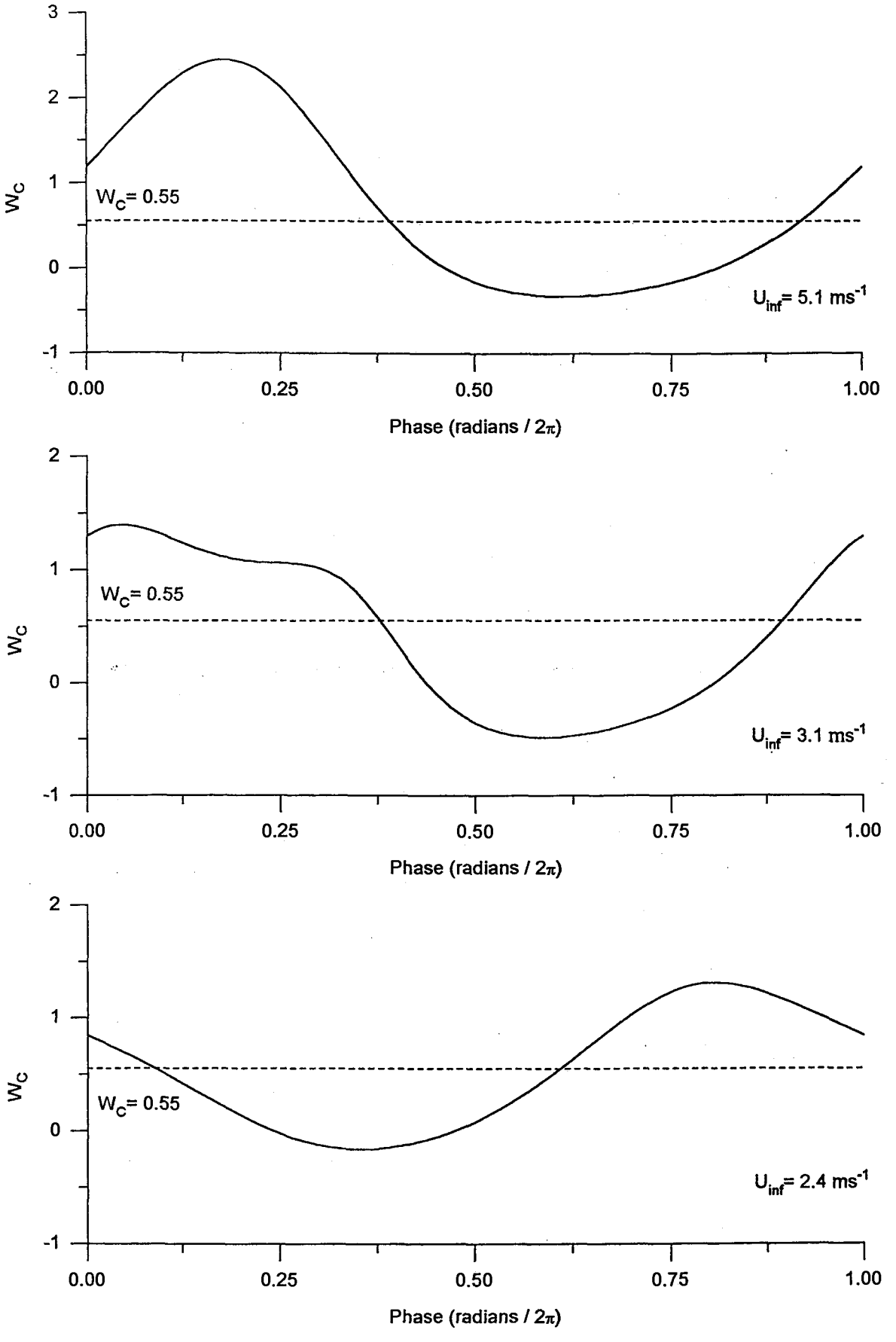


Figure 5.11: Variation of wake parameter W_C with phase

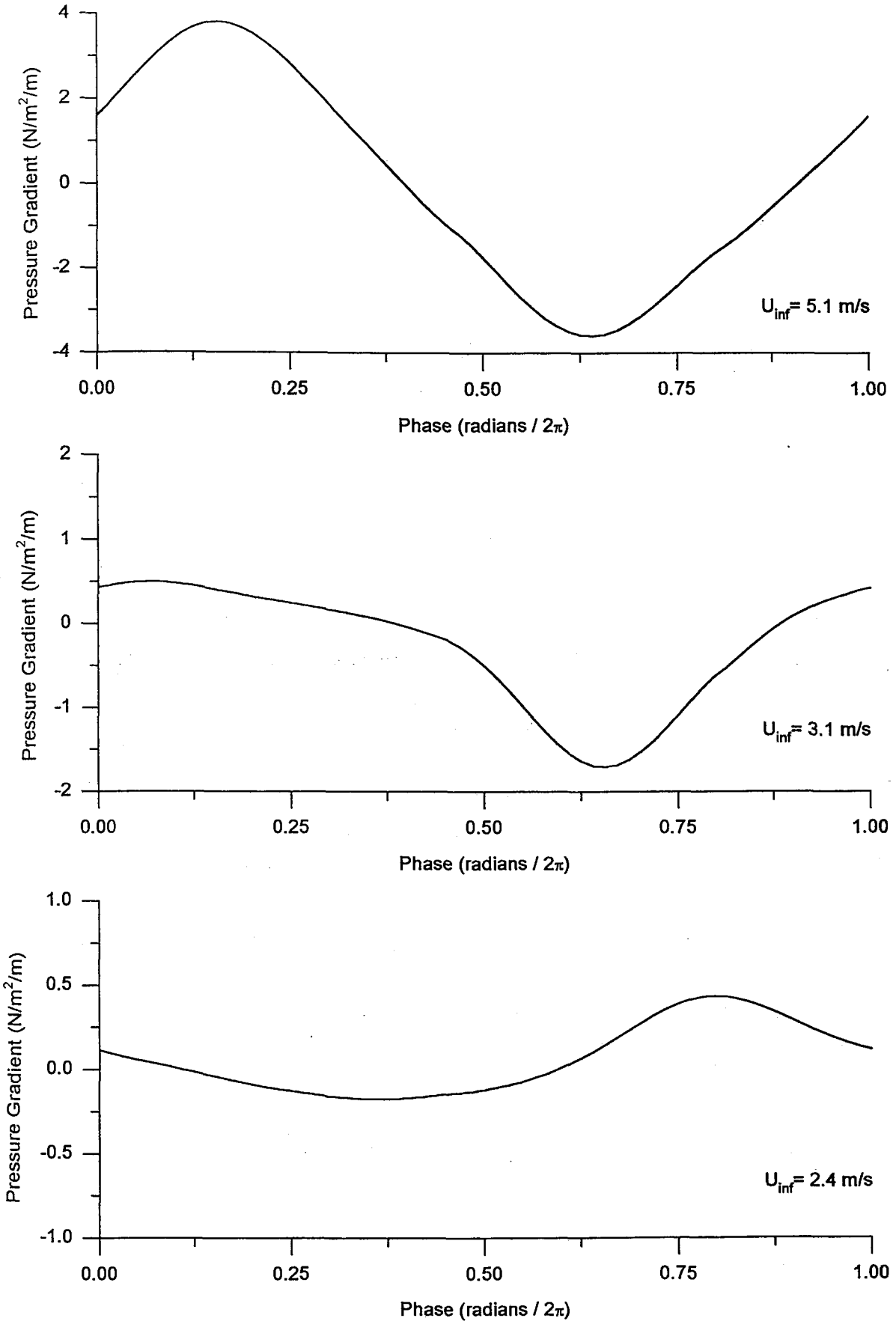


Figure 5.12: Phase variation of pressure gradient calculated using the wake parameters

U_∞	Law of Wake		White (eqn 5.10)	
(m/s)	$\overline{W}_c$	$W_{c_{amp}}$	$\overline{p}'$ (Pa/m)	p'_{amp} (Pa/m)
2.4	0.533	0.738	0.0599	0.305
3.1	0.442	0.942	-0.2583	1.106
5.1	0.742	1.386	0.0475	3.701

Table 5.5: Mean and amplitude of wake parameter and pressure gradients.

The amplitude of the phase averaged wake parameter in Table 5.5 increases with increasing wind speed, signifying a larger variation of the pressure gradients. There does not appear to be a clear pattern in the variation of the average wake parameter with free-stream velocity, contrary to the observed decrease with increasing free-stream velocity of the wake parameters calculated from the time averaged velocity profiles. The mean values for the $U_\infty = 2.4$ and 3.1 m/s cases are similar to those calculated from the time averaged profiles, but for the $U_\infty = 5.1$ m/s case, the mean value in Table 5.5 implies an adverse pressure gradient, whilst the mean velocity profile suggests a favourable gradient. This inconsistency is probably a result of the poor fit by the Coles' profile at certain phases, as illustrated by Figure 5.6.

The phase averaged streamwise pressure gradients, calculated from the phase averaged wake parameters, are given in Figure 5.12. A similar trend is observed in the pressure gradients for both the $U_\infty = 3.1$ and 5.1 m/s cases. The pressure minima are between the zero downcrossing and trough, and the maxima between the zero upcrossing and crest. The pressure gradient is favourable on the leeside of the crest, and adverse on the windward side. This is contrary to the near-surface pressure gradients deduced from consideration of the flow structure in Chapter 4, where the pressure minima were found to be upstream of the wave crest, and the maxima ahead of the wave trough. The pattern of the pressure gradients shown in Figure 5.12 is as envisaged in the discussion in Chapter 4, except that the sense of the pressure gradients is the opposite to that

anticipated. This inversion is perhaps to be expected since, in Chapter 4, the near-surface pressures were being considered, and the pressure gradients determining the nature of the wake profile are more likely to be those in the outer region of the flow.

Consider again the phase averaged velocity profiles for $U_\infty = 3.1$ and 5.1 m/s, presented in Figure 5.6. The data to which the Coles' profile provided the poorest fit was that above the zero down crossing, which appeared to demonstrate double curvature. It is suggested that this double curvature effect is a result of a change in the sense of the stream-wise pressure gradient. In both cases, close to the surface, above the zero downcrossing there was a significant adverse pressure gradient, which is reflected in the profile at lower elevations showing a large deviation from the law of the wall profile. At greater elevations, above approximately $y^* = 0.10$ m, the profile appears to start to turn back towards the law of the wall fit. This would suggest the existence of a favourable pressure gradient in the upper part of the boundary layer. The profiles at the crest suggest a similar behaviour. Close to the water surface, the adverse pressure gradient is very small and this is reflected in only a slight deviation of the measured profiles above the log-linear region before moving down below the log-linear line at greater elevations, suggesting a favourable pressure gradient. This flow behaviour is clearly very complex, and does not conform to the standard boundary layer model.

The profiles for $U_\infty = 3.1$ and 5.1 m/s above the zero upcrossing and the trough appear to be well fitted by the Coles' profile and show typical wake behaviour. However, the flow above the zero up crossing is subject to a very strong favourable pressure gradient close to the water surface, as the flow accelerates towards the wave crest. This is the reason why the profile above the zero up crossing deviates from the log-linear plot at a much greater height than for the zero down crossing profile, the favourable pressure gradient causing little deviation of the velocity profile from the law of the wall fit. At greater elevations, the flow above the zero upcrossing appears to experience a strong adverse pressure gradient, diverging rapidly from the log-linear plot. For the trough profile, there appears to be a small, favourable, near-surface pressure gradient, but at greater elevations an adverse pressure gradient develops.

Perhaps the most convincing support for this argument is the form of the phase averaged velocity profiles as they approach the edge of the boundary layer (Figure 5.6). Those for the crest and zero down crossing curve downwards relative to their respective law of the wall fits towards the free stream velocity, suggesting a favourable pressure gradient in the upper part of the boundary layer, while those for the trough and zero up crossing curve upwards, suggesting an adverse pressure gradient. The effect is difficult to quantify, but is perhaps better understood by considering fitting a straight line between $y^* = 0.02$ and 0.05 m to each profile. It is seen that the crest and zero downcrossing data show little deviation from this straight line, suggesting a favourable pressure gradient, whereas the trough and zero upcrossing profiles diverge above, again implying an adverse pressure gradient. Close to the water surface, particularly above the crest and zero downcrossing where there is an adverse pressure gradient, there is evidence of a change in pressure gradient, shown by points of inflection in the velocity profiles. The effect is not so apparent when there is a favourable pressure gradient close to the surface, since the profile simply maintains log-linear behaviour over a greater depth, before sharply turning above the log-linear line as the flow experiences an adverse pressure gradient. It does appear therefore that the pressure gradients close to the water surface are the opposite of those at greater elevations. This effect is further considered in the next section.

For the $U_\infty = 2.4$ m/s case, the phase averaged velocity profiles (Figure 5.7) show similar behaviour to those for the first two cases, however the flow is shifted down stream by approximately 90°. The profile above the crest shows significant double curvature, reflecting the observed strong adverse pressure gradient close to the surface, and favourable gradient at greater elevations. The profile above the zero down crossing is subject to large favourable pressure gradients close to the surface, which tend to enlarge the log-linear region, and then large adverse pressure gradients at greater elevations, which the Coles' profile fits well. Figure 5.12 shows that the favourable pressure gradients are on the windward side of the crest, and the adverse pressure gradients are on the leeward side. Again this is the opposite of the near-surface pressure distribution deduced in Chapter 4, in which the pressure maximum was between the crest and zero downcrossing, and the minimum was around the wave trough.

5.4 Calculation of Surface Stresses

In the following two sections, the normal and shear stresses at the air water interface are estimated from the measured velocities in the airflow. Expressions are developed to relate the velocities in the airflow to the normal and shear stresses close to the water surface, and the stresses so calculated are then presented and discussed.

5.4.1 Normal Stress

The velocity could not be measured at the water surface itself, but in all cases data was collected in the inertial sub layer (Chapter 4). An expression is therefore developed for the normal stress in the inertial sub layer, which should provide a good indication of the normal stress at the surface itself.

The equation of motion for a two-dimensional flow in the x-direction may be expressed as

$$\frac{\partial u}{\partial t} + u\frac{\partial u}{\partial x} + v\frac{\partial u}{\partial y} = -\frac{1}{\rho}\frac{\partial p}{\partial x} + \nu\nabla^2 u \tag{5.15}$$

The viscous stresses in the inertial sub layer are zero, so the final term in equation 5.15 can be neglected. Consider a frame of reference which is moving at the phase velocity of the mechanically generated waves. By time averaging equation 5.15, the temporal derivative becomes zero, and the equation of motion reduces to

$$\overline{u\frac{\partial u}{\partial x}} + \overline{v\frac{\partial u}{\partial y}} = \overline{-\frac{1}{\rho}\frac{\partial p}{\partial x}} \tag{5.16}$$

The horizontal and vertical velocity components can be decomposed as in Chapter 3 into

$$u = (\overline{U} - c) + \tilde{u} + u'$$

$$v = \tilde{v} + v'$$

Substituting the decomposed velocities into equation 5.16 yields

$$\overline{(\overline{U}-c)\frac{\partial \tilde{u}}{\partial x}} + \overline{\tilde{u}\frac{\partial \tilde{u}}{\partial x}} + \overline{\tilde{v}\frac{\partial(\overline{U}-c)}{\partial y}} + \overline{\tilde{v}\frac{\partial \tilde{u}}{\partial y}} = \overline{\frac{1}{\rho}\frac{\partial p}{\partial x}} - \overline{\frac{\partial (u')^2}{\partial x}} - \overline{\frac{\partial (u'v')}{\partial y}} \qquad (5.17)$$

In the inertial sub layer, the shear stress is a constant, with value $\tau = -\rho u_*^2$. The turbulent stresses in the inertial sub layer may be approximated by $u' \cong 2u_*$, hence $\overline{(u')^2} \cong 4u_*^2$, and $\overline{-u'v'} \cong u_*^2$ (Tennekes and Lumley, 1993). Hence, substituting for the turbulent fluctuations

$$\overline{\frac{1}{\rho}\frac{\partial p}{\partial x}} = -\overline{(\overline{U}-c)\frac{\partial \tilde{u}}{\partial x}} - \overline{\tilde{u}\frac{\partial \tilde{u}}{\partial x}} - \overline{\tilde{v}\frac{\partial(\overline{U}-c)}{\partial y}} - \overline{\tilde{v}\frac{\partial \tilde{u}}{\partial y}} - 4\overline{\frac{\partial}{\partial x}u_*^2} + \overline{\frac{\partial}{\partial y}u_*^2} \qquad (5.18)$$

The derivative of the friction velocity with respect to the vertical co-ordinate is zero in the inertial sub layer, since the shear stress is constant. An estimate of the streamwise pressure gradient can therefore be obtained from

$$\overline{\frac{1}{\rho}\frac{\partial p}{\partial x}} = -\overline{(\overline{U}-c)\frac{\partial \tilde{u}}{\partial x}} - \overline{\tilde{u}\frac{\partial \tilde{u}}{\partial x}} - \overline{\tilde{v}\frac{\partial(\overline{U}-c)}{\partial y}} - \overline{\tilde{v}\frac{\partial \tilde{u}}{\partial y}} - 4\overline{\frac{\partial}{\partial x}u_*^2} \qquad (5.19)$$

which can be integrated with respect to the streamwise co-ordinate x to provide an expression for the variation in pressure with phase. The most significant shortcoming of this approach is that, although the turbulent stress is approximately constant over the inertial sub layer, the wave-induced velocity field is not. Hsu and Hsu (1983) suggested that the wave-induced stresses show a large variation across the region. It was thought that using the lowest measured velocities would provide the best estimate for the surface pressure gradient which, even if not numerically exact, would show the true pattern of

the variation. The constant of integration is not considered in the analysis, since it is the wave-induced pressure and not the mean pressure which is of interest.

The surface pressure gradients $\partial p/\partial x$ for each wind speed case are presented in Figure 5.13, and the corresponding wave-induced pressure obtained by integration in Figure 5.14. The amplitudes of the pressure gradients and pressure perturbations, together with the amplitudes of the pressure perturbations both in phase with the surface elevation and in phase with the wave slope (the real and imaginary parts respectively), are given in Table 5.6.

U_∞ (m/s)	p'_{amp} (N/m^2)	p_{amp} (N/m^2)	$\Re[p]_{amp}$ (N/m^2)	$\Im[p]_{amp}$ (N/m^2)
2.4	1.425	0.302	-0.00746	0.283
3.1	2.160	0.383	0.0574	-0.399
5.1	15.533	3.290	-0.420	-3.220

Table 5.6: Measured surface normal stresses

The variation of the streamwise pressure gradient with phase, shown in Figure 5.13, demonstrates similar patterns for the $U_\infty = 3.1$ and 5.1 m/s flows, although the amplitude of the variation is an order of magnitude greater for $U_\infty = 5.1$ m/s. In each case, the pressure gradient is favourable upwind of the crest, and adverse on the downwind face. This is demonstrated in Figure 5.14, the plots of the variation of pressure with phase, showing that, for the $U_\infty = 5.1$ m/s case, the pressure minimum is just upwind of the crest, and for the $U_\infty = 3.1$ m/s case, slightly downwind of the crest.

The change in the pressure gradient for both cases is greater across the wave crest than across the wave trough. The pressure gradient variations are therefore asymmetric, with the peak favourable, and adverse pressure gradients closer to the crest than to the trough, which is reflected in the relatively narrow 'negative pressure' region around the

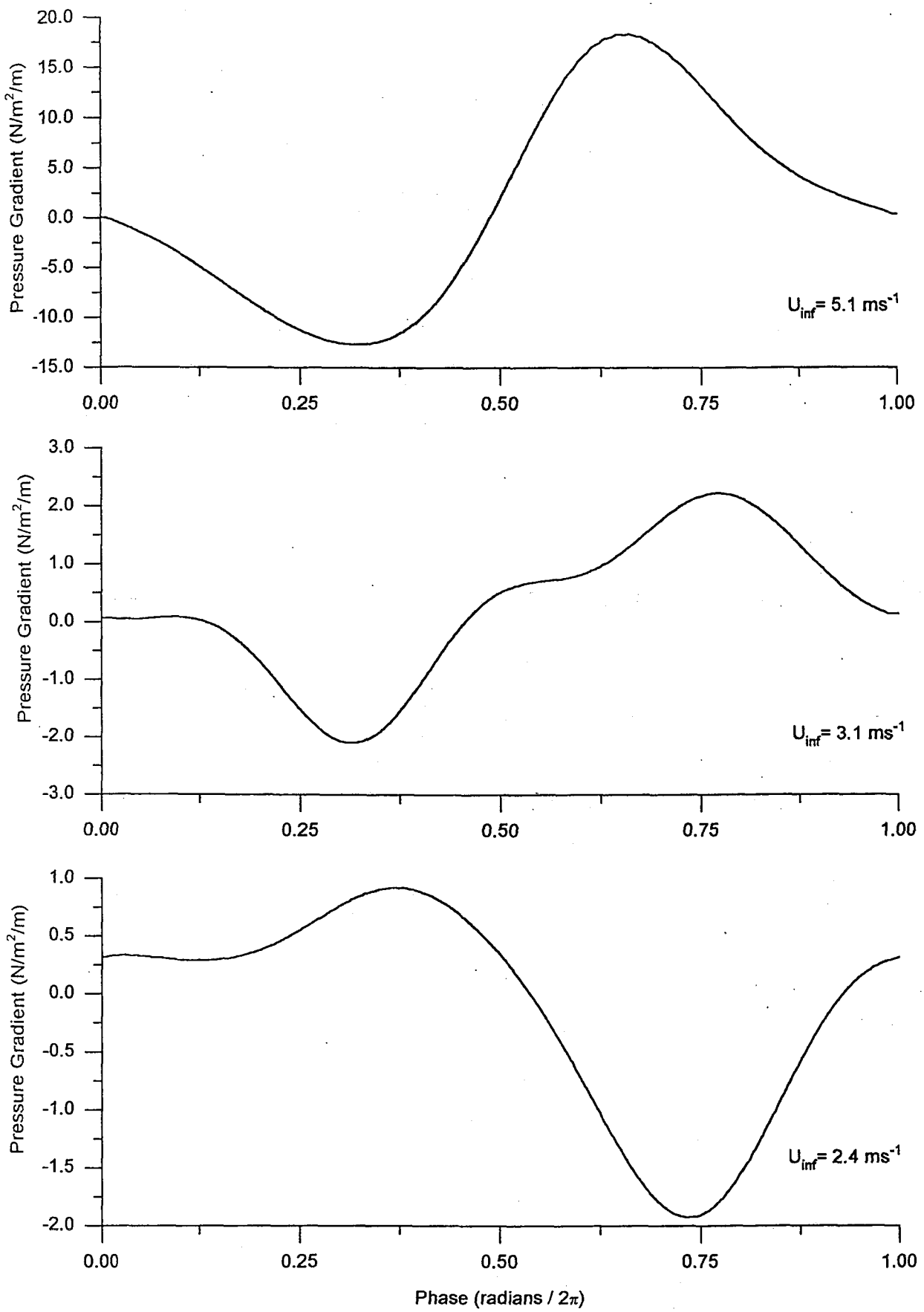


Figure 5.13: Near surface streamwise pressure gradients

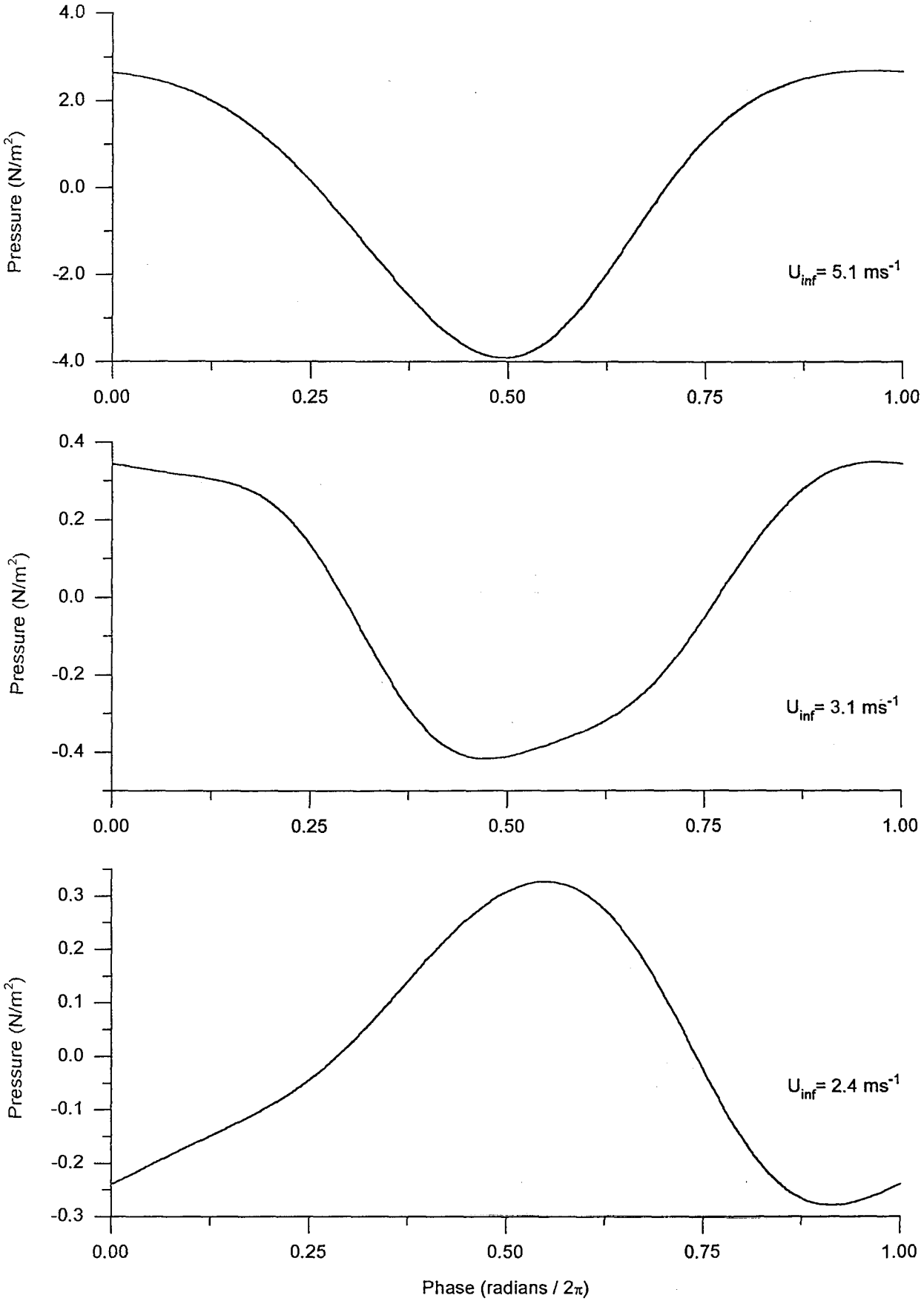


Figure 5.14: Wave-induced near-surface pressure

crest in Figure 5.14. The magnitude of the minimum pressure above the crest is therefore greater than the magnitude of the maximum pressure above the trough. The phase of the near-surface pressure distribution corresponds to the near-surface streamline patterns described in Chapter 4.

The pressure gradients for the $U_\infty = 2.4$ m/s case are almost 180° out of phase with those for the two faster cases. The pressure gradient is favourable on the leeward side of the crest, and adverse on the windward side of the crest, with the maximum favourable pressure gradient above the zero downcrossing, and the maximum adverse gradient between the zero upcrossing and crest (Figure 5.13). As for the $U_\infty = 3.1$ and 5.1 m/s cases, the pressure gradient is asymmetric, with the magnitude of the maximum favourable pressure gradient being greater than the magnitude of the maximum adverse pressure gradient, and the pressure gradient being favourable only over approximately 3/8 ths of the wave cycle. The maximum pressure is just downwind of the wave crest, as shown in Figure 5.14, with the asymmetry of the pressure variation clearly demonstrating the larger pressure gradients on the leeward side of the wave crest. The pressure gradients and pressure distribution reflect the streamline pattern described in Chapter 4, in particular the high pressure region above the wave crest, and the large flow accelerations on the leeward side of the crest. The amplitudes of the pressure and pressure gradient fluctuations are smaller, but of the same order of magnitude as for the $U_\infty = 3.1$ m/s case.

The pressure gradients shown in Figure 5.13 can be compared with those in Figure 5.12. The pressure gradients in Figure 5.13 were deduced from the flow very close to the water surface, whereas those in Figure 5.12 are dependent upon the flow in the wake region, in the outer region of the boundary layer. As was discussed in the previous section, the pressure gradients inferred from the near-surface flow structure are the opposite to those calculated from consideration of the wake profile. There are two possible explanations for this apparent contradiction. Firstly, it is possible that the near-surface pressure distribution is in anti-phase with the pressures in the wake region. The velocity measurements presented in Chapter 4 showed significant phase shifts with increasing elevation above the water surface, which would correspond to phase shifts in

the pressure distribution. It is possible that, if there is a high pressure region close to the water surface, there may be a corresponding low pressure region at the same phase in the outer region of the flow, and vice versa.

This explanation seems improbable, since it is unlikely that such radical changes in pressure would occur across the depth of the flow. The second explanation is related to shortcomings in the boundary layer theory outlined at the beginning of this chapter. Boundary layer theory assumes a constant streamwise pressure gradient but, as discussed above, the pressure gradient shows large variations with phase. As described in section 5.3 and shown in Figures 5.6 and 5.7, where the near-surface pressure gradient is large, such as around the zero downcrossings for the $U_\infty = 3.1$ and 5.1 m/s cases, then the velocity profiles become significantly distorted. In these cases there is a very large near-surface adverse pressure gradient, arising from the non-separated sheltering effects already described, but it would be expected that this would only be a near-surface effect, with the magnitude of the pressure gradient reducing rapidly with increasing elevation. The velocity profile therefore suggests there is a favourable pressure gradient, whereas in fact in the wake region the pressure gradient may still be adverse, but with a magnitude significantly smaller than that close to the water surface. The converse may be expected to apply for a large near-surface favourable current. The Coles' profile and boundary layer theory cannot account for such complexities.

5.4.2 Shear Stress

The time averaged total shear stress exerted by the wind on the water surface can be approximated by:

$$\overline{\tau_s} = -\left(\overline{u'v'} + \overline{\tilde{u}\tilde{v}}\right) \tag{5.20}$$

where $-\overline{u'v'}$ is the turbulent Reynolds shear stress, and $-\overline{\tilde{u}\tilde{v}}$ the wave associated Reynolds shear stress (Hsu, Hsu and Street, 1981). The shear stress is evaluated in the inertial sub-layer, rather than at the surface, since, as explained for the normal stress,

velocity measurements could not be made at the surface itself. In the inertial sub-layer, the turbulent shear stress is constant, and is by definition $-\overline{u'v'} = u_*^2$. The time averaged total shear stress is therefore:

$$\overline{\tau_s} = \overline{u_*^2} - \overline{\tilde{u}\tilde{v}} \tag{5.21}$$

The wave-associated stress $-\overline{\tilde{u}\tilde{v}}$, however, is not constant across the inertial sub-layer, and has been found to vary significantly when measured close to the water surface (Hsu and Hsu, 1983). The wave-associated stresses would be expected to increase with reducing elevation above the water surface to a point at a small height above the surface, before reducing rapidly towards the surface itself in a similar manner to the turbulent vertical velocity fluctuations (Figure 4.27). The elevation of the wave-associated stress maxima cannot be determined from the velocity measurements, since the maxima appear to be beneath the lowest velocity measurements. It is not apparent at what elevation the wave-associated stress should be measured for the purpose of determining the 'surface' shear stress; whether it should be the maximum stress or an average value is unclear. However, as in the calculation of the normal stresses, the lowest velocity measurements are used to calculate the shear stresses. By using data at a single elevation above the water surface, and using the same data as was used to calculate the normal stresses, it was thought that comparable, if not numerically precise, values would be obtained.

The variation of the surface total shear stress with the phase of the underlying waves is given in Figure 5.15 for each of the wind speed cases. The corresponding mean shear stress values are given in Table 5.7 below, together with the amplitude of the variation with the phase of the long wave, and the amplitude of the resolved components of the stresses in phase with the surface profile and in phase with the wave slope.

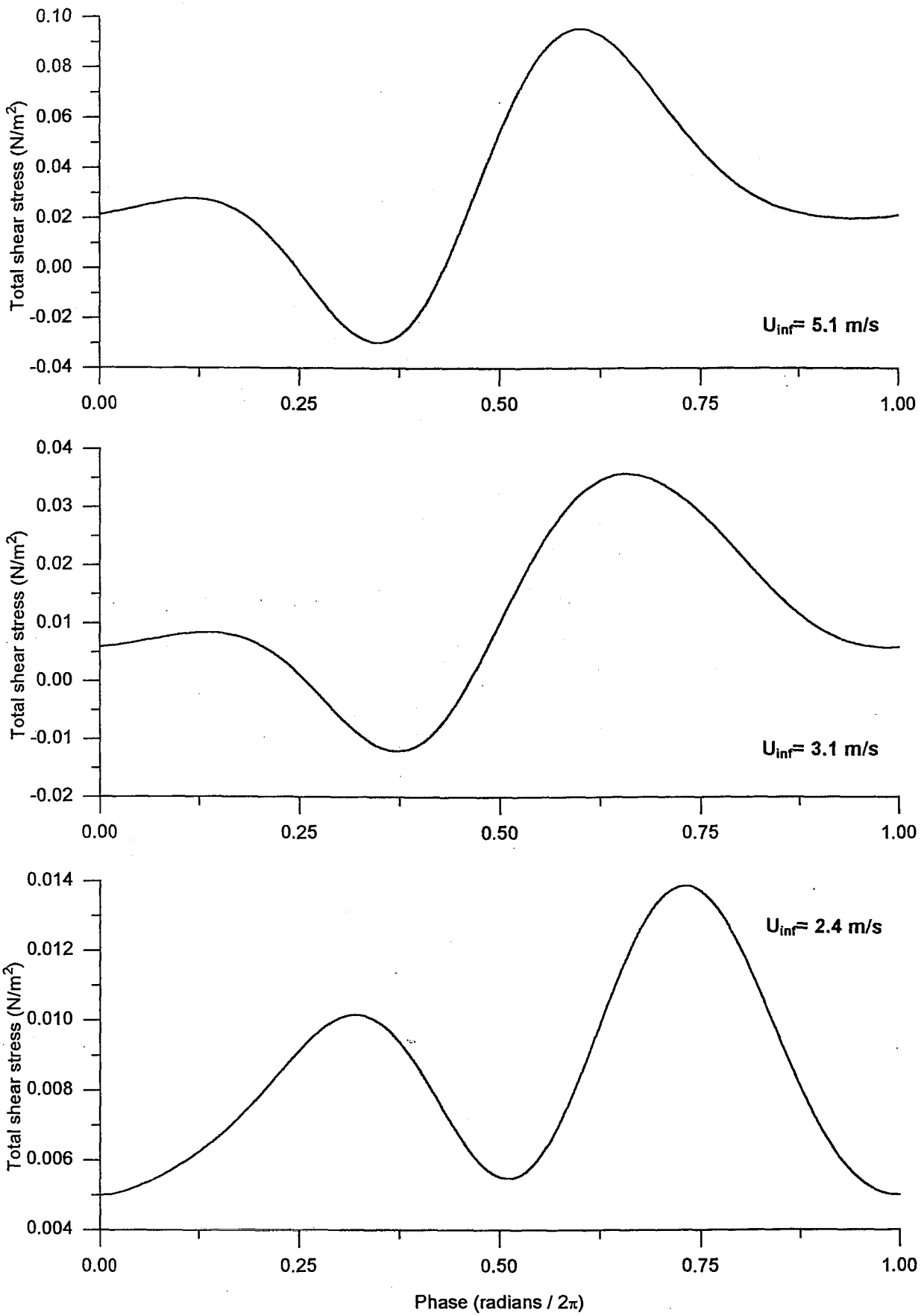


Figure 5.15: Total shear stress at surface

U_∞ (m/s)	$\overline{\tau_s}$ (N/m^2)	$\tau_{s_{amp}}$ (N/m^2)	$\Re[\tau_s]_{amp}$ (N/m^2)	$\Im[\tau_s]_{amp}$ (N/m^2)
2.4	0.00838	0.00944	0.000887	-0.00157
3.1	0.0111	0.0239	0.00131	-0.0158
5.1	0.0297	0.0626	0.01103	-0.0323

Table 5.7: Measured surface shear stresses

The mean shear stress and the amplitude of the phase varying shear stress increase with increasing free-stream velocity. The variation of the total shear stress with the phase of the long waves is very similar for the $U_\infty = 3.1$ and 5.1 m/s cases (Figure 5.15). The peak shear stress is approximately mid-way between the crest and zero downcrossing on the leeward side of the crest, at $\phi = 0.60$ for $U_\infty = 5.1$ m/s and $\phi = 0.68$ for $U_\infty = 3.1$ m/s. The minimum shear stresses, which are negative, lie approximately mid-way between the zero upcrossing and the wave crest, and have a much smaller magnitude than the shear stress maxima. In each case, the shear stress from the zero upcrossing to a point just before the crest is negative, implying that the airflow is being sheared by the water flow, rather than the airflow shearing the water surface. This suggests that the surface current at this phase of the long wave is very large, releasing the shear stress in the airflow. The shear stress between the zero down crossing and the zero upcrossing is small and positive and approximately constant in each case. Clearly, the distributions are therefore highly asymmetric, with the maximum and minimum values approximately $\phi = 0.125$ either side of the wave crest.

For the $U_\infty = 2.4$ m/s flow case, the shear stress variation with phase has similarities with the two faster cases. The peak shear stress is at the zero down crossing, slightly further downstream than in the previous two cases, but there is a second distinct peak on the windward side of the crest, just downstream of the zero upcrossing at $\phi = 0.33$. There is actually a small peak in the first two cases between the trough and zero

upcrossing, but not so distinct as in the present case. It is the corresponding peak as the whole pressure distribution appears to have been shifted downstream by approximately $\phi = 0.125$. There are correspondingly minima above the wave crest and trough. The magnitude of the shear stress in this case is small, and the shear stress is positive at all phases, suggesting that the wind-induced surface current is not so great in this case, causing little of the shear stresses in the airflow to be released at the interface. Further consideration of the surface stresses is made in Chapter 6, in relation to the wind-induced surface currents, and in Chapter 8, where the resulting water surface roughness is examined.

6. WATER KINEMATICS MEASUREMENTS

In the two preceding chapters, the kinematics of the airflow above water waves were examined. The velocity data was decomposed into its mean, wave-induced and turbulent components, and presented in a wave-following frame. This chapter investigates the kinematics in the water beneath the airflow, and uses analysis methods and a co-ordinate frame similar to those used in the airflow. The time averaged velocities or currents are first presented, and analysed using the boundary layer theory introduced in Chapter 5. The phase averaged velocities are then analysed, examining the modified wave motion and attempting to identify the phase varying wind-induced water velocities.

6.1 Experimental Programme

The horizontal and vertical velocities in the water flow under the 1 Hz, 22.5 mm amplitude long waves have been measured, with an overlying airflow of $U_\infty = 3.1$ and 5.1 m/s, and with no airflow. The two airflow cases correspond to the conditions used for the wind velocity measurements presented in Chapter 4. The data was collected at the same fetch as for the air measurements, and was analysed in a similar way. In addition to the above measurements, the near-surface horizontal velocities in the water were measured in the absence of the mechanically generated waves, with only wind-generated waves for free-stream velocities of $U_\infty = 2.4$, 3.1 and 5.1 m/s.

6.2 Experimental Methods and Data Analysis

The experimental methods used to measure the kinematics under the wave were similar to those used in the air flow. Velocity measurements were made using the laser Doppler anemometer system which was used for the airflow measurements, with 'Timron Supersilk', a fine white powder, to seed the water flow. A relatively small but uniform amount of seeding was found to give the optimal signal-to-noise ratio. As for the air flow measurements, the system was allowed to run for at least one hour before any data was sampled.

Velocity measurements were collected from 20 mm above still water level, just beneath the wave crest, down to the bed of the tank. A nominal sampling frequency of 256 Hz was adopted but, towards the bed of the tank where the velocities were very small, the maximum data rate obtainable was only approximately 100 Hz. The target sampling frequency of 256 Hz corresponded to a resolution of 256 samples per wave for the mechanically generated waves, and 50 samples per wave for a 5 Hz wind-wave. Each velocity was sampled for a total of 200 seconds. Data was sampled at a vertical spacing of 2.5 mm close to the water surface, the region of greatest interest, and at 20 mm towards the bed, the spacing increasing incrementally between. At each elevation, the horizontal and vertical velocity components were measured in turn, together with the water surface elevation.

The measured velocities were decomposed using phase averaging routines similar to those used in the air flow. The time averaged, phase averaged and turbulent velocities are all presented in subsequent sections. The velocities were transformed in to a new co-ordinate frame, similar to that used for the airflow, defined by:

$$t = t^* \qquad x = x^* \qquad y^* = y - \tilde{\eta}\frac{\sinh k(d+y)}{\sinh kd} \tag{6.1}$$

where d is the still water depth and y^* is defined as being positive upwards from the water surface, so the bed of the flume is at $y^* = -d$. The co-ordinate system used is illustrated in Figure 6.1 overleaf.

6.3 Time Averaged Horizontal Velocity Profiles

The time averaged horizontal velocity profiles for wind-generated waves, for long waves in the absence of wind, and for combined wind-generated and long waves have been calculated. The time averaged horizontal velocity in a water flow is normally referred to as the current velocity. The wind-driven currents in the absence of mechanically generated waves were measured for two reasons: firstly, to provide validation for the velocity measurements, since a number of existing sets of measurements for wind-driven

currents in the absence of long waves were available; and secondly, measurements in the absence of the long waves could be made very close to the water surface, whereas in the presence of the long waves, measurements could be made, at best, to within 5 mm of the instantaneous water surface, due to the set up time of the system. It was thought that some indication of the flow behaviour very close to the water surface for the combined wind and long wave cases could be inferred from the near-surface wind only measurements.

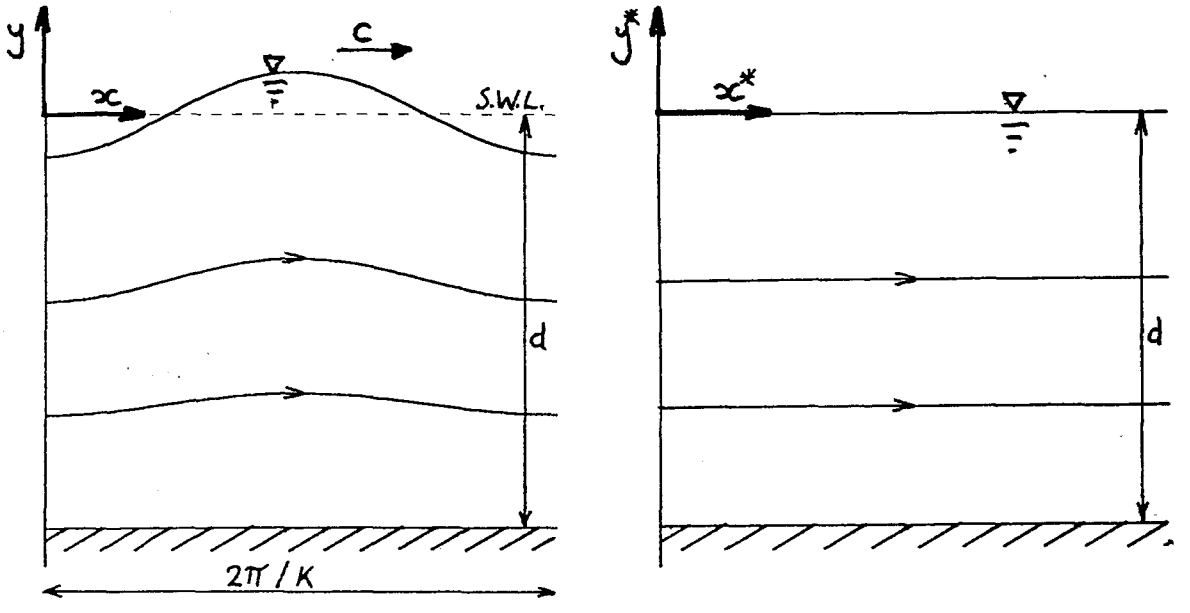


Figure 6.1: Co-ordinate frame beneath the water waves

The measured wind-driven current in the presence of the long waves includes the effect of a back flow associated with the wave motion. The particle orbits in a wave are not closed, and there is a drift velocity, the Stokes' drift, associated with the wave motion. This drift velocity is a Lagrangian quantity. The laser is at a fixed point in space, therefore measuring in an Eulerian frame, and unable to measure the Lagrangian Stokes' drift current. Instead, the laser measures the backflow which results from the Stokes' drift. (This backflow will also be present in the wind only case but will be very small). The measured wind-generated current in the presence of the wave is therefore the sum of the wind-generated current and the back flow associated with the wave motion. To a first order of approximation, the actual wind-generated current is the difference between the measured current in the presence of wind and waves, and the back flow measured

under the mechanically generated waves in the absence of an overlying airflow. It is assumed, at least as far as the mean flow is concerned, that there is no interaction between the wave and the wind-generated current, and that the wind-generated current itself does not generate a significant backflow in the wave flume, so it may then be assumed that the Stokes' drift and associated backflow will remain unaltered.

6.3.1 Wind only Currents

The wind-driven current profiles, in the absence of the long waves, are presented in Figure 6.2 for free-stream velocities $U_\infty = 2.4$, 3.1 and 5.1 m/s. The velocities were measured only in the upper region of the flow, from within 1 mm of the water surface, down to an elevation where the current was less than 5 mm/s. The profiles are presented in Cartesian co-ordinates which, in the absence of the long waves, are equivalent to the transformed co-ordinates defined in equation 6.1. However, for data close to still water level for high wind speeds with correspondingly large wind-generated waves, time averaged velocities in a Cartesian frame are not meaningful, since the velocity records are not continuous.

From Figure 6.2a, it is clear that the greater the free-stream velocity, the greater the surface velocity, and the larger the near-surface velocity gradients. In Figure 6.2b, the data measured in the top 5 mm of the velocity profiles plotted in linear co-ordinates show that close to the water surface, for the slower wind speed cases, the profiles tend towards a straight line. This behaviour is consistent with the existence of a boundary layer, the data demonstrating recognisable viscous and inertial sub layers. Assuming that the flow can be considered hydro-dynamically smooth, then, for the inertial sub layer, the velocity profile is given by the law of the wall, which may be expressed as

$$\frac{U}{u_*} = -\frac{1}{\kappa} In\left(-\frac{y^* u_*}{\nu}\right) + C \qquad (6.2)$$

A least-squares curve-fitting routine was used to curve fit the measured velocity profiles. Figure 6.2c applies semi-log co-ordinates and shows that the profiles exhibit

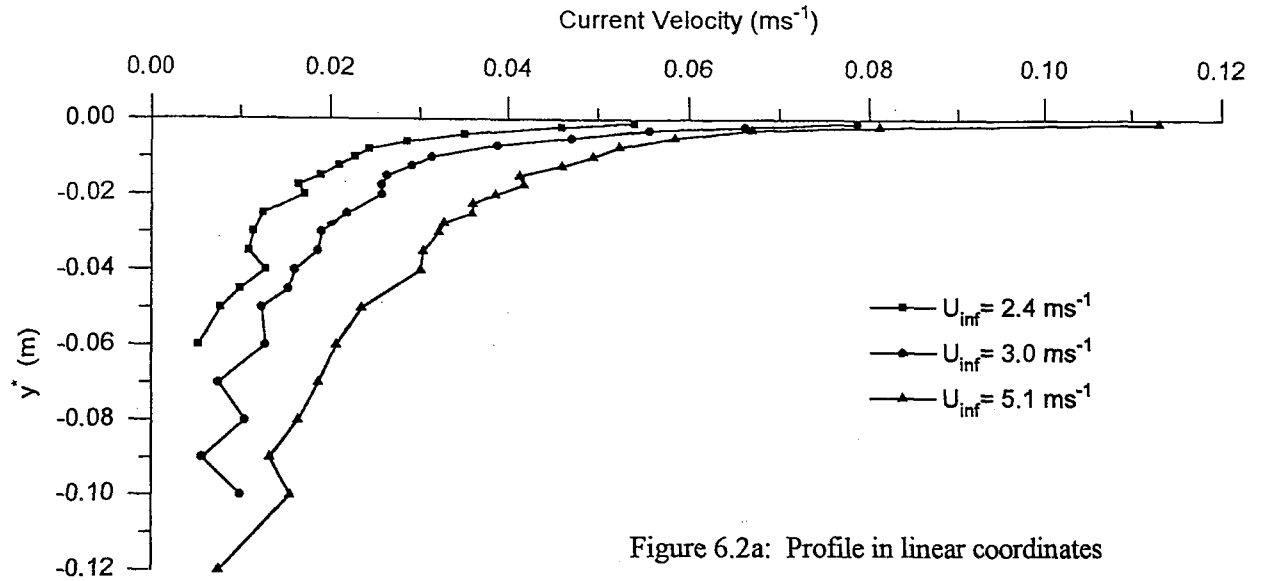


Figure 6.2a: Profile in linear coordinates

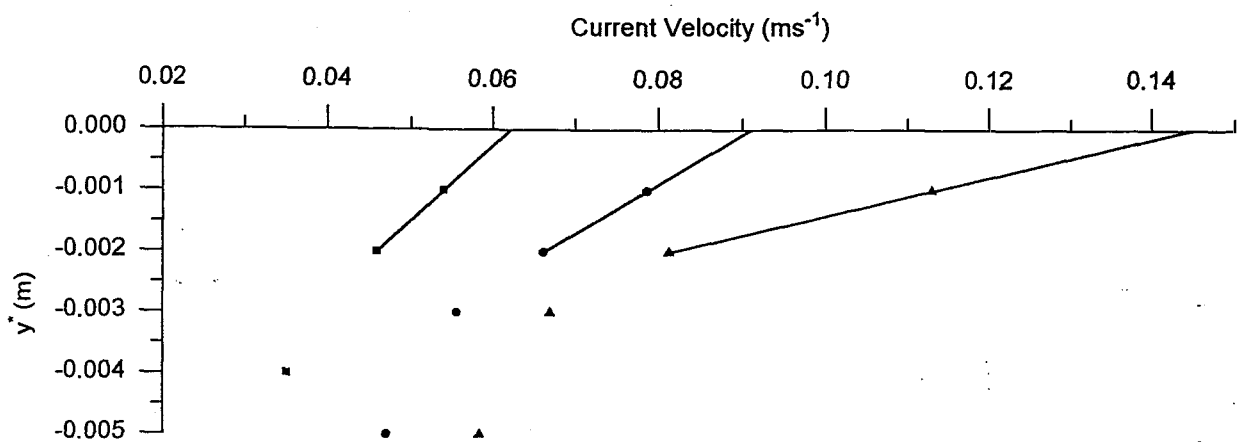


Figure 6.2b: Near surface profile in linear coordinates

Figure 6.2c: Near surface profile in semi-log coordinates

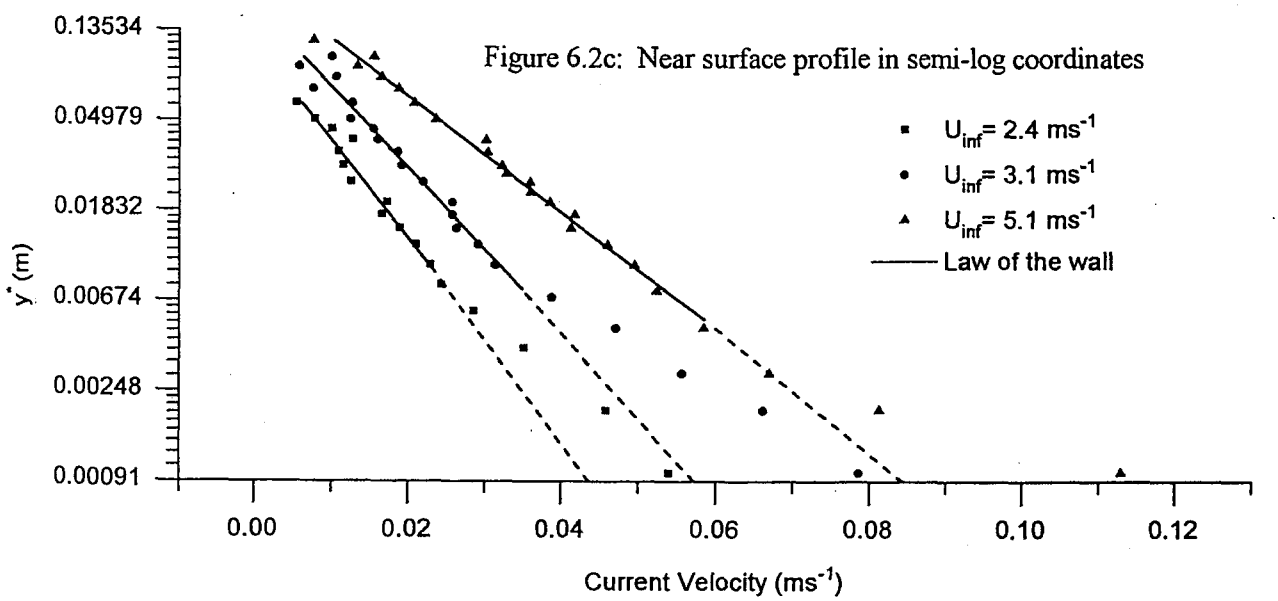


Figure 6.2: Wind generated currents in the absence of waves

log-linear behaviour over a considerable proportion of their depth. The values of u_* and C obtained by fitting the data to equation 6.2 are presented in Table 6.1.

U_∞ (m/s)	u_* (m/s)	C	$30\nu/u_*$ (m)	$5\nu/u_*$ (m)
2.4	0.00372	14.8	0.00923	0.00154
3.1	0.00447	16.3	0.00768	0.00128
5.1	0.00622	17.9	0.00552	0.00092

Table 6.1: Inertial sub layer parameters from law of the wall curve-fit

The profile analysis was undertaken using data starting from the lower limit of the inertial sub-layer, at $y^* = 30\nu/u_*$ (Table 6.1). From boundary layer theory, the inertial sub layer extends up to $y^* = 0.1 - 0.2\delta$, but in this case it is difficult to identify the thickness of the boundary layer δ. If it is assumed that the boundary layer thickness is approximately $\delta \approx 0.10$ m, then the outer edge of the inertial sub layer may be expected to be at approximately $y^* = 0.02$ m. Log-linear profiles in this region provided a good fit to the measured velocity data, and there appeared to be little deviation from the log-linear plot at even greater depths. The free stream velocity in the water flows is zero, and there is no evidence of wake-type behaviour, although the velocities at greater depths in the 'wake' region are very small and subject to large errors.

The friction velocity (Table 6.1) increases with increasing wind speed, corresponding to the observed greater near-surface velocity gradients in the water flow. This is to be expected due to the increased shear stress exerted at the surface by the faster airflow, and the larger induced surface velocities. The values of the constant C are large and increase with increasing wind velocity. Unlike the values of C in the airflow, the increasing height of the wind-waves does not appear to cause C to reduce. This is due to the greater depth of the viscous sub layer in the water than in the airflow, so that a given roughness height would have less effect in the water than in the air. The roughness Reynolds number for a given roughness height would be less in the water flow than in

the air. The large values of C are a result of the moving surface, and their increase with wind speed is due to the observed corresponding increase in the surface velocity. The fact that the large increase in the current between $U_\infty = 3.1$ and 5.1 m/s is not reflected in a large increase in C perhaps suggests that the increased roughness does have some effect. Cheung and Street (1988) find that for $U_\infty > 3.2$ m/s the profiles lie in the fully rough regime, so perhaps roughness effects should be considered for the fastest case.

The height of the viscous sub layer, $y^* = 5\nu/u_*$ is given in Table 6.1. The lowest measured velocities lie within the viscous sub layer. The velocity profile in the viscous sub layer is linear, and the gradient is related to the friction velocity by

$$U_s - U = \frac{u_*^2}{\nu} y^* \tag{6.3}$$

where U_s is the surface current velocity. The depth of the viscous sub layer is 1-2 mm, and therefore only a single data point in each case lies within the viscous sub layer. However, the data at $y^* = 2$ mm is only just in the buffer layer, at which point the gradient of the velocity profile would be expected to be little different to that in the viscous sub-layer. The data points at $y^* = 1$ and 2 mm were therefore used to calculate the approximate gradient of the velocity profile in the viscous sub layer, and to extrapolate for the values of the surface current. There are potentially large errors associated with this approach, but it does afford a means of assessing the validity of boundary layer theory, which was not possible using the airflow measurements. The values of the friction velocity and surface drift are presented in Table 6.2, and compared with those obtained from analysis of data in the inertial sub-layer.

U_∞	Viscous sub layer		Inertial sub layer	
(m/s)	u_* (m/s)	U_s (m/s)	u_* (m/s)	U_s (m/s)
2.4	0.00304	0.0621	0.00372	0.0737
3.1	0.00377	0.0910	0.00447	0.0953
5.1	0.00603	0.1448	0.00622	0.1422

Table 6.2: Viscous and inertial sub layer parameters

The values of the friction velocity found using equation 6.3 show remarkably good agreement with the friction velocities calculated from the inertial sub-layer: the greatest difference is 18% for the $U_\infty = 2.4$ m/s case, and only 3% for the $U_\infty = 5.1$ m/s case. The values of the friction velocity calculated from the gradient between the two uppermost velocity measurements are less than those evaluated in the inertial sub-layer, since the lower of the two uppermost points lies within the buffer layer, and the velocity gradients in the buffer layer will be less than for those in the viscous sub layer. The values of the surface current calculated by extrapolation from the two uppermost velocity measurements would therefore also be expected to be too small. However, the reasonable agreement between the values of the friction velocity calculated from each region provides a useful confirmation of the applicability of boundary layer theory.

There are a number of sources of potentially significant errors associated with using the two uppermost velocity measurements to calculate the surface current velocity. As already discussed, the measurements at $y^* = 2$ mm lie in the buffer layer, rather than within the viscous sub-layer. Attempting to take measurements at such close spacings in y^* makes laser alignment errors more significant. The spatial resolution of the laser measuring volume itself starts to become a limiting factor. In addition, the velocity measurements are subject to errors resulting from an intermittent signal and seeding difficulties which are encountered when measuring velocities very near the surface. An alternative approach to deducing the surface current from the velocity data is based upon linking the velocity profile in the viscous sub layer to that in the inertial sub layer.

It allows calculation of the surface current using data from the inertial sub-layer, so eliminating the need for data very close to the water surface which, as discussed, may not be wholly reliable in the present case, and which could not be measured in the presence of the long waves. If is assumed that the inertial and viscous sub-layer profiles intersect at $y^* = 11\,\nu/u_*$ (Tennekes and Lumley, 1992), the linear profile in the viscous sub layer (equation 6.3) can be equated with the logarithmic profile in the inertial sub layer (equation 6.2). An expression for the surface current can therefore deduced:

$$U_s = u_*\left(-\frac{1}{\kappa}In(11) + C + 11\right) \tag{6.4}$$

The values of the surface current calculated using this expression are also given in Table 6.2, and show good agreement with the values deduced from the viscous sub layer. For $U_\infty = 3.1$ and 5.1 m/s, the agreement was better than 5%, but for $U_\infty = 2.4$ m/s the difference was 15%, corresponding to the large discrepancy in the friction velocities, which it was thought was due to poor near-surface velocity data. However, the reasonable agreement between the values suggests that this approach is valid, and is more likely to produce reliable surface currents since it is based upon a relatively large number of data points which are not very close to the water surface. The values found using this approach are therefore adopted for use in the subsequent work, and this method is used to deduce the surface currents in the presence of the long waves.

The value of the surface drift is often expressed in non-dimensional form, either in respect to the free-stream velocity or the friction velocity in the air. These values are given below in Table 6.3, taking the surface velocity values calculated using equation 6.4, and are compared with values obtained by other workers:

U_∞ (m/s)	U_s (m/s)	u_{*a}(m/s)	U_s/U_∞	U_s/u_{*a}	U_s/U_∞ [1]	U_s/u_{*a} [2]
2.4	0.0737	0.1097	0.0307	0.672	0.0310	0.52
3.1	0.0953	0.1256	0.0307	0.759	0.0324	0.52
5.1	0.1422	0.1965	0.0279	0.724	0.0355	0.52

[1] Wu (1975), [2] Cheng & Mitsuyasu (1992)

Table 6.3: Comparison of measured surface velocity parameters.

The values of U_s/U_∞ are smaller than those found by Wu (1975) by approximately 15%, probably due to the shorter fetch wind tunnel used here. The ratio U_s/u_{*a} is found to have an average value of approximately 0.52 by both Cheng & Mitsuyasu (1992) and Wu (1975), but both reported a large amount of scatter in the data with no systematic variations. The values for U_s/u_{*a} calculated from the data are greater than this value, but are within the range found by both sets of authors.

Having determined the surface currents, the values of the constant C can be reconsidered. The values of the constant presented in Table 6.1 include the effect of the surface current, in that the velocity profiles are offset by the value of the surface current, and this offset is included in the constant. To eliminate this variation, the law of the wall can be expressed in the form

$$\frac{U_s - U}{u_*} = \frac{1}{\kappa} In\left(\frac{yu_*}{\nu}\right) + C' \tag{6.5}$$

where C' is the constant with the effect of the surface current removed. The values are given in Table 6.4 for both the surface current deduced from the viscous sub layer, and from the inertial sub layer.

			Viscous sub layer		Inertial sub layer	
U_∞ (m/s)	C	u_* (m/s)	U_s (m/s)	C'	U_s (m/s)	C'
2.4	14.82	0.00372	0.0661	2.95	0.0737	5.00
3.1	16.31	0.00447	0.0961	5.19	0.0953	5.00
5.1	17.86	0.00622	0.1422	5.00	0.1422	5.00

Table 6.4: Corrected values of the 'constant' C.

The values of C' calculated by extrapolation from the velocity measurements in the inertial sub layer are all equal to 5.0 as a result of the assumptions made for the height of the intersection of the viscous and inertial sub-layer velocity profiles. However the values calculated based upon data from the viscous sub layer are also approximately 5.0, except for the $U_\infty = 2.4$ m/s case. As already discussed, there appears to be a problem with the velocity data in this case and, if the fastest wind speed case can be classified as smooth, then it would be expected that the slowest case may also be classified as smooth. The values for $U_\infty = 3.1$ and 5.1 m/s show that the flow is aerodynamically smooth, and the use of the smooth form of the velocity equations is justified a posteriori for all cases. Although the value of C' is smaller than expected for $U_\infty = 2.4$ m/s, its value still suggests that the smooth form of the law of the wall should be used.

The values of the friction velocity calculated in the air can be compared with those in the water by calculating the surface shear stresses. Although the values of the friction velocity are very different due to the difference in the viscosity of air and water, the shear stress across the air-water interface should be constant. The values of the shear stress calculated from each side of the interface and averaged over a whole wave cycle are compared in Table 6.5.

U_∞ (m/s)	$\rho_w u_{*w}^2$ (N/m^2)	$\rho_a u_{*a}^2$ (N/m^2)
2.4	0.0138	0.0156
3.1	0.0200	0.0205
5.1	0.0387	0.0502

Table 6.5: Surface stresses

The stresses across the interface appear to be approximately constant for the $U_\infty = 2.4$ and 3.1 m/s cases, the shear stresses being within approximately 10%, with the values calculated in the air being greater than those from the water. For the $U_\infty = 5.1$ m/s case, the air shear stress is more than 20% greater than that in the water. The agreement is still quite good considering the possible inaccuracies.

Figure 6.3 shows the root mean square horizontal turbulent velocity profiles with depth for each velocity case. The turbulent fluctuations appear to be a maximum at approximately $y^* = 30\nu/u_*$, the level of the expected interface of the buffer layer and inertial sub-layer. It was explained in Chapter 5 that in the viscous sub layer, the shear stresses are entirely viscous, and in the inertial sub-layer, the stresses are entirely inertial. In the buffer layer the two swap over, so at $y^* = 30\nu/u_*$, the lower edge of the inertial sub-layer, the inertial stresses are a maximum, but reduce to zero at $y^* = 5\nu/u_*$. This suggests that the flow may be regarded as hydraulically smooth. It also shows clearly that a boundary layer exists, and that the theory is applicable.

Figure 6.4 shows the vorticity profiles for the three cases. The vertical velocities were not measured in this study, so the vorticity is approximated by the first vorticity term

$$\omega \approx -\frac{\partial u}{\partial y^*} \tag{6.6}$$

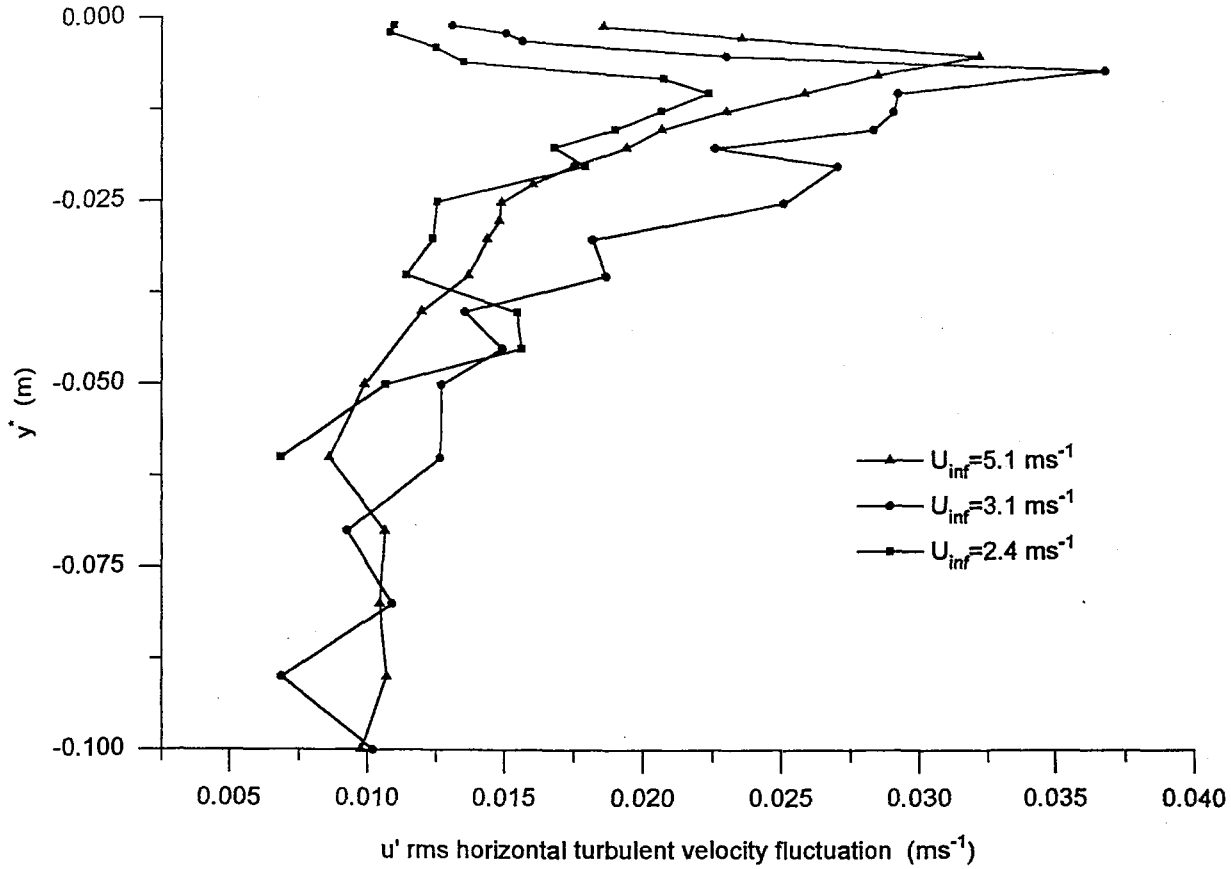


Figure 6.3: Turbulence profiles u' rms

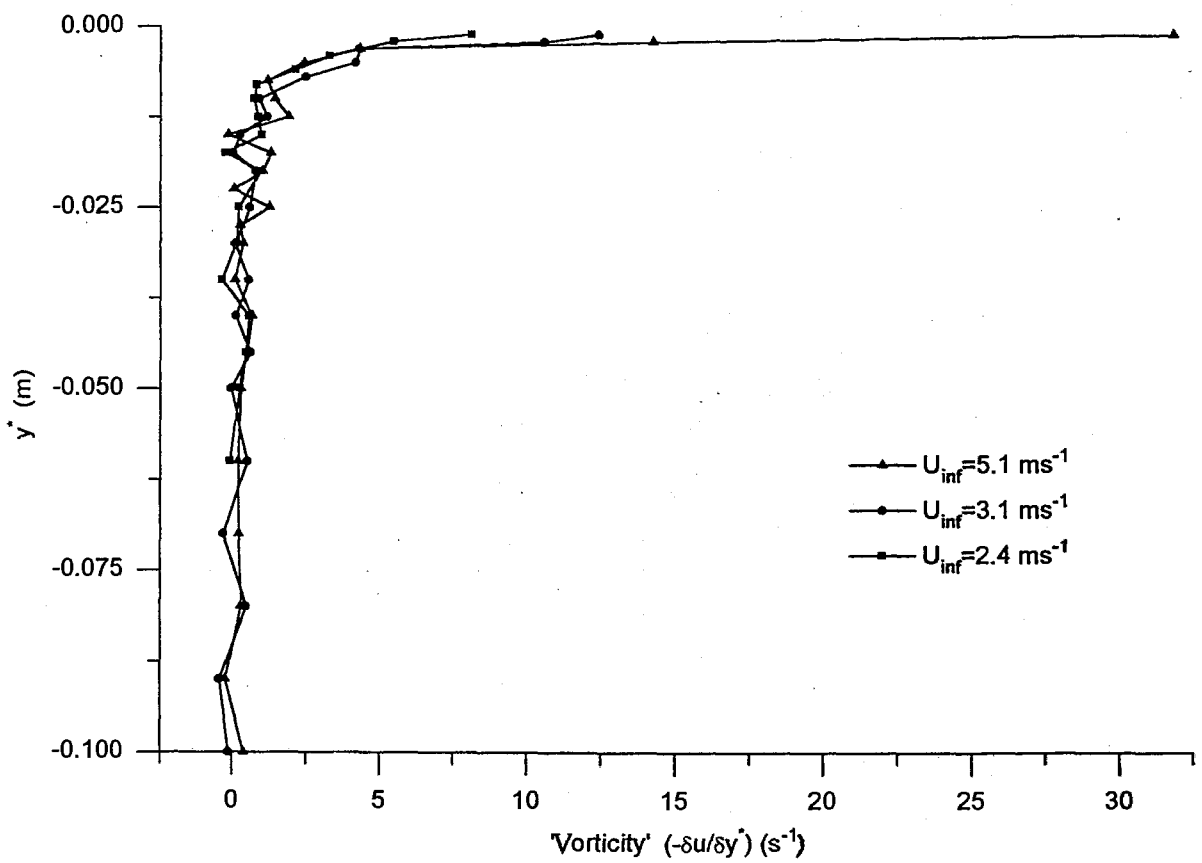


Figure 6.4: Vorticity profiles

which provides some indication of the large vorticity variation with depth, particularly close to the water surface. The vorticity is further discussed in Chapter 7.

6.3.2 Wave only Current.

The current velocity profile measured under the mechanically generated waves in the absence of an overlying airflow is shown in Figure 6.5. The profile is presented in transformed co-ordinates, with the velocities being measured to within 5 mm of the water surface. The profile is for the upper part of the flow only, corresponding to the observed region of significant wind-driven currents. The current under the mechanically generated waves is negative in the upper region of the flow, so the velocities are in the opposite direction to the propagation of the waves. The magnitude of the back flow reduces with increasing depth beneath the water surface, and is of similar form to the profiles presented by Swan (1990). Although the profiles over the whole depth have been found by others (including Swan, 1990) to be exponential in form, it was considered that, in this upper part of the flow, the best fit to the data was a linear plot. A linear least squares straight line fit to the measured current is shown dotted in Figure 6.5.

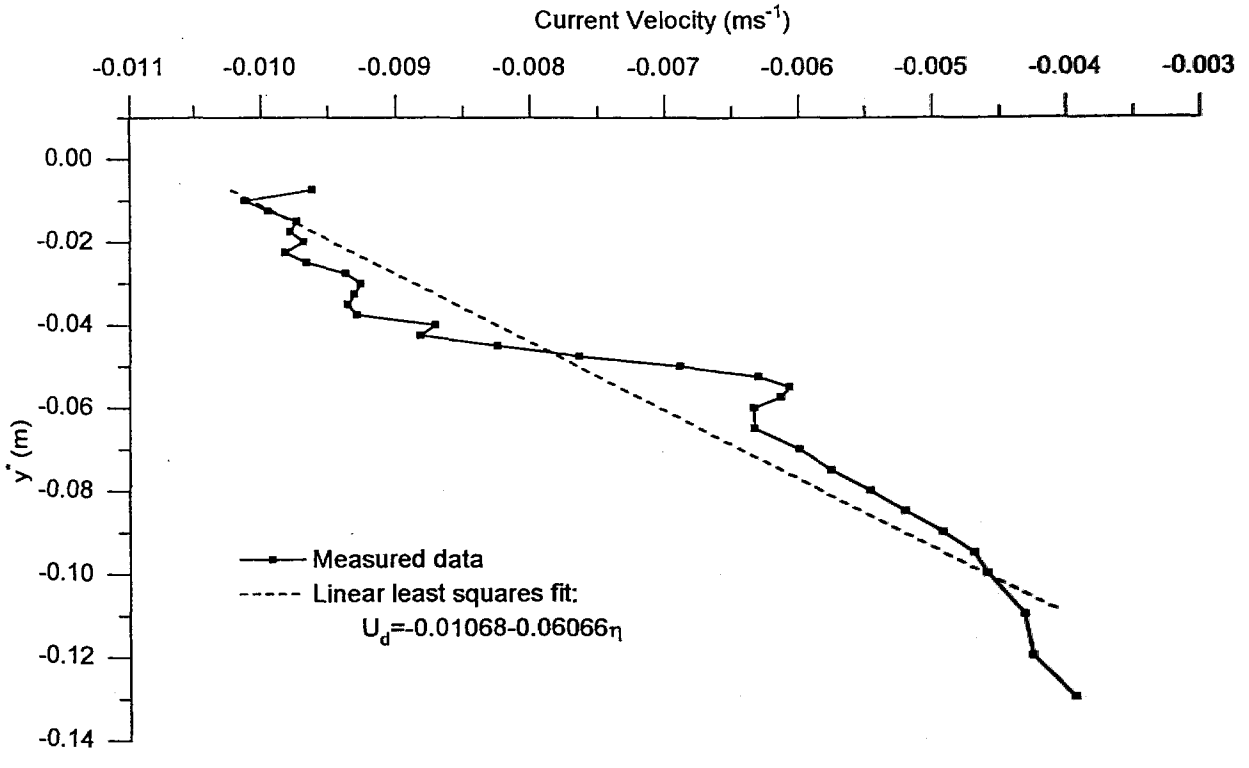


Figure 6.5: Wave only current

6.3.3 Currents in Combined Wind and Waves

The wind-generated current profiles for free-stream velocities $U_\infty = 3.1$ and 5.1 m/s in the presence of mechanically generated waves are presented in Figure 6.6. The velocities have been corrected for the back flow associated with the long wave motion, by subtracting the best-fit current profile for the wave in the absence of wind (Figure 6.5). The corrected profiles are therefore the average effect of the wind on the water over the whole wave cycle, and are comparable with the wind only velocity profiles presented in Figure 6.2.

The current profile for $U_\infty = 5.1$ m/s case shows a much thicker highly sheared region than that for the $U_\infty = 3.1$ m/s case. This is illustrated by plotting the profiles in log-linear co-ordinates (Figure 6.6c). Using equation 6.2, the friction velocity and constant C were calculated (Table 6.6) by linear least-squares fitting to the log-linear region of each profile. Data from the bottom of the inertial sub layer, $30\nu/u_*$ up to the limit of the apparent log-linear region was used in the curve fits, as for the wind only profiles.

U_∞ (m/s)	u_* (m/s)	C	$30\nu/u_*$ (m)	$5\nu/u_*$ (m)
3.1	0.00373	13.1	0.00726	0.00121
5.1	0.00595	15.5	0.00578	0.00096

Table 6.6: Inertial sub layer best-fit parameters and layer thickness

The friction velocity increases with the free stream air velocity, as does the value of C, reflecting the increasing surface current. The trends are similar to those for the wind only waves, but the values of both u_* and C are smaller than for the wind only cases. The values of the friction velocity are approximately 5% less for the combined wind and waves case than for the corresponding wind only case, and the values of C are up to 20% less. Cheung and Street (1988) also find this and suggest that the wave provides some sheltering effects from the wind in the wave trough, leading to a lower mean drift velocity. However, Cheung and Street (1988) present their results in a Cartesian frame,

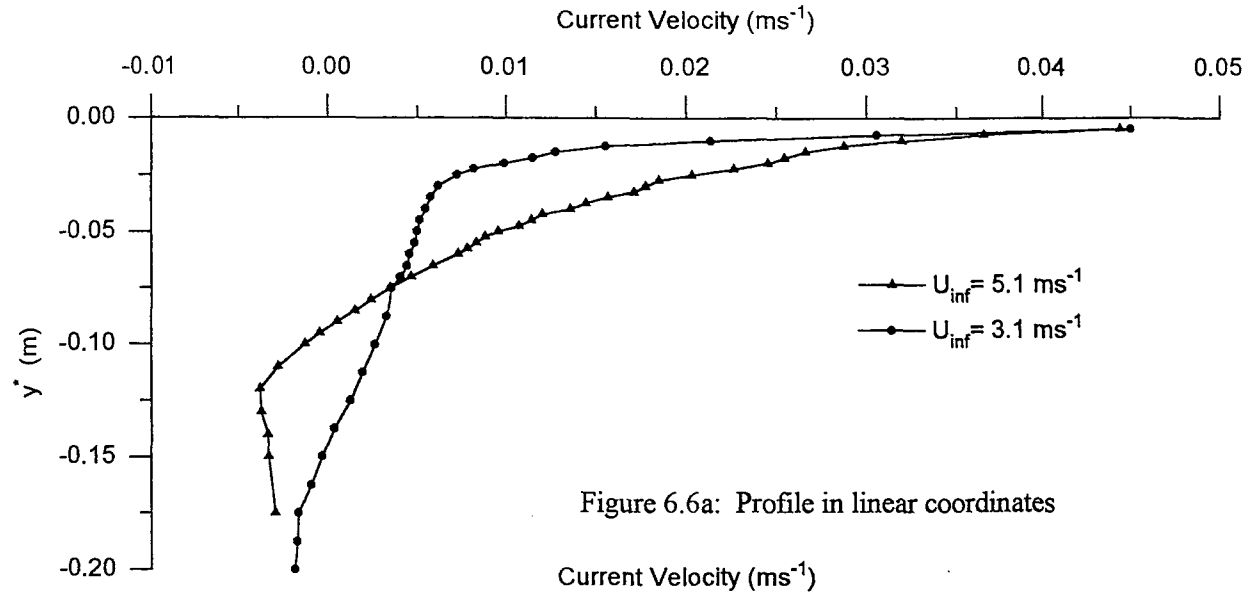


Figure 6.6a: Profile in linear coordinates

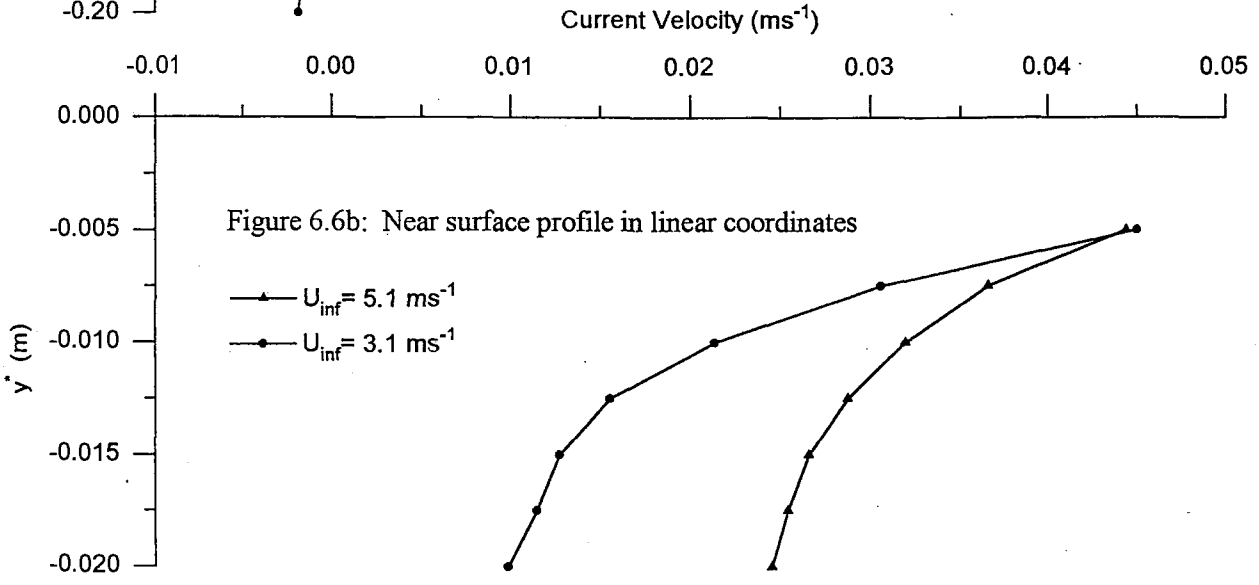


Figure 6.6b: Near surface profile in linear coordinates

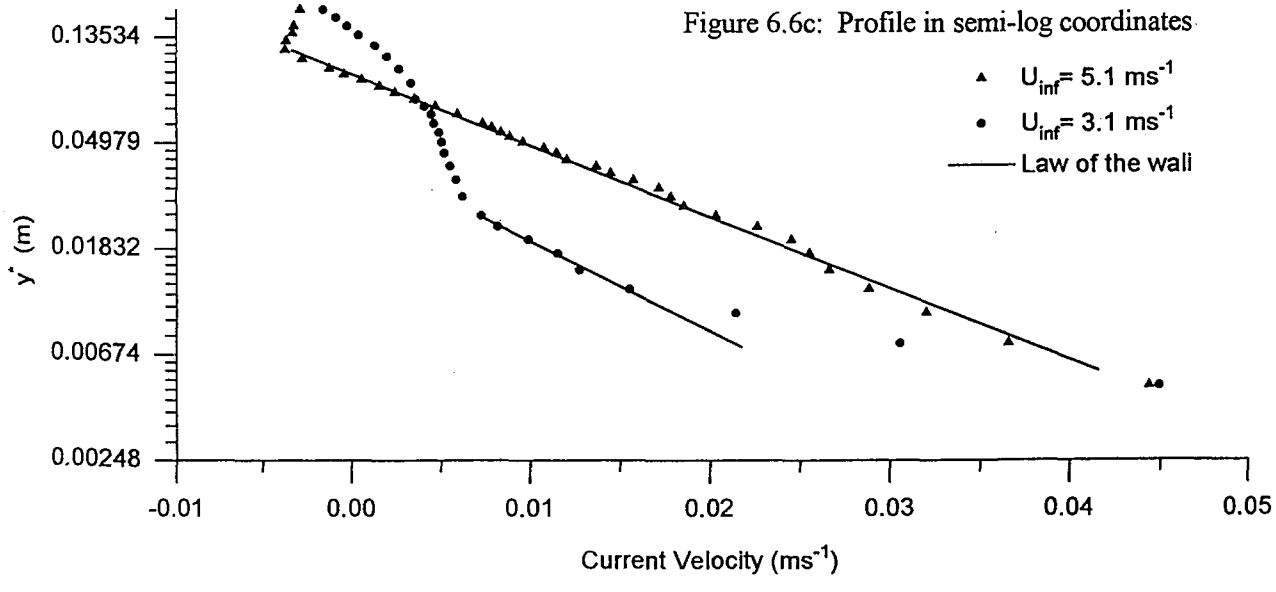


Figure 6.6c: Profile in semi-log coordinates

Figure 6.6: Wind generated currents in the presence of long waves

and sample no data above trough level, so their results are questionable. The smaller values of C in the combined wind and waves cases suggest that the corresponding surface current is less than for the wind only case, supporting the idea of a sheltering effect.

A key quantity to be determined from the water velocity measurements is the magnitude of the surface current, which can be used to relate the surface stresses and roughness parameters. Velocities could only be measured to within 5 mm of the water surface in the presence of the long waves so, unlike in the wind only cases, there was no data in the viscous sub-layer. Linear extrapolation of the profiles would lead to the surface velocity being significantly under-estimated. If the structure of the flow for the combined wind and wave cases can be assumed to be similar to that for the wind only cases, then the velocity profiles in the viscous sub layer and the inertial sub layer can be linked at $y^* = 11\nu/u_*$, and equation 6.4 used to calculate the surface velocity. This approach was validated for the wind only cases where data could be measured in the viscous sub layer (section 6.3.1), and it should also be applicable here. The values of the surface current predicted using equation 6.4 are given in Table 6.7.

U_∞ (m/s)	U_s (m/s)	u_{*_w} (m/s)	u_{*_a} (m/s)	U_s/U_∞	U_s/u_{*_a}	U_s/u_{*_a} [1]
3.1	0.0856	0.00373	0.1157	0.0276	0.740	0.46
5.1	0.1221	0.00595	0.1940	0.0239	0.629	0.46

[1] Cheng & Mitsuyasu (1992)

Table 6.7: Surface current and non-dimensional parameters

The magnitudes of the surface currents for the combined wind and waves cases are approximately 15% less than those for the wind only cases. The values of the friction velocity in the airflow are smaller in the combined wind and waves cases than in the wind only cases, which may explain, at least in part, the reduced current. The reduction in the friction velocity however is less than the reduction in the surface current, so the ratios of U_s/u_{*_a} are less in the present cases than for the wind only cases. Wu (1975)

does not consider the combined wind and waves case, but Cheng & Mitsuyasu (1992) found that the ratio U_s/u_{*a} is reduced in the presence of the long waves, compared with the wind only cases, although they considered the difference to be due to changed experimental conditions. The observed values of U_s/u_{*a} are again significantly greater, by up to 30%, compared with the values obtained by Cheng & Mitsuyasu (1992). The ratios are smaller than those for the wind only case, by 2.5% for $U_\infty = 3.1$ m/s, and 12.5% for $U_\infty = 5.1$ m/s. This suggests that relative to the friction velocity, the surface current is less than in the wind only cases. Although there is some uncertainty regarding the back flow due to the wave motion, since the back flow in the waves only case is almost an order of magnitude less than the surface wind-induced currents, this effect is not regarded as significant.

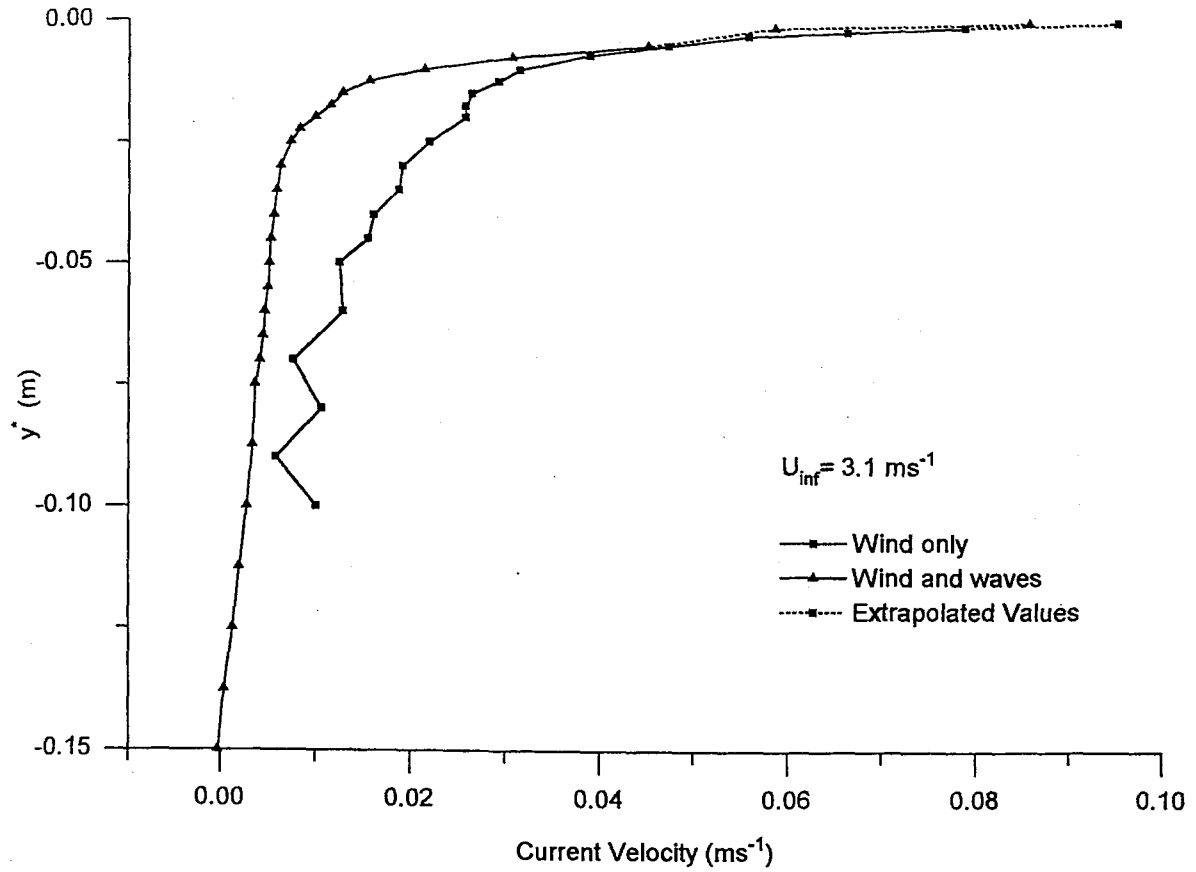
The current profiles for each velocity case, in both the presence and absence of the mechanically generated waves, are compared in Figure 6.7. The surface velocities obtained by extrapolation using equation 6.4 are also shown. The wind only currents are clearly more highly sheared close to the surface than the combined wind and waves profiles, and the values are correspondingly greater at given elevations. The effect of the back flow and the resulting profiles at greater depth is difficult to quantify.

6.4 Phase Averaged Velocities

The phase averaged velocity profiles at the wave crest and the trough, and the amplitude of the velocity variation are first examined. The nature of the near-surface flow in the water is then investigated in detail, by looking at the variation of the wave-induced velocity with the phase of the underlying long wave.

6.4.1 Phase Average Velocity Profiles

The phase averaged horizontal velocity profiles at the wave crest and trough are shown in Figure 6.8 for mechanically generated waves in the absence of wind, and with overlying airflows of $U_\infty = 3.1$ and 5.1 m/s. The profiles are shown for the upper part of the flow only, corresponding to the region in which the wind-driven currents are



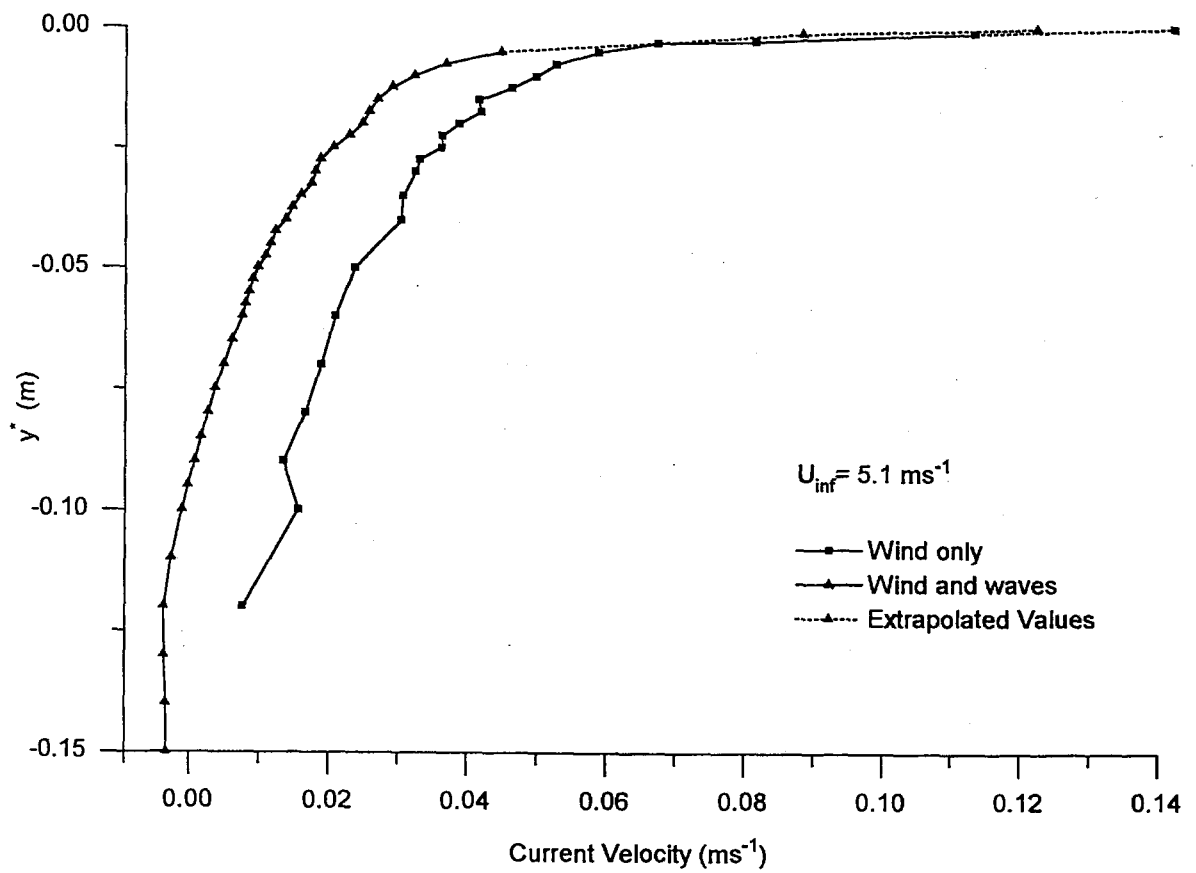


Figure 6.7: Comparison of wind only and combined wind and waves current profiles

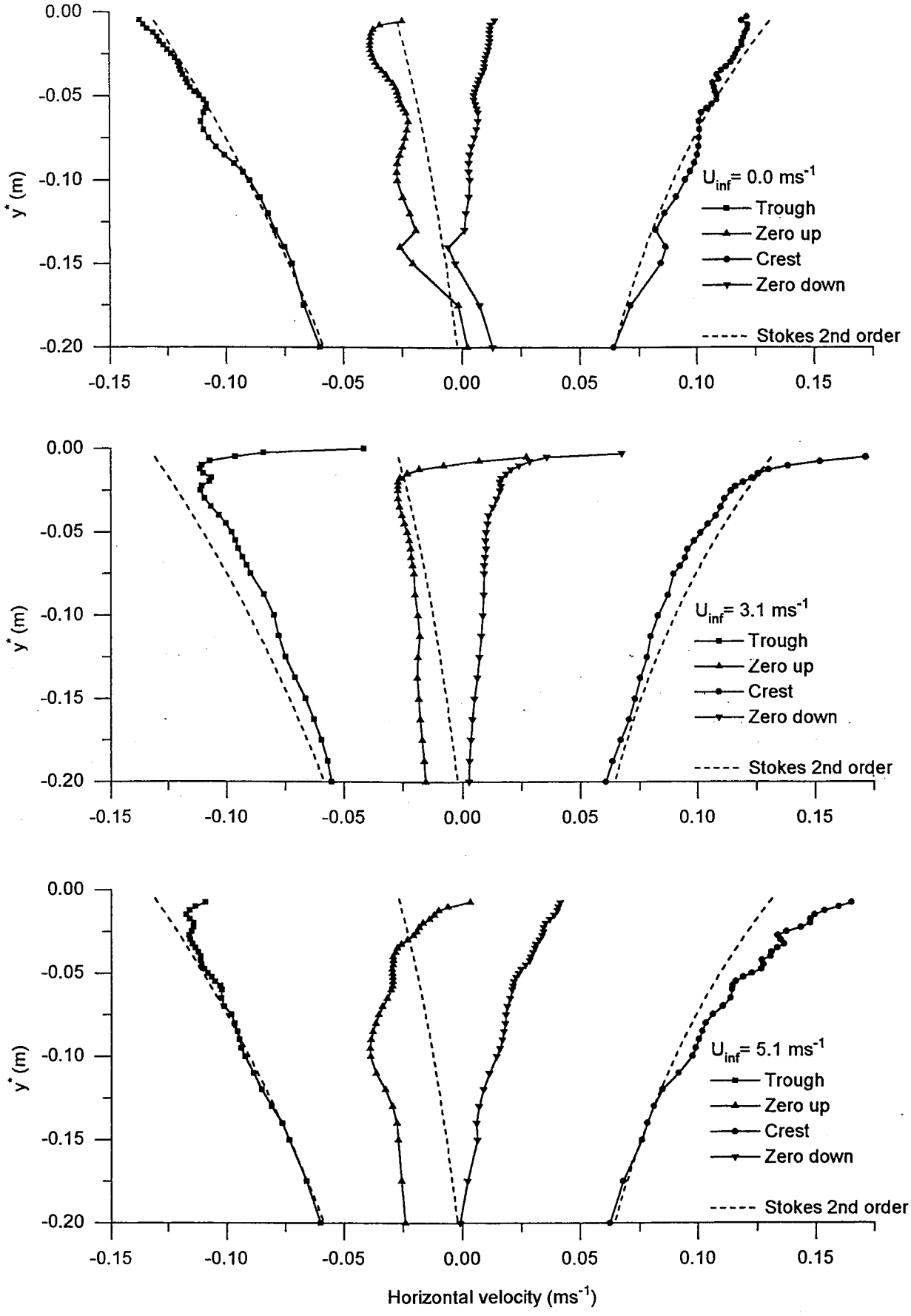


Figure 6.8: Phase averaged horizontal velocity profiles for wind and wave U_{inf}= 0.0, 3.1 & 5.1 ms^{-1}

significant. For each case, the measured profiles are compared with the linear sum of the best-fit back flow for the wave only case (Figure 6.5) and the kinematics predicted by Stokes' second order irrotational wave theory, calculated using the measured wave parameters. This allows a direct comparison between the measured velocities and the irrotational velocities for each case.

For the long waves in the absence of wind, the crest and trough profiles show good agreement with theory. The discrepancies between theory and the measured values correspond to the differences apparent between the time averaged measured back flow and the linear fit to the measured back flow (Figure 6.5). This is confirmed by calculating the velocity amplitude, taken as half the difference between the crest and trough values, which shows excellent agreement with the amplitude calculated from second order irrotational theory (Figure 6.9a).

The phase averaged velocity profiles for the two combined wind and waves cases clearly demonstrate the effect of the wind-driven current (Figures 6.8b and 6.8c). Significant deviations from the irrotational velocities are observed for both wind speed cases. Beneath the wave crest, close to the water surface, there is a significant increase in the velocity in each case. Beneath the trough, however, the effect of the wind-driven current is to reduce the magnitude of the orbital velocity, since the wave velocity and current act in opposite directions. In each case, the largest negative velocity is at approximately $y^* = -0.02$ m, above which the value of the velocity increases, so reducing the velocity magnitude. The velocity measurements closest to the surface beneath the troughs are negative in each case but, at the surface itself, the profiles in Figures 6.8b and 6.8c, together with the time averaged extrapolated current profiles in Figure 6.7, suggest that the velocities could be close to zero or even positive. It seems likely that, for the $U_\infty = 5.1$ m/s case, the surface velocity will be positive at all phases of the wave cycle.

The velocity profiles for the $U_\infty = 5.1$ m/s case (Figure 6.8c) show that the velocity is increased significantly beneath the wave crest from the surface to approximately $y^* = -0.10$ m. The increased velocity at the crest is much greater than the reduction in

magnitude at the trough over this region, although the difference at the water surface itself cannot be assessed. This asymmetry is perhaps as anticipated, since the orbital velocity and current at the crest are in the same direction and may be expected to have a greater effect on the velocity magnitude than at the trough, where the current is in the opposite direction to the orbital velocities. In addition, however, it would seem unlikely that the wind-induced 'current' at the crest would be exactly equal to that at the trough, due to the variations with phase of the airflow velocities and resulting surface stresses. A greater effect may be expected at the crest rather than at the trough, which is as observed. The net effect of the greater increase at the crest than the trough is that the velocity amplitude (Figure 6.9c) is increased significantly relative to the irrotational solution to a depth of $y^* = -0.15$ m. To around the mid-depth of the tank, the measured velocity amplitude shows excellent agreement with the irrotational velocities, but, towards the bed, the amplitude increases relative to the Stokes' solution, to be approximately 10% greater close to the bed.

The phase averaged velocity profiles for the $U_\infty = 3.1$ m/s case, however, demonstrate somewhat different behaviour. The velocities beneath the crest, very close to the water surface, are significantly greater than the Stokes' solution, as a result of the wave-induced favourable current. Below $y^* = -0.02$ m, the velocity beneath the crest is less than the irrotational solution, and remains so over the remainder of the depth. This reduced velocity corresponds to the observed backflow in the current profile shown in Figure 6.7. As a result of this backflow, the magnitude of the measured velocities beneath the trough would be expected to be greater than that of the irrotational velocities. However, the measured velocities beneath the trough were found to have a smaller magnitude than the irrotational solution. Close to the surface, there is a significant wind-induced velocity effect, which causes a large reduction in the velocity magnitude. At greater depths, the velocity magnitude remains less than the Stokes' solution, suggesting there is a favourable current rather than the expected backflow. It would appear as if there is a forward current beneath the crest, and a reverse current beneath the trough in the region for $y^* < -0.02$ m. It almost appears as if there is a varying current which is approximately 180° out of phase with the wave motion. This

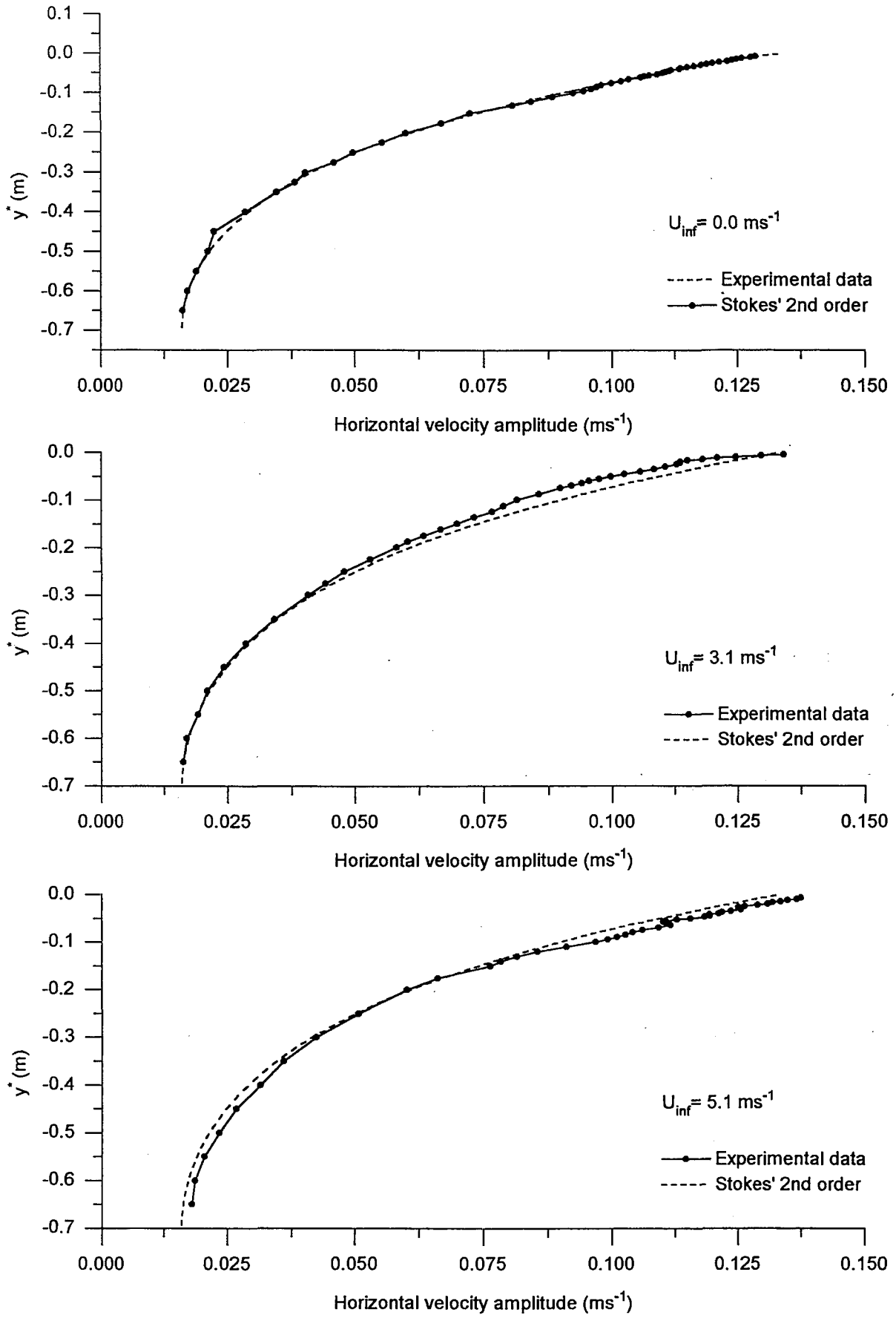


Figure 6.9: Horizontal wave velocity amplitude profiles for wind and wave U_{inf}= 0.0, 3.1 & 5.1 ms^{-1}

effect is discussed further in the next section. The net effect is that the measured velocity amplitude is less than the Stokes' solution down to $y^* = -0.3$ m, and is greater than the Stokes' solution only very close to the water surface (Figure 6.9b). At greater depths, the measured velocity amplitude shows excellent agreement with the irrotational velocities.

6.4.2 Phase Averaged Wind-Induced Velocities

The asymmetry of the near-surface velocities revealed by the phase averaged profiles (Figure 6.8) can be investigated by examining the phase averaged horizontal velocity traces. The near-surface phase averaged velocities for the $U_\infty = 3.1$ m/s case at elevations from $y^* = -5.0$ to -20 mm at 2.5 mm spacings, the highly sheared region of the flow, are shown in Figure 6.10. The velocity traces show a considerable asymmetry about the wave crest. For a wave in the absence of wind, the velocities would be expected to be symmetric about the crest. That the near-surface velocity gradients $\partial u/\partial y^*$ are considerably greater on the windward side of the crest than on the leeward side is clearly demonstrated in Figure 6.10 by the spacing of the velocity traces. The velocities close to the surface are consequently greater on the windward side of the crest than at the corresponding phase on the leeward side of the crest. The phase of the maximum horizontal velocity therefore moves upstream of the crest as the water surface is approached. The velocity traces become more asymmetric close to the surface, with the magnitude of the stream-wise accelerations $\partial u/\partial x$ on the windward side of the crest being greater than the declarations on the leeward side. The asymmetry reduces quickly with depth so that, by $y^* = -20$ mm, the velocity is relatively symmetric about the wave crest. Beneath this level, the asymmetry of the velocities appears to reverse, with the velocities becoming greater downstream of the crest, before returning to being in phase with the surface profile at greater depths.

To a first order, the horizontal velocities in the presence of a current are the sum of the irrotational wave velocities and the current. The wind-generated currents shown in Figure 6.6 were calculated by finding the mean value of the phase averaged velocities;

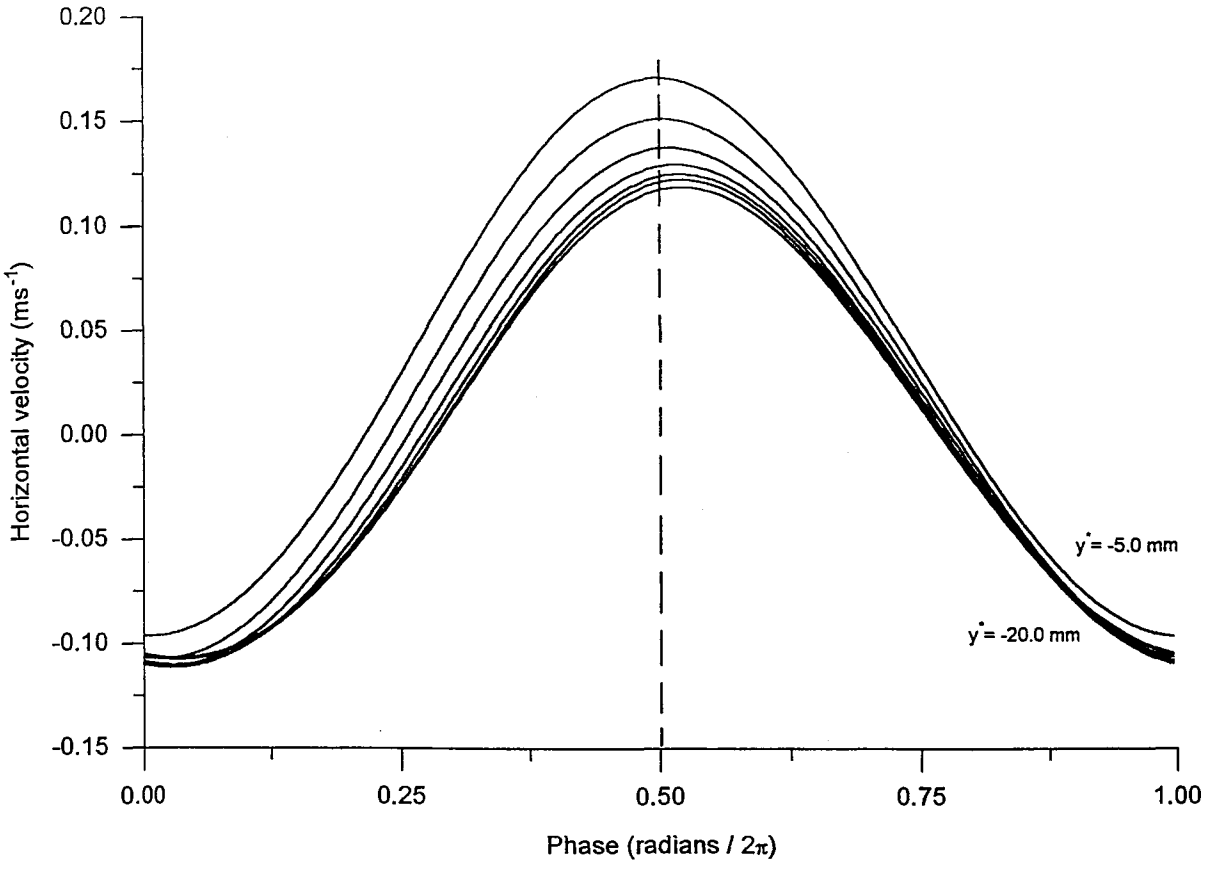


Figure 6.10: Phase averaged horizontal velocities at given y^* (U_{inf}= 3.1 ms^{-1})

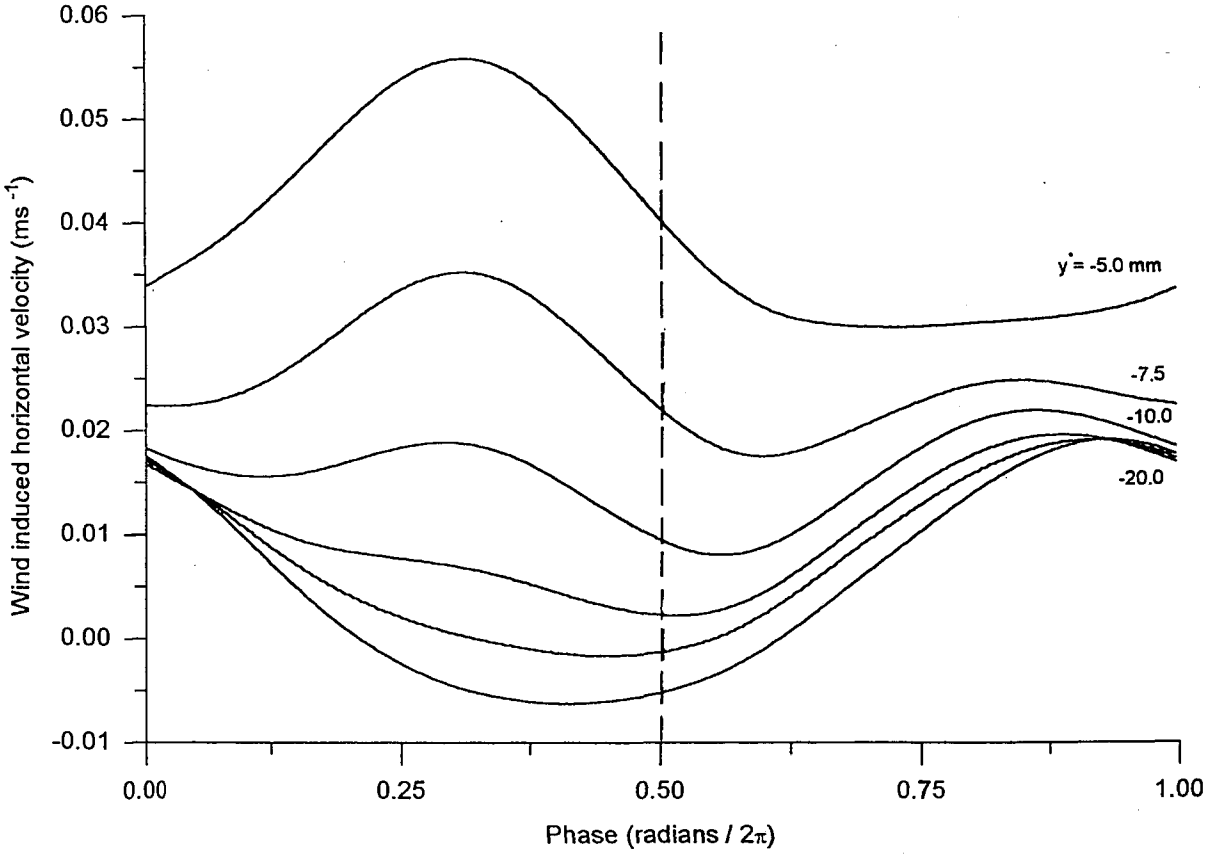


Figure 6.11: Phase averaged wind induced horizontal velocities at given y^* (U_{inf}= 3.1 ms^{-1})

they are therefore the average effect of the wind on the wave over the whole wave cycle. However, simply summing the current so calculated and the irrotational wave motion will not produce the velocities in Figure 6.10. Since the near-surface wind velocities and the surface stresses show significant phase variations, it would follow that the magnitude of the wind-induced current and its profile with depth will also show a variation with the phase of the long wave. It will be this phase varying wind-driven current, resulting from the phase variations in the overlying airflow, which will determine the wave kinematics.

To investigate the variation of the wind-induced currents with phase requires the decomposition of the measured phase averaged velocities to remove the orbital wave motion. If it is assumed that the wind-induced current does not affect the wave motion, and that the flow therefore remains irrotational, then this can be done by simply subtracting the Stokes' second order wave velocities calculated using the measured wave properties. This approach is valid to a first order, and should provide a good enough estimate to show the basic flow behaviour. It is to be expected that there will be some interaction between the wave and the current, but it is thought that the wind-induced current will be the dominant effect.

The decomposed phase averaged wind-induced currents for the U_∞ = 3.1 m/s case in the region y^* = -5 to -20 mm are presented in Figure 6.11. Close to the water surface, the maximum wind-induced velocity is between the zero upcrossing and wave crest, showing a distinct peak on the windward side of the crest, with the current almost constant over the leeward side of the crest. The current is significantly greater on the windward side of the crest than on the leeward side. On the windward side of the crest, there is a large streamwise acceleration $\partial u/\partial x^*$ between the trough and the zero upcrossing, and then a large deceleration between the upcrossing and the wave crest, whilst the accelerations are virtually zero on the leeward side of the crest. The velocity gradients with depth, $\partial u/\partial y^*$ appear to be a maximum around the peak velocities, and a minimum on the leeward side of the crest. At the water surface itself therefore, the currents on the windward side of the crest will be considerably greater than those on the

leeward side. The magnitude of the surface current is also significant: linear interpolation, which will under-estimate the surface values, predicts a surface current of approximately 0.10 m/s at the zero upcrossing, which is of the same order as the orbital velocity at the wave crest. As a result of the large gradients on the windward face, the currents reduce very quickly with depth below the surface, so at $y^* = -20$ mm, the current on the leeward side of the crest is greater than that at the corresponding phase on the windward side. The wind-generated current at $y^* = -20$ mm is close to being 180° out of phase with the near-surface current: the current is favourable beneath the wave trough, and adverse beneath the crest. This reflects the velocity profiles in Figure 6.8, the measured velocities beneath the crest being less than irrotational velocities as a result of the adverse current, and the magnitude of the measured velocities beneath the trough less than the irrotational velocities due to the favourable current. By considering continuity, it would be expected that a very large favourable near-surface current would have to be compensated for at greater depths by an adverse current, which is as observed beneath the upcrossing.

The time averaged velocity profiles corresponding to the phase averaged velocities in Figure 6.11 were presented in Figure 6.6. The profile shows a log-linear region between $y^* = -10$ and -25 mm, implying the existence of an inertial sub-layer in that region. Velocity profiles with the vertical co-ordinate y^* were plotted using the phase averaged decomposed wind-induced currents presented in Figure 6.11, and were found to demonstrate a log-linear region between $y^* = -10$ and -20 mm. There is insufficient data, with the data subject to potentially large errors, to make a meaningful quantitative analysis. However, it is clear from the velocity traces in Figure 6.11 that the maximum friction velocity would be between the zero upcrossing and the crest, with the minimum around the wave trough. The friction velocity beneath the wave appears therefore to be approximately in phase with the surface wind-generated current.

The wind-induced currents for the $U_\infty = 3.1$ and 5.1 m/s air flow cases are dependent upon the time-history of the total surface shear stress (Figure 5.15). The phases of the maximum and minimum wind-induced surface currents, which are just downstream of

the zero upcrossing and the crest respectively, correspond to the phases at which the shear stress is zero. Prior to the zero upcrossing the stress has been positive since the wave crest, approximately 75% of the wave cycle, and hence the current is a maximum. The only region of negative shear stress occurs between the zero upcrossing and the crest, which is the same area in which the measured current decelerates rapidly.

The maximum surface acceleration is between the trough and the zero upcrossing, on the windward face of the wave crest, while the maximum deceleration of the surface current is between the zero upcrossing and crest. The latter reflects the negative surface shear stress maximum, but the very large positive shear stresses on the leeward side of the crest correspond to near-constant wind-induced surface currents. The large accelerations between the trough and zero upcrossing similarly correspond to small shear stresses. It would thus appear that there is a delay in the response of the water surface to the applied stress. The reason for this delay is the other component of the surface current, namely the orbital wave velocity. On the leeward side of the crest, between the crest and the zero downcrossing, the orbital motion is reducing from a maximum at the crest to zero at the down crossing, and then accelerating the surface in the opposite direction to a maximum negative velocity at the trough. The acceleration is negative on the leeward side of the crest, which is in the opposite sense to the acceleration caused by the surface stress. It is only beyond the wave trough that the orbital velocity acceleration becomes positive, and the water at the surface is accelerated forwards by both components. The large deceleration in the orbital motion therefore appears to prevent the airflow from accelerating the water surface.

The orbital velocities can also be used to account for a number of other effects. The negative shear stresses between the upcrossing and crest are a result of the large orbital velocities in this region. The water surface is effectively moving faster than the overlying airflow, so that the water surface shears the airflow, rather than the airflow causing a shearing at the water surface. There is a resulting large release of shear stress, with the surface appearing to be super smooth, which is reflected in C being a maximum and the friction velocity a minimum. Conversely, around the downcrossing, where there is the apparent conflict between orbital velocities and the wind-induced accelerations, the

friction velocity and turbulence in the airflow are at a maximum, due to the resulting disturbance in the airflow, and the parameter C is a minimum, which implies rough surface conditions. The influence of each of these effects on the surface roughness is examined in Chapter 8.

Although the results of this analysis have been presented only for the $U_\infty = 3.1$ m/s case, similar effects were apparent for the $U_\infty = 5.1$ m/s case. However, the effects are not so evident for the faster case, since the boundary layer is much thinner, and very little velocity data could be measured in the inertial sub layer.

7. COMBINED WIND-WAVE-CURRENT MODEL

7.1 Introduction

Two of the fundamental assumptions on which existing wave solutions are based appear to be invalid in the presence of a significant wind velocity: firstly, that there are no non-conservative forces acting on the wave-form, so the fluid motion may be assumed to be irrotational; and secondly, at the water surface, the normal stress is constant, with no tangential stress. The results presented in the previous chapter showed that the wind generates a strongly sheared near-surface current which has a large, depth varying vorticity. In the presence of such a depth varying vorticity profile, the wave motion is unlikely to remain irrotational. The results of the analysis of the airflow measurements (Chapter 5) demonstrated that both the normal and shear stresses showed significant phase variations, and that the tangential stress was definitely non-zero.

The stresses exerted by an airflow on the surface of a water wave can be resolved into components acting normal and tangential to the water surface. Each component consists of a mean and fluctuating part:

$$P_n = \overline{P}_n + \hat{P}_n e^{i(kx-\sigma t)} \tag{7.1}$$

$$\tau_s = \overline{\tau}_s + \hat{\tau}_s e^{i(kx-\sigma t)} \tag{7.2}$$

where $\overline{P}_n$ and $\overline{\tau_s}$ are the time averaged normal and shear stresses, and $\hat{P}_n$ and $\hat{\tau}_s$ are the amplitudes of the fluctuating normal and shear stresses respectively. The fluctuating components are complex terms, with the real part being the fluctuation in-phase with the surface elevation, and the imaginary part the component in phase with the wave slope.

Swan (1992) considered the stresses acting on the surface of a water wave and showed that, to a first order of wave steepness, the mean component of the shear stress produces a current in the ξ-direction. At a first order of wave steepness, this does not affect the orbital wave motion, but at a second order there will be a wave-current

interaction. Similarly, the mean component of the normal stress does not appear to affect the first order wave motion. However, Swan finds that the fluctuating surface stress components do cause a modification to the orbital wave motion at a first order. There would therefore appear to be two distinct effects of the wind on the wave motion: firstly, the mean shear stress producing a current which interacts with the wave motion at a second order; and secondly, the fluctuating normal and shear surface stresses which modify the wave motion directly at a first order. In the following sections, each of these effects is considered in turn, and then an assessment made of the dominant effect on the wave motion.

7.2 Wave-Current Interaction

7.2.1 Overview

Consider the interaction between a series of two-dimensional progressive gravity waves and a steady co-flowing current. The most simple case is that of a uniform current, where the vorticity is zero over the entire depth of the flow. The wave motion remains irrotational, and the kinematics are the linear sum of the irrotational motion and the uniform current. The only interaction is within the dispersion equation which, at a second order of wave steepness, is given by the Doppler shifted solution:

$$c = \frac{\sigma}{k} = \left[\frac{g}{k}\tanh kd\right]^{1/2} + \overline{U} \tag{7.3}$$

where c is the phase velocity, σ the wave frequency, k the wave number, d the water depth, and $\overline{U}$ the mean current. The wave motion propagating on a linearly sheared current, where the vorticity remains constant over the whole depth, will also remain irrotational (Tsao, 1959). Kishida and Sobey (1988) found to a second order of wave steepness, assuming the current is of the same order as the first order wave motion, that the dispersion equation is:

$$c = \frac{\sigma}{k} = \left[\frac{g}{k}\tanh kd\right]^{1/2} + U_s - U_s' \frac{\tanh kd}{2k} \tag{7.4}$$

where U_s is the surface current and U_s' denotes a derivative with respect to y. Many current profiles can be approximated by either a uniform or linearly sheared profile, but wind-driven currents, such as those presented in the previous chapter, are a notable exception. These profiles are highly sheared close to the water surface with a corresponding high vorticity, and will have a highly non-uniform vorticity distribution with depth. In the presence of such rotational currents, Tsao (1959) found that the wave motion itself becomes rotational. Chaplin (1990), Swan (1992), and Cummins and Swan (1994b) showed that for highly sheared currents having a depth-varying vorticity distribution, the distribution of the vorticity significantly affects the wave-current interaction. The resulting non-linear wave-current interaction is very complex, and in general has to be considered using numerical models.

A number of such wave-current numerical models have been developed. Dalrymple (1974) considered a stream function model with a bi-linear sheared current. The flow is divided into two layers, with a linear but differently sheared velocity profile in each region. The vorticity is therefore constant in each layer, but there is a vorticity discontinuity at the interface between the layers. This approach has been developed by others, including Cummins and Swan (1993) who extended Dalrymple's model to five layers, and thereby produced an improved description of the vorticity distribution. A second type of model is that based upon Dalrymple's (1977) finite difference formulation to solve the dynamic free surface boundary condition. Chaplin (1990) and Thomas (1990) developed this model, demonstrating its applicability for steep waves and highly sheared wind-driven currents. Cummins and Swan (1993) have compared the results of their five layer model with those of Chaplin (1990) and found the results to be identical.

Analytical models based on series expansions may also be developed to model the wind-wave interaction. They suffer the disadvantage of having to be truncated at low order

because the mathematics becomes rather overwhelming at higher orders. For highly non-linear waves, numerical models are essential. However, for relatively linear waves, such as those encountered in the present study, an analytical solution, even truncated at relatively low order, might be expected to provide a reasonable description of the wave kinematics. For the present purposes, an analytic solution is essential in order to allow for it to be combined with the varying surface stresses to produce a combined wind-wave-current solution.

Swan (1992) developed an analytic stream function solution for waves on a strongly sheared current. The scheme is outlined below and developed to predict the wave kinematics for the measured averaged currents. The results of the model are compared with a three layer version of the numerical model proposed by Cummins and Swan (1993).

7.2.2 Wave-Current Model

Swan (1992) presents the solution to a perturbation expansion for small amplitude waves on a strongly sheared current. The analysis is undertaken in an orthogonal curvi-linear co-ordinate system (ξ,η), translating with the phase velocity c to create a steady frame of reference. The transformation from Cartesian co-ordinates is defined by:

$$\eta = z - \sum_{n=1}^{N} A_n \frac{\sinh(nkd + nk\eta)}{\sinh(nkd)} \cos(nk\xi) - B_n \tag{7.5}$$

$$\xi = x - \sum_{n=1}^{N} A_n \frac{\cosh(nkd + nk\eta)}{\sinh(nkd)} \sin(nk\xi) \tag{7.6}$$

where the symbols have their usual meaning and the constant coefficients A_n and B_n are defined as part of the solution. The Jacobian for the transformation is given in Appendix C. This transformation is similar to the one used for the experimental data in that it provides a steady wave following co-ordinate frame. However, because the velocity components are defined in (ξ,η) co-ordinate directions, rather than in the Cartesian

directions, the two sets of velocity data will only be directly comparable at the wave crest and trough.

The current profile is described in this co-ordinate system by a third order polynomial in the region $0 \geq \eta \geq -md$ by

$$U = (P + 2Q\eta + 3R\eta^2 + 4S\eta^3)\delta_s(\eta + md) \tag{7.7}$$

where m is a constant $0 \leq m \leq 1$, and δ_s is the unit step function defined as

$$\delta_s(\eta + md) = 1 \qquad \text{if} \quad (\eta + md) \geq 0$$

$$\delta_s(\eta + md) = 0 \qquad \text{if} \quad (\eta + md) \leq 0$$

The current in the upper region of the flow, $0 \geq \eta \geq -md$, is therefore defined by a cubic polynomial profile which, it was thought, would be suitable to model the measured highly sheared wind-driven currents (Figure 7.1). The current in the lower region of the flow, $-md \leq \eta \leq -d$, is constant and is zero in the above formulation. However, a constant can be added which shifts the whole profile and allows the current in the lower region to be set to a constant non-zero velocity.

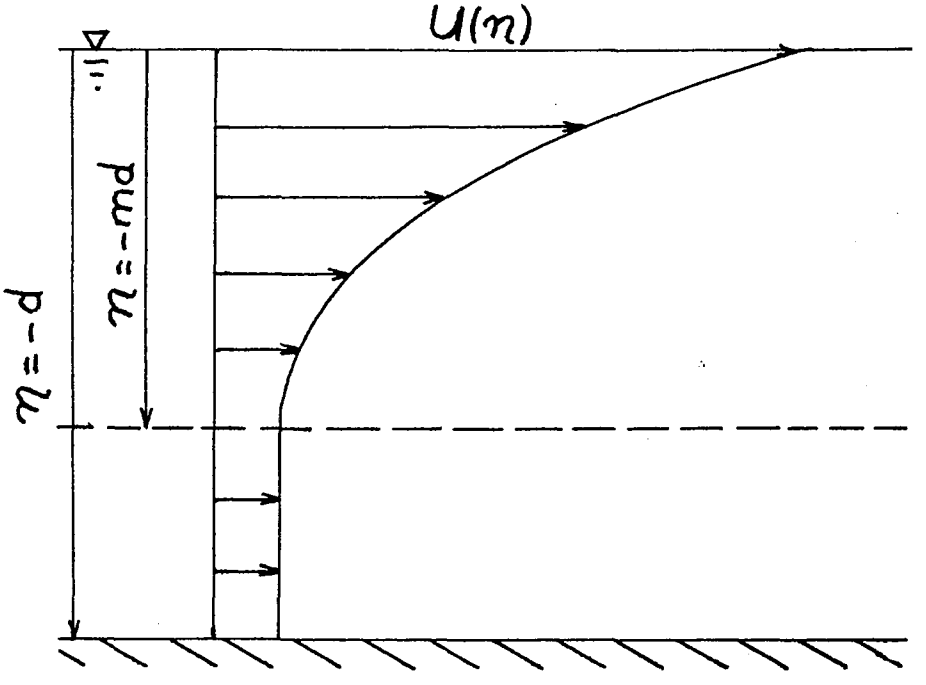


Figure 7.1: Wave-current model definitions sketch

To ensure the convergence of the above scheme, the current must be at least one order of magnitude smaller than the phase velocity, and of the same order of magnitude as the first order wave motion. If the current and phase velocity are of the same order, the problem becomes indeterminate. Compatibility constraints at the interface η =-md on the velocity u_ξ and the vorticity lead to two constraints on the current profile:

$$P - 2Qmd + 3Rm^2d^2 - 4Sm^3d^3 = 0 \tag{7.8}$$

$$Q - 3Rmd + 6Sm^2d^2 = 0 \tag{7.9}$$

The analysis solves the two-dimensional inviscid vorticity equation

$$\frac{\partial(\psi, J\nabla^2\psi)}{\partial(\xi,\eta)} = 0 \tag{7.10}$$

using perturbation expansions in terms of the wave steepness ak for the stream function ψ, the surface elevation ζ and the Jacobian J. The perturbation expansions are truncated above a second order of wave steepness to provide a first approximation of the wave-current interaction. The vorticity equation is solved subject to the usual boundary conditions and a further set of boundary conditions related to continuity across the boundary η = -md (Appendix A).

The stream function is found to be:

$$\psi_o = -c\eta$$

$$\psi_1 = \left(Q\eta^2 + R\eta^3 + S\eta^4\right)\delta_s(\eta + md) - P\eta\delta_s(-\eta - md)$$

$$\psi_2 = a\left(2Q\eta + 3R\eta^2 + 4S\eta^3 + \frac{6S\eta}{k^2} + F_a\right)\frac{\sinh k(d+\eta)}{\sinh(kd)}\cos(k\xi)\delta_s(\eta + md)$$

$$+a\left(-\frac{3R\eta}{k} - \frac{6S\eta^2}{k} + F_b\right)\frac{\cosh k(d+\eta)}{\sinh(kd)}\cos(k\xi)\delta_s(\eta + md)$$

$$+aF_c\sinh k(d+\eta)\cos(k\xi)\delta_s(-\eta - md) \tag{7.11}$$

where F_a, F_b and F_c are constants determined from the wave and current parameters, and are given in Appendix A.

The corresponding dispersion equation, at a second order of wave steepness, for the phase velocity relative to a stationary observer is given by:

$$c=\frac{\sigma}{k}=\left(\frac{g}{k}\tanh kd\right)^{1/2}+P-\frac{Q}{k}\tanh kd+\frac{3R}{2k^2}-\frac{3S}{k^3}\tanh kd-\frac{F_a}{2}\frac{1}{\cosh^2 kd} \tag{7.12}$$

The total velocity in the ξ-direction is evaluated from the stream function, and can be expressed in terms of the perturbation expansion as

$$(U+u)_\xi = J^{1/2}\frac{\partial\psi}{\partial\eta}=\left[1+\frac{1}{2}(ak)J_1+\frac{1}{2}(ak)^2J_2-\frac{1}{8}(ak)^2J_1^2\right]$$
$$\left[\frac{\partial\psi_0}{\partial\eta}+(ak)\frac{\partial\psi_1}{\partial\eta}+(ak)^2\frac{\partial\psi_2}{\partial\eta}\right] \tag{7.13}$$

Expanding the perturbation series above and neglecting terms above a second order of wave steepness, the total velocity in the ξ-direction is the sum of the irrotational and rotational velocities.

Irrotational: $$(U+u)_\xi=\frac{\partial\psi_0}{\partial\eta}+\frac{1}{2}J_1\frac{\partial\psi_0}{\partial\eta}+\frac{\partial\psi_0}{\partial\eta}\left(\frac{1}{2}J_2-\frac{1}{8}J_1^2\right) \tag{7.14}$$

Rotational: $$(U+u)_\xi=\frac{\partial\psi_1}{\partial\eta}+\frac{\partial\psi_2}{\partial\eta}+\frac{1}{2}J_1\frac{\partial\psi_1}{\partial\eta} \tag{7.15}$$

The zero order irrotational term $\partial\psi_0/\partial\eta$ is the axis translation. The remaining irrotational terms produce the classical second order Stokes' solution, as used to calculate the irrotational velocities presented in Chapter 6. The first order rotational

term $\partial\psi_1 / \partial\eta$ is simply the current, and the remaining rotational terms, which are second order, define the wave-current interaction. Explicit expressions for the irrotational and rotational velocities in the ξ-direction are presented in Appendix A.

7.3 Wind-Wave Interactions

7.3.1 Overview

The wave-current model developed in the previous section considers the effect of the time-averaged tangential stress. This component of the tangential stress affects the wave motion indirectly, by generating a current at first order which interacts with the wave motion at a second order. In this section, the effects of significant fluctuating stresses at the water surface are investigated. A first order perturbation expansion solution to the stream function incorporating varying surface stresses, developed by Swan (1992), is outlined and the kinematics deduced. By truncating the solution at first order, the interaction with the generated current can be neglected, and only the direct effects of the varying stresses on the wave motion are considered.

7.3.2 Wind-Wave Model

The analysis is similar to that used to develop the wave-current model. A curvi-linear co-ordinate system (ξ,η) is adopted, defined as in equations 7.5 and 7.6, but with $n = N = 1$ since this analysis is only developed to a first order of wave steepness. The water surface profile is correspondingly sinusoidal:

$$\zeta(x,t) = \Re\left[ae^{i(kx-\sigma t)}\right] \tag{7.16}$$

where $\Re[...]$ denotes the real part of the function. The curvi-linear co-ordinates translate with the phase velocity c in order to produce a quasi-steady state. Wind-wave generation and viscous attenuation are time dependent, but it is considered that these effects are small in comparison with the underlying long wave motion. The wind-

generated waves are assumed to be small compared with the underlying long wave, which is the case for the wind ruffled waves considered in the present study.

The first order vorticity equation in the (ξ,η) co-ordinate system to be solved is

$$\nabla^4\psi_1 + \frac{c}{\nu_w}\frac{\partial}{\partial\xi}\left(\nabla^2\psi_1\right) = 0 \tag{7.17}$$

where c is the phase velocity and ν_w the kinematic viscosity of water. Neglecting viscous effects at the bed, the general solution of equation 7.17 is

$$\varepsilon\psi_1 = \Re\left[\left\{Ae^{\alpha\eta} + B\cosh(k\eta) + C\sinh(k\eta)\right\}e^{ik\xi}\right] + F(\eta) \tag{7.18}$$

where A, B, and C are constants, and $\alpha = (1+i)\beta$, where β is the inverse of the boundary layer thickness, defined as $\beta^2 = (\sigma/2\nu_w)$ and σ is the wave frequency. This solution corresponds to the development of a viscous boundary layer at the water surface.

Four boundary conditions are applied to the flow. Two represent the standard kinematic constraints, applied at the bed and water surface (see Appendix A), while the other two concern the surface stress conditions. The surface stresses applied by the overlying airflow are

$$P_n = \overline{P}_n + \hat{P}_n e^{i(kx-\sigma t)}$$
$$\tau_s = \overline{\tau}_s + \hat{\tau}_s e^{i(kx-\sigma t)}$$

Because the tangential stresses are equal on either side of the air water interface, the tangential stress at the water surface in the airflow can be related to the velocity gradients in the water flow. To a first order of approximation this boundary layer condition can be expressed as

$$\overline{\tau_s} + \hat{\tau}_s e^{ik\xi} = \mu_w \left(\frac{\partial^2 \psi_1}{\partial \eta^2} - \frac{\partial^2 \psi_1}{\partial \xi^2} - c \frac{\partial J_1}{\partial \eta} \right) \tag{7.19}$$

where μ_w is the molecular viscosity of water (or $\rho \nu_w$). By averaging in the ξ-direction this reduces to

$$\overline{\tau_s} = \mu_w \overline{\frac{\partial^2 \psi_1}{\partial \eta^2}} = \mu_w \frac{\partial^2 F(\eta)}{\partial \eta^2} \tag{7.20}$$

which indicates that, at a first order, the mean component of the shear stress does not affect the wave motion.

The normal stress, or pressure P_n, in the water flow can be evaluated using the Navier Stokes' equations. The normal stress boundary condition at a first order of approximation is

$$ik\hat{P}_n e^{ik\xi} = GJ^{-\frac{1}{2}} + c \frac{\partial^2 \psi_1}{\partial \eta \partial \xi} - \frac{1}{2} c^2 \frac{\partial J_1}{\partial \xi} \tag{7.21}$$

where G is the external body force per unit mass, or the acceleration due to gravity g. At a first order of approximation therefore, the mean component of the normal stress $\overline{P_n}$ does not affect the wave motion. For both the tangential and normal surface stresses, it is the fluctuating stress components, and not the mean stress components which affect the wave motion to a first order of approximation.

The stream function to a first order is found to be

$$\psi_0 = -c\eta$$

$$\psi_1 = \left(\frac{iak\sigma}{\beta^2} - \frac{i\hat{\tau}}{\sigma \rho_w} \right) \left(e^{\alpha \eta} - \cosh(k\eta) - \frac{\sinh(k\eta)}{\tanh(kd)} \right) e^{ik\xi} \tag{7.22}$$

and the corresponding dispersion equation, derived from the dynamic free surface boundary condition (see Appendix A), is

$$\frac{1}{\rho_w}\left[\hat{P}_n + \frac{i\hat{\tau}}{k}(\alpha - k\tanh(kd))\right] = c^2 ak\coth(kd) - ag \tag{7.23}$$

The imaginary terms in the dispersion equation are associated with wave growth (Lin, 1955). It has been found by other investigators, (Miles, 1957, Longuet-Higgins, 1963, Belcher and Hunt, 1993), that it is the normal stress component in phase with the wave slope and the tangential stress component in phase with the surface elevation which are responsible for wave growth. This is consistent with the dispersion equation above, but, because α has both real and imaginary parts, the component of the tangential stress in-phase with the wave slope appears also to be responsible for wave growth. This additional effect was not identified by Swan (1992).

The real part of the dispersion equation corresponds to the change in the phase speed

$$c^2 = \frac{\tanh kd}{k}\left\{g + \frac{\Re\left[\hat{P}_n\right]}{a\rho_w} + \frac{\Im[\hat{\tau}]}{a\rho_w}\left(\coth(kd) - \frac{\beta}{k}\right) - \frac{\Re[\hat{\tau}]\beta}{ak\rho_w}\right\} \tag{7.24}$$

where $\Im[...]$ denotes the imaginary part of the function. Swan (1992) found that it is the normal stress in phase with the surface elevation, and the tangential stress in phase with the wave slope which cause a change to the phase velocity. However, there is again a cross-term from the complex α, and the tangential stress in-phase with the water surface profile therefore appears also to modify the phase velocity.

The first order wave motion in the ξ-direction can be found from the stream function

$$u_\xi = J^{1/2}\frac{\partial\psi}{\partial\eta} = \frac{1}{2}J_1\frac{\partial\psi_0}{\partial\eta} + \frac{\partial\psi_1}{\partial\eta} \tag{7.25}$$

The first term is the usual first order irrotational Stokes' velocity. The second term is an additional irrotational velocity induced by the fluctuating surface stresses. By substituting in the stream function solution (equation 7.22), an expression for the real velocity in the ξ-direction can be evaluated (see Appendix B):

$$u_\xi = \cos(k\xi)\left[-\frac{\Im[\hat{\tau}]}{\sigma\rho_w}\left(k\sinh(k\eta)+k\frac{\cosh(k\eta)}{\tanh(kd)}\right)\right]$$
$$+\sin(k\xi)\left[-\frac{\Re[\hat{\tau}]}{\sigma\rho_w}\left(k\sinh(k\eta)+k\frac{\cosh(k\eta)}{\tanh(kd)}\right)\right]$$
$$+\beta e^{\beta\eta}[....] \qquad (7.26)$$

It is the tangential stress component, and not the normal stress, which is associated with the development of the surface boundary layer, thus altering the wave kinematics. The above expression for the velocity component in the ξ-direction suggests that the amplitude of the tangential stress in phase with the wave slope is responsible for modifying the velocity in phase with the surface profile, and the amplitude of the tangential stress in phase with the surface profile for modifying the velocity in-phase with the wave slope. Velocities in phase with the wave slope, in addition to those in phase with the surface profile, are to be expected since the wave form is being subjected to out-of phase surface stresses. The final term, which is small except very close to the water surface, corresponds to the development of a viscous boundary layer at the surface and the production of a strongly sheared velocity profile. Terms of order $1/\beta^2$ have been neglected, since $\beta \sim 10^3$.

7.4 Comparison between Experimental and Theoretical Results

The wave-current and wind-wave models, developed in the preceding sections were used to predict the wave kinematics for the $U_\infty = 3.1$ and 5.1 m/s air flow cases. The kinematics are calculated for both cases using each model and compared with the

measured velocities to allow the relative significance of the interaction mechanisms to be assessed.

7.4.1 Wave-Current Model

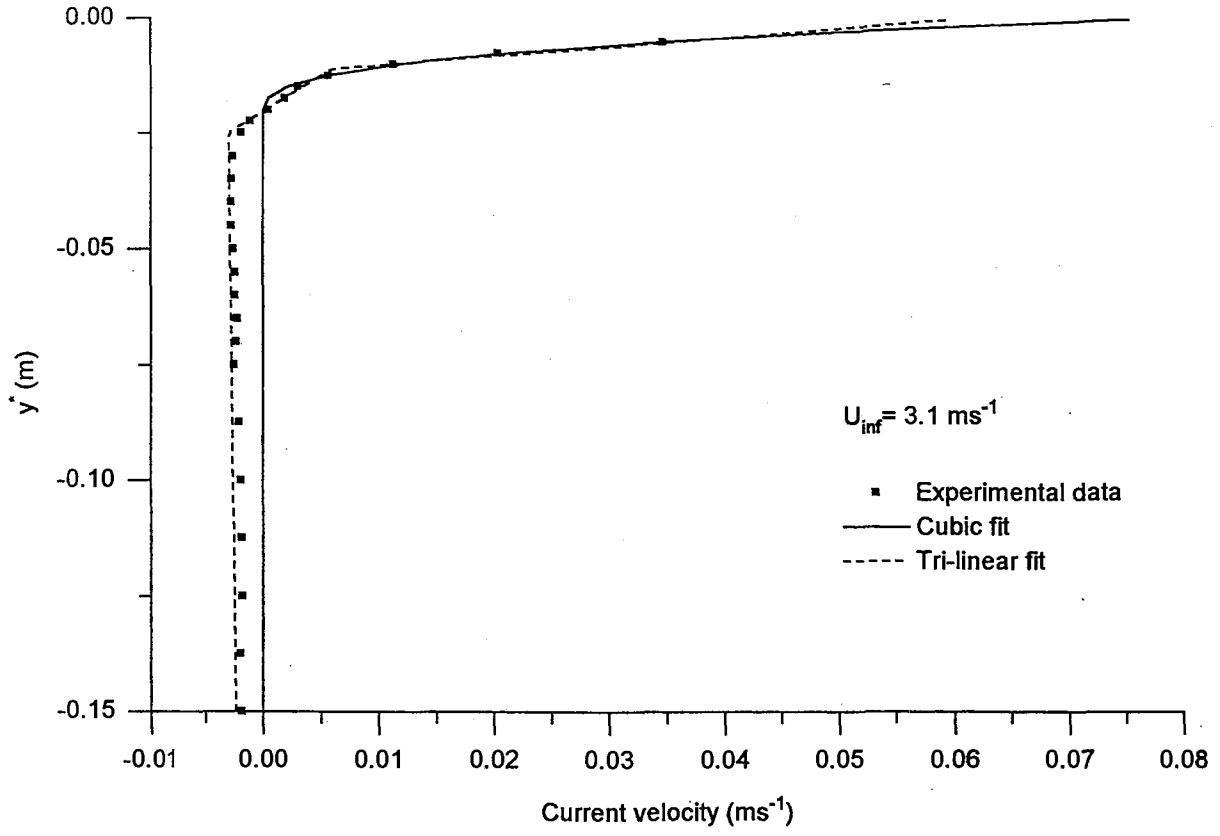
The inputs required for the wave-current model described in section 7.2.2 are the coefficients of the third order polynomial, describing the current profile, and the wave characteristics. Figure 7.2 shows the measured time averaged currents under the 1 Hz, 22.5 mm amplitude waves, with overlying free stream air flows of U_∞ = 3.1 and 5.1 m/s, together with least squares best fit third order polynomial and tri-linear curve fits to the measured velocities. The latter description is used in the three-layered numerical model developed by Cummins and Swan (1993), which was described in section 7.2.1. Both curve-fits appear to provide a reasonable description of the current profiles. For the third order polynomial fits, the current beneath the highly-sheared near-surface region is assumed to be zero. There are variations in the current with depth beneath the surface layer, but they are an order of magnitude less than the surface values and are related to the return flows in the wave flume, so are not considered significant.

The coefficients of the third order polynomial linear least squares curve-fits to the measured currents are given in Table 7.1 below:

U_∞ (m/s)	m	P	Q	R	S
3.1	0.02857	0.07525	5.198	158.4	1794
5.1	0.09500	0.03552	0.6551	5.107	13.70

Table 7.1: Coefficients of cubic polynomial curve fits to current profiles.

The phase velocities calculated using equation 7.12 are given in Table 7.2, and compared with the measured phase velocities (see section 8.3.2) and the phase velocities calculated using a first order irrotational wave theory.



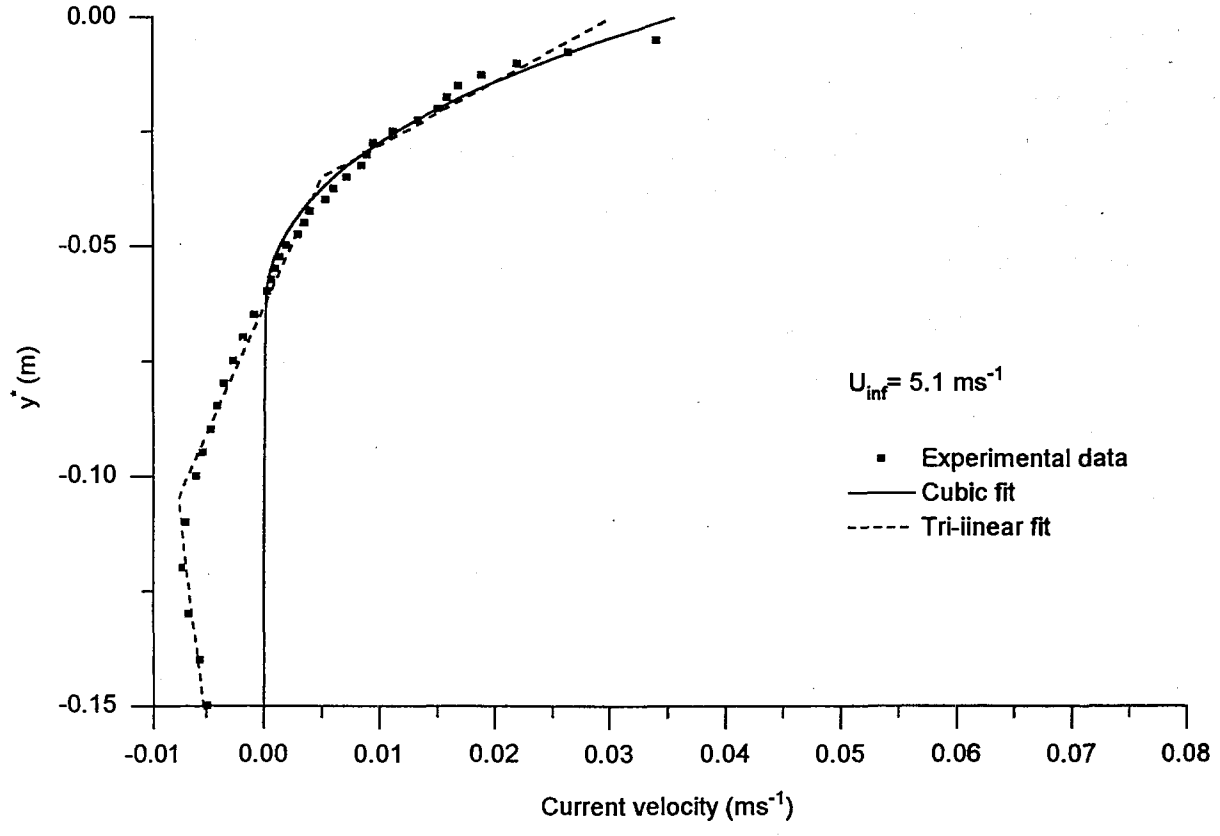


Figure 7.2: Wind driven current - experimental data and least squares fits

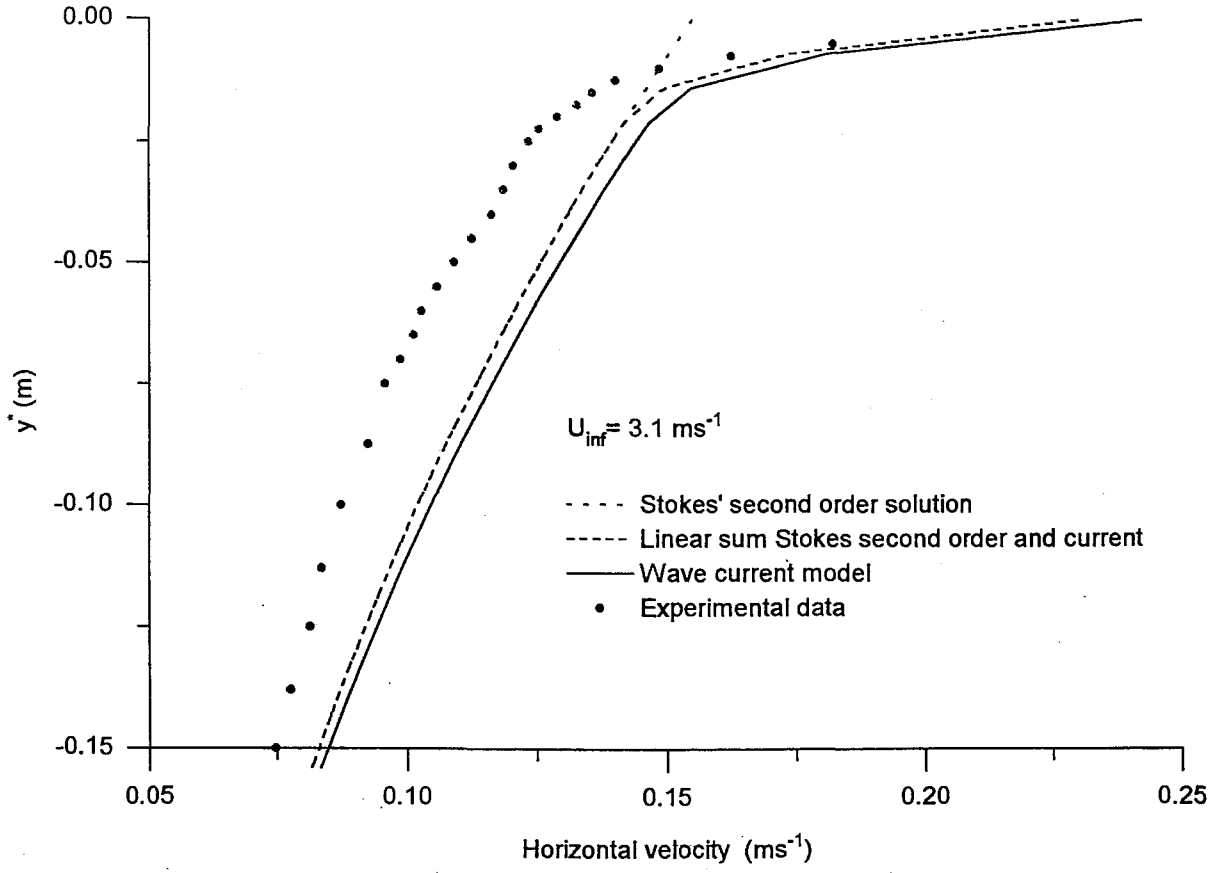
U_∞ (m/s)	Measured (data) c (m/s)	First order theory (waves only) c (m/s)	Wave-current model (waves and current) c (m/s)
3.1	1.57	1.54	1.55
5.1	1.59	1.54	1.56

Table 7.2: Phase velocity calculated from wave-current model

The phase velocity calculated using the wave-current model is slightly greater than the first order phase velocity, but by less than 1% even for the faster flow case. This small change in the phase velocity is due to the fact that the effect of the Doppler shift, caused by the surface current, is counteracted by the effects of the near-surface vorticity distribution. This effect was identified by Swan (1992). In each case, the measured phase velocity is between 1-2% greater than that predicted by the wave-current model. It appears that the wave-current interaction accounts for only a part of the observed increase in the phase velocity. However, as discussed in section 8.3.2, the increases in the measured phase velocity are very small, and are subject to experimental errors.

The velocity profiles beneath the wave crest calculated using the wave-current model are shown in Figure 7.3, and are compared with the measured data. In addition, the velocity profiles calculated using Stokes' second order irrotational theory and the velocity profiles obtained by taking the linear sum of the irrotational velocities and the measured current are shown.

The velocities for each case were also calculated using the three layer numerical model developed by Cummins and Swan (1993). The agreement between the velocities from the analytical wave-current model and the three layer model was excellent, suggesting that the analytical model is valid for these cases. However, the rotational wave component, which may be considered in Figure 7.3 to be the difference between the velocities calculated using the wave-current model and the linear sum of the irrotational



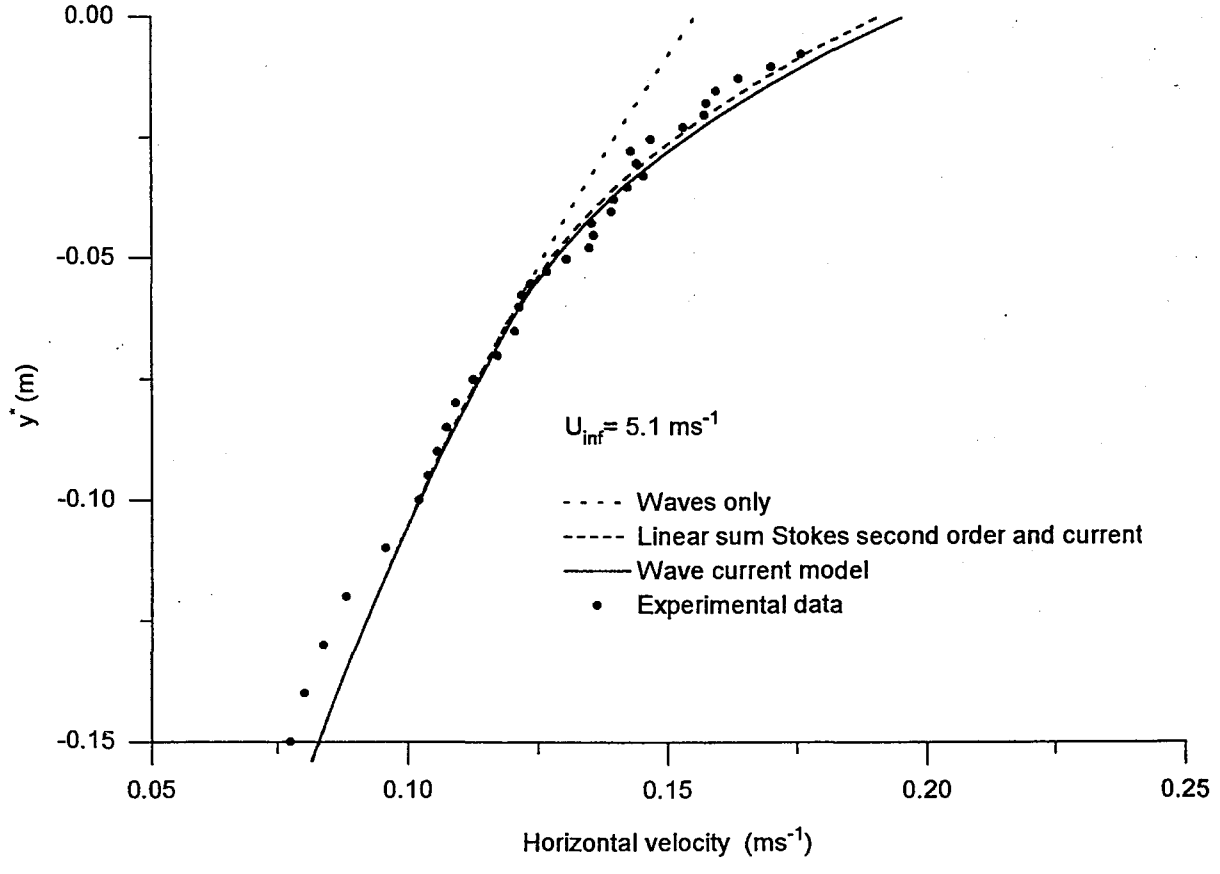


Figure 7.3: Comparision of wave current theory with measured velocities at the wave crest

velocity and measured current, is very small in both cases. For example, at the water surface the magnitude of the term is approximately 3% of the irrotational velocity. The analytical wave-current model considers only the first order wave-current interaction, which is a good approximation for the relatively linear waves used in the present study. For steeper non-linear waves, the rotational wave component will be more significant, and higher orders of wave-current interaction must be considered. Indeed, it was found for steeper non-linear waves that the analytical model significantly under-estimated the velocities compared with the three layer model.

The wave-current model and the linear sum of the irrotational velocities and current both provide an excellent fit to the measured velocities for the $U_\infty = 5.1$ m/s case, although there is some scatter in the data (Figure 7.3). The agreement is very good close to the water surface, but at greater depths there is some divergence as a result of the return flow in the wave flume which was not modelled by the third order polynomial. It appears that the wind-generated current is responsible for the observed modified wave kinematics, and since the rotational wave component is small, a good approximation to the measured velocities may be obtained simply by summing the irrotational solution and the wind-induced current.

For the $U_\infty = 3.1$ m/s case, the measured velocities very close to the water surface showed good agreement with the velocities predicted using the wave-current model, but, beneath the highly sheared surface layer, the measured velocities are significantly less than those predicted by the model. This is a result of the observed phase varying backflow which was discussed in the previous chapter. As shown in Figure 6.11, at the wave crest a significant return flow is generated beneath the large forward current induced at the water surface. The wave-current model developed above considers only a steady current which does not vary with phase, so cannot take account of the variations in the wind-generated current.

In both the $U_\infty = 3.1$ and 5.1 m/s cases, the magnitude of the fluctuations of the wind-induced current are significant compared with the orbital motion, and have a significant effect on the wave kinematics. The agreement of the kinematics close to the water

surface in each case is due to the fact that the current at the crest is approximately equal to the average current (see Figure 6.11). However, for instance in the $U_\infty = 3.1$ m/s case, the kinematics predicted by the model (using the average current) at the zero upcrossing, where the wave-induced current is a maximum, would be very different to the observed kinematics. The applicability of models which use the average current for predicting the kinematics in the presence of a significant airflow is therefore questionable. This effect is discussed further at the end of this chapter.

7.4.2 Wind-Wave Model

The wind-wave model described in section 7.3.2 requires, in addition to the wave characteristics, the amplitudes of the components of the surface stresses, which were estimated in Chapter 5. The amplitudes of the surface stress components are given in Table 7.2 below:

U_∞	$\Re[\hat{\tau}]_{amp}$	$\Im[\hat{\tau}]_{amp}$	$\Re[\hat{P}_n]_{amp}$	$\Im[\hat{P}_n]_{amp}$
(m/s)	(N/m^2)	(N/m^2)	(N/m^2)	(N/m^2)
3.1	0.00131	-0.0158	0.0574	-0.3996
5.1	0.01103	-0.0323	-0.420	-3.220

Table 7.3: Measured surface stress coefficients

The phase velocities calculated from the wind-wave model are given in Table 7.4 below, and compared with the measured phase velocities and those calculated from first order irrotational theory.

U_∞ (m/s)	Measured c (m/s)	First order c (m/s)	Wind-wave model c (m/s)
3.1	1.57	1.54	1.58
5.1	1.59	1.54	1.60

Table 7.4: Phase velocity calculated from the wind-wave model

The phase velocities calculated using the wind-wave model (Table 7.4) are significantly greater than those calculated using the wave-current model (Table 7.2), thereby suggesting that the surface stresses are more significant in predicting the appropriate form of the dispersion equation. However, it should be noted from Table 7.4 that the wind-wave model appears to over-predict the measured data, although given the inaccuracies involved these results appear convincing.

The velocity profiles beneath the wave crest calculated using the wind-wave model are shown in Figure 7.4 for the $U_\infty = 3.1$ and 5.1 m/s cases. They are compared with the measured velocities, and the velocities calculated using first order irrotational wave theory, since the wind-wave model considers only first order terms. From Figure 7.4, by comparing the waves only irrotational velocities with the velocities predicted by the wind-wave model, it is apparent that for both the $U_\infty = 3.1$ and 5.1 m/s cases, the wind-wave component is very small over most of the depth of the flow. The velocities predicted by the wind-wave model are greater than the Stokes' first order solution by a small amount over almost the entire depth for both airflow cases as a result of the greater phase velocity calculated from the wind-wave model, this effect being most significant at greater depths.

The effect of the airflow on the wave motion is principally through the additional terms in the dispersion equation, except very close to the water surface. Over almost the entire depth of the flow, the additional velocity terms are insignificant in both the cases being considered in the present study, but very close to the water surface, the $e^{\beta\eta}$ terms become significant and cause a rapid reduction in the orbital velocity as the water

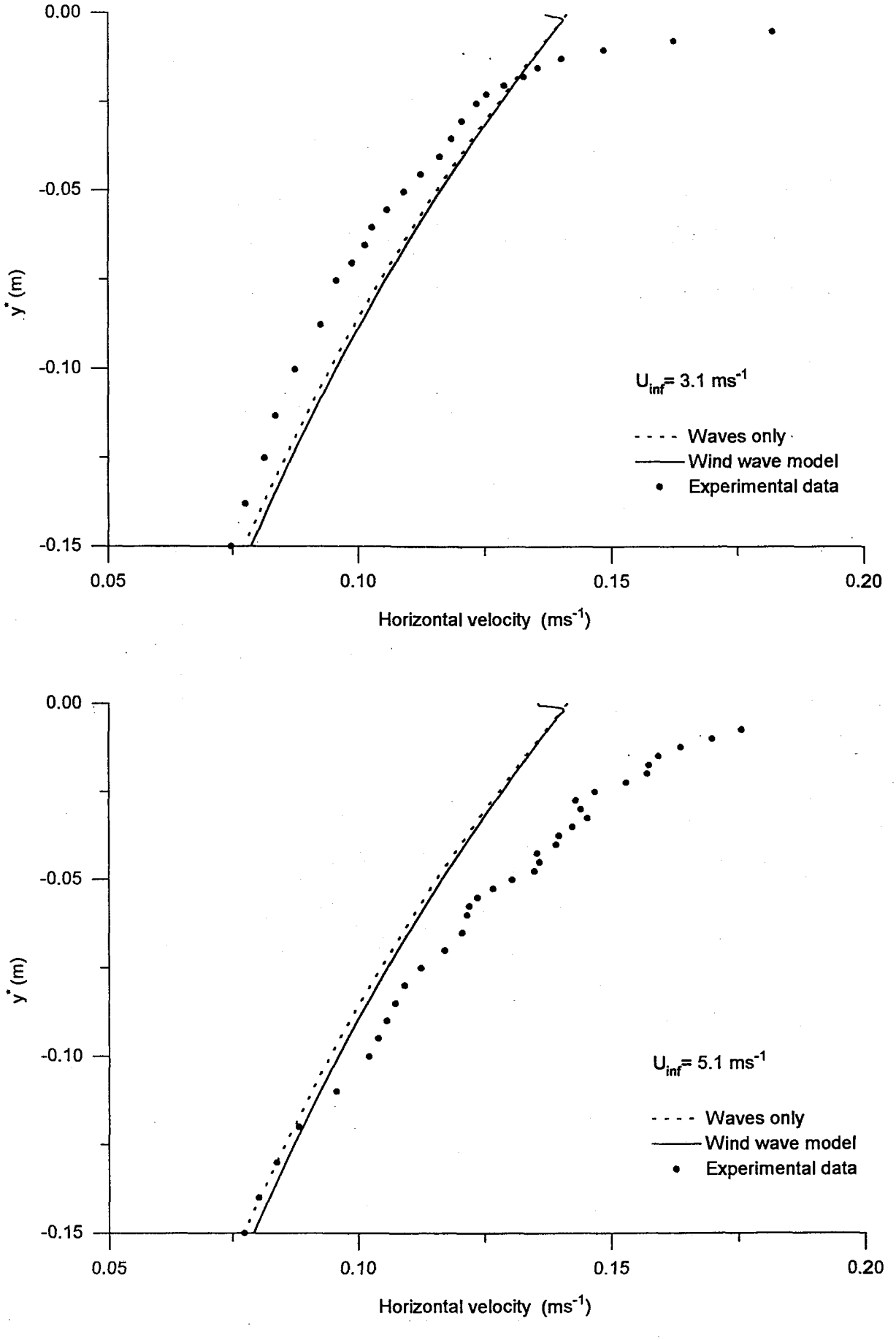


Figure 7.4: Comparision of wind wave theory with measured velocities at the wave crest

surface is approached. This effect is counter to the wind-induced current, which increases up to the water surface, and is related to the development of a near-surface boundary layer.

The velocities calculated using the wind-wave model do not provide a good fit to the measured velocities. The dominant effects observed in the data are related to the phase varying wind-induced current, which was discussed in the previous section. The two effects which appear from the wind-wave model to be significant for the kinematics in the present cases are the modification to the wavenumber caused by the additional terms in the dispersion equation, and the reduction in velocity as a result of the viscous boundary layer terms very close to the water surface. The latter effect is apparently significant only very near the water surface, within 5 mm, and since no data could be collected in that region in the present study, it was not possible to investigate this effect. The former effect, resulting from the additional terms in the dispersion equation, appears to account for the observed increased phase velocity, although it predicts a larger value than that measured.

7.4.3 Concluding Remarks

From the comparisons of the results of the wave-current and wind-wave models with the Stokes' irrotational solutions in sections 7.2.2 and 7.3.2 respectively, it is apparent for the cases considered in this study that a good approximation to the wave velocity can be made by simply summing the irrotational velocity and the phase varying current. The wind-induced current, which is of the same order as the irrotational wave motion, provides the dominant modification to the wave motion. The modification to the wavenumber caused by the additional terms in the dispersion equation and the wave-current rotational velocity component are second order terms, and have a comparatively small effect on the wave kinematics. However, for steeper non-linear waves, these interaction effects may be more significant, and the analytical models, which are truncated at low order, may not be applicable and full numerical solutions may be required to evaluate the wind-wave-current interaction. The very near-surface reduction

in velocity caused by the development of a boundary layer through the wind-wave model could not be verified from the measured velocities.

There is clearly an incongruity in comparing the results of the wind-wave and wave-current models because the wind-wave model is truncated at a first order of wave steepness, whereas the wave-current interaction is at a second order of wave steepness. The comparison is consistent in that the terms of the first order of interaction are compared, since there is no wave-current interaction at a first order of wave steepness, but strictly the second order wind-wave interaction terms should also be considered.

The magnitude of the wave-current and wind-wave interactions in the cases studied, at most 5% of the irrotational velocity, are not significant compared to the variations of the wind-induced current with the phase of the long waves. In order to predict the wave kinematics in the presence of a significant overlying airflow, the phase varying current must be taken into account. By using simply the mean current then, depending upon the phase and magnitude of the wind-induced current, the wave kinematics and in particular the velocity amplitude and crest velocity may be significantly over or under estimated. It is however difficult to envisage a wave-current model which could incorporate such a rapidly varying current and predict the resulting kinematics: it is difficult to unambiguously decompose the measured velocities to identify the phase varying current, but even more difficult to accurately predict the phase varying wind-induced current.

8. WATER SURFACE ELEVATION MEASUREMENTS

Measurements of the water surface elevation were made in order to investigate the effect of an airflow on the underlying long waves, and to examine the nature of the wind-generated waves. The measured surface elevation was decomposed into the underlying long waves and the superposed wind-generated waves. The purpose of the investigation was to attempt to relate the measured surface stresses and water wave kinematics to the observed water surface profile. The underlying long waves are considered first, examining both the wave parameters and the nature of the waveform itself. The wind-waves are then analysed, examining the variations in the wave parameters and the form of the wind-waves with both the free stream velocity and the phase of the underlying long waves.

8.1 Experimental Programme

The elevation of the water surface was measured for a 1 Hz, 22.5 mm amplitude wave with overlying airflows of $U_\infty = 3.1$, 4.1 and 5.1 m/s. Both the mechanically generated waves and the free stream velocities of $U_\infty = 3.1$ and 5.1 m/s correspond to those used for the kinematics measurements. The surface elevation was sampled at the same fetch ($x = 9.0$ m), so the measurements correspond to the kinematics measurements already presented. Measurements were not made for $U_\infty = 2.4$ m/s because preliminary tests showed that virtually no wind-waves were generated by this wind speed in the tank, and there appeared to be little change to the underlying long waves. An additional intermediate wind speed of $U_\infty = 4.1$ m/s was therefore used instead.

In addition to measuring the surface elevation for the combined wind and mechanically generated waves cases, the surface elevation for mechanically generated waves in the absence of wind was measured in order to assess the effect of the wind on the long waves. Conversely, to assess the effect of the long waves on the wind-waves, the surface elevation was measured for wind-generated waves in the absence of the long waves.

8.2 Experimental Methods and Data Analysis

The water surface elevation was measured using the wave gauges described in Chapter 3. For each case, data was sampled at a rate of 256 Hz for 800 seconds, which corresponded to 800 long waves. Preliminary experiments showed the smallest observed wind-waves to have a wavelength of approximately 0.05 m, and a frequency of 7 Hz. Sampling at 256 Hz therefore provided a minimum of 35 samples per wind-wave, and 256 samples per long wave, each of which was considered adequate to describe the respective wave forms.

To measure the phase velocity, the signals from two wave gauges of known spacing were cross correlated. It was considered that the optimal gauge spacing was between one half and two thirds of the expected wavelength, maximising the gauge spacing so as to reduce measurement errors, whilst still being certain that the gauges were closer than the shortest wavelength. For long waves, a spacing of exactly 1m was used, and for the wind-waves, 35 mm. In the latter case, the gauges were energised at high but different frequencies to minimise interference between the two gauges.

In order to legitimately compare the underlying long waves between airflow cases, it was essential that exactly the same mechanically generated waves were generated in each case. This was done by taking all the measurements involving the long waves whilst keeping the wave maker running continuously with a constant input. The mechanically generated waves with no wind were sampled first, after which the three airflow cases were set up and sampled. The fan was then switched off, and the long waves in the absence of wind re-sampled to ensure that they had not changed. As found from the preliminary data, the wave maker produced a stable output over long periods, and there was no apparent variation in the mechanically generated waves. The same wind speeds were then re-set, which could be done very accurately, and the surface measurements in the absence of the long waves taken. In all cases, after changing any of the flow parameters, at least one hour was allowed before sampling any data to give the system time to become steady.

The surface elevation in the combined wind and waves cases was decomposed in a similar way to the velocity data, as described in Chapter 3. The instantaneous surface elevation may be expressed as

$$\eta(x,t) = \overline{\eta}(x) + \tilde{\eta}(x,t) + \eta'(x,t) \tag{8.1}$$

where $\overline{\eta}(x)$ is the time averaged elevation relative to still water level, $\tilde{\eta}(x,t)$ is the underlying long wave, and $\eta'(x,t)$ the decomposed wind-waves and capillary ripples. An upcrossing analysis, similar to that described for the velocity data, was used to calculate the phase averaged long wave $\tilde{\eta}(x,t)$ and its amplitude and frequency. By subtracting the phase averaged waves and the wave set-up from the original time trace, the fluctuations $\eta'(x,t)$ were isolated. The time trace $\eta'(x,t)$ can be considered equivalent to the wind only wave records measured in the absence of the long waves. The wind only wave records were analysed in a similar way to the $\eta'(x,t)$ fluctuations, considering the wind-waves simply as a surface roughness, calculating the root mean square of the surface elevation, and also as waves, evaluating the average wave parameters.

8.3 Long Wave Analysis

8.3.1 Wave Forms

The measured wave frequency and amplitude for the underlying long waves are given in Table 8.1 below.

U_∞ (m/s)	f (Hz)	a (mm)	$\Re[a]_{amp}$ (mm)	$\Im[a]_{amp}$ (mm)
0.0	0.9993	22.10	21.71	0.08
2.4	0.9997	22.05	21.68	0.38
3.1	0.9995	22.03	21.63	0.40
4.1	0.9998	21.54	21.72	0.63
5.1	0.9997	21.40	21.58	0.89

Table 8.1: Long wave parameters

The long wave frequency, calculated using the upcrossing analysis described in Chapter 3, appears to remain constant with wind speed, the standard deviation between the values given above being less than 0.02%. The frequency could be expected to remain constant with wind speed, and the observed small variation demonstrates the constancy of the paddle output as well as the validity of the analysis routines used. The wave amplitude reduces with increasing wind speed, although the effect is very small with only a 3% reduction from the no wind to the fastest wind speed case. The waveforms for the no wind, $U_\infty = 3.1$ and 5.1 m/s cases are shown in Figure 8.1. The phase averaged mechanically generated waves in the absence of an overlying airflow appear to be symmetrical about the crest, and slightly non-linear. Compared with a linear wave of the same amplitude, the crest is slightly sharper and higher, with the trough broader and less deep. The wave is also compared in Figure 8.1a with a Stokes' second order wave defined by:

$$\eta = a\cos[kx - \sigma t] + \frac{ak}{4}\frac{\cosh kd}{\sinh^3 kd}(2 + \cosh(2kd))\cos[2(kx - \sigma t)] \qquad (8.2)$$

which shows an excellent agreement with the measured waveform. According to Dean's (1970) classification (Appendix D), the wave height, period and water depth suggest that the wave should be considered as being of second order. This would appear to be confirmed by the shape of the waveform itself.

With increasing wind speed, the waveforms appear to become increasingly asymmetric and more non-linear. Figures 8.1b and 8.1c shows that with increasing free-stream velocity, the troughs becomes progressively shallower, and the crests narrower and sharper. Asymmetry about the crest develops, whereby the gradient on the windward side of the crest is reduced, and that on the leeward side increased. The crest appears flatter and broader with relatively small curvature upwind of the crest, whilst being sharper and narrower with a much larger curvature on the downwind face, particularly close to the wave crest itself. This asymmetry corresponds to that observed in the near-surface velocities presented in Figure 6.10, which was due to the large wind-induced

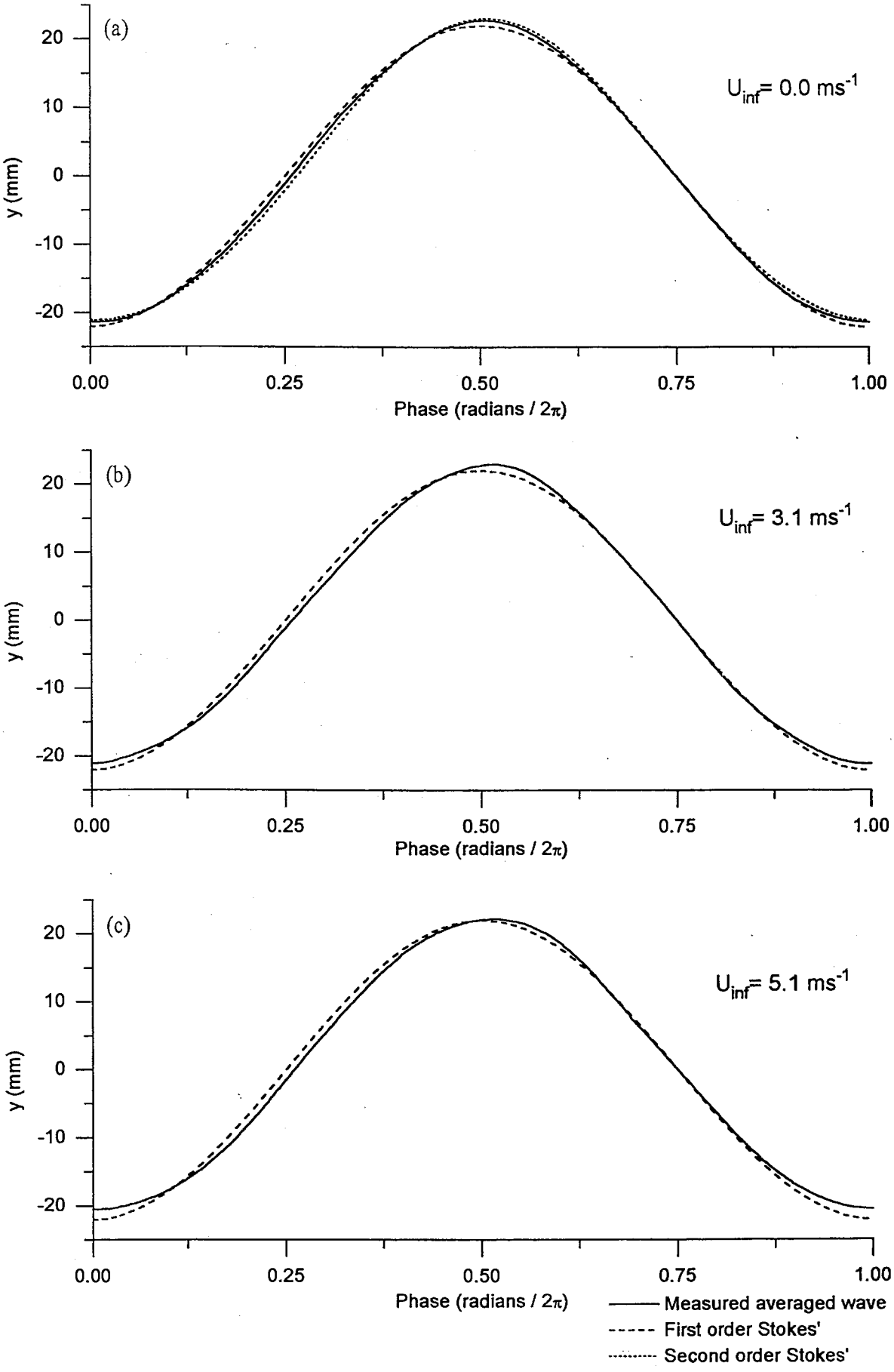


Figure 8.1: Comparisons between a cosine wave and measured waves
(a) U_{inf}= 0.0, (b) U_{inf}= 3.1 m/s, (c) U_{inf}= 5.1 m/s.

current on the windward side of the crest. The streamwise velocity gradients are reflected in the gradients of the surface profile, as would be expected, and the wave forms show similar phase shifts to those observed in the surface current. It appears that the effect of the airflow is to push the wave crest downstream, so producing the reduced curvature upstream of the crest, and the increased curvature downstream. The wave forms for the combined wind and wave cases are shown compared with the linear wave form of the same amplitude as the wave only case. The phase of all the waves is referenced relative to the zero down crossing, which is consistent with the kinematics data already presented. Clearly, the phase must be arbitrarily referenced when the waves become asymmetric.

The increasing wave asymmetry produces an out-of-phase wave component. Using a linear least-squares fitting routine, the measured phase averaged waves were resolved into components in phase with the surface elevation and in phase with the surface gradient, which are denoted by the amplitude of the real and imaginary components of the surface elevation respectively in Table 8.1. The magnitude of the in phase component appears to remain near constant with wind speed, but that of the out-of-phase component increases significantly, from less than 0.4% of the magnitude of the in phase component for the no-wind case, to 5% for the $U_\infty = 5.1$ m/s case. The apparent increasing non-linearity of the waves produces the expected shallower and broader trough and narrower crest, but the height of the crest reduces rather than increases. This leads to the observed small reduction in the wave amplitude. It appears that the reduced crest elevation is related to the large surface current, which tends to stretch the wave, so preventing the formation of a sharp crest.

8.3.2 Phase Velocity

The phase velocity of the long waves was calculated in each case using the wave records from the two gauge set up described in section 8.2. The correlation function between the two wave records was evaluated using a fast Fourier transform-based routine, and the time corresponding to the correlation function maximum found. This time was taken as the time for the wave to travel between the two gauges, which allowed the phase

speed of the waves to be calculated since the gauge spacing had been measured accurately.

The values of the measured phase velocity for the long waves are presented in Table 8.2, and compared with values predicted by irrotational theory and the combined wind-wave-current model developed in Chapter 7.

U_∞	Measured	First order	Bowden (1948) (3rd order)	Combined wind-waves
(m/s)	c (m/s)	c (m/s)	c (m/s)	c (m/s)
0.0	1.56	1.54	1.56	-
2.4	1.57	1.54	1.56	-
3.1	1.57	1.54	1.56	1.59
4.1	1.58	1.54	1.56	-
5.1	1.59	1.54	1.56	1.61

Table 8.2: Comparison of measured and predicted long wave phase velocity.

As would be expected, the values of the measured phase velocity increase with increasing free-stream wind velocity, since the wind-induced current increases with free-stream velocity. However, the differences in the measured phase velocity are very small, with the increase from the no wind to the fastest airflow case being less than 1.5%. The measured values are compared with a number of theoretical predictions. For second order waves, in the absence of wind, the dispersion equation to a third order of wave steepness is given by Bowden (1948) as

$$\sigma^2 = gk\tanh(kd)\left[1+\frac{a^2k^2}{8\sinh^4 kd}\left\{8\sinh^4(kd)+8\sinh^2(kd)+9-2\tanh^2(kd)\right\}\right] \quad (8.3)$$

The measured phase velocity for the waves in the absence of wind is in good agreement with the value predicted using the above equation (Table 8.2). The phase velocity measurements for the combined wind and waves cases are all greater than this predicted value. The measured variations in the phase velocity with the free stream velocity are however very small, so experimental uncertainties are large in relation to the differences between values. The values were, however, found by averaging the results of a large number of runs, with little variation between the values for each run observed, and the experiments were carried out in a systematic fashion, so errors in the relative values would therefore be expected to be considerably less than errors in the absolute values.

The measured phase velocities are also compared with the values predicted from the combined wind-wave-current models presented in Chapter 7. The phase velocities calculated from the model are between 1-2% greater than the measured phase velocity values. These effects were discussed in detail in section 7.4.3.

8.3.3 Wave Spectra

The wave spectra were found for each case using a fast Fourier transform. Because of the limited capacity of the processor used, each 800 second record was split in to twenty five segments, the spectrum found for each segment, and then all the spectra ensemble averaged. The wave spectra for the waves only and combined wind and long wave cases are given in Figure 8.2, plotted in semi-log co-ordinates. The waves only spectrum shows the expected behaviour with a very large sharp peak at 1 Hz, the fundamental frequency, then a second peak at 2 Hz, of two orders of magnitude less than the fundamental corresponding to the second harmonic, and finally a very small and rapidly reducing amount of energy at higher frequencies. The spectra for the $U_\infty = 3.1$, 4.1 and 5.1 m/s cases are shown compared with the wave only spectrum. With increasing wind speed, there appears to be a growth of the second and particularly the third harmonic peaks, which corresponds to the observed increasing non-linearity. The magnitude of the first harmonic peak (Table 8.3) at exactly 1 Hz appears to remain near constant, reflecting the near constant long wave amplitude.

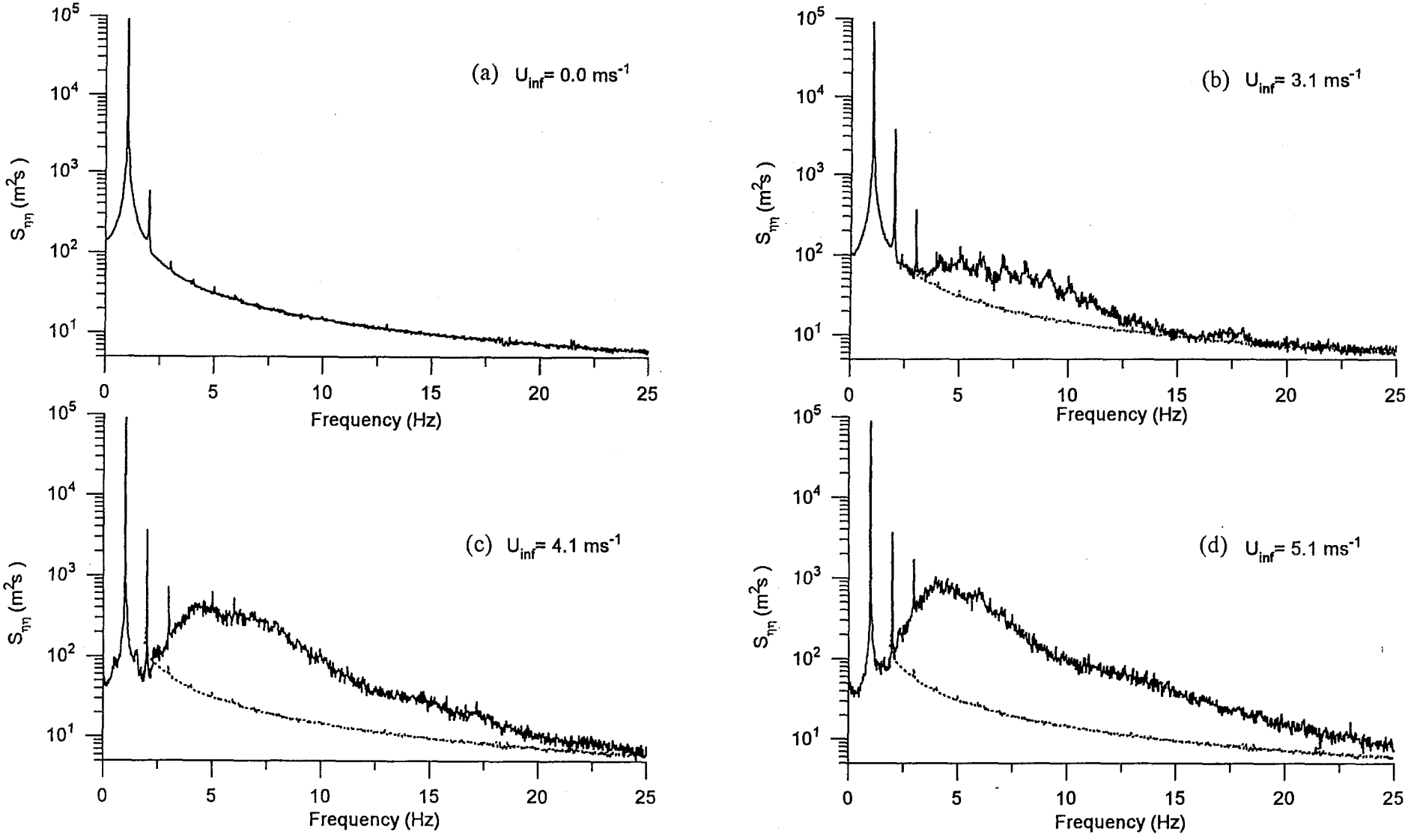


Figure 8.2: Spectra for combined wind and waves.
(a) U_{inf}= 0.0, (b) U_{inf}= 3.1 m/s, (c) U_{inf}= 4.1 m/s, (d) U_{inf}= 5.1 m/s.
------ no wind, ——— wind and waves.

U_∞ (m/s)	f_1 (Hz)	$S_{\eta\eta 1}$ (m^{2}s)	$S_{\eta\eta 2}$ (m^{2}s)
0.0	1.000	88470	4418
2.4	1.000	88580	4597
3.1	1.000	88560	4638
4.1	1.000	88840	6338
5.1	1.000	89000	7660

Table 8.3: Combined wind and waves spectra values

Although the value of the first harmonic increases by only a small amount, the total wave energy increases significantly, from the no-wind to the fastest airflow case. Some of this increase is in the first three harmonics ($S_{\eta\eta 1}$, $S_{\eta\eta 2}$ and $S_{\eta\eta 3}$) but most is a result of the growth of a broad peak at higher frequencies, which corresponds to the growing wind-waves (Figure 8.2). For the $U_\infty = 3.1$ m/s case, the peak is relatively small but broad, with its maximum at around 6 Hz. With increasing wind speed, the amplitude of the peak becomes greater, and the frequency of the maxima reduce. This corresponds to the expected increase in the amplitude of the wind-generated waves, and a reduction in the wave period with increasing free-stream velocity. The wind-wave spectral peaks are better defined at faster wind speeds, but appear to become double peaked, in particular for the $U_\infty = 5.1$ m/s case. The energy at higher frequencies also increases, reflecting the increased roughness of the surface by capillary ripples. The detailed nature of these spectra is discussed in the next section.

8.4 Wind-Wave Analysis

8.4.1 Wave Spectra

The spectra of wind-generated waves in the absence of mechanically generated waves with free-stream velocities of $U_\infty = 3.1$, 4.1 and 5.1 m/s are given in Figure 8.3. The spectra are characterised by two broad but distinct peaks, the frequency of which

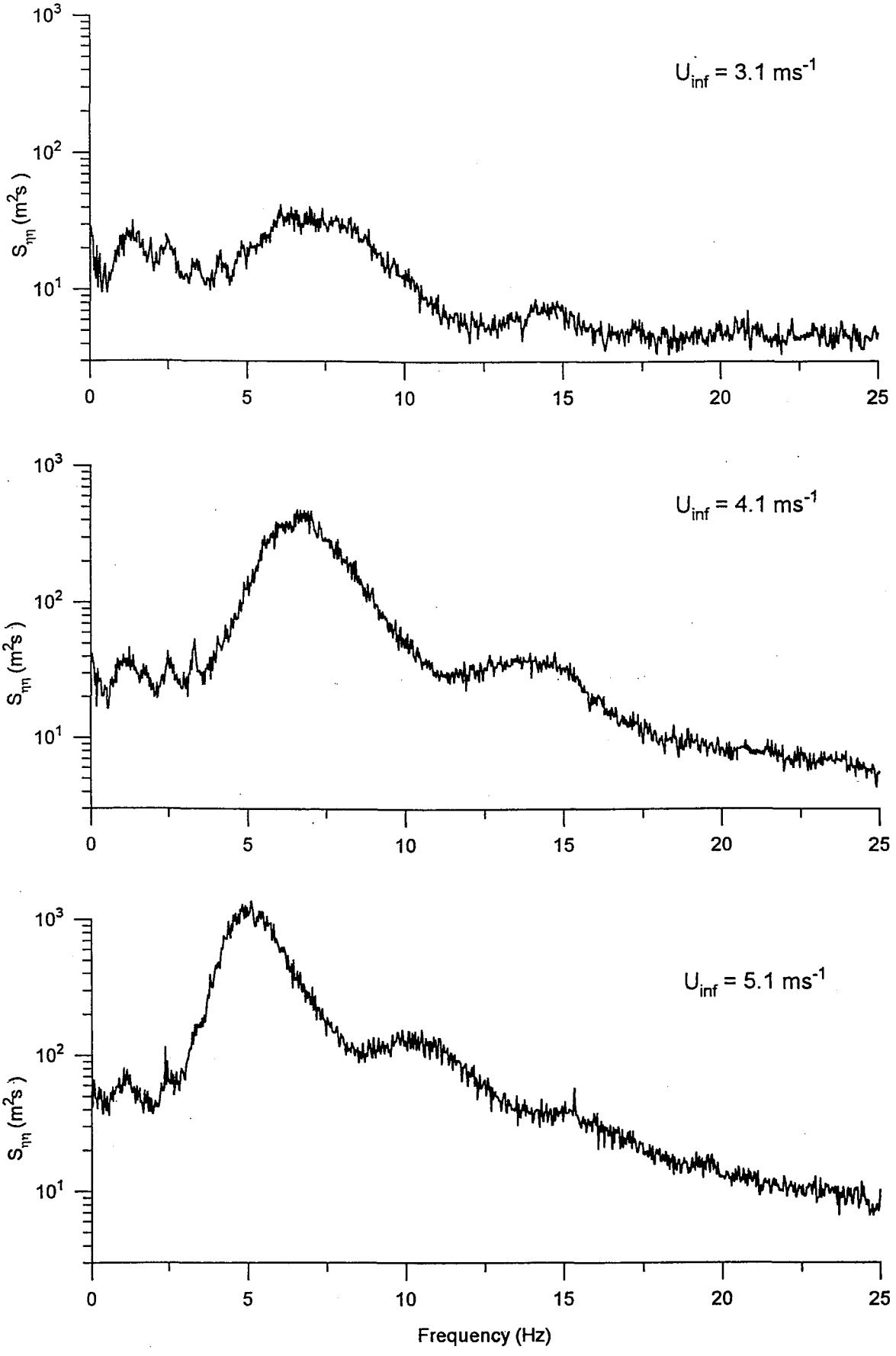


Figure 8.3: Wind wave spectra

decrease with increasing free-stream velocity. The dominant peak is at approximately 7 Hz for the $U_\infty = 3.1$ m/s case, moving to 5 Hz for $U_\infty = 5.1$ m/s, and increasing in height by more than one order of magnitude (Table 8.4). At lower frequencies there is very little energy. The decreasing frequency and increasing magnitude of the peaks with increasing free stream velocity corresponds to the generation of larger, longer period waves at faster wind speeds.

U_∞	f_1	$S_{\eta\eta 1}$	f_2	$S_{\eta\eta 2}$	$\int_0^\infty S_{\eta\eta} d\omega$
(m/s)	(Hz)	(m^2s)	(Hz)	(m^2s)	(m^2)
3.1	6.95	42.6	14.6	7.57	1068
4.1	6.59	480	14.0	37.5	2407
5.1	5.09	1370	10.3	151	4358

Table 8.4: Wind only waves spectral properties

In all cases, the second peak, which is approximately one order of magnitude less than the main peak, is at exactly twice the frequency of the main peak. It is evident that the main peak corresponds to the fundamental mode or first harmonic of the wind-waves, and the second peak to the second harmonic. This effect is most apparent for the fastest wind speed ($U_\infty = 5.1$ m/s), where the first three harmonics are all clearly identifiable. The comparative magnitudes of the peaks suggests that the wind-waves will be steep and non-linear, in comparison with the long waves.

The shape of the fundamental peak changes significantly with free-stream velocity. At the slowest wind speed, the peak is relatively symmetric, but becomes more asymmetric with increasing wind speed: the spectra are much steeper on the low frequency side of the peak than on the high frequency side. The peak also becomes sharper at higher wind speeds, with the waves appearing to become more narrow banded. In addition to the increasing amount of energy of the first few harmonics at faster wind speeds, there also appears to be an increase in energy at higher frequencies. As suggested in the previous

section, this is thought to correspond to the roughening of the surface by capillary waves and ripples.

The values of the frequency and spectral density at the peaks (Table 8.4) demonstrate the exponential type nature of wave growth. The peak frequency reduces by 5% from $U_\infty = 3.1$ to 4.1 m/s, but then by over 20% from $U_\infty = 4.1$ to 5.1 m/s. The total energy approximately doubles between $U_\infty = 3.1$ and 4.1 m/s, and then doubles again from $U_\infty = 4.1$ to 5.1 m/s. The peak values increase significantly, their magnitude being influenced both by the total energy and the shape of the peak.

The spectra for the combined wind and long waves were presented in Figure 8.2. To compare the spectra of the wind-waves in the absence of the long waves, with the combined wind and waves cases, that part of the spectra associated with the long waves must be removed. For the combined wind and waves cases therefore, the spectra of the decomposed wind-waves $\eta'(x,t)$, found by subtracting the phase averaged long wave from the original elevation record, were determined and are presented in Figure 8.4, together with the spectra for wind only waves. A small peak at 1 Hz remains, but is three orders of magnitude less than that in the combined wind-wave spectrum and is insignificant compared with the rest of the spectrum, suggesting that the decomposition approach is valid. (The relative wave amplitudes are confirmed by the wind-wave amplitudes which are presented in Section 8.4.4.)

From Figure 8.4, the spectral density for the $U_\infty = 3.1$ m/s case is less for the wind only waves than in the combined wind and waves case in the region of the spectral peak, suggesting the amplitude is also less. However, as the free stream velocity increases, the magnitude of the spectral peak for the wind only waves increases relative to that for the combined wind and mechanically generated waves: for the $U_\infty = 5.1$ m/s case, the magnitude of the peak is greater than that for the combined wind and waves case, suggesting that the amplitude of the wind only waves is greater.

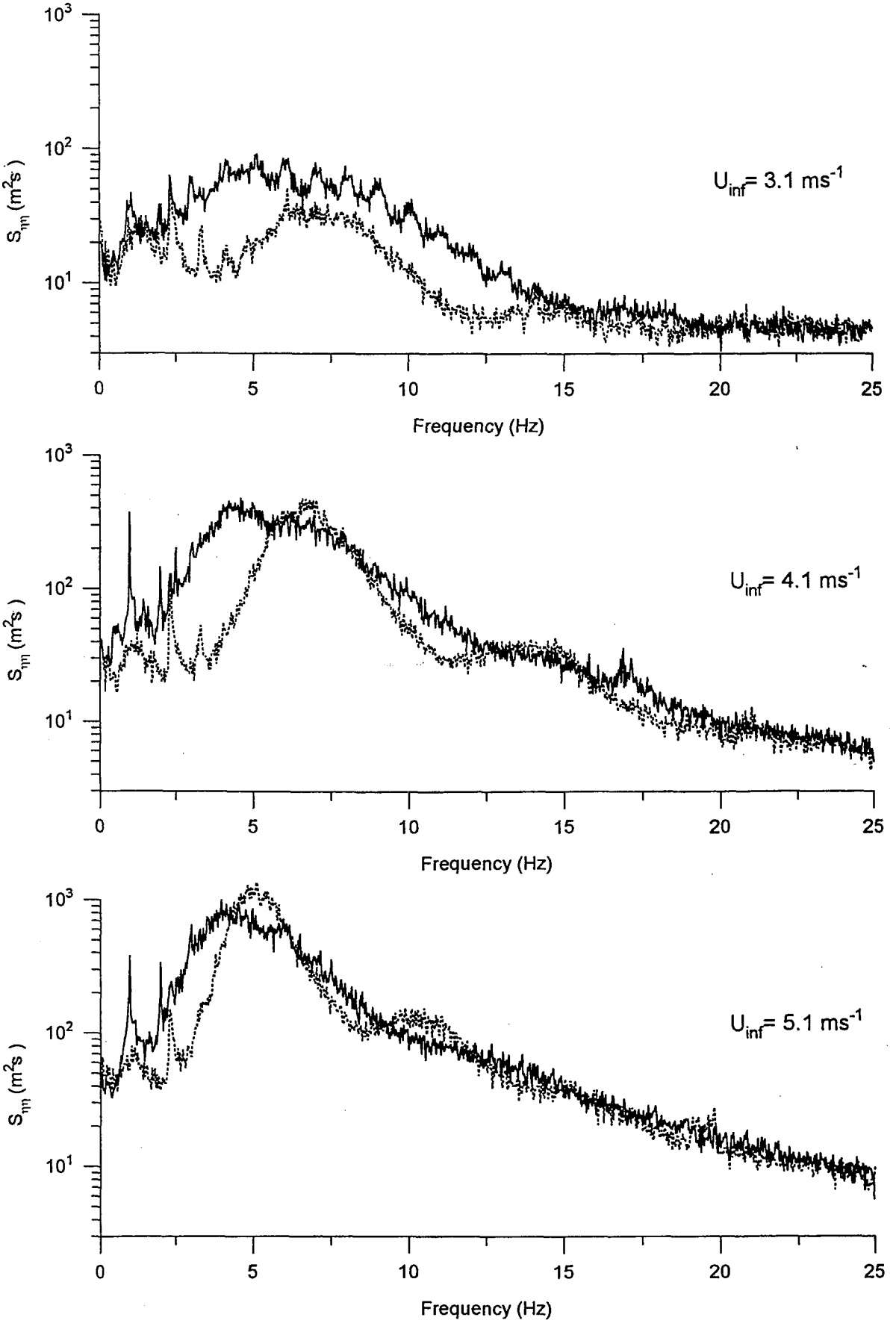


Figure 8.4: Spectra for decomposed ripple field from combined wind and wave cases
------ no waves ——— wind and waves.

These variations reflect the significant difference in the form of the spectra for the wind-waves in the presence of the long waves compared with the wind only spectra. The peak corresponding to the fundamental frequency of the wind-waves in the presence of the long waves is much broader than for the wind only cases. At the faster wind speeds, $U_\infty = 4.1$ and 5.1 m/s, it is apparent that there are two peaks forming the broad fundamental peak, and these are too close together to be harmonics. The spacing of these peaks reduces with increasing free-stream velocity, as the fundamental frequency reduces. The peak for the wind only waves appears to lie between the two peaks for the combined wind and waves cases. The larger of the two peaks lies at a frequency lower than the wind only peak, and the slightly smaller peak is at a higher frequency. The same asymmetry observed in the wind only spectra is apparent in the combined wind and waves spectra, with much steeper gradients on the low frequency than on the high frequency side.

It appears that the effect of the long waves on the wind-wave spectra is to cause a spreading of the energy in the frequency domain. In all cases, at the frequency of the wind only waves' first harmonic, there is a local trough in the spectrum in the presence of long waves, with peaks on either side. This behaviour is also apparent at higher frequencies: for the $U_\infty = 5.1$ m/s case, at 10 Hz the second harmonic for the wind only waves shows a distinct peak, which corresponds to a localised trough in the combined wind and wave spectrum. Above approximately 15 Hz, for each wind speed, the wind only and combined wind and wave spectra are almost identical, suggesting similar surface roughness conditions in the presence and absence of the long waves.

It is thought that the apparent spreading of the energy in the frequency domain and the resulting dual peaks around the wind only fundamental frequency are a result of the modulation of the wind-wave frequency, as measured by a fixed gauge, due to advection by the varying surface velocity. Phillips (1981) and Chu, Long & Phillips (1992) considered a train of short monochromatic gravity waves superposed upon a series of long waves. He found that the long and short waves interact, causing the short waves to be distorted. The frequency of the short waves measured by a fixed gauge, the so-called 'apparent frequency', is subject to large modulations as a result of Doppler shifting by

the long wave orbital velocities. Phillips found that relative to the intrinsic frequency of the short waves, the apparent frequency at the crests of the long waves is increased, but reduced in the long wave troughs.

For a long wave of frequency F and slope AK, and a short wave travelling in the same direction with intrinsic frequency f, Phillips (1981) found that the apparent frequency at the long wave crest is:

$$f_{app} = f\left[1 + \frac{f}{F} AK(1 + AK)\right] \tag{8.4}$$

and at the trough

$$f_{app} = f\left[1 - \frac{f}{F} AK(1 - AK)\right] \tag{8.5}$$

The apparent frequency is a maximum at the crest and a minimum at the trough. At a first order of approximation, the frequency variation with the phase of the long wave will be sinusoidal, so equations 8.4 and 8.5 may be combined to give the approximate variation in apparent frequency with the phase of the long wave

$$f_{app} = f\left[1 + \frac{f}{F} AK\sin(kx)(1 + AK\sin(kx))\right] \tag{8.6}$$

In order to investigate the effect of this frequency modulation on the wave spectra, consider a single frequency component, a thin 'slice' of the wind only waves spectrum at the fundamental frequency. This 'slice' of spectrum corresponds to a monochromatic regular wave, and its frequency is taken as the intrinsic frequency of the wave. If this short wave were then superposed on a long wave, and the frequency of the short waves measured using a fixed gauge, the measured or apparent frequency would vary with the phase of the long wave. The resulting apparent frequency variation to a first order of

magnitude can be calculated using equation 8.6, and is shown in Figure 8.5. The distribution of the short wave's energy with frequency will no longer be a single spike at the intrinsic frequency, but will be spread over a range of frequencies from a minimum frequency at the trough to the maximum at the crest. Assuming that the amount of energy within a given frequency band is proportional to the fraction of the phase angle for which the apparent frequency of the short waves lies within that frequency band, then the modified spectrum may be calculated.

The 'apparent' spectrum for this monochromatic short wave, which has been superposed on a long wave, is shown in Figure 8.6. The total energy of this modified spectrum is equal to that of the single spike. The spectrum for this single component shows that in the presence of long waves, the minimum spectral density is at the intrinsic frequency, with two maxima at the extreme frequency values, corresponding to the apparent frequencies at the crest and trough. It shows that the spectrum is asymmetric about the intrinsic frequency, resulting from the apparent frequency at the crest being larger than the value at the trough, relative to the intrinsic frequency. The spectral density is therefore greater at a given frequency which is less than the intrinsic frequency, compared with that at the corresponding frequency which is greater than the intrinsic frequency.

The behaviour demonstrated by this simple model is very similar to that observed in the measured combined wind and long wave spectra. The observed double peak with a local minimum at the frequency of the wind only waves' spectral peak, is very similar to the spreading effect shown with the single component in Figure 8.6. The asymmetric spectral peaks and the higher peak at the lower frequency corresponds to the asymmetries introduced by Phillips' equations for the apparent frequency, this effect also being apparent in Figure 8.6. The smoothing of the spectra at higher frequencies may also be related to this spreading of energy for the higher harmonics. The broader spectral peaks at lower wind speeds reflect the larger phase variation in the apparent frequency for the higher frequency wind-waves.

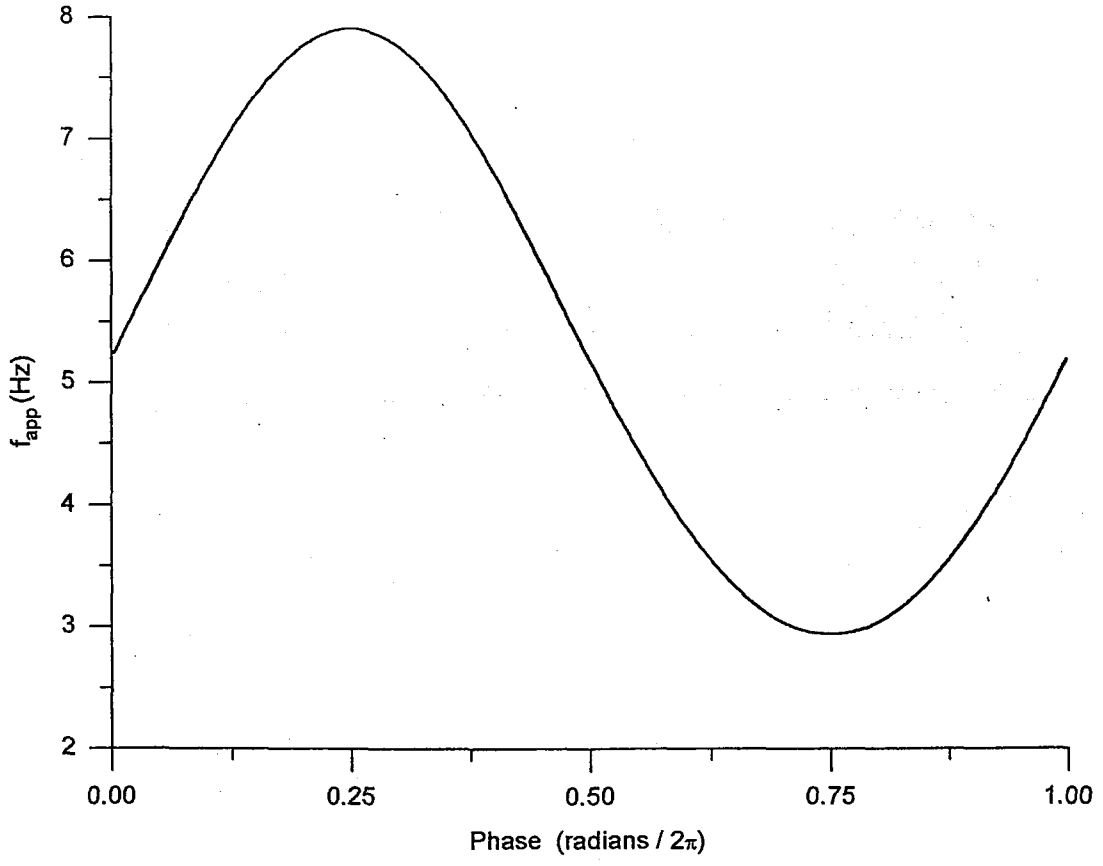


Figure 8.5: Variation of apparent frequency of wind waves with phase of long wave

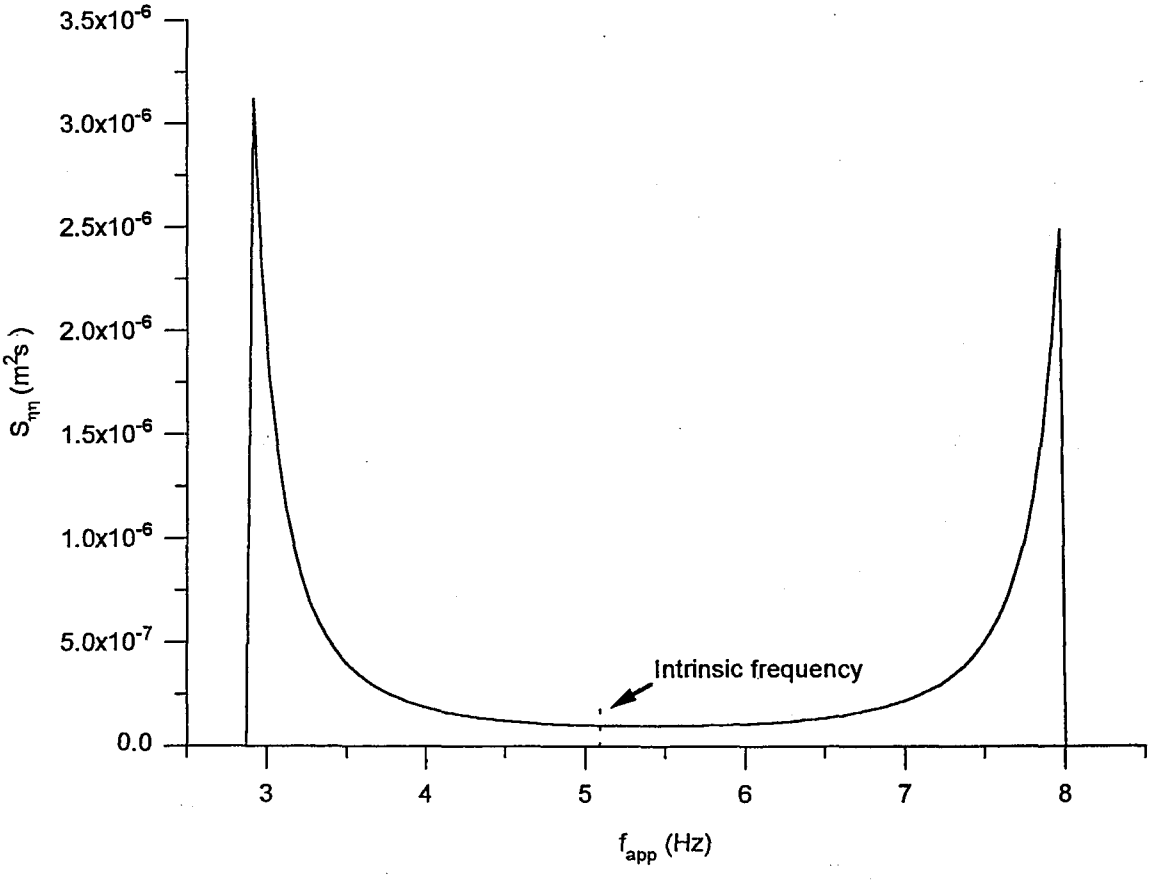


Figure 8.6: Effect on spectrum due to modulation of apparent frequency

The combined wind and long wave cases are much more complex than the monochromatic long and short waves in the absence of an airflow which are considered in this model. The wind-waves are broad-banded with higher harmonics and, in addition to the long wave orbital velocities, there is also the varying wind-induced velocity, which produces a phase varying surface current and a highly-sheared near-surface current profile. Phillips' simple model does not permit modelling of such effects, but does provide a clear indication of the processes involved.

8.4.2 Frequency

The frequency of the wind-waves was found using an upcrossing analysis routine. Because of the relatively small amplitude of the wind-waves, the small amount of noise on the surface elevation signal becomes significant and disrupts the analysis routine. The wave records were therefore filtered above 20 Hz before carrying out the upcrossing analysis, cutting out the capillary ripples and any (spurious) electronic noise. The time averaged wind-wave frequency was calculated in each case and, for the wind-waves in the presence of long waves, the phase averaged frequency of the wind-waves was also calculated.

The time averaged frequencies of the wind-generated waves, both in the absence and the presence of the long waves are given in Table 8.5.

	Wind only	Combined wind and waves	
U_∞ (m/s)	$\bar{f}$ (Hz)	$\bar{f}$ (Hz)	$\tilde{f}_{amp}$ (Hz)
3.1	6.888	6.083	1.324
4.1	6.713	5.934	1.392
5.1	5.544	5.180	1.280

Table 8.5: Wind-wave frequency

The frequency of the wind-generated waves decreases with increasing free-stream velocity, decreasing by 2.5% between $U_\infty = 3.1$ and 4.1 m/s, and almost 20% between $U_\infty = 4.1$ and 5.1 m/s. The decreasing frequency reflects the generation of larger, longer period waves at higher wind speeds, and the larger reduction in frequency at higher wind speeds again demonstrates an exponential dependence on wind speed. The average frequency for the combined wind and waves cases is approximately 10% less than the average frequency for the corresponding wind only cases. Because the average friction velocity is greater for the wind only cases than for the combined wind and waves, larger lower frequency waves would be expected for the wind only case, but this is the opposite to the observed trend. It seems probable that advection by the orbital velocities described in the previous section, as well as by the varying wind-induced current causes an increased mean apparent frequency.

The amplitude of the variation of the wind-wave frequency with the phase of the long waves also reduces with increasing free-stream velocity (Table 8.5). The maximum and minimum frequencies appear to correspond with the frequencies of the two peaks for the spectra (Figure 8.4). The amplitude of the variation reduces with increasing free-stream velocity, as predicted by equations 8.4 and 8.5, since the amplitude of the apparent frequency variation is proportional to the frequency of the short waves.

The variation of the frequency of the wind-waves with the phase of the underlying long waves appears to be approximately in-phase with the long wave surface elevation, but shows distinct asymmetry, particularly at slower wind speeds (Figure 8.7). This asymmetry appears to reflect the measured surface current, which showed larger values and steeper streamwise gradients on the windward face than at the corresponding phase on the leeward side of the crest. The shape of the distribution changes from being very broad crested at $U_\infty = 3.1$ m/s, to being almost sinusoidal at $U_\infty = 5.1$ m/s. The flattening of the peak of the frequency variation at the wave crest is apparent for the $U_\infty = 3.1$ and 4.1 m/s cases, with the distribution being relatively sinusoidal up to a frequency of 7 Hz, but then waves do not appear to be formed at higher frequencies. The shape of the distribution, which is similar to Phillips' (1981) model, (equations 8.5 and 8.6) suggests that advection by the orbital velocities would produce higher apparent

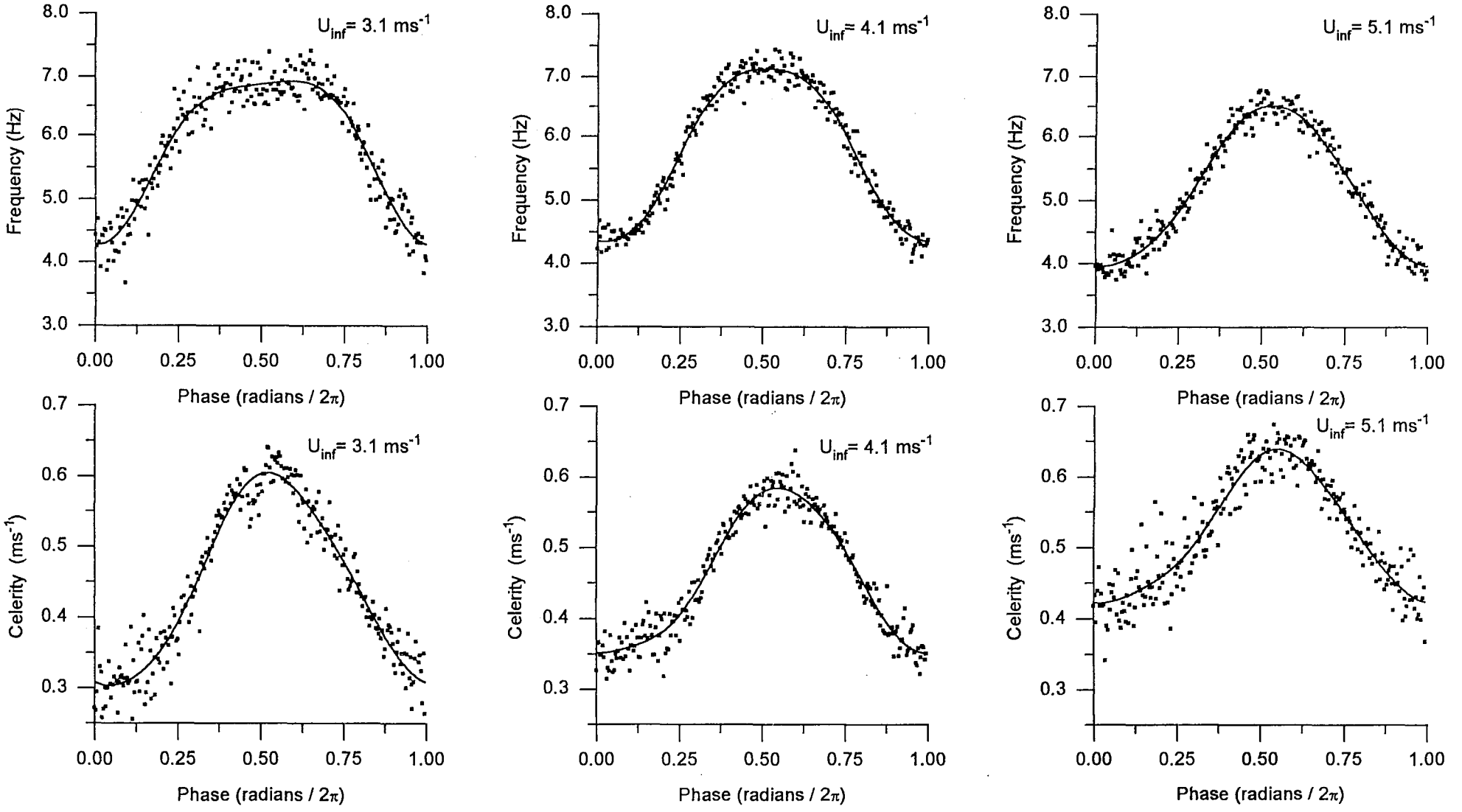


Figure 8.7: Variation of wind wave frequency and celerity (or phase velocity) with the phase of the long wave. ▪ measured data, —— best fit line

frequencies than those observed. For the $U_\infty = 4.1$ m/s case, the intrinsic wave frequency is smaller, so the 7 Hz ceiling has less effect; at $U_\infty = 5.1$ m/s, the frequencies are well below this value, so there is no flattening of the peak. However, in the $U_\infty = 5.1$ m/s case, the opposite effect is perhaps apparent in that the troughs of the distribution become wider and flatter, suggesting there is also a lower wave frequency limit. The orbital motion of the underlying wave is changing relatively little between the three flow cases, suggesting that these effects are related to the phase varying wind-induced current.

8.4.3 Phase Velocity or Wave Celerity

The phase speed of the wind-waves was calculated using the zero upcrossing analysis described above, for both the wind only and combined wind and waves cases. The cross correlation routine used to calculate the phase velocity of the long waves could not be used for the wind-waves because the phase velocity had to be calculated at a number of phases throughout the wave cycle. The time difference between corresponding zero upcrossings in each record is the time for the wind-wave to travel the measured distance between the two gauges, and hence the phase velocity can be calculated. The phase of the long wave corresponding to the average of the zero upcrossing times was calculated, which enabled phase averaging to determine the variation of the phase velocity of the wind-waves with the phase of the underlying long wave. This analysis method, as well as the spacing between the gauges, was verified by measuring the phase velocity of the mechanically generated wave in the absence of wind, with the gauges in their 35 mm spacing configuration. The discrepancy with the phase velocity measured by the gauges at a spacing of 1 m was less than 4%, which is excellent agreement considering the close gauge spacing.

The mean phase velocity of the wind-waves increases with free-stream velocity in both the presence and absence of long waves (Table 8.6). This is a result of the waves generated at faster wind speeds having a greater wavelength, hence a larger phase velocity, and of the increasing wind-induced surface current, which will advect the waves more quickly. There is a relatively small increase in the average phase velocity

between $U_\infty = 3.1$ and 4.1 m/s, only about 2%, but a much larger increase, almost 20% between $U_\infty = 4.1$ and 5.1 m/s. This again demonstrates the exponential nature of wave growth with wind speed. The phase velocity for the combined wind and waves cases is approximately 20% greater than for the wind only cases. This would most likely seem to be a result of the modulations caused by the orbital velocities and varying current.

	Wind only	Combined wind and waves	
U_∞ (m/s)	$\bar{c}$ (m/s)	$\bar{c}$ (m/s)	$\tilde{c}_{amp}$ (m/s)
3.1	0.363	0.449	0.151
4.1	0.371	0.458	0.116
5.1	0.434	0.520	0.108

Table 8.6: Wind-wave phase velocity.

The variations in the phase velocity of the wind-waves with the phase of the long waves for the three wind speed cases are shown in Figure 8.7. The phase velocity is approximately in-phase with the surface elevation, with the maximum phase velocity at the wave crest. The distribution of the phase velocity is however highly asymmetric about the wave crest. Between the wave trough and zero upcrossing, there is only a small increase in phase velocity but, between the zero upcrossing and crest, the phase velocity increases very rapidly. On the leeward side of the crest, the phase velocity reduces much more slowly, and the values are considerably larger on the leeward face than at the corresponding phase on the windward face. This asymmetry increases with increasing free-stream velocity, and appears to reflect the asymmetry observed in the near-surface velocities. The surface velocity on the upwind face of the crest is greater than at a corresponding phase on the leeward face but, as shown in Figure 6.11, the velocity gradients $\partial u/\partial y^*$ are also much greater on the windward face of the crest. From the discussion of wave-current interactions in section 7.2, the largest increase in phase velocity for a given surface current is for a uniform current, whilst the smallest is for a highly sheared current. This effect arises as a direct consequence of the vorticity

distribution. The current profiles on the leeward side of the crest are relatively uniform compared with the highly sheared current on the windward face, and so, despite the greater surface current on the windward face of the crest, the greatest increase in phase velocity will be on the leeward side of the crest. The points of greatest asymmetry are either side of the trough, where the shear of the current profiles changes most rapidly. The phase velocity of the waves is therefore dependent upon the surface current and the near-surface current profile or the vorticity distribution.

The amplitude of the phase velocity variation decreases with increasing free-stream velocity (Table 8.6). This corresponds to the reducing amplitude of the apparent frequency with increasing free stream air velocity, due to the increasing wave length and the reducing intrinsic frequency.

8.4.4 Amplitude

The upcrossing analysis used to find the frequency of the wind-waves was also used to determine the wind-wave amplitude, which was defined as half the difference in elevation between the wave crest and trough. The wind-waves were also considered simply as a surface roughness, and the root mean square surface elevation calculated for both the wind only case and for the decomposed $\eta'(x,t)$ wind-waves in the combined wind and long waves cases. The amplitudes and root mean square elevations were phase averaged for the combined wind and waves cases, and the mean amplitude and root mean square elevation calculated in all cases.

The time averaged amplitude of the wind-waves is given below in Table 8.7. The amplitude of the wind-waves increases with wind speed for both the wind only and combined wind and waves cases. For the $U_\infty = 3.1$ and 4.1 m/s cases, the wave amplitude in the combined wind and wave cases is approximately 20% greater than for the wind only cases, but for the $U_\infty = 5.1$ m/s case, the amplitude for the wind only case is 10% greater than for the combined case. The latter is to be expected, since the average friction velocity is greater in the wind only cases than for the combined wind and waves. The larger amplitude at the slower velocities for the combined wind and

waves cases is perhaps due to the fluctuations in the friction velocity, the peak values having a proportionately greater effect than the minima, compared with the mean value. These values are very small, and there is considerable scatter in the data, but the amplitudes were averaged over a large number of waves, and the trends appear to be consistent. The values of the amplitude are consistent with the mean root mean square surface elevation.

	Wind only	Combined wind and waves	
U_∞ (m/s)	$\bar{a}$ (mm)	$\bar{a}$ (mm)	$\tilde{a}_{amp}$ (mm)
3.1	0.540	0.668	0.0250
4.1	1.194	1.357	0.0608
5.1	2.376	2.171	0.0688

Table 8.7: Wind-wave amplitude

The magnitude of the variation in the phase averaged wind-wave amplitude for the combined wind and waves cases increases with free-stream velocity, reflecting the increasing amplitude of the friction velocity variation. The relatively large increase between $U_\infty = 3.1$ and 4.1 m/s corresponds to a large increase in the amplitude of the phase variation of the friction velocity. Plots of the variation of the wave amplitude with the phase of the long waves are given in Figure 8.8. For the $U_\infty = 4.1$ and 5.1 m/s cases, the amplitude minimum is on the windward face of the crest, between the zero upcrossing and crest. The amplitude is a maximum at the corresponding phase on the leeward side of the crest, between the crest and zero downcrossing. There is a second peak in the wave amplitude around the long wave trough. The wind-wave amplitude appears to correspond to the wind-induced surface current, with the minimum amplitude corresponding to the maximum wind-induced current, and the maximum amplitude to the minimum current. The correlation appears to be with the wind-induced current, rather than the total surface velocity which includes the effect of the underlying wave motion.

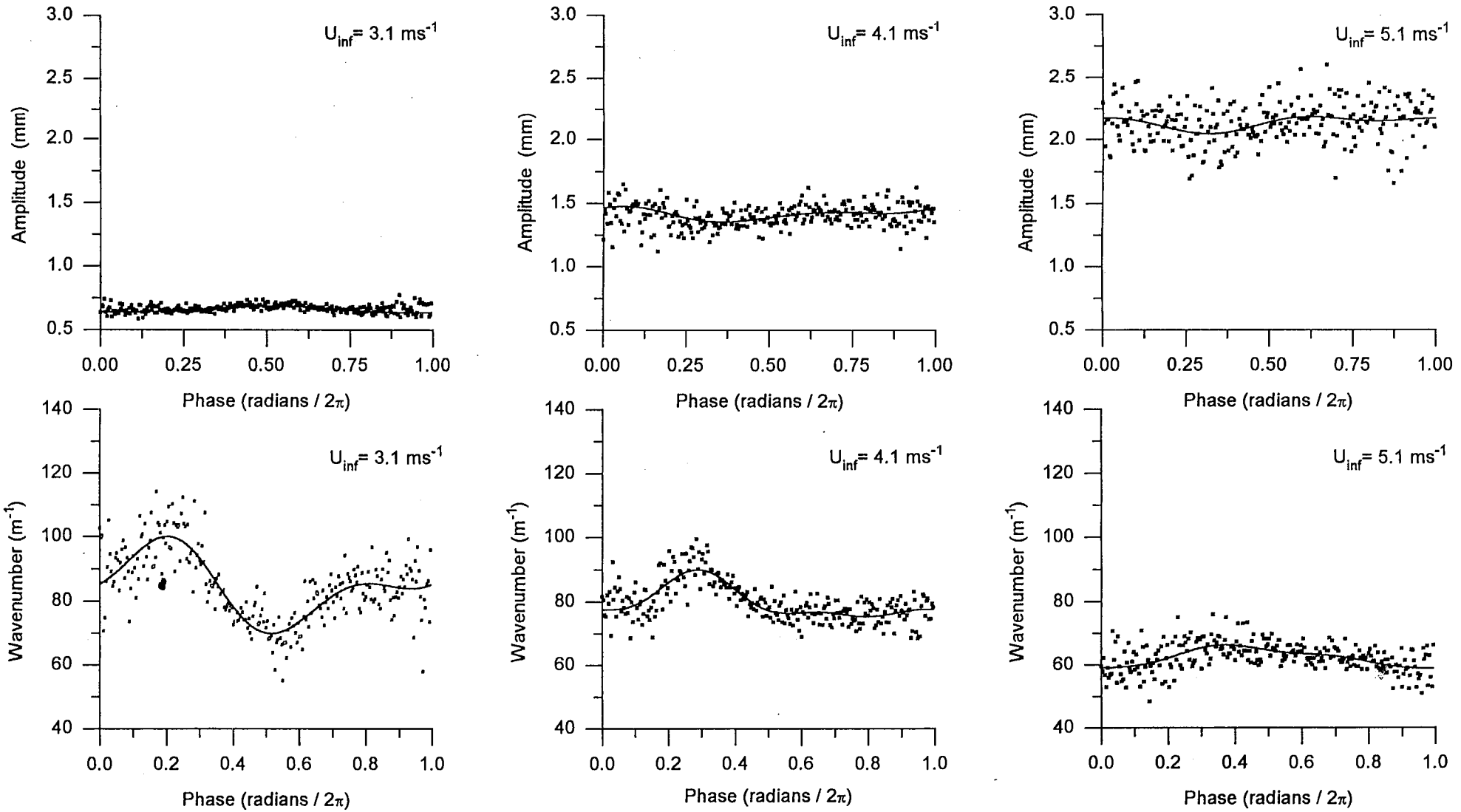


Figure 8.8: Variation of wind wave amplitude and wavenumber with the phase of the long wave. • measured data, ——best fit line.

The variation in amplitude of the wind-waves appears to correspond to the measured variations in the total surface shear stress and the value of C in the airflow. The minimum amplitude, which is on the windward face of the crest, corresponds to the minimum shear stress and the maximum value of C, the latter suggesting that the water surface is smoothest, in agreement with the measured amplitude. The maximum amplitude, which is between the crest and zero down crossing, corresponds to the maximum surface shear stress and the minimum C, which implies the roughest water surface. The variation in the amplitude of the wind-waves with the phase of the long waves for the $U_\infty = 3.1$ m/s case is very small. Indeed, in each of the three cases presented in Figure 8.7, the scatter of the data is such that definite conclusions are difficult to make. However, the remarks noted above relating to the faster flow cases appear consistent with earlier results.

There are two mechanisms which could account for the observed variation in the wind-wave amplitude with the phase of the long waves. Consider first the interaction between the long and short waves, which was described in section 8.4.1. Longuet-Higgins and Stewart (1960) found that short waves become shorter and steeper at the crests of long waves, and longer and less steep at the troughs: the amplitude of the short waves correspondingly increases at the long wave crests, and reduces in the troughs. For long waves, with a wave length of the same order as the water depth, and short waves, which may be considered as deep water waves with a frequency considerably greater than that of the long waves, Longuet-Higgins and Stewart (1960) found that the amplitude of the short waves varies as

$$a' = a_1 + a_1 a_2 k_2 \left[\frac{1}{4} \tanh(k_2 d) + \frac{3}{4} \coth(k_2 d) \right] \cos(k_2 x - \sigma_2 t - \pi) \qquad (8.7)$$

where the short waves are characterised by a_1, k_1, and the long waves by a_2, k_2, σ_2. For the $U_\infty = 4.1$ and 5.1 m/s cases, the amplitude of the variation calculated from equation 8.7 is approximately three times the observed amplitude, and the experimental data showed neither a distinct maximum at the wave crest, nor a minimum at the trough.

For the $U_\infty = 3.1$ m/s case, the phase of the variation in the amplitude is closer to that predicted by Equation 8.7, but the amplitude predicted is approximately 2.5 times larger than that measured. It appears therefore that the interaction between long and short waves does not account for the observed amplitude variations.

The second possible mechanism for the observed amplitude variations is the variation in near-surface velocities. The stretching of the wind-waves by the increased surface velocity would be expected to reduce the amplitude of the waves. For irrotational waves on a uniform current $\overline{U}$ which varies only slowly in the streamwise direction, Sleath (1984) notes that the change in the wave amplitude caused by the current is

$$\frac{a}{a_o} = \left[\frac{\left(1 + \frac{2k_o d_o}{\sinh(2k_o d_o)}\right)\left(1 - \frac{k\overline{U}}{k_o c_o}\right)}{\left(\frac{k_o}{k} - \frac{\overline{U}}{c_o}\right)\left(1 + \frac{2kd}{\sinh(2kd)}\right) + \frac{2\overline{U}}{c_o}} \right]^{\frac{1}{2}} \tag{8.8}$$

where k_o, c_o, d_o and a_o are the wave number, phase velocity, depth and amplitude respectively in the absence of the current, and k, c, d and a, the corresponding parameters in the presence of the current. The depth in the presence of the current is defined by

$$d = d_o - \frac{\overline{U}^2}{2g} \tag{8.9}$$

In the present situation, the wave motion is not irrotational, and the current is neither uniform nor varying slowly in the streamwise direction, so there is considerable uncertainty as to the validity of the above approach. However, some indication of the expected phase and magnitude of the variation in the wind-wave amplitude caused by the varying wind-induced current can be obtained from equation 8.8. To calculate the approximate amplitude of the variation, the difference between the amplitude of the wind-waves at the long wave trough, where the wind-induced current is a minimum, and

the wind-wave amplitude between the zero upcrossing and the crest, where the current is a maximum (Figure 6.11), was calculated using equation 8.8. The wind-wave characteristics at the wave trough were therefore taken as the no-current case, those around the zero upcrossing as the wave characteristics in the presence of the current, and the magnitude of the current as the difference in the measured current between the two points.

The current itself is clearly non-uniform, but it can be approximated to a uniform current by calculating the equivalent uniform current. Because the wind-waves are of large wave number, it is only the near-surface wind-induced current which is of interest. Since the large currents at the surface itself could not be measured, an approximation to the equivalent uniform current was taken as the current measured closest to the water surface. Calculation of the equivalent uniform current for the time averaged velocities using estimated near-surface velocities showed this to be a good approximation.

As already discussed, the phase of the variations in the wind-wave amplitude appear to correspond to the wind-induced currents, except for the $U_\infty = 3.1$ m/s case. For the $U_\infty = 5.1$ m/s case, the change in amplitude between the trough and zero upcrossing was within 25% of that measured which, considering the assumptions made, is a good agreement. Both the phase and the amplitude of the variations in wind-wave amplitude therefore appear to correspond to the wind-induced current, suggesting it is the wave-current interaction, rather than the wave-wave interaction, which has the dominant effect on the wind-wave amplitude.

8.4.5 Wavenumber

The average wave numbers for the wind only and combined wind and waves cases, calculated from the measured wind-wave phase velocity and frequency are given below in Table 8.8. The wave number decreases with increasing free-stream velocity since, as might be expected, longer waves are generated at higher wind speeds. The wave numbers for the combined wind and waves cases are 20% less than those for the wind only cases, corresponding to the faster phase velocity of the wind-waves in the presence

of the long wave. It appears that the long waves stretch the wind-waves, producing smaller values of the wavenumber. There is a large decrease in wavenumber between the $U_\infty = 4.1$ and 5.1 m/s cases compared with that between the $U_\infty = 3.1$ and 4.1 m/s cases, demonstrating again the exponential nature of wave growth with wind velocity.

	Wind only	Combined wind and waves	
U_∞ (m/s)	$\bar{k}$ (m^{-1})	$\bar{k}$ (m^{-1})	$\tilde{k}_{amp}$ (m^{-1})
3.1	119.2	85.18	15.09
4.1	113.8	81.48	7.260
5.1	80.27	62.57	3.692

Table 8.8: Wind-wave wavenumber

The variations in the wave number with the phase of the long waves for the combined wind and waves cases are given in Figure 8.8. In all cases, the maximum wavenumber, and hence the minimum wave length is around the zero upcrossing, moving downstream towards the crest with increasing wind speed. There is a distinct narrow peak at this maximum, less than one quarter of a wavelength wide, with little variation in the wavenumber over the rest of the wave. At the wave crest for the $U_\infty = 3.1$ m/s case, the wavenumber appears to be a minimum but, with increasing free-stream velocity, the value increases. For the two faster cases the minimum is at the trough, but is not as distinct as the maximum.

Longuet-Higgins and Stewart's (1960) long wave/short wave analysis suggested that the wavelength of the wind-waves increases in the troughs, and reduces at the crests. Using the same notation as equation 8.7, and under the same conditions, the wave number is modified according to

$$k' = k_1 + a_2 k_1 k_2 \coth(k_2 d)\cos(k_2 x - \sigma_2 t - \pi) \tag{8.10}$$

The wavenumber would therefore be a maximum at the crest, and a minimum in the trough. In the absence of any wind-generated currents, the long wave/short wave interaction would lead to a variation in wavenumber in phase with the surface elevation. Any departure from such a variation is likely to be a result of the wind-generated current. The plots of the wavenumber variation in Figure 8.8 show an increase between the trough and the zero upcrossing, and a decrease from the zero downcrossing to trough, as predicted by Longuet-Higgins and Stewart (1960). However, for the $U_\infty = 3.1$ m/s case in particular, there is a rapid reduction in the wavenumber between $\phi = 0.15$ and 0.50, and hence an increase in the wavelength compared with that expected from equation 8.10. This region corresponds to the phase of the maximum wind-induced current (Figure 6.11). The large wind-induced current causes an increase in wavelength, and hence the apparent reduction in wavenumber. Beyond the wave crest, the wind-induced current has a relatively small value, and hence the wavenumber increases, corresponding to a reduction in wavelength. The observed amplitude of the wavenumber variation is approximately 50% less than that calculated from equation 8.10 due to the wavenumber reduction at the crest caused by the wind-induced current.

Similar patterns were observed for the $U_\infty = 4.1$ and 5.1 m/s cases, although the effect is not so apparent at these faster wind speeds as for the $U_\infty = 3.1$ m/s case. The phase at which the wavenumber starts to reduce as a result of the wind-induced current moves progressively downstream towards the crest with increasing wind speed, and the reduction itself becomes less pronounced. This suggests that, although the wind-generated current is greater at faster wind speeds, the wave-wave interaction effect becomes more dominant than the wave-current effect at faster wind speeds. This corresponds to the observed exponential type growth of the wind-waves with increasing free stream velocity, compared with the linear dependence of the wind-generated current on the free stream velocity.

8.4.6 Surface Roughness

Two measures of surface roughness are presented in Figure 8.9, and Tables 8.9 and 8.10. The wind-wave steepness ak and the roughness Reynolds number R_k each provide

some measure of the relative roughening of the water surface by the wind-generated waves. Steeper wind-waves, with a larger *ak*, would be expected to signify a rougher water surface. The data below (Table 8.9) shows that the average wind-wave steepness increases with increasing free stream wind velocity, as might be expected. The steepness of the wind-waves in the absence of the long waves is greater than that in the presence of the long waves, consistent with the observation that the wind-waves appear to be stretched in the presence of the long waves.

	Wind only	Combined wind and waves	
U_∞ (m/s)	$\overline{ak}$	$\overline{ak}$	$(ak)_{amp}$
3.1	0.0644	0.0569	0.00831
4.1	0.136	0.111	0.00726
5.1	0.191	0.136	0.00557

Table 8.9: Wind-wave steepness *ak*

The variations in the wave steepness with the phase of the long waves are small (Figure 8.9) and correspond to the variations in the wavenumber, which are relatively much greater than the amplitude variations. The amplitude of the steepness variation with phase decreases with increasing free stream velocity, which also reflects the wavenumber variations. The maximum wave steepness appears to be around the zero upcrossing for the $U_\infty = 3.1$ and 4.1 m/s cases, moving towards the crest for the $U_\infty = 5.1$ m/s case. For the $U_\infty = 3.1$ and 4.1 m/s cases, the phase of the peak wave steepness corresponds to the maximum wind-induced current (Figure 6.11) and the end of the positive shear stress region (Figure 5.15). The zero upcrossing may therefore be expected to be the phase at which greatest wind-wave growth has occurred, and hence the greatest wave steepness. Beyond the zero upcrossing towards the crest, the wind-induced current becomes significant and reduces the wave steepness. The steepest waves appear to be in the region of greatest water surface acceleration, the steeper waves assisting the airflow to accelerate the water surface. The steepest wind-waves for

the $U_\infty = 5.1$ m/s case are around the long wave crest, which is as found by Longuet-Higgins and Stewart (1960) on the basis of wave-wave interaction, and reflects the observed wavenumber variation (section 8.4.5).

The second measure of surface roughness considered, the roughness Reynolds number, was defined in Chapter 5 as

$$R_k = k_r u_* / \upsilon \tag{8.11}$$

where k_r is a representative length scale for the roughness, in this case taken as the root mean square surface elevation. If $R_k < 5$, the surface may be regarded as fully smooth, and fully rough if $R_k > 30$. In Table 8.10 below, the average roughness values suggest that the water surface is smooth for the $U_\infty = 3.1$ m/s case, and rough for the $U_\infty = 5.1$ m/s case. The roughness Reynolds number for the wind-waves in the absence of the long waves is less than that in the presence of the long waves, suggesting that the water surface is smoother in the absence of the long waves, which is contrary to the observed wind-wave amplitude and wave steepness.

	Wind only	Combined wind and waves	
U_∞ (m/s)	$\overline{R_k}$	$\overline{R_k}$	$\widetilde{R}_{k_{amp}}$
3.1	3.50	7.16	4.54
5.1	24.1	39.6	17.5

Table 8.10: Wind-wave roughness Reynolds number R_k

From Figure 8.9, it appears in each case that the maximum roughness is between the crest and zero downcrossing, which corresponds to the phase of the maximum friction velocity. The maximum value of R_k for the $U_\infty = 5.1$ m/s case does approximately correspond to the maximum wind-wave slope although there is a large amount of scatter

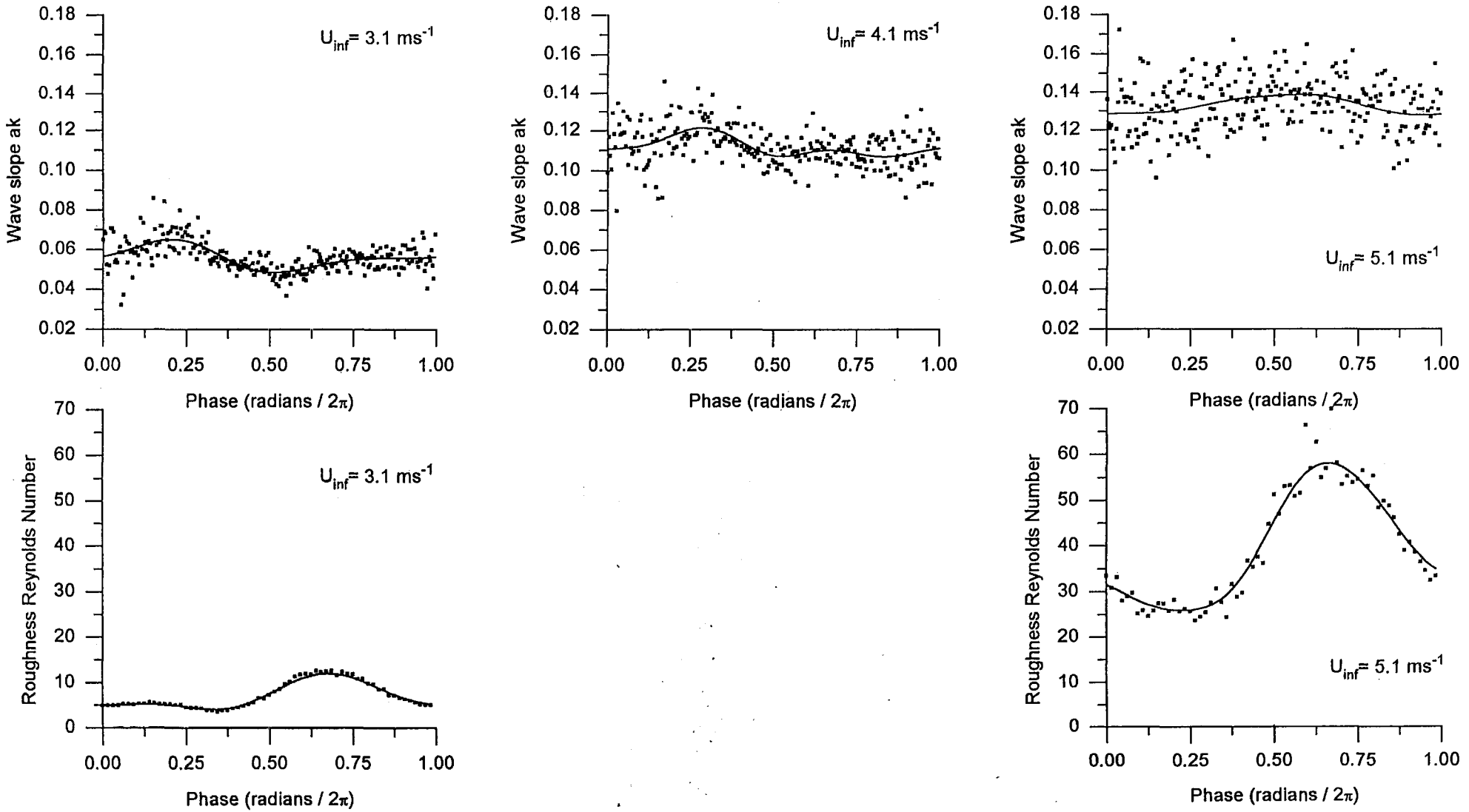


Figure 8.9: Variation of wind wave steepness and roughness Reynolds number with the phase of the long wave. • measured data, ——best fit line

in the data, but the peak value for the $U_\infty = 3.1$ m/s case does not correspond with the peak wave slope. The reason for these discrepancies is related to the variations in the friction velocity, which are principally due to non-separated sheltering effects over the long wave, rather than the roughness of the water surface itself. The roughness Reynolds number does not provide a fundamental measure of the roughness of the water surface, but rather a measure of how rough the flow senses the water surface is. The airflow above the wave affects the surface roughness in terms of the wind-generated waves' steepness and height, as already discussed, but the nature of the surface roughness itself does not have a significant effect upon the airflow. The non-separated sheltering effects over the long waves are dominating over the surface roughness effects in determining how rough the surface of the wave appears to the airflow.

The same effect accounts for the mean values of the roughness Reynolds numbers (Table 8.10) being greater for the combined wind and waves cases than for the wind only cases. The non-separated sheltering effects essentially cause the water surface to appear rougher than the roughness elements on the water surface would suggest. The flow is not separating over the long waves, so they cannot be classified as roughness elements, but they are affecting the 'apparent roughness' of the water surface. The wind-waves are larger for the wind only waves, but the smaller wind-waves in the combined cases appear rougher due to the greater friction velocity caused by non-separated sheltering effects over the long waves.

A third measure of the water surface roughness, the surface parameter C, was presented in Chapter 5. The surface parameter C, calculated from the measured velocities in the airflow, represents the roughness of the water surface. However, as described in Chapters 5 and 6, the calculated value of C includes the effect of the surface current, which makes the water surface appear smoother than the actual surface condition by releasing a portion of the shear stress at the water surface. The effect of the surface current may be removed from the values of C by rearranging equation 6.5 to

$$C' = C - \frac{U_s}{u_*} \tag{8.12}$$

where C' is the constant with the effect of the surface current removed. The variation of C with the phase of the underlying long waves showed a maximum value around the zero upcrossing (Figure 5.9), which corresponds to the phase of the maximum wind-generated current. It is very difficult to extrapolate with any measure of confidence the measured phase averaged velocities to deduce a value for the surface current U_s. However, approximations showed that for the $U_\infty = 3.1$ m/s case, the maximum value of C', and hence the smoothest water surface, was between the wave trough and zero upcrossing, and the minimum value of C', and the smoothest surface, is around the zero downcrossing. This again is contrary to the measured wind-generated waves, but is in agreement with the roughness Reynolds number. This is perhaps to be expected since the surface parameter again describes how the water surface appears to the overlying airflow, which again appears to be dominated by non-separated sheltering effects.

9. SUMMARY AND CONCLUSIONS

9.1 Introduction

The objectives of the present work were stated in Chapter 1 as being to investigate the airflow above the wave, to examine the wave kinematics in the water beneath the wave, and to consider the fundamental mechanisms of wind-wave interaction. In this final chapter, the results of the airflow and water flow investigations, together with the surface profile measurements are reviewed and brought together in order to understand the overall flow structure. Firstly however, the performance of the new wind-wave facility, as well as the instrumentation and experimental programme, is reviewed.

9.2 Experimental

The new wind-wave facility, which was designed and constructed as part of the present work, was found to perform very well. Airflow measurements and flow visualisation demonstrated that the intake structure and transition plate functioned as anticipated, producing a steady airflow in the working section. Velocity measurements over a flat smooth bed placed in the wind tunnel showed the velocity profiles to be as predicted by boundary layer theory, and turbulence levels were comparable with similar wind tunnels. Cross tank and along tank measurements showed that the airflow along the tunnel centre-line could be regarded as two-dimensional. The mechanically generated waves were repeatable and remained steady over time, and the wind-generated waves showed the form and growth rates anticipated. The magnitude of the wind-generated currents were similar to those measured by other researchers.

The measuring systems as well as the decomposition and transformation routines appeared to work very effectively, particularly in producing velocity data very close to the water surface in both the airflow and the water. Velocity measurements using the new laser processor under a regular sinusoidal wave with no wind showed excellent agreement with Stokes' second order theory. The use of a fixed laser outside the tunnel was considered preferable to a wave following device, since it did not disturb flow, and

provided greater certainty as to the measuring position. This was particularly important close to the water surface.

9.3 Airflow

One of the principal contributions of the present work is the evaluation of the streamlines in the airflow above the waves for a number of values of c/U_∞. The streamlines have not before been quantitatively determined, and their evaluation allows a detailed examination of the flow structure. The streamline plots show that there are fundamental changes in the structure of the airflow with c/U_∞. In particular, it was found that the structure of the airflow was determined by the elevation of the matched height relative to the water surface, and the development of large-scale recirculation cells. The matched height varies rapidly with the free stream velocity, increasing by more than an order of magnitude between $c/U_\infty = 0.30$ and 0.65. For the fastest free stream velocity case, $c/U_\infty = 0.30$, the matched height was less than 1 mm, but its presence was still seen to have a significant effect on the streamlines above. For the slowest case, $c/U_\infty = 0.65$, the matched height is of the order of the wave amplitude, with the recirculation cells being almost three times as deep as the water wave height.

The matched height also varies significantly with the phase of the long waves, which determines the form of the recirculation cells and the near-surface flow structure. The flow in the outer region is not determined by the wave form itself, but rather by the near-surface flow structure, or more particularly, by the pressure distribution at the edge of the recirculation cells. As shown by the profile of the streamlines' amplitude with elevation for the $c/U_\infty = 0.65$ case, very complex flow structures are set up as result of the pressure distribution at the edge of the recirculation cells.

The recirculation cells are similar in form to those proposed by Lighthill (1962), which were shown in Figure 2.1, but with the flow structure phase shifted by an amount dependent upon the free stream velocity. The recirculations also show some similarity with the numerical predictions of Gent and Taylor (1976), but again with the whole structure is phase shifted. Non-separated sheltering effects appear to be dominant,

particularly at faster wind speeds. The flow is very similar to potential flow at faster wind speeds, apart from non-separated sheltering effects with the disturbed region being only very close to the water surface. The streamlines showed that the long waves did not act as surface roughness, with no separation occurring in the lee of the crest, although the flow was disturbed and a high pressure region formed.

The time averaged velocity profiles in the airflow above the water waves were similar in form to those measured above a flat bed, although the flow recirculations described above produce significant distortions. The velocity profiles displayed a distinct log-linear region which was well fitted by the law of the wall, suggesting the existence of an inertial sublayer, and also a wake region which was well fitted by Coles' (1956) profile. These time averaged velocity profiles above the waves were not, however, fundamentally meaningful due to the large variations in the flow with the phase of the long waves. These arise as a result of the flow structure described above. Although the time averaged profiles provide a useful indication of the mean wind loading, horizontal velocity fluctuations with an amplitude of up to 15% of the free stream velocity were observed. These would clearly provide a significant cyclical loading on an offshore structure.

The turbulence measurements reflected the observed flow structure. For the two faster cases higher turbulence levels were observed on the lee of the crest, in the region of non-separated sheltering, than on the windward side. For the slower airflow case, the turbulence levels were high between the recirculation cells. In all cases there were significant turbulence variations with the phase of the long waves. This is clearly very complex behaviour for the purposes of predicting dispersion in the air over a wave.

The velocity measurements were used to deduce the surface stresses. Again, this task had not been previously attempted by other researchers. The airflow was analysed using the law of the wall and Coles' law of the wake. The friction velocity, surface roughness parameter C and wake parameter were calculated and their phase dependency examined. The variations in the flow parameters were found to reflect the non-separated sheltering effects. Using these flow parameters, estimates for both the shear and the normal surface

stresses could be made. In particular, data is provided to describe the variations in the surface stresses with the phase of the underlying long wave.

The normal stress was calculated both from the wake parameter using Coles' profile, which is proportional to the pressure gradient, and from first principles using the equations of motion. The normal stress calculated using the equations of motion confirms the expected pressure gradients deduced from the observed streamline pattern, with the pressure minima at the crest for the faster flow cases. In contrast, the variations in the normal stresses calculated from the Coles' profiles, are of the opposite sign to that expected. This is a result of the large pressure gradients $\partial p/\partial y$ close to the water surface, which reduce very rapidly with elevation above the water surface, coupled with the rapidly varying streamwise pressure gradients, which causes boundary layer theory to break down where there are large adverse pressure gradients.

The total shear stress is taken as the sum of the turbulent and wave associated shear stresses. The present results suggest that both the shear stress and C are determined by the opposing effects of surface roughness and release of the surface shear stress by the surface current.

9.4 Water Kinematics

The airflow above the water waves generates currents in which the surface values are of the same order as the orbital velocities, and which are very highly sheared close to the water surface. The wind-induced current for the faster airflow cases leads to the velocity at the water surface being positive over all phases of the wave cycle, and causes an increase in the velocity amplitude. However, there is a corresponding large return flow at greater depths, which can cause a reduction in the velocity amplitude. The wind-generated currents both in the absence and presence of long waves showed boundary layer-type behaviour. Unlike in the airflow, where the viscous sublayer was too thin, it was possible to take velocity measurements within the viscous sublayer for the wind-generated waves, and thus further verify the applicability of boundary layer theory.

As described in the previous section, the surface shear stress varies with the phase of the long wave, so it is therefore to be expected that the wind-generated current will also vary with the phase of the long wave. This effect has not been investigated by other researchers, but it is clearly crucial in understanding the nature of the wind-wave interaction. As a first approximation, the wind-induced current is isolated from the orbital velocities by assuming that the orbital motion can be described by a second order Stokes' solution, calculated using the measured wave parameters, and subtracting this irrotational velocity from the measured velocities.

The variations in the wind-induced current appear to correspond to the variations in the total surface shear stress calculated from the airflow velocity measurements. For the $U_\infty = 3.1$ and 5.1 m/s cases, the peak current occurs close to the zero upcrossing. Prior to this point the total shear stress has been positive and has thus accelerated the water flow. Beyond the zero upcrossing there is a short negative stress region to the crest, in which the negative stress decelerates the surface current. As a result a minimum velocity occurs just before the wave crest. This negative stress region corresponds to the maximum orbital velocities, suggesting that the orbital velocities are causing the water surface to drag the airflow at the air water interface, rather than vice versa.

The measured surface stresses deduced from the velocity measurements demonstrated that the airflow applied a significant mean shear stress to the water surface, and that the variations in the surface stresses with the phase of the long wave were significant. In addition, the surface shear stress produced a large variation in vorticity with depth, particularly close to the water surface. Existing wave solutions were not therefore valid in the presence of an overlying airflow.

A wave-current model, which took account of the mean shear stress, and a wind-wave model, which incorporated the effects of the fluctuating surface stresses, were developed. By examining the effect of each model separately, it was found that the dominant effect on the kinematics was the wind-generated current. Since this current varied significantly with the phase of the long waves, the task of modelling the wave-current interaction is particularly difficult. Very close to the water surface, the viscous

terms in the wind-wave model cause a reduction of the velocity, and additional terms in the dispersion equation modify the kinematics through the wavenumber. However, in the cases considered this effect was relatively small. The investigation demonstrated that when attempting to predict the wave kinematics in the presence of a significant overlying airflow, it is essential to consider the phase varying wind-induced current and not just the mean current.

9.5 Surface Elevation

The shape of the near sinusoidal long waves which were generated by the wave maker was modified by the overlying airflow. The wave forms became flatter with a reduced curvature on the windward side of the crest, and steeper with a greater curvature on the leeward side of the crest. This is consistent with the wind-induced current which was a maximum on the windward side of the crest, and a minimum on the leeward side. The spectra of the long waves showed that there was little change in the energy of the first harmonic, reflecting the observed negligible growth of the long wave amplitude along the tank. However, there was a significant growth in the energy of the second and third harmonics, reflecting the modified wave form described above. At the higher frequencies, there was a significant increase in energy as a result of the wind-generated waves.

The wind-generated waves were studied both in the presence and the absence of the long waves. The spectra for the wind-generated waves in the absence of the long waves showed distinct first, second, and in the faster cases, third harmonics. Their relative magnitude confirmed the observation that the wind-generated waves were steeper and more non-linear than the long waves. At frequencies above the third harmonic there was an increase in energy with increasing free stream velocity, relating to the generation of capillary ripples. The wind-wave spectra in the presence of the long waves showed a spreading of energy in the frequency domain. Careful comparison confirmed that this was due to the advection of the wind-waves by the long wave orbital velocities.

If the wind-waves were only modified due to the interaction with the long waves, then the apparent wavenumber would be expected to increase at the crests, and reduce in the

troughs of the long waves (Longuet-Higgins and Stewart, 1960). However, the measured wavenumber did not exhibit this trend. Instead there is a rapid reduction in the wavenumber before the wave crest, because the interaction of the wind-waves with the wind-generated current dominates over the wave-wave interaction. The current stretches the wind-waves and causes a reduction in the wavenumber. This effect is most apparent at the slower wind speeds, with wave-wave interaction appearing to become more important at faster wind speeds as the wave steepness increases.

9.6 Practical Applications

The principle aim of the present work was to investigate the fundamental interaction mechanisms between wind and waves, and not to attempt to formulate new design solutions. However, there are a number of practical applications for the key conclusions of the work. For the offshore engineer attempting to predict the wave loading on an offshore structure, one of the key findings of the present study is that it is essential to consider the phase varying wind-induced current, and not just the time averaged current. The large magnitude of the phase averaged wind-induced current fluctuations relative to the irrotational wave motion may cause models which consider only the time averaged current to significantly over or under estimate the wave kinematics, in particular close to the water surface.

In the airflow, it can be concluded that it is valid to use the wind velocity profiles as used over land in the design of offshore structures, but with careful consideration to roughness height used, which should not be the height of the long waves. The presence of the matched height and its elevation in relation to the wave amplitude is very important in determining the flow structure, which was found to be very complex, and will produce complex loadings and dispersion characteristics. An important effect of the recirculating flow structure is on wave hindcasting, based on wind speed measurements. It is likely that wind speed measuring devices, particularly those attached to buoys, will be within the recirculating region of the flow. As a result, significantly smaller velocities will be recorded. This will undoubtedly lead to misleading wave height predictions.

9.7 Further Work

The present study has highlighted several areas requiring further work:

a) In order to fully investigate the turbulent structure of the flow, in particular bursting phenomenon, the instantaneous Reynolds stress is required. This can only be obtained by measuring the two velocity components simultaneously, and thus requires a two component Doppler burst analyser. Having a two component system would also significantly reduce the time required to measure the velocities for further cases.

b) The present study has only considered favourable airflow cases, where the directions of airflow and wave propagation are coincident. Although this is perhaps the more extreme design case, the adverse case is also of practical interest, in particular the resulting modifications to the waves. The wind-wave interaction facility was designed with the flexibility to enable the fan to be positioned at the opposite end of the facility to the wave generator, and so produce an airflow in the opposite direction to wave propagation, whilst maintaining the other elements of the wind tunnel unaltered.

c) As discussed in Chapter 4, the present work has investigated the flow fields in the air and water for a number of values of the ratio c/U_∞, rather than for a range of wave steepnesses. Although the variation in the flow structure with c/U_∞ is perhaps of greater interest to the offshore engineer, who is principally interested in the flow over a prescribed long wave, the effect of wave steepness on the overall flow structure may also be important. Indeed, Gent and Taylor (1976), suggest that a more distinct separation type behaviour was likely at greater wave steepness. For the wind-generated waves which are superposed on the underlying long waves, the effect of an airflow on steeper waves and the influence of varying wave steepness, as well as the resulting disturbances in the airflow, would be useful in understanding the processes at the air water interface. Measurements for a number of further cases using mechanically generated waves of different steepness and a given airflow should therefore be undertaken.

d) Further work is required to compare the experimental results found in the present study with the theoretical models of Belcher, Harris and Street (1994) and Harris, Belcher and Street (1996). The present work provides the first set of measurements of the whole flow, encompassing the air, water and water surface, which is therefore suitable for comparison with the coupled air and water model developed by Belcher

et al. (1994,1996). This would allow further validation of the relative importance of the various wind-wave interaction mechanisms.

e) Surface elevation measurements in the present study were limited to determining the underlying long waves and the wind-waves with a fundamental frequency of less than approximately 7 Hz. No consideration was given to the higher frequency waves and capillary ripples. Although possibly not of great interest for the engineer, further knowledge of the surface roughness would permit a greater understanding of the stresses at the air water interface which determine the overall flow behaviour. This would require measurement of the small amplitude, high frequency wind-waves and ripples, and in particular determination of the variation in their characteristics with the phase of the long waves, using either high resolution wave gauges or optical instruments.

CITED LITERATURE

Baldock, T.E., Swan, C. & Taylor, P.H. 1996. A laboratory study of nonlinear surface waves on water. Phil. Trans. T. Soc. Lond. A, **354**, pp 649-676.

Banner, M.L. & Melville, W.K. 1976. On the separation of air flow over water waves. J. Fluid Mech., **77**, pp 825-842.

Belcher, S.E. & Hunt, J.C.R. 1993. Turbulent shear flow over slowly moving waves. J. Fluid Mech., **251**, pp 109-148.

Belcher, S.E., Newly, T.M.J. & Hunt, J.C.R. 1993. The drag on an undulating surface induced by the flow of a turbulent boundary layer. J. Fluid Mech., **249**, pp 557-596.

Belcher, S.E., Harris, J.A. & Street, R.L. 1994. Linear dynamics of wind waves in coupled turbulent air-water flow. Part 1. Theory. J. Fluid Mech., **271**, pp 119-151.

Bole, J.B. & Hsu, E.Y. 1969. Response of gravity water waves to wind excitation. J. Fluid Mech., **35**, pp 657-675.

Bowden, K.S. 1948. Observations of waves in a tidal current. Proc. Roy. Soc. A, **192**, pp 403-425.

Brooke Benjamin, T. 1959. Shearing flow over a wavy boundary. J. Fluid Mech., **6**, pp 161-205.

Chaplin, J.R. 1990. Computation of steep waves on a current with strong shear near to the surface. Water Wave Kinematics, A. Torum & O.T. Gudmestad (eds.), Kluwer Academic Publishers, pp 429-436.

Charnock, H. 1955. Wind stress on a water surface. Q. J. R. Met. Soc., **81**, pp 639-640.

Cheng, Z. & Mitsuyasu, H. 1988. Laboratory studies on the surface drift current induced by wind and swell. J. Fluid Mech., **243**, pp 247-259.

Cheng, Z. & Mitsuyasu, H. 1992. Laboratory studies on the surface drift current induced by wind and swell. J. Fluid Mech., **243**, pp 247-259.

Cheung, T.K. & Street, R.L. 1988. The turbulent boundary layer in the water at an air-water interface. J. Fluid Mech., **194**, pp 133-151.

Chu, J.S., Long, S.R. and Phillips, O.M. 1992. Measurements of the interaction of wave groups with shorter wind-generated waves. J. Fluid Mech., **245**, pp 191-210.

Coles, D. 1956. The law of the wake in the turbulent boundary layer. J. Fluid Mech., **1**, pp 191-226.

Cummins, I. & Swan, C. 1993. Non-linear wave-current interactions. Wave kinematics and Environmental Forces. Society for Underwater Tech., **29**, pp 35-51.

Cummins, I. & Swan, C. 1994a. An experimental study of non-linear wave-current interactions. Proc. 7th. Int. Conf. Behaviour of Offshore Structures, **2**, pp 393-403.

Cummins, I. & Swan, C. 1994b. Vorticity effects in combined waves and currents. Proc. 24th Int. Conf. Coastal Eng, Kobe.

Dalrymple, R.A. 1974. Water waves on a bi-linear shear current. Proc. 14th Conf. Coastal Eng., Hamburg, pp 626-641.

Dalrymple, R.A. 1977. A numerical model for periodic finite amplitude waves on a rotational current. J. Comp. Phys., **24**, pp 29-42.

Davis, R.E. 1970. On the turbulent flow over a wavy boundary. J. Fluid Mech., **42**, pp 721-731.

Davis, R.E. 1972. On prediction of the turbulent flow over a wavy boundary. J. Fluid Mech., **52**, pp 287-306.

Dean, R.G. 1970. Relative validities of water wave theories. J. Waterways and Harbors Div. ASCE, **96**, pp 105-119.

Dobson, F.W. 1971. Measurements of atmospheric pressure on wind-generated sea waves. J. Fluid Mech., **48**, pp 91-127.

Elliot, J.A. 1972. Micoscale pressure fluctuations near waves being generated by the wind. J. Fluid Mech., **54**, pp 427-448.

Gent, P.R. & Taylor, P.A. 1976. A numerical model of the air flow above water waves. J. Fluid Mech., **77**, pp 105-128.

Gent, P.R. & Taylor, P.A. 1977. A note on 'separation' over short wind waves. Boundary-Layer Meteorology, **11**, pp 65-87.

Gent, P.R. 1977. A numerical model of the air flow above water waves: Part 2. J. Fluid Mech., **82**, pp 349-369.

Harris, J.A., Belcher, S.E. & Street, R.L. 1996. Linear dynamics of wind waves in coupled turbulent air-water flow. Part 2. Numerical model. J. Fluid Mech., **308**, pp 219-254.

Hasselman, K. 1962. On the nonlinear energy transfer in a gravity wave spectrum: Part 1. J. Fluid Mech., **12**, pp 481-500.

Hasselman, K., Barnett, T.P., Bouws, E., Carlson, S., Cartwright, D.E., Enke, K., Ewing, J.A., Giennapp, H., Hasselmann, D.E., Kruseman, P., Meersburg, A., Müller, P., Olbers, D.J., Richter, K., Sell, W. & Walden, H. 1973. Measurements of wind-wave

growth and swell decay during the joint North Sea wave project (JONSWAP). Deutche Hydr. Zeit., suppl. A, **8**, 12.

Helmholtz, H. 1868. Uber discontinuirliche Flussigkeitsbewegungen. Mber. preuss. Akad. Wiss., pp 215-228.

Holmes, P. 1963. Wind generation by waves. Unpublished Ph.D. thesis, College of Swansea, University of Wales, UK.

Hsu, S.A. 1974. On the log-linear wind profile and the relationship between shear stress and the stability characteristics over the sea. Boundary-Layer Meteorology, **6**, pp 509-514.

Hsu, C-T. & Hsu, E.Y. 1983. On the structure of turbulent flow over a progressive water wave: theory and experiment in a transformed wave-following co-ordinate system. Part 2. J. Fluid Mech., **131**, pp 123-153.

Hsu, C-T., Hsu, E.Y & Street, R.L. 1981. On the structure of turbulent flow over a progressive water wave: theory and experiment in a transformed, wave-following co-ordinate system. J. Fluid Mech., **105**, pp 87-117.

Jeffreys, H. 1925. On the formation of water waves by wind. Proc. Roy. Soc., A, **107**, pp 189-206.

Kawamura, H., Okuda, K. and Toba, Y. 1981. Structure of turbulent boundary layer over wind waves in a wind wave tunnel. Tohoku Geophys. J. (Sci. Rep. Tohoku Univ. Ser. 5) **28**, pp 69-86.

Kawamura, H. & Toba, Y. 1988. Ordered motion in the turbulent boundary layer over wind waves. J. Fluid Mech., **197**, pp 105-138.

Kendall, J.M. 1970. The turbulent boundary layer over a wall with progressive surface waves. J. Fluid Mech., **41**, pp 259-281.

Kishida, N. and Sobey, R.J. 1988. Stokes' theory for waves on linear shear currents. J. Eng. Mech. ASCE, **114**, pp 1317-1334.

Kondo, J., Fujinawa, Y. & Naito, G. 1973. High-frequency components of ocean waves and their relation to aerodynamic roughness. J. Phys. Oceanography, **3**, pp 197-202.

Krügermeyer, L., Grünewald, M. & Ducknel, M. 1978. The influence of sea waves on the wind profile. Boundary-Layer Meteorology, **14**, pp 403-414.

Lamb, H. 1932. Hydrodynamics. Cambridge University Press.

Lighthill, M.J. 1962. Physical interpretation of the mathematical theory of wave generation by wind. J. Fluid Mech., **14**, pp 385-398.

Lin, C.C. 1995. The theory of hydrodynamic stability. Cambridge University Press.

Loehrke, R.I. & Nagib, H.M. 1976. Control of free-stream turbulence by means of honeycombs: a balance between suppression and generation. J. Fluids Eng., **98I**, pp 342-394.

Longuet-Higgins, M.S. 1963. The propagation of short surface waves on longer gravity waves. J. Fluid Mech., **177**, pp 293-306.

Longuet-Higgins, M.S. 1969a. A nonlinear mechanism for the generation of sea waves. Proc. Roy. Soc. A, **311**, pp 371-389.

Longuet-Higgins, M.S. 1969b. Action of a variable stress at the surface of water waves. Phys. Fluids **12**, pp 737-740.

Longuet-Higgins, M.S., Cartwright, D.E. and Smith, N.D. 1963. Observations of the directional spectrum of sea waves using the motions of a floating buoy. Ocean Wave Spectra. Prentice-Hall. pp 111-132.

Longuet-Higgins, M.S. & Stewart, R.W. 1960. Changes in the form of short gravity waves on long waves and tidal currents. J. Fluid Mech., **8**, pp 565-583.

Magnaudet, J. & Thais, L. 1995. Orbital rotational motion and turbulence below laboratory wind water waves. J. Geophys. Res., **100**, pp 757-771.

Mehta, R.D. 1977. The aerodynamic design of blower tunnels with wide-angle diffusers. Prog. Aerospace. Sci., **18**, pp 59-120.

Mehta, R.D. 1978. Aspects of the design and performance of wind tunnel components. Unpublished PhD Thesis, Imperial College, London.

Miles, J.W. 1957. On the generation of surface waves by shear flows. J. Fluid Mech., **3,** pp 185-204.

Miles, J.W. 1959a. On the generation of surface waves by shear flows. Part 2: J. Fluid Mech., **6,** pp 568-582.

Miles, J.W. 1959b. On the generation of surface waves by shear flows. Part 3: Kelvin-Helmholtz instability. J. Fluid Mech., **6**, pp 583-598.

Miles, J.W. 1960. On the generation of surface waves by turbulent shear flows. J. Fluid Mech., **7**, pp 469-478.

Mitsuyasu, H. & Honda, T. 1982. Wind-induced growth of water waves. J. Fluid Mech., **123**, pp 425-442.

Morel, T. 1975. Comprehensive design of axisymmetric wind tunnel contractions. J. Fluids Eng., **2I**, pp 225-236.

Motzfeld, H. 1937. Die turbulente Strömung an welligen Wänden. Z. angew Math. Mech. **17**, pp 193-212.

Papadimitrakis, Y.A., Hsu, E.Y. & Street, R.L. 1984. On the structure of the velocity field over progressive mechanically-generated water waves. J. Phys. Oceanography, **14**, pp 1937-1948.

Papadimitrakis, Y.A., Hsu, E.Y. & Street, R.L. 1986. The role of wave-induced pressure fluctuations in the transfer processes across an air-water interface. J. Fluid Mech., **170**, pp 113-137.

Papadimitrakis, Y.A., Hsu, E.Y. & Street, R.L. 1988. The bursting sequence in the turbulent boundary layer over progressive, mechanically generated water waves. J. Fluid Mech., **193**, pp 303-345.

Phillips, O.M. 1957. On the generation of waves by turbulent wind. J. Fluid Mech., **2**, pp 417-445.

Phillips, O.M. 1977. Dynamics of the Upper Ocean. Cambridge University Press.

Phillips, O.M. 1981. The dispersion of short wavelets in the presence of a dominant long wave. J. Fluid Mech., **107**, pp 465-485.

Rae, W.H. & Pope, A. 1984. Low speed wind tunnel testing, 2nd ed, Wiley, New York.

Shemdin, O.H., & Hsu, E.Y. 1967. Direct measurement of aerodynamic pressure above a simple progressive gravity wave. J. Fluid Mech., **30**, pp 403-416.

Shemdin, O.H. 1970. Wave influence on wind velocity profile. J. Waterways, Harbours and Coastal Engineering Division, ASCE, **96**, pp 795-814.

Sleath, J.F.A. 1984. Sea Bed Mechanics. John Wiley & Sons, New York.

Smith, S.D. 1980. Wind stress and heat flux over the ocean on gale force winds. J. Phys. Oceanogr., **10**, pp 709-726.

Snyder, R.L. 1974. A field study of wave-induced pressure fluctuations above surface gravity waves. J. Mar. Res., **32**, pp 497-532.

Snyder, R.L. and Cox, C.S. 1966. A field study of the wind generation of ocean waves. J. Mar. Res., **25**, pp 141-193.

Snyder, R.L., Dobson, F.W., Elliot, J.A. & Long, R.B. 1981. Array measurements of atmospheric pressure fluctuations above surface gravity waves. J. Fluid Mech., **102,** pp 1-59.

Stewart, R.H. 1970. Laboratory studies of the velocity field over deep-water waves. J. Fluid Mech., **42,** pp 733-754.

Swan, C. 1990. Convection within and experimental wave flume. J. Hydr. Res., **28,** pp 273-282.

Swan, 1992. A stream function solution for waves on a strongly sheared current. Coastal Eng. Conf., Venice, pp 684-697.

Swan, C. 1992. Wind wave interactions. BOSS Inter. Conf., London. pp 146-157.

Tennekes, H. and Lumley, J.L. 1992. A First Course in Turbulence. The M.I.T. Press, Cambridge, Mass.

Thais, L. and Magnaudet, J. 1995. A triple decomposition of the fluctuating motion below laboratory wind water waves. J. Geophys. Res., **100**, pp 741-755.

Thomas, G.P. 1990. Wave-current interactions: an experimental and numerical study. Part 2: Non-linear waves. J. Fluid Mech., **216**, pp 505-536.

Thomson, Sir W. 1871. Hydrokinetic solutions and observations. Phil. Mag. (4), **42**, pp 368-372.

Townsend, A.A. 1972. Flow in a deep turbulent boundary layer over a surface distorted by water waves. J. Fluid Mech., **55**, pp 719-735.

Tsao, S. 1959. Behaviour of surface waves on a linearly varying flow. Moskow Fiz. Tech. Inst. Issl. Mekh. Prikl. Mat., **3**, pp 66-84.

Ursell, F. 1956. Wave generation by wind. Surveys in Mechanics, Batchelor & Davies, Camb. Univ Press, 1956. pp 216-249.

White, F.M. 1985. Viscous Fluid Flow. McGraw Hill, New York.

Wills, J. 1990. Wind measurements: West Sole. ETSU Report.

Wu, 1968. Laboratory studies of wind-wave interactions. J. Fluid Mech., **34**, pp 91-111.

Wu, J. 1975. Wind-induced drift currents. J. Fluid Mech., **68**, pp 49-70.

APPENDIX A: WAVE-CURRENT MODEL

1. Transformations

$$\eta = z - \sum_{n=1}^{N} A_n \frac{\sinh(nkd + nk\eta)}{\sinh(nkd)} \cos(nk\xi) - B_n$$

$$\xi = x - \sum_{n=1}^{N} A_n \frac{\cosh(nkd + nk\eta)}{\sinh(nkd)} \sin(nk\xi)$$

2. Jacobian

$$J_o = 1$$

$$J_2 = -2ak \frac{\cosh k(d+\eta)}{\sinh kd} \cos k\xi$$

$$J_2 = -a^2k^2 \frac{\cosh(2k(d+\eta))}{2\sinh^4(kd)} \left[2\sinh^2(kd) + 3\right] \cos(2k\xi)$$

$$+a^2k^2 \frac{\cos(2k\xi)}{2\sinh^2(kd)} + a^2k^2 \frac{\left[\cosh(2k(d+\eta)) + 2\right]}{2\sinh^2(kd)}$$

3. Boundary conditions

The three usual boundary conditions are applied:

Bed assumed to be horizontal and impermeable

$$-J^{1/2} \frac{\partial \psi}{\partial \xi} = 0 \quad \text{on} \quad \eta = -d$$

Velocity normal to the surface is zero

$$-J^{1/2} \frac{\partial \psi}{\partial \xi} = 0 \quad \text{on} \quad \eta = 0$$

Dynamic free surface boundary condition

$$\frac{\partial p}{\partial \xi} = F_\xi J^{-1/2} - \frac{1}{2} \frac{\partial J}{\partial \xi} \left[\frac{\partial \psi}{\partial \eta}\right] - J \frac{\partial \psi}{\partial \eta} \frac{\partial^2 \psi}{\partial \eta \partial \xi} = 0 \quad \text{on} \quad \eta = 0$$

where $F_\xi = -g \sin(\theta)$ and θ is the angle between the y and η directions.

A further set of boundary conditions arises at the interface $\eta = -md$:

The time averaged vorticity must be zero at the lower edge of the current profile

$$\lim_{(\eta \to -mh)}(\omega) = 0$$

The value of the stream function and the velocity components must be continuous across the interface

$$\lim_{(\eta^+ \to -md)}(\psi) = \lim_{(\eta^- \to -md)}(\psi)$$

$$\lim_{(\eta^+ \to -md)}\left(J^{1/2}\frac{\partial \psi}{\partial \eta}\right) = \lim_{(\eta^- \to -md)}\left(J^{1/2}\frac{\partial \psi}{\partial \eta}\right)$$

$$\lim_{(\eta^+ \to -md)}\left(-J^{1/2}\frac{\partial \psi}{\partial \xi}\right) = \lim_{(\eta^- \to -md)}\left(-J^{1/2}\frac{\partial \psi}{\partial \xi}\right)$$

4. Stream function

$$\psi_o = -c\eta$$

$$\psi_1 = \left(Q\eta^2 + R\eta^3 + S\eta^4\right)\delta_s(\eta + md) - P\eta\delta_s(-\eta - md)$$

$$\psi_2 = a\left(2Q\eta + 3R\eta^2 + 4S\eta^3 + \frac{6S\eta}{k^2} + F_a\right)\frac{\sinh k(d+\eta)}{\sinh(kd)}\cos(k\xi)\delta_s(\eta + md)$$

$$+a\left(-\frac{3R\eta}{k} - \frac{6S\eta^2}{k} + F_b\right)\frac{\cosh k(d+\eta)}{\sinh(kd)}\cos(k\xi)\delta_s(\eta + md)$$

$$+aF_c \sinh k(d+\eta)\cos(k\xi)\delta_s(-\eta - md)$$

5. Dispersion Equation

$$c = \frac{\sigma}{k} = \left(\frac{g}{k}\tanh kd\right)^{1/2} + P - \frac{Q}{k}\tanh kd + \frac{3R}{2k^2} - \frac{3S}{k^3}\tanh kd - \frac{F_a}{2}\frac{1}{\cosh^2 kd}$$

6. Irrotational Kinematics

$$(U+u)_{\xi_{IRR}} = a\sigma\frac{\cosh k(d+\eta)}{\sinh(kd)}\cos(k\xi)$$

$$+a^2\sigma k\left[\frac{1}{4}\frac{\cosh 2k(d+\eta)\left[2\sinh^2(kd)+3\right]}{\sinh^4(kd)}\cos(2k\xi) - \frac{1}{4}\frac{\cos(2k\xi)}{\sinh^2(kd)}\right.$$

$$\left.-\frac{1}{4}\frac{\left[2+\cosh(2k(d+\eta))\right]}{\sinh^2(kd)} + \frac{1}{2}\frac{\cosh^2(k(d+\eta))}{\sinh^2(kd)}\cos^2(k\xi)\right]$$

7. Rotational Kinematics

$$(U+u)_{\xi_{ROT}} = (2Q\eta + 3R\eta^2 + 4S\eta^2)\delta_s(\eta + md) - P\delta_s(-\eta - md)$$

$$+a\left(2Q + 3R\eta + 6S\eta^2 + \frac{6S}{k^2} - kF_b\right)\frac{\sinh(k(d+\eta))}{\sinh(kd)}\cos(k\xi)\delta_s(\eta + md)$$

$$+a\left(-\frac{3R}{k} - \frac{6S\eta}{k} + F_a k\right)\frac{\cosh(k(d+\eta))}{\sinh(kd)}\cos(k\xi)\delta_s(\eta + md)$$

$$+a\left(Pk\frac{\cosh(k(d+\eta))}{\sinh(kd)} + F_c k\cosh(k(d+\eta))\right)\cos(k\xi)\delta_s(-\eta - md)$$

8. Constants

$$F_a = \frac{Q}{k}\frac{\cosh(kd)}{\sinh(kd)} - \frac{6S}{k^3}\frac{\cosh(kd)}{\sinh(kd)}\sinh^2(kd(1-m))$$

$$+\frac{(3R - 12Smd)}{k^2}\frac{\cosh(kd)}{\sinh(kd)}\sinh(kd(1-m))\cosh(kd(1-m))$$

$$F_b = -F_a\frac{\sinh(kd)}{\cosh(kd)}$$

$$F_c = \frac{Q}{k}\frac{\cosh(kd)}{\sinh^2(kd)} + \frac{6S}{k^3}\frac{\sinh(kd(1-m))\cosh(kd(1-m))}{\sinh(kd)} - \left(P + \frac{6Smd}{k^2}\right)\frac{1}{\sinh(kd)}$$

$$+\frac{(3R - 12Smd)}{k^2}\frac{\cosh(kd)}{\sinh^2(kd)}\sinh(kd(1-m))\cosh(kd(1-m))$$

$$-\frac{(3R - 12Smd)}{k^2}\frac{\cosh^2(kd(1-m))}{\sinh(kd)} - \frac{6S}{k^3}\frac{\cosh(kd)}{\sinh^2(kd)}\sinh^2(kd(1-m))$$

APPENDIX B: WIND-WAVE MODEL

1. Transformations

$$x = \xi - \frac{a\cosh(k(d+\eta))}{\sinh(kd)}\sin(k\xi)$$

$$z = \eta - \frac{a\sinh(k(d+\eta))}{\sinh(kd)}\cos(k\xi)$$

2. Stream Function

$$\psi_0 = -c\eta$$

$$\psi_1 = \left(\frac{iak\sigma}{\beta^2} - \frac{i\hat{\tau}}{\sigma\rho_w}\right)\left(e^{\alpha\eta} - \cosh(k\eta) - \frac{\sinh(k\eta)}{\tanh(kd)}\right)e^{ik\xi}$$

3. Dispersion Equation

$$c^2 = \frac{\tanh kd}{k}\left\{g + \frac{\Re\left[\hat{P}_n\right]}{a\rho_w} + \frac{\Im[\hat{\tau}]}{a\rho_w}\left(\coth(kd) - \frac{\beta}{k}\right) - \frac{\Re[\hat{\tau}]\beta}{ak\rho_w}\right\}$$

4. Rotational Kinematics

$$\Re[u_\xi] = \cos(k\xi)\left[-\frac{\Im[\hat{\tau}]}{\sigma\rho_w}\left(k\sinh(k\eta) + \frac{k\cosh(k\eta)}{\tanh(kd)}\right)\right]$$

$$+\sin(k\xi)\left[-\frac{\Re[\hat{\tau}]}{\sigma\rho_w}\left(k\sinh(k\eta) + \frac{k\cosh(k\eta)}{\tanh(kd)}\right)\right]$$

$$+\beta e^{\beta\eta}\left[\left(\cos(\beta\eta) - \sin(\beta\eta)\right)\left\{\frac{\Im[\hat{\tau}]}{\sigma\rho_w}\cos(k\xi) + \frac{\Re[\hat{\tau}]}{\sigma\rho_w}\sin(k\xi) - \frac{ak\sigma}{\beta^2}\sin(k\xi)\right\}\right]$$

$$-\beta e^{\beta\eta}\left[\left(\sin(\beta\eta) + \cos(\beta\eta)\right)\left\{\frac{\Im[\hat{\tau}]}{\sigma\rho_w}\sin(k\xi) - \frac{\Re[\hat{\tau}]}{\sigma\rho_w}\cos(k\xi) + \frac{ak\sigma}{\beta^2}\cos(k\xi)\right\}\right]$$

APPENDIX C: THIRD ORDER IRROTATIONAL WAVE THEORY

With: $\varphi = k(d+y))$

$\theta = (\sigma t - kx)$

$$u = a\sigma\coth(kh)\left\{C'\cosh(\varphi)\cos(\theta) + D\cosh(2\varphi)\cos(2\theta) + E\cosh(3\varphi)\cos(3\theta)\right\}$$

$$w = -a\sigma\coth(kh)\left\{C'\sinh(\varphi)\sin(\theta) + D\sinh(2\varphi)\sin(2\theta) + E\sinh(3\varphi)\sin(3\theta)\right\}$$

$$p = \rho g a\left\{\left[C\cosh(\varphi) - G\cosh(3\varphi)\right]\cos(\theta) + \left[D\cosh(2\varphi) - K\right]\cos(2\theta) - K\cosh(2\varphi) + \left[E\cosh(3\varphi) - G\cosh(\varphi)\right]\cos(3\theta)\right\}$$

$$c^2 \equiv \frac{\sigma^2}{k^2} = \frac{g}{k}\tanh(kd)\left\{1 + a^2k^2(F)\right\}$$

$$\zeta = a\cos(\theta) + \frac{a^2k\coth(kd)}{4\sinh^3(kd)}\left[2\cosh^3(kd) + \cosh(kd)\right]\cos(2\theta) - \frac{a^2k}{2\sinh(2kd)} + \frac{3a^3k^2}{64\sinh^6(kd)}\left[8\cosh^6(kd) + 1\right]\cos(3\theta)$$

where:

$$C = \frac{1}{\cosh(kd)}\left\{1 + \frac{a^2k^2}{8}\left(3 - \frac{\left[3 - 2\tanh^2(kd)\right]}{\sinh^2(kd)} + \frac{3}{\sinh^4(kd)}\right)\right\}$$

$$C' = \frac{1}{\cosh(kd)}\left\{1 - \frac{a^2k^2}{8}\left(5 + \frac{\left[11 - 2\tanh^2(kd)\right]}{\sinh^2(kd)} + \frac{\left[6 - 2\tanh^2(kd)\right]}{\sinh^4(kd)}\right)\right\}$$

$$D = \frac{3ak}{4\sinh^3(kd)\cosh(kd)}$$

$$E = -\frac{a^2k^2\left\{4\sinh^2(kd)-9\right\}}{64\sinh^6(kd)\cosh(kd)}$$

$$F = \frac{1}{8\sinh^4(kd)}\left\{8\sinh^4(kd)+8\sinh^2(kd)+9-2\tanh^2(kd)\right\}$$

$$G = \frac{3a^2k^2}{8\sinh^4(kd)\cosh(kd)}$$

THE EXPANDED JACOBIAN

$$J_0 = 1.0$$

$$J_1 = -2ak\frac{\cosh\left[k(d+\eta)\right]}{\sinh(kd)}\cos(k\xi)$$

$$J_2 = -a^2k^2\frac{\cosh\left[2k(d+\eta)\right]}{2\sinh^4(kd)}\left\{2\sinh^2(kd)+3\right\}\cos(2k\xi)+\frac{a^2k^2\cos(2k\xi)}{2\sinh^2(kd)}$$
$$+a^2k^2\frac{\left\{\cosh\left[2k(d+\eta)\right]+2\right\}}{2\sinh^2(kd)}$$

$$J_{31} = a^3k^3\frac{\left\{\cosh(2kd)+2\right\}\sinh\left[k(d+\eta)\right]}{\sinh(kd)\sinh(2kd)}\cos(k\xi)$$
$$+a^3k^3\frac{\cosh^3\left[k(d+\eta)\right]}{\sinh^5(kd)}\left\{2\sinh^2(kd)+3\right\}\cos(k\xi)$$
$$+a^3k^3\frac{\cosh\left[k(d+\eta)\right]}{8\sinh^5(kd)}\left\{10\sinh^4(kd)+4\sinh^2(kd)+9\right\}\cos(k\xi)$$

$$J_{33} = a^3k^3 \frac{\cosh^3[k(d+\eta)]}{8\sinh^7(kd)}\left\{-24\sinh^4(kh) - 48\sinh^2(kh) - 27\right\}\cos(3k\xi)$$

$$+a^3k^3 \frac{\cosh[k(d+\eta)]}{32\sinh^7(kd)}\left\{88\sinh^4(kd) + 168\sinh^2(kd) + 81\right\}\cos(3k\xi)$$

$$J_4 = a^4k^4\left\{A\cosh^4[k(d+\eta)] + B\cosh^2[k(d+\eta)] + C\right\}$$

$$-a^4k^4 \frac{\{\cosh(2kd) + 2\}\sinh[2k(d+\eta)]}{2\sinh(2kd)\sinh^2(kd)}$$

where

$$A = \frac{1}{\sinh^4(kd)} + \frac{3}{\sinh^6(kd)} + \frac{9}{4\sinh^8(kd)}$$

$$B = -\frac{5}{4\sinh^2(kd)} - \frac{4}{\sinh^4(kd)} - \frac{51}{8\sinh^6(kd)} - \frac{9}{4\sinh^8(kd)}$$

$$C = -\frac{5}{8\sinh^2(kd)} - \frac{3}{8\sinh^4(kd)} + \frac{9}{16\sinh^6(kd)} + \frac{27}{32\sinh^8(kd)}$$

APPENDIX D: THE VALIDITY OF VARIOUS WAVE THEORIES

(after Dean, 1970)

